THE EFFECTS OF A HIGHLY VISCOUS LIQUID PHASE ON TWO-PHASE FLOW IN A VERTICAL PIPE AND PIPELINE COMPONENTS.

ALASTAIR DAVID STUART, BEng

Submission for Degree of PhD

Heriot-Watt University
School of Engineering &
Physical Sciences

August 2005

ACKNOWLEDGEMENTS

I am particularly indebted to Dr. David A. McNeil for his invaluable support, expertise and great patience.

I am also grateful to all the staff and technicians of the Heriot-Watt School of Engineering and Physical Science, most notably Mr Richard Kinsella, who was responsible for the majority of the test rig construction.

And finally thanks to Dr. Stanley Morris and the funding provided by the European Commission (DGXII – Science Research and development) through the INOVVATOR project (Environment and Climate programme).

CONTENTS

LIST OF TABLES

LIST OF FIGURES

LIST OF PLATES

NOMENCLATURE

A_1	Parameter defined by Equation 2.54	
A_2	Parameter defined by Equation 2.55	
A_3	Parameter defined by Equation 2.56	
A	Flow area	m^2
A_g	Flow area of gas	m^2
A_l	Flow area of liquid	m^2
A_o	Flow area of orifice plate	m^2
B	Chisholm B parameter	
C	Chisholm C parameter	
c_D	Discharge coefficient	
c_m	Momentum correction factor	
c_V	Velocity coefficient	
$\dot{D}$	Deposition rate	Kg/m^2s
D	Diameter of pipe	m
E	Entrained liquid fraction	
E_1	Parameter defined by Equation 2.70	
E_2	Parameter defined by Equation 2.71	
f	Friction factor	
F	Frictional energy loss per unit mass	Jkg^{-1}
Fr	Froude number	
g	Gravitational constant, 9.81	ms^{-2}
G	Mass flow rate/unit area	kg/m^2s
G_g	Mass flow rate/unit area of gas	kg/m^2s
G_l	Mass flow rate/unit area of liquid	kg/m^2s
G_{le}	Mass flow rate/unit area of the liquid entrained	kg/m^2s
G_{lf}	Mass flow rate/unit area of the liquid film	kg/m^2s
h_l	Head loss	m
I	Intensity of gamma radiation passing through the tube	Counts s^{-1}
I_o	Initial intensity of gamma radiation	Counts s^{-1}

I_l	Intensity of gamma radiation passing through the tube full of liquid	Counts s^{-1}
I_g	Intensity of gamma radiation passing through the tube full of gas	Counts s^{-1}
J	Momentum flux	N/m^2
K_c	Loss coefficient Equation 6.5	
k	Slip ratio	
L	Length	m
M	Mass flow rate	kgs^{-1}
Ma	Mach number	
M_g	Mass flow rate of gas	kgs^{-1}
M_l	Mass flow rate of liquid	kgs^{-1}
n	Flow behaviour index	
P	Pressure	N/m^2
Q	Volume flow rate	m^3/s
Q_g	Volume flow rate of gas	m^3/s
Q_l	Volume flow rate of liquid	m^3/s
R	Dimensional entrainment parameter Equation 2.47	
R	Radius	m
Re	Reynolds number	
S	Pipe perimeter	m
S	Diameter ratio Equation 2.26	
t	Wall thickness or thickness of homogeneous material	m
u_a	Average velocity	m/s
u_{gs}	Superficial velocity of the gas	m/s
u_g	Gas velocity	m/s
u_{gj}	Drift velocity of the gas relative to the mean fluid velocity	m/s
u_l	Liquid velocity	m/s
u_{ls}	Superficial velocity of the liquid	m/s
u_{lj}	Drift velocity of the liquid relative to the mean fluid velocity	ms^{-1}
v	Specific volume	m^3/kg
v_C	Specific volume of core	m^3/kg

v_g	Specific volume of gas	m^3/kg
v_g	Specific volume of liquid	m^3/kg
v_m	Specific volume of mixture	m^3/kg
We	Weber number	
x	Quality (by mass)	
X	Martinelli parameter	

Greek Letters

α	Kinetic energy correction factor	
α	Void fraction	
α_l	Liquid fraction	
β	Loss coefficient	
Γ	Physical property parameter, Equation 7.22	
γ	Isentropic index of air	
δ	Liquid film thickness	m
δ^+	Non-dimensional liquid film thickness	
ε	Energy	J
μ_g	Viscosity of gas	$N\ s/m^2$
μ_h	Homogeneous viscosity	$N\ s/m^2$
μ_l	Viscosity of liquid	$N\ s/m^2$
ρ	Density	kg/m^3
ρ_h	Homogeneous density	kg/m^3
ρ_l	Density of liquid	kg/m^3
ρ_g	Density of gas	kg/m^3
σ	Surface tension	N/m
σ_g	Mass attenuation coefficient for gas	

σ_l	Mass attenuation coefficient for liquid	
σ_t	Mass attenuation coefficient for pipe	
τ	stress	N/m^2
τ_w	Wall shear stress	N/m^2
ϕ^2	Two-phase multiplier	
ϕ_g^2	Two-phase multiplier, gas single-phase flow, gas mass flux of Gx	
ϕ_{go}^2	Two-phase multiplier, gas single-phase flow, gas mass flux of G	
ϕ_l^2	Two-phase multiplier, liquid single-phase flow, liquid mass flux of G(1-x)	
ϕ_{lo}^2	Two-phase multiplier, liquid single-phase flow, liquid mass flux of G	
ς	Ratio of valve opening to fully open position	

Subscripts

av	Average
c	Characteristic
d	Down stream
e	Entrainment
f	Film
g	Gas
go	All-gas
h	Homogeneous
i	Gas or liquid phase
l	Liquid
lo	All-liquid
m	Mixture
n	Nominal
tp	Two-phase
u	Up stream
w	wall

Chapter 1

INTRODUCTION

This study examines those issues peculiar to two-phase flows where the viscosity of the liquid phase is considerably higher than that of water. Flows of this kind are prevalent in industry. A particular instance has been identified in the emergency venting of polymerisation reactors. During the manufacture of styrene, for example, under blow down conditions a highly viscous two-phase flow occurs. The safe passage of this two-phase mixture from the reactor vessel to a holding tank relies on the application of appropriate design criteria. Due to an absence in the literature of conclusive studies in this area, there exists an element of uncertainty in this design and the selection of suitable components for associated emergency relief systems.

The behaviour of single-phase flows in pipes and pipeline components has been extensively investigated. With respect to highly viscous single-phase flows the literature is evidently deficient although some standard pipe line components have been investigated. An even greater deficiency exists with regard to highly-viscous two-phase flows in pipes. No data were found for highly viscous two-phase flows in standard pipeline components. As there is little, or in some cases no, highly viscous data, the empirical verification of models is not possible. Some authors have addressed specific issues relating to highly viscous flows but these are either very narrow in their application or the viscosity range is limited. No current publication provides a thorough review of existing correlations with respect to highly viscous flows.

A fundamental requirement of this work was the acquisition of highly viscous single-phase and two-phase data. This was achieved through the design and construction of a purpose built test facility. Data obtained from this test facility was used to evaluate the performance of current design methods and models. Evaluations made against experimental data allowed the formulation of recommendations with regard to the most reliable models to employ and the accuracy with which highly viscous flows can be predicted. It is envisaged that the application of these recommendations will improve the certainty with which highly viscous pipeline systems can be designed.

Chapter 2 presents a detailed review of the literature. The design methodology and test facility are described in Chapter 3. Chapter 4 provides a detailed description of the instrumentation installed in the test facility and the corresponding calibration procedures. Experimental procedures, techniques for data processing and commissioning tests are described in Chapter 5. Chapter 6 presents a synopsis of all test data. In Chapter 7 test data are analysed and comparisons are made with models taken from the literature. Final conclusions and recommendations are made in Chapter 8.

Chapter 2

LITERATURE REVIEW

2.1 Introduction

A two-phase mixture is the combination of two of three possible phases; solid, liquid and gas. For this study the simultaneous flow of a gas and liquid under adiabatic conditions is investigated i.e., there is negligible change of phase of either one of the components through evaporation or condensing. In spite of this simplification, the two-phase flows remain complex. The two major contributors to their complexity are;

i. The large number of influential variables that need to be considered in an analysis of a two-phase system e.g., mass flow rate, mass ratio of components, surface tension and the density and viscosity of each phase.

ii. The continually changing boundary between the phases, the shape and distribution of which has a major effect on the flow characteristics of the mixture.

This latter characteristic, the deformability of the gas-liquid interface, gives rise to the distinguishable patterns or flow regimes of two-phase flows. Much work has been done to categorise these regimes with the results usually presented as flow pattern maps. These results allow the application of regime dependant flow models. Difficulties in this approach arise due to the ambiguous nature of the transition zones that are used to distinguish between flow regimes.

The methods used by two-phase investigators to develop flow models loosely fall into three categories, Hewitt [1] (1982).

The *Empirical Approach*: Correlating equations are fitted to experimental data. This approach can produce convenient design relationships that can be applied independently of flow pattern, e.g. the C parameter method of Chisholm [2] (1967).

The *Analytical Approach:* Starting from first principles, local instantaneous equations are constructed to describe phase and interface conditions. Resulting in relationships which are more systematic and rigorous than those derived using an empirical approach. These models require more knowledge of flow parameters and are flow pattern dependent, e.g. drift flux model as described by Wallis [3] (1969).

The *Phenomenological Approach:* This requires a greater understanding of the interfacial distribution and other occurring phenomena to be obtained and is therefore flow pattern dependent. The more in depth the knowledge, the better the phenomena are described using theoretical and semi-theoretical models.

Development in measuring techniques has enabled two-phase investigators to define correlations based on relatively easily measured parameters. A good example of this is void fraction, the knowledge of which is key to various pressure drop correlations and as a result many experimental methods for measuring and correlating equations for predicting the void fraction have been developed.

Pressure drop prediction is of primary interest in many two-phase applications. Certain two-phase models have received more attention than others due either to the ease of application or to their general applicability. The two most dominant are the homogeneous and separated flow models, both of which make simplifying assumptions to reduce the complexity of the analysis. More sophisticated models have also emerged which try and capture the more complex relationships encountered in gas-liquid systems.

Due to differing approaches of investigators, the varied applications of two-phase flows, its inherent complexities, and experimental variations such as orientation, pipe size, and viscosity, a large number of publications have been generated. This extent of literature, even accepting variations in experimental practice, has in its self added confusion to an already difficult subject. Recent work has focused on assessing the effectiveness and applicability of existing methods. With out such reviews it would prove difficult to confidently apply two-phase methods, Simpson *et al* [4] (1987)

The focus of this review is to highlight the significant developments in two-phase flow, with particular reference to the annular flow regime, then extract correlations and models that contribute and improve modelling of highly-viscous gas-liquid flows. The review begins by examining the relevant aspects of single-phase flows and then the basics of two-phase flow, there by giving access to the more difficult concepts and correlations. The most relevant correlations and applicable two-phase models are identified and reviewed.

2.2 Single-Phase Flow

The major complication of a single-phase flow is the existence of the two distinct behaviours or flow regimes, laminar and turbulent. The implication of these flow regimes has been thoroughly investigated in the literature and so long as the flow regime of a liquid is established, appropriate frictional relationships can be used to great effect. The prevalence of a turbulent or laminar flow regime in a single-phase flow is determined from the Reynolds number. Pipe flows of low Reynolds number, less than 2000, are laminar in nature, between 2000 and 10,000 there exists a transition zone, and flows above 10,000 flows are fully turbulent. In a straight length of pipe the transition will be a strong factor of the roughness of the pipe wall. In a pipeline component the transition zone is strongly dependent on geometry. The more involved and abrupt the geometry of a pipeline component the lower the Reynolds number at which turbulent flow will occur.

2.2.1 Flow in Pipes

Fluid flowing in a pipe is understood to move in streams, for an early example see Johansen [5] (1930). The layer of fluid immediately in contact with the pipe wall is stationary and the fluid stream in the pipe centre travels with the greatest velocity. If the velocity of each stream of a fluid flowing in a pipe was measured, the velocity would be found to increase from a minimum, at the pipe wall, to a maximum, at the pipe centre. The velocity profile of the fluid streams is different for turbulent and laminar flows. The turbulent velocity profile is flat and shallow where as the laminar velocity profile is far more parabolic and consequently has a far greater effect on the application of momentum and energy balances. The normal practice is to use an average fluid velocity to represent all fluid velocities present in a flow and then compensate for the effect of the velocity profile by using momentum and energy correction factors.

The difference between turbulent and laminar velocity profiles is illustrated by the difference in magnitude of their corresponding momentum and kinetic energy correction factors that are found in the literature. The momentum correction factor for a turbulent flow is 1.02 compared to 1.33 for laminar flow. The kinetic energy correction factor for turbulent flow is 1.058, compared to 2 for laminar flow.

The losses incurred by the movement of a fluid in a pipeline system are due to pipe friction or form losses from geometry change.

The reported settling length for a turbulent flow, the distance required before the turbulent velocity profile is fully established, is approximately 30 pipe diameters. The *Blasius* correlation is used to relate the friction factor, f, to the Reynolds number, Re thus;

$$f = 0.079\,\mathrm{Re}^{1/4} \qquad (2.1)$$

For a straight pipe of length, L, and diameter, D, the head loss of a flow travelling with an average velocity, u_{av}, is given by *Darcys'* formula;

$$h_l = \frac{4fL}{D}\frac{u_{av}^2}{2g} \qquad (2.2)$$

The reported settling length for laminar flow is proportional to the Reynolds number. In comparison to turbulent flows the settling length for laminar flows is far less at low Reynolds number and far greater at high Reynolds number. A laminar flow will require a settling length of typically 100 pipe diameters to fully develop close to transition. In the case of high viscosity liquids this will result in flows of low Reynolds number requiring only short settling lengths to fully develop. The friction factor of a laminar flow is wholly dependent on the Reynolds number and is independent of the pipe wall roughness, allowing *Poiseulies'* formula to be used to give an explicit solution for the *Darcys'* formula, Equation 2.2, thus;

$$f = \frac{16}{\mathrm{Re}} \qquad \& \qquad \Delta p = \frac{8\mu LQ}{\pi r^4} \qquad (2.3)$$

Since the Reynolds number is dependent on viscosity, a highly viscous flow will remain in the laminar flow regime long after a low viscosity flow of an equivalent mass flow rate. This is because the disruption to the flow streams in a fluid, normally caused by component geometry and surface roughness, which lead to turbulent flow requires a greater dynamic force to overcome the retarding effects that viscosity has on the inertia of the fluid.

2.2.2 Flow in Pipeline Components

When a pipeline component is included in the flow path of a fluid, additional energy losses are incurred. These additional energy losses are due to the geometry of the pipeline component and can involve abrupt changes in direction, contractions and expansions, and non-uniform sections. The losses incurred due to the movement of the fluid inside the component are summed with losses induced in the upstream and downstream pipes to give the total energy losses.

Several approaches have been made to standardise the procedure for calculating the energy loss associated with pipeline components. The not so widely used equivalent length method introduces a hypothetical length of pipe to represent the total loss of the component. A major disadvantage of this method for turbulent flows is its reliance on the Reynolds number and consequently the relative roughness of the pipe wall. The implication being that the energy loss becomes dependent on the pipe wall friction factor used to determine the equivalent length. This is not a disadvantage when applying this method to laminar flows since the friction factor does not need to be considered. Kitteredge & Rowley [6] (1957) improved on the equivalent length method by presenting what they call the no-length friction coefficient, compensating for the tendency of the equivalent length method to over predict the pressure drop for laminar flows.

A more common approach for calculating losses due to pipeline components is to use a loss coefficient, β, specific to every fitting. The energy loss, ε, attributable to a pipeline component with a loss coefficient, β, is given by;

$$\varepsilon = \beta \frac{u_{av}^2}{2} \tag{2.4}$$

Turbulent flows loss coefficients are predominantly a function of the fitting geometry and as a result the literature provides theoretical solutions and correlations for turbulent flows. However loss coefficients in the laminar regime are far less available. This is because the velocity profile is critical in determining kinetic energy and momentum forces present in a fluid and the inability to fully ascertain velocity distributions through pipeline restriction makes the theoretical calculation of laminar loss coefficients much more difficult. The determination of energy losses through pipeline components for low Reynolds number flows is achieved by using empirically derived coefficients. Technically all instances of laminar flow can be theoretically resolved by solving the Navier-Stokes Equations, although this is not always practical.

Several investigators have determined loss coefficients for a range of standard pipe fittings. Hooper [7] (1981) and Hooper [8] (1988) correlation employs a two-k method to accommodate a range of component sizes for Reynolds numbers of 1 upwards. For an orifice plate with a diameter ratio, S, Hooper [8] gives the correlation;

$$\beta = \left[2.72 + S^2\left(\frac{120}{\mathrm{Re}} - 1\right)\right]\left[1 - S^2\left[\frac{1}{S^4} - 1\right]\right] \tag{2.5}$$

The correlation for an abrupt enlargement is given as;

$$\beta = 2\left[1 - \frac{1}{S^4}\right] \tag{2.6}$$

And for a globe valve, Hooper [7] gives the correlation;

$$\beta = \frac{1500}{\mathrm{Re}} + 4 \tag{2.7}$$

Kitteridge & Rowley [6] (1957) determined loss coefficients for a number of standard fittings over the range of Reynolds numbers approximately 20 to a 1000. Two test fluids were used, kerosene and SAE 10 oil, viscosities of 1.63 and 33 m Pas respectively. The fittings were tested on a 12.7 mm diameter pipe system.

Alvi *et al* [9] 1978 conducted experiments on orifice plates and nozzles using a 54 mm diameter pipe system. Four oils having viscosities of 10.5, 20 100 and 350 CS were used allowing loss coefficients to be determined over a Reynolds number range of 1 to 10000.

Edwards *et al* [10] 1985 determined loss coefficients for a number of standard fittings for pipe diameter ranging from 12.7 mm to 50.8 mm. To achieve a range of Reynolds numbers from 0.1 through to 1000 several test liquids were used. These included Newtonian fluids glycerol-water, viscosity range 110 to 580 mPas and lub oil, viscosity 251 mPas. They also included non-Newtonian fluids CMC-water and china clay-water.

Bannerjee *et al* [11] (1969) produced general correlations to predict frictional pressure drop across a 12.7 mm globe valve in the horizontal flow plane for laminar flows. A solution of sodium salt of carboxymethylcellulose was used to provide four tests liquids with viscosities of 14, 122, 342 and 711 m Pas. If the ratio of opening to the full opening of a globe valve is, ζ, then the pressure loss is correlated by;

$$\frac{\Delta p}{\rho u^2} = 8.266\,\mathrm{Re}^{-0.061}\,\varsigma^{-0.797} \tag{2.8}$$

A review by McNeil & Morris [12] (1994) reported discrepancies that occur when comparing the theoretical correlations of Hooper [7] (1981) and Hooper [8] (1988) to empirically derived loss coefficients. Agreement between theory and data was described as poor for abrupt enlargements and orifice plates. However the data of Edwards *et al* [10] for the 25.4 mm globe valve was reasonably well represented by the Hooper [7] correlation.

The laminar flow work of Alvi *et al* [9] 1978, Edwards *et al* [10], and Kitteridge & Rowley [6] all demonstrate that above some critical value of Reynolds number the loss coefficient is wholly dependent on the geometry of the restriction. And that below this critical value the loss coefficient is strongly dependent on the Reynolds number. Edwards *et al* [10] reported on the critical Reynolds number for several fittings. For a 25.5 mm diameter globe valve the critical Reynolds number was observed to be around

10. Above this value the loss coefficient was 25.4 and below it the loss coefficient was correlated by;

$$\beta = 384/\mathrm{Re} \qquad \mathrm{Re} < 10 \qquad (2.9)$$

For an abrupt enlargement of diameter ratio 2.18, Edwards *et al* [10] found the critical Reynolds number to be around 250. Above this value the loss coefficient was 0.62 and below it the correlation for the loss coefficient is given as;

$$\beta = 150/\mathrm{Re} \qquad \mathrm{Re} < 250 \qquad (2.10)$$

Using an orifice plate with a diameter ratio of 0.577, Edwards *et al* [10] found the critical Reynolds number to be around 60. Below this Reynolds number the correlation given for the loss coefficient is;

$$\beta = 154/\mathrm{Re} \qquad \mathrm{Re} < 60 \qquad (2.11)$$

Edwards *et al* [10] and Alvi *et al* [9] both reported that for orifice plates the critical Reynolds number was also a function of the diameter ratio.

A study by Kitteridge & Rowley [6] using 12.7 mm diameter 'composition' globe valve showed that the critical Reynolds number was around 350. Below the critical Reynolds number the loss coefficient for the globe valve was correlated by;

$$\beta = C/\mathrm{Re}^{n} \qquad \mathrm{Re} < 350 \qquad (2.12)$$

where constants C and n are 203 and 0.5 respectively.

The existence of a critical Reynolds number in the laminar flow regime was confirmed by a recent study by McNeil *et al* [13] (1999) on viscous flow through contractions. A Luviskol K90 solution was used to explore the discharge behaviours of low Reynolds numbers. It was concluded that between Reynolds numbers of 50 to 200 there is a transition zone, where both viscous and inertia forces must be considered. This is in keeping with the review of McNeil & Morris [12] who advised the treatment of loss coefficients for laminar flows to be in terms of a low Reynolds number range and higher Reynolds number range. Thus accommodating loss coefficients derived when the losses are dominated by either the viscous or inertia-driven forces.

The dependency of loss coefficients derived at low Reynolds numbers on the Reynolds number is due to the presence of molecular friction fluid losses. These viscous losses, generated as the fluid passes through the non-uniform sections of the pipeline component, are not inconsiderable compared to form losses and are the dominant cause of energy loss at very low Reynolds numbers. McNeil [14] (1998) has published a model that predicts the behaviour of highly viscous flows through an abrupt enlargement. The difficulties associated with modelling laminar flows were tackled by treating the flow as having two distinct streams, a core and an annulus stream. This allowed the momentum and kinetic energy stored in the velocity distributions of the fluid flow to be represented by altering the relative area of one stream to another. By treating an abrupt enlargement as consisting of two parts, a gradual expansion and a settling length, the variations in momentum and kinetic energy that occur as a flow proceeds through an expansion are mirrored. This is a simplistic model but its application is of importance as the energy loss mechanisms that occur in an abrupt enlargement occur in many other pipeline fittings.

2.2.3 Summary

Single-phase flow of fluids in pipes is well understood. Easily applied solutions derived from energy and momentum balances exist for a fully developed flow. The application of theoretical solutions is linked to a single distinguishing factor, the Reynolds number, which is an indication of the nature of the flow, either laminar or turbulent. Single-phase flows are in reality two-dimensional, the velocity of the flow across any given section is not constant.

Momentum and energy correction factors determined for turbulent flows are of little consequence due to the shallow nature of the turbulent velocity profile. This is not the same for laminar flows where the far more pronounced velocity profile is of major consideration. As it is difficult to predict the velocity distribution of flow in pipeline components investigators employ empirical loss coefficients when evaluating energy losses incurred by pipeline components. Loss coefficients for turbulent flows are well established because they are singularly dependent on the geometry of the pipeline component.

The determination of loss coefficients for high viscosity low Reynolds number flows is less certain. The velocity profile of a laminar flow is more influential than that of the turbulent flow and this coupled with the effects of large viscous forces causes losses to become a strong function of the Reynolds number. The loss coefficient of a pipeline component is a function of the Reynolds number and geometry below a critical Reynolds number. Above this critical Reynolds number the loss coefficient is geometry dependent only, even though the flow may still be in the laminar flow regime.

Treatment in the literature of the behaviour of low Reynolds number flows through pipeline components has not been exhaustive. A deficiency exists in provision of loss coefficients for standard fittings subjected to high viscosity flows. Single-phase loss coefficients are important in the study of two-phase flows, as the prediction of single-phase losses is frequently used as a basis for the prediction of two-phase losses. The lack of existing knowledge necessitates the empirical determination of single-phase loss coefficients for any pipeline components under consideration in this study.

2.3 Two-Phase Flow Terminology

A major complexity in two-phase flow is the many parameters required to define the simultaneous flow of two fluids. The terminology has been further complicated by the increasing number of differing methods and correlations that add more definitions. A reasonable well accepted approach is to make a distinction between liquid and gas properties using the subscripts l and g respectively. This method is advantageous when analysis requires not only individual phase properties to be considered but also properties of the two phases acting together e.g., mixture properties.

If the total mass flow rate of a two-phase flow in a pipe is *M*, then using the above notation, the liquid mass flow rate is M_l and the gas mass flow rate is M_g. The gas fraction of the mass flow rate is termed the quality and is related to the mass flow rate thus;

$$x = \frac{M_g}{M} \tag{2.13}$$

The velocity at which a phase would flow if it were to flow alone in a pipe is called the superficial velocity. The specific volume of a phase, v_i, can be used to calculate the superficial velocity, u_{is}, from the phase mass flow rate for a total flow area of, *A*, using;

$$u_{is} = \frac{M_i v_i}{A} \qquad i = l \text{ or } g \tag{2.14}$$

The mass flux, *G*, of each phase is calculated by dividing the phase mass flow rate by the total flow area. If the definition of mass flux is used in Equation 2.14 then the superficial velocities become;

$$u_{is} = G_i v_i \tag{2.15}$$

The ratio between the actual average gas and liquid phase velocities, not the superficial velocities, is called the slip ratio, *k*;

$$k = \frac{u_g}{u_l} \tag{2.16}$$

If the volume flow of each phase entering a pipe is known, the volume fraction at any given point within the pipe is not necessarily known. When the phases differ in density and/or viscosity, a velocity difference is generated as one phase slips past the other i.e., slip ratio. The 'slip' leads to a change in the cross sectional area occupied by each phase relative to what would be determined using their volume flow rates. The 'holdup' or void fraction is the fraction of a pipe cross section occupied by the gas phase and is given by;

$$\alpha = \frac{A_g}{A} \tag{2.17}$$

As the full cross section must be entirely occupied by the two-phase flow the fraction of the pipe occupied by the liquid phase must then be;

$$1 - \alpha = \frac{A_l}{A} \tag{2.18}$$

Mass continuity allows the mass flow rate for the gas and liquid phases to be written as;

$$M_g = \frac{\alpha A u_g}{v_g} \qquad \& \qquad M_l = \frac{(1-\alpha) A u_l}{v_l} \tag{2.19}$$

Equation 2.16 gives the definition of the slip ratio and combining this with the above definitions for the mass flow rate of each phase and with the Equation 2.13 gives;

$$\frac{x}{1-x} = \frac{\alpha}{1-\alpha} k \frac{v_l}{v_g} \tag{2.20}$$

Allowing the void fraction to be written as;

$$\alpha = \frac{x v_g}{x v_g + k(1-x) v_l} \tag{2.21}$$

The void fraction and slip ratio are interrelated, knowledge of the void fraction allows the slip ratio to be determined and vice-versa.

Once the proportions of the cross-section occupied by each phase have been established an effective mixture specific volume, v_m, can be determined from;

$$v_m = \frac{x v_g + k(1-x)v_l}{x + k(1-x)} \tag{2.22}$$

2.4 Gas-Liquid Flow Regimes and Transitions

Some two-phase flow models are flow pattern dependent. It is therefore necessary to specify the flow regime either by transition criteria or flow map.

2.4.1 Flow Regimes

The interaction leading to separation and dispersion of two phases flowing together in a pipe has been a starting point for many investigations. By simply visually observing a two-phase flow through a transparent section, the effects of the dominant forces can be seen to perpetuate distinctive patterns. For many applications it is sufficient to describe regimes using the most commonly recognised patterns for which there are six for horizontal flows and four for vertical flows, see Orkiszewski [15] (1967), Delhaye *et al* [16] (1981) and Whalley [17] (1987). In addition to the four main patterns for vertical flow some authors define a further two, Calvert & Williams [18] (1955), Govier *et al* [19] (1957) and Oshinowo & Charles [20] (1974).

The main flow patterns encountered in two-phase flows are separated by periods of transition which are more difficult to classify. Authors have attempted to define all the intermediate stages of two-phase flow regimes. For horizontal flows Wong & Yau [21] (1997) defined 16 and Spedding & Nguyen [22] (1979) defined 13 distinguishable flow patterns. Similarly with vertical flows, the number of regimes discernible has been expanded beyond six. In comparison with horizontal flows there are less observable regimes in vertical flows. This is because horizontal flows are subjected to stratification owing to gravitational effects on the flow distribution.

The flow patterns of interest to this study are the four major flow patterns commonly used to describe vertical flow regimes and are shown in Figure 2.1. These are *bubbly, slug, churn* and *annular flow*. It is normal to investigate these flow regimes by supplying a constant flow rate of liquid and then gradually increase the gas mass flow rate. When this procedure is followed the following observations can readily be made;

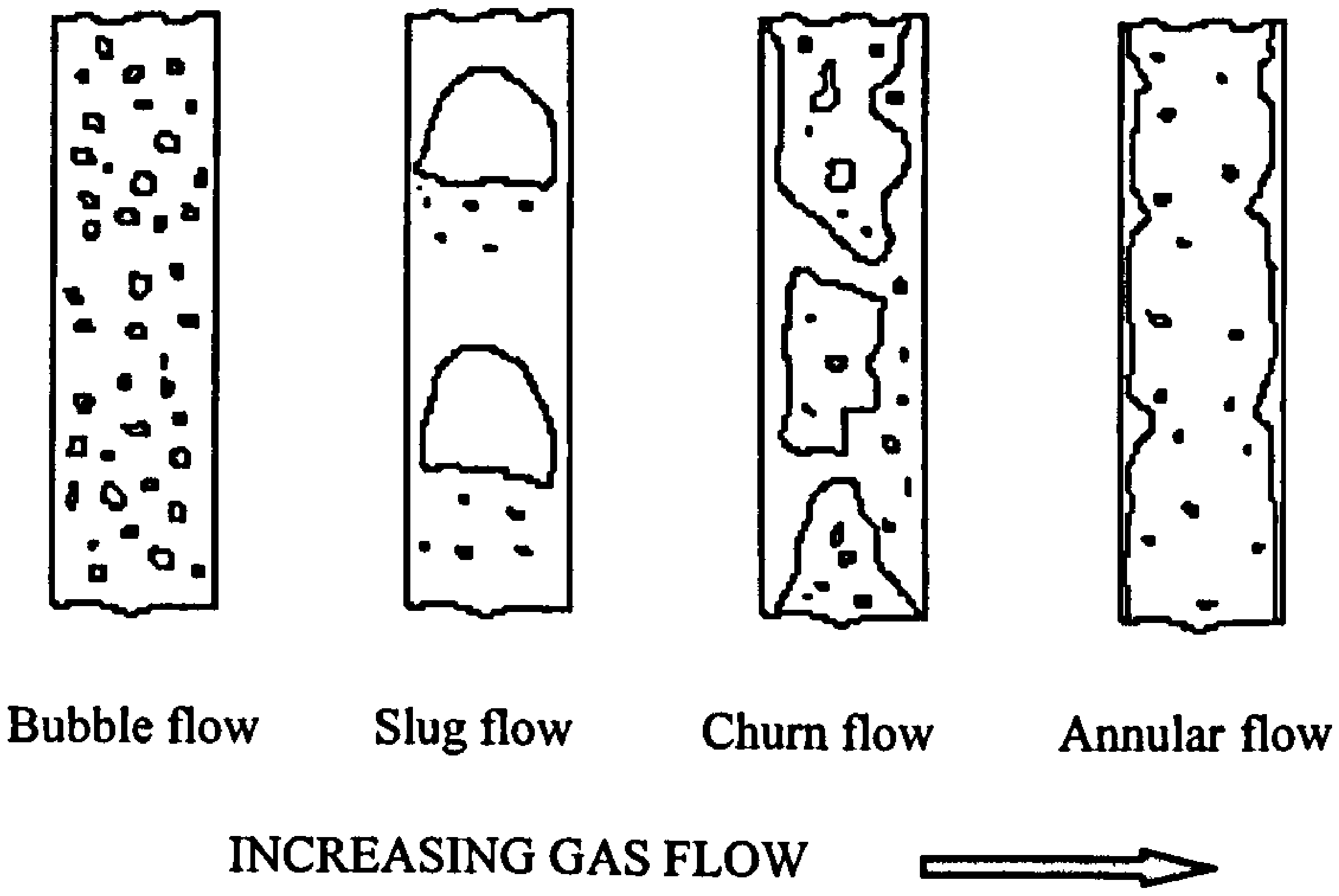

Figure 2.1: Flow patterns in vertical flow.

I. At low qualities, when the flow is predominantly liquid, *bubbly flow* occurs. The gas rises through the liquid in the form of small bubbles. These bubbles are of approximately uniform size due to the force of surface tension.

II. As the gas velocity is increased, the small bubbles get closer together and collide more frequently. These collisions result in the bubbles coalescing to form bullet-shaped slugs, or 'Taylor' bubbles, characteristic of *slug flow*. The thin liquid film surrounding these bullet-shaped slugs tends to flow counter currently as the slugs rise up through the liquid. With further increases of the gas flow the diameter of bullet shaped slugs will progressively approach that of the pipe.

III. *Churn flow* occurs as the velocity of the large slugs of gas increases and they become unstable and break down, giving way to an oscillatory motion of the bubbles. The process involved in the transition from slug flow to churn flow is highly complex and in depth classifications of this regime are given by Jayanti & Hewitt [23] (1992), Jayanti *et al* [24] (1993), and a follow up communication Hewitt & Jayanti [25] (1993).

IV. At a high enough velocity, the gas is able to continuously support the liquid as a film on the walls of the pipe while occupying the central core. This is *Annular flow* and although the boundary of the two phases is strongly defined, small droplets of liquid are often entrained in the central gas core. According to Govier *et al* [19] (1957) and Wallis [3] (1969), under certain conditions, i.e., sufficiently high gas rates, the number of water droplets entrained in the gas core will result in the complete removal of the liquid film, creating a fine mist. The complete dispersion of the liquid phase in the gas phase cannot happen in an adiabatic system, Hewitt & Hall-Taylor [26] (1970).

A regime which has been reported but is more difficult to qualify is 'froth flow'. This regime occurs at transition from churn flow to annular flow and is not unrelated to what Hewitt & Hall-Taylor [26] call 'wispy-annular flow'. Froth flow is not readily recognised as it is difficult to distinguish from churn flow. Wispy-annular can occur on flows involving high mass fluxes. It is named after the liquid drops which lump together in the gas core forming 'wisps' or 'fingers'. An up todate study of wispy-annular flow is given by Hawkes *et al* [27] (2000).

The four flow regimes defined above are adequate to describe vertical isothermal flows for the majority of applications. The situation is more complex when evaporation and condensation influences the behaviour of a two-phase flow.

2.4.2 Flow Pattern Maps

Some of the earliest two-phase publications were by investigators attempting to define all possible gas-liquid interactions and their governing parameters. The approach that was most widely adopted was the use of flow pattern maps to classify the flow regimes that occurred under two-phase flow conditions. A flow pattern map is a graph separated into areas corresponding to the various flow patterns.

A sketch of the Taitel & Dukler [28] (1976) flow pattern map for vertical flow in a 50mm diameter tube is shown in Figure 2.2. The bold lines indicate the transition zones between the more commonly recognised flow regimes and the labelled regions correspond to the flow regimes described above and depicted in Figure 2.1. The broken lines represent the transition from a slug flow to annular flow i.e., churn flow. The onset of churn flow is related to the pipe diameter and this has been indicated by the series of broken lines on the flow pattern map. The bold transition lines could be misinterpreted as indicating a sudden transition from one flow regime to another. In reality the transition between regimes is gradual and a more accurate portrayal would be to use much broader boundaries.

Despite the many attempts that have been made, no single method of deriving mapping parameters or flow pattern map has received universal acceptance, Spedding *et al* [29] (1998). This is because the interpretation of the different flow regimes is subjective. Consequently there is varying opinion on the appropriate mapping parameters to employ, see Whalley [17] and Mukherjee & Brill [30] (1985). Difficulties also stem from the visual nature of the methodology requiring the investigator to relate measured parameters with observed phenomena.

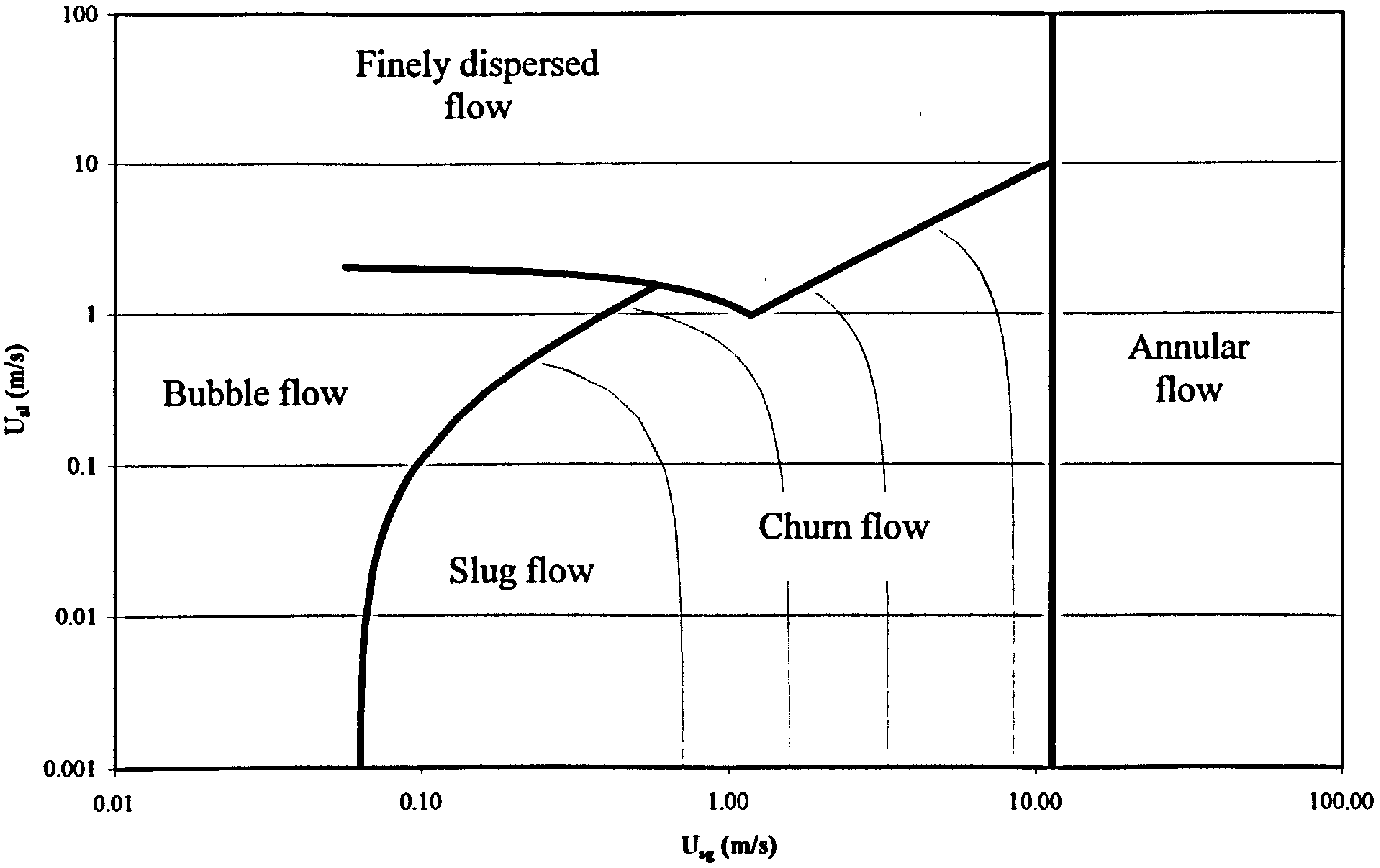

Figure 2.2: Flow pattern map for vertical flow, Taitel & Dukler [28]

The visual method of characterising flow patterns has been linked to other indicators. Govier *et al* [19] related pressure gradient to flow pattern, working on the basis that a systematic change in gas or liquid flow rate should coincide with a flow pattern change. Like many experimental correlations, this approach was only valid for systems operating with near to, or the same conditions as the originating experimental work. It was obvious to investigators that it would be advantageous to derive theoretical indicators as they could be applied generally. Taitel *et al* [31] (1976) and later Mishima & Ishi [32] (1984) attempted to do this by providing a theoretical basis for each region of transition. The Taitel theory gave reasonable agreement with air-water data but the method has been criticised by Spedding *et al* [29] for being pipe diameter dependent and therefore semi-empirical in nature.

In addition to photographic techniques to improve the visual method of detecting flow patterns, other specialist instrumentation has been developed. Jones & Zuber [33] (1975) utilised a linearised X-ray void measurement system. This technique had the added advantage of being able to distinguish flow patterns in opaque pipes and was applied to both vertical and horizontal systems. Although successful in identifying the major flow regimes, this method became a subjective exercise when determining the subgroups and interceding transitions and it also incurred high operating costs.

Legius *et al* [34] (1998) have employed advanced modelling techniques to marry quantitative measurements with visual observations. Using an Auto-Regressing modelling technique, an accurate method to differentiate between transitions and established flow regimes was devised. This method is advantageous as it provides a mapping system that is independent of the original experimental conditions. However, the technique is complex and employs a flow intrusive probe.

The most frequently used sets of parameters for mapping flow patterns are the total mass flux, quality, the superficial velocities and superficial momentum. More recent authors have explored the use of other mapping parameters, for instance, Mishma & Ishi [32] employed void fraction as a less complex alternative. Non-dimensional groups have been used, see Weisemen & Kang [35] (1981).

The majority of flow pattern maps in the literature deal with either vertical or horizontal pipe orientations. Far more pattern data exist for horizontal flows than for vertical flows. One of the few flow maps for vertical flow, recommended by Whalley [17] and Hewitt [36] (1987), is that of Hewitt & Roberts [37] (1969). The map, plotted in terms of superficial momentum fluxes, is applicable to air-water flows in small pipe diameters for a wide range of pressures. Authors have attempted to provide as thorough investigations for inclined flows as exist for vertical and horizontal flow pattern maps. Weisman & Kang [35] proposed a dimensionless correlation for inclined flows, Barnea *et al* [38] (1980) provide further experimental measurements to validate earlier work and Mukherjee & Brill [30] present new transition equations and compare them to existing ones.

Flow pattern studies by definition deal with the full scope of encountered flow regimes. Some two-phase phenomena peculiar to certain flow regimes and associated transitions have proved important enough to merit individual investigation. For Slug flow, see Griffith & Wallis [39] (1961) and Bilicki & Kestin [40] (1987) and for bubbly to slug flow see Tutu [41] (1984).

2.4.3 Viscous Effects on Flow Patterns

A recent study by Furukawa & Fukano [42] (2001) investigated the effect of liquid viscosity on the flow patterns of a vertical flow. An aqueous glycerol test solution was used with the viscosity varying between 1 and 15 mPas. Comparisons were made with existing flow maps. Although devised for horizontal flow, the flow pattern map of Baker [43] (1954) correlated comparatively well with viscous data in the froth annular regions but boundaries of bubble and slug flow regimes did not. Whalley [17] also suggests that the Baker map is a reasonable representation of oil-gas mixtures in pipes of less than 50 mm diameter.

Troniewski & Spisak [44] (1987) studied the vertical down flow of an air-mineral oil system. A glass test length of 2 m was used with internal diameters of 10, 15 and 25 mm. The liquid viscosity was temperature controlled over the range of 180 to 7700 mPas. The study describes eight distinctive flow patterns and concludes that viscosity effects could be better identified through the derivation of a flow pattern map specific to highly viscous flows.

2.4.4 Summary

The flow regimes exhibited by the upward vertical flow of gas-liquid mixtures in a pipe are generally categorised by four flow regimes, bubbly, slug, churn and annular flow. As the transition between regimes is not sudden but gradual, further transitional patterns have been identified.

A relatively large amount of work has been placed in the investigation of flow pattern maps. Much of this work has concentrated on ascertaining universal mapping parameters for horizontal flows. This has proved illusive, and even advanced visualisation techniques have not resolved the subjective and empirical nature of the study of flow patterns.

Comparatively very little flow pattern data has been published for upward vertical flows. The most notable being that of Hewitt & Roberts [37] which is applicable to low-pressure air-water and high-pressure steam-water flows in small diameter pipes. There is even less published directly concerned with viscosity effects on flow patterns. Furukawa & Fukano [42] made a comparison of flow pattern maps with vertical flow data. The flow map of Baker [43] was found to be the most suitable candidate to accommodate viscous effects even though it was devised for horizontal flows.

2.5 Pressure Drop Prediction in Pipes

It is often necessary to predict the pressure drop of a two-phase system. Two-phase flows are complex, owing to the difficulty in accurately evaluating the governing forces of gravity, momentum and friction. The complexity is further exacerbated by the interaction of the two-phases. All expressions derived to predict the pressure drop of two-phase flows rely to some degree on simplifying assumptions. It is currently not possible to analytically quantify certain two-phase flow properties. This has influenced the broad range and large mix of analytical and empirical approaches that exist.

The complexity of two-phase flow has, as yet, eliminated the possibility of the derivation of a single-model that can confidently be applied across all regimes and flow conditions. Thus the approach taken by most investigators is to ascertain the range of operation of their application and to apply the most appropriate model accordingly.

2.5.1 One-Dimensional Flow

The assumption that a two-phase flow is one-dimensional was made in order to simplify the application of the conservation laws. To describe the flow as one-dimensional is to make the following simplification;

> *Across any section of a two-phase flow in a tube there is a constant pressure and velocity, although the velocity of either phase may be different.*

The one-dimensional assumption means that variations in the flow with respect to distance along the pipe are considered whilst property changes across the pipe are ignored. The two most predominant applications of the one-dimensional assumption for gas-liquid, two-phase flows are the homogeneous model and the separated flow model, see Section 2.5.5 and 2.5.9 respectively. It is also convenient in the derivation of two-phase models to assume that thermal equilibrium exists between the phases so that the temperature of the gas phase is equal to that of the liquid phase.

2.5.2 Conservation of Mass

For mass to be conserved, the mass flow is constant, i.e., the mass flow will not vary between any two given points in a flow. Thus a mass balance on the gas phases will give;

$$G_g A = GxA = \frac{u_g A_g}{v_g} = \frac{u_g A \alpha}{v_g} \tag{2.23}$$

Similarly a mass balance on the liquid phase will give;

$$G_l A = G(1-x)A = \frac{u_l A_l}{v_l} = \frac{u_l A(1-\alpha)}{v_l} \tag{2.24}$$

2.5.3 Conservation of Momentum

It has been shown by Butterworth & Hewitt [45] (1977) that a force analysis on a cylindrical volume of perimeter, S, results in the two-phase momentum equation;

$$\int_A \left\{ p - \left(p + \frac{\partial p}{\partial z} \delta z \right) \right\} dA = \int_S \tau_0 \delta z dS + \int_A \frac{\partial}{\partial z} \left(G_l u_l + G_g u_g \right) \delta z dA + \int_A \frac{g}{v} \sin \theta \delta z dA \tag{2.25}$$

The one-dimensional flow assumption and the conservation of mass Equation 2.23 & 2.24 simplifies this to;

$$-\frac{dp}{dz} = \frac{S}{A} \tau_0 + G^2 \frac{d}{dz} \left\{ \frac{x^2 v_g}{\alpha} + \frac{(1-x)^2 v_l}{(1-\alpha)} \right\} + g \sin \theta \left\{ \frac{\alpha}{v_g} + \frac{(1-\alpha)}{v_l} \right\} \tag{2.26}$$

Without some means to obtain the wall shear stress and the void fraction, Equation 2.26 cannot be used to evaluate a two-phase pressure gradient.

2.5.4 Conservation of Energy

Similarly, for an energy balance, Butterworth & Hewitt [45] showed that the resulting two-phase energy equation is;

$$-\frac{dp}{dz}\left[x v_g + (1-x) v_l\right] = \frac{dF}{dz} + \frac{G^2}{2}\frac{d}{dz}\left\{\frac{x^3 v_g^2}{\alpha^2} + \frac{(1-x)^3 v_l^2}{(1-\alpha)^2}\right\} + g\sin\theta \quad (2.27)$$

where, F, is the frictional energy loss.

From the application of the momentum and energy conservation laws, it can be seen that a two-phase pressure gradient is a combination of frictional, accelerational and gravitational pressure gradients. That is, the pressure gradient for a two-phase flow can be treated as;

$$-\frac{dp}{dz} = -\frac{dp_F}{dz} + \frac{dp_A}{dz} + \frac{dp_G}{dz} \quad (2.28)$$

where subscripts, *F*, *A* and *G* refer to friction, acceleration and gravitation gradients respectively. These three components will only hold the same value for both the momentum and energy balances under particular conditions i.e., for the specific case of no slip between the phase and that of incompressible horizontal flow. This is because the gravitational term of the momentum balance represents a force on the fluid within the pipe, whilst, in the energy balance, it is derived from the potential energy gained by the fluid over a unit distance. The frictional term in the energy balance differs from that in the momentum balance because it includes, in addition to friction losses at the pipe wall, losses due to the relative motion of the two phases. And the accelerational terms have a different weighting between the phases as they are derived either from the kinetic energy flux or the momentum flux. For incompressible flows, the momentum equation would be sufficient but where there are compressibility effects, the energy equation would have to be used.

2.5.5 Homogeneous Model

The homogeneous model provides one of the simplest methods to represent two-phase flows. The basis of the homogeneous model is that the two phases' flow as a homogeneous mixture i.e., they have the same velocity, slip ratio = 1. The method originates from the design of water-tube boilers, Chisholm [46] (1963).

This simplification enables the void fraction given by Equation 2.21 to be substituted into Equations 2.26 and 2.27. The total pressure gradient given by the two-phase momentum equation is;

$$-\frac{dp}{dz}=\frac{S}{A}\tau_0+G^2\frac{dv_h}{dz}+\frac{1}{v_h}g\sin\theta \tag{2.29}$$

And the total pressure gradient given by the two-phase energy equation is;

$$-\frac{dp}{dz}=\frac{1}{v_h}\frac{dF}{dz}+G^2\frac{dv_h}{dz}+\frac{1}{v_h}g\sin\theta \tag{2.30}$$

where v_h is given by;

$$v_h=xv_g+(1-x)v_l \tag{2.31}$$

For more detail and derivations of the homogeneous model see Butterworth & Hewitt [45], Govier & Aziz [47] (1972) and Collier & Thome [48] (1994).

The homogeneous model cannot provide an entirely analytical solution because there is no means by which to define the frictional pressure gradient. The frictional gradient must be based either upon measurements or generalisations based upon measurements, Hewitt & Hestroni [36]. A semi-empirical approach is to use a correlation to determine frictional pressure drop. This can be achieved by using single-phase equations allowing the frictional pressure gradient to be written as;

$$\frac{dp_F}{dz}=-\frac{4f_{tp}}{D}\frac{G^2v_h}{2}=-\frac{S}{A}\tau_0 \tag{2.32}$$

This approach requires the properties of a two-phase friction factor, f_{tp}, to be defined. The two-phase friction factor can be evaluated using a mean two-phase viscosity. Several definitions exist for the two-phase viscosity. The following are given by Collier & Thome [48], and their references McAdams *et al* (1942), Cicchitti *et al* (1960) and Dukler *et al* (1964);

$$\frac{1}{\mu_{tp}} = \frac{x}{\mu_g} + \frac{(1-x)}{\mu_l} \tag{2.33}$$

$$\mu_{tp} = x\mu_g + (1-x)\mu_l \tag{2.34}$$

$$\mu_{tp} = \frac{1}{v_h}\left[x v_g \mu_g + (1-x)v_l \mu_l\right] \tag{2.35}$$

All of the above satisfy the conditions $x = 0$, $\mu_{tp} = \mu_l$ and $x = 1$, $\mu_{tp} = \mu_g$.

A fourth equation for the homogeneous viscosity is given by Beattie & Whalley [49] (1982) which is;

$$\mu_{tp} = \mu_g \alpha_h + \mu_l (1-\alpha_h)(1+2.5\alpha_h) \tag{2.36}$$

As an alternative to using a homogeneous friction factor a common method for determining the frictional pressure gradient is to employ a two-phase multiplier, ϕ^2. If the frictional pressure gradient for an equivalent single-phase flow is calculated, the two-phase multiplier is the factor by which the single-phase frictional pressure gradient must be multiplied to obtain the two-phase pressure gradient. There are several two-phase multipliers that can be employed and they differ as a result of the single-phase properties chosen as a basis for evaluation. If the frictional single-phase pressure drop was calculated using the liquid flowing alone in the pipe, the frictional pressure drop for the two-phase flow would be obtained from a liquid-only two-phase multiplier. A commonly used method using this approach is that of Chisholm [2] and is given by;

$$\frac{dp_F}{dz} = \left(\frac{dp_F}{dp}\right)_l \phi_l^2 \tag{2.37}$$

If the frictional single-phase pressure gradient was calculated using the total mass flux flowing in the pipe and the properties of the liquid phase, the two-phase multiplier would be called the all-liquid multiplier. A commonly used method that uses this approach is that of Friedel [50] (1979) and is given by;

$$\frac{dp_F}{dz} = \left(\frac{dp_F}{dp}\right)_{lo} \phi_{lo}^2 \tag{2.38}$$

In a similar way, two-phase multipliers can be defined using the gas phase flowing alone in the pipe or the total mass flux flowing in the pipe and the properties of the gas.

2.5.6 Lockhart – Martinelli Correlation

One of the earliest and most widely used correlations for two-phase flow is that of Lockhart & Martinelli [51] (1949) and was the first to incorporate slip effects. The basis of the correlation is notionally one of separated flow. A parameter X, now known as the Martinelli parameter, was defined for the correlation. The application of this parameter depends on the use of phase-alone flows. The phases flowing alone can be regarded as being either laminar, originally termed viscous, or turbulent in nature. As it is possible that one phase may be laminar whilst the other is turbulent, Lockhart & Martinelli [51] provided four two-phase multipliers to cover all variations. The two-phase multipliers are retrieved from a graphical representation by first determining the X parameter which is given by;

$$X^2 = \frac{(dp_F/dz)_l}{(dp_F/dz)_g} = \frac{(1-x)}{x}\left(\frac{f_l}{f_g}\frac{v_l}{v_g}\right)^{1/2} \tag{2.39}$$

The Lockhart-Martinelli correlation does not perform well under all conditions. One reason for this is, like all correlations, it cannot justifiably be applied to situations that are outside of the original experimental conditions i.e., horizontal two-phase flow close to atmospheric pressure and temperature, see Thom [52] (1968). Secondly, the Lockhart-Martinelli correlation under estimates the influence of mass flux. Over certain ranges this can cause large errors, Chisholm [46], Hewitt & Hestroni [36] and Collier & Thome [48].

2.5.7 The Chisholm C Parameter

Chisholm [2] (1967) chose to produce an analytical presentation of the Lockhart-Martinelli correlation. To assist in its application, Chisholm provided a C parameter defined for the liquid only two-phase multiplier as;

$$\phi_l^2 = 1 + \frac{C}{X} + \frac{1}{X^2} \tag{2.40}$$

and for the gas only two-phase multiplier as;

$$\phi_g^2 = 1 + CX + X^2 \tag{2.41}$$

As with the Lockhart-Martinelli two-phase multiplier, values for the C parameter corresponded to laminar or turbulent flow conditions in each phase. Table 2.1 gives the C parameters given by Chisholm to fit the Lockhart-Martinelli curves.

Lockhart-Martinelli curve		**C**
Gas	*Liquid*	
Turbulent	Turbulent	21
Laminar	Turbulent	12
Turbulent	Laminar	10
Laminar	Laminar	5

Table 2.1: Chisholm C parameter values

It is possible to use the Chisholm C parameter to represent a homogeneous flow, Hewitt & Boure [53] (1973). In the case of homogeneous flow the C parameter is calculated from;

$$C = \left(\frac{v_l}{v_g}\right)^{0.5} + \left(\frac{v_g}{v_l}\right)^{0.5} \tag{2.42}$$

2.5.8 The Friedel Correlation

According to Whalley [17], it is widely agreed that the Friedel [50] correlation is the best generally applicable correlation. The claim is justified by the meticulous manor in which it was obtained e.g., the extensive comparisons of 25000 data points. The Friedel correlation is an optimised equation for an all liquid two-phase multiplier and is calculated from;

$$\phi_{lo}^2 = A_1 + \frac{3.24 A_2 A_3}{Fr^{0.045} We^{0.035}} \tag{2.43}$$

where,

$$A_1 = (1-x)^2 + x^2\left(\frac{v_g f_{go}}{v_l f_{lo}}\right) \tag{2.44}$$

$$A_2 = x^{0.78}(1-x)^{0.224} \tag{2.45}$$

$$A_3 = \left(\frac{v_g}{v_l}\right)^{0.91}\left(\frac{\mu_g}{\mu_l}\right)^{0.19}\left(1-\frac{\mu_g}{\mu_l}\right)^{0.7} \tag{2.46}$$

$$Fr = \frac{G^2 v_h^2}{gD} \tag{2.47}$$

$$We = \frac{G^2 D v_h}{\sigma} \tag{2.48}$$

It is not recommended to apply the Friedel correlation to two-phase flow where the viscosity ratio (μ_l/μ_g) exceeds 1000, Whalley [17].

2.5.9 Separated Flow Model

In contrast to the homogeneous flow model, the separated flow model, or slip model, evaluates a two-phase flow by assuming the two phases flow entirely separately in the tube. Like the homogeneous model, empirical correlations are required to determine the effects of friction on the two-phase pressure gradient. Unlike the homogeneous model, where mixture properties may be used, the analytical treatment of the separated flow model starts with distinct equations for each phase. These basic equations can be solved simultaneously along with additional equations describing how the two phases interact. Equations describing the interaction of the phases are usually functions of void fraction and shear stress.

In a similar manner to the derivation of the homogeneous model, the introduction of single-phase relationships in the energy Equation 2.27, allows the separated flow model to be expressed in terms of three pressure gradients i.e., gravity, friction and acceleration thus;

$$\frac{dp_G}{dz} = -\frac{g}{v}\sin\theta \tag{2.49}$$

$$\frac{dp_F}{dz} = -\frac{2f_l}{D} G^2 v_l (1-x)^2 \phi_l^2 \tag{2.50}$$

$$= -\frac{2f_{lo}}{D} G^2 v_l \phi_{lo}^2$$

$$\frac{dp_A}{dz} = -\frac{1}{2v} G^2 \frac{d}{dz}\left[\frac{x^3 v_g^2}{\alpha^2} + \frac{(1-x)^3 v_l^2}{\alpha^2}\right] \tag{2.51}$$

where the specific volume term, v, in Equations 2.49 & 2.51 is given by Equation 2.31.

Just as with the homogeneous model, the two-phase friction term of Equation 2.27 cannot be found by a purely analytical approach. Equation 2.50 incorporates a two-phase multiplier allowing the single-phase liquid friction factor to be used. An obvious improvement of the separated flow model over the homogeneous model is the incorporation of the slip ratio allowing the model to be adapted for a wider range of conditions. This improvement can also be an impediment to using the separated flow model as it requires the determination or measurement of the void fraction. For example Chisholm [54] (1972) provides this correlation for slip ratio;

$$k = \left[1 - x\left(1 - \frac{v_g}{v_l}\right)\right]^{1/2} \tag{2.52}$$

If the phase velocities were assumed to be the same i.e., slip=1, then the equations for separated flow would reduce to those of the homogeneous model. The homogeneous and separated flow models are two extremes representing opposing conditions. In practice the true nature of two-phase flows generally sits some where between the two.

This became evident in a study by Andeen & Griffith [55] (1968) where the homogeneous model was found to give the best prediction of momentum flux for the majority of the data they examined. Andeen & Griffith [55] described this as a surprising result especially considering that a separated flow model corresponding to proven slip ratio should also be a good predictor of void fraction and hence momentum flux. Whalley [17] and Chisholm [56] (1983) attributed the inability of the separated flow model to predict the momentum flux to the existence of a pronounced velocity profile, resulting in the measured momentum flux being greater than that predicted. Both authors conclude that the homogeneous model is only a good predictor of momentum flux by accident, since the assumptions embodied by the model prevent it from being a theoretically based predictor of momentum flux.

In addition to the velocity profile theory, Chisholm [54] suggested that another factor inhibiting the separated flow model from being a good predictor of the momentum flux was the effect of the entrained liquid fraction. Chisholm calculates an apparent entrainment fraction of 0.6 to match the data of Andeen & Griffith. Obviously a large proportion of the liquid travelling at a significantly higher velocity than the liquid film will increase the momentum beyond that predicted by the separated flow model. In light of this a modified separated flow model has been proposed by Hewitt & Hall-Taylor [26], where the two-phase flow is considered as having three components, a gas core, a liquid film and an entrained liquid fraction, changing Equation 2.41 to;

$$\frac{dp_A}{dz} = -\frac{1}{2v}\frac{d}{dz}\left[\tfrac{1}{2}xu_g^2 + \tfrac{1}{2}(1-x)Exu_{le}^2 + \tfrac{1}{2}(1-x)(1-E)u_{lf}^2\right] \qquad (2.53)$$

where subscripts e and f denote entrained and film liquid fractions respectively.

A recent model for the momentum flux given by McNeil [57] (1998) operates between the boundaries set by the homogeneous and separated flow models. In effect this approach simplifies the method described by Chisholm [54]. Movement between the boundaries is achieved through the incorporation of an entrained liquid fraction. A proportion of the liquid phase, from the liquid annulus, is considered to be travelling in the gas core at the gas velocity. Using an entrained liquid fraction, *E*, the model defines a momentum correction factor, c_m, as;

$$c_m = [x + k(1-x)]\left\{x + (1-x)\left[E + \frac{(1-E)^2}{(k-E)}\right]\right\} \tag{2.54}$$

Suitable correlations for the slip ratio and the entrained liquid fraction are Premoli *et al* [58] (1970), Section 2.5.13, and Govan *et al* [59] (1988), Section 2.5.12 respectively. Using Equation 2.31 for the specific volume for the mixture, Equation 2.54 allows the acceleration pressure gradient defined by Equation 2.53 to be re defined as;

$$\frac{dp_A}{dz} = -G^2 \frac{d}{dz}(c_m v) \tag{2.55}$$

2.5.10 The Drift Flux Model

The drift flux model was developed to address the inaccuracies incurred by models that were formulated around the assumption of one-dimensional flow, i.e., the homogeneous and separated flow models. Wallis [3] describes the drift flux model as a separated flow model with the emphasis shifted from the motion of the individual phases to the relative motion of the phases. To establish the model, equations were derived to determine the relative motion of the phases from parameters independent of the phase flow rates. As buoyancy and drag forces were initially used, and the density and velocity distribution were accounted for, the model is particularly useful for the bubbly and slug flow regimes. Bankoff [60] (1960) applied the method to low quality steam-water flow in the bubbly flow regime. The applicability of this method was improved by Zuber & Findlay [61] (1965) but according to Collier & Thome [48] the drift flux model is still limited to bubbly, slug and churn flow regimes.

2.5.11 The Annular Flow Model

The annular flow regime is of particular interest to this study as it is the most commonly occurring flow pattern in two-phase systems and the majority of the two-phase data generated will lie in this region. A typical depiction of vertical annular flow is given in

Figure 2.3. The flow consists of a liquid phase flowing as an annular film on the pipe wall with the gas phase forming a central core. The gas core can contain a quantity of liquid in the form of droplets, commonly referred to as the entrained liquid fraction. The gas core travels at a higher velocity than that of the liquid film. The velocity of the entrained liquid is also higher than that of the liquid film but less than that of the gas core.

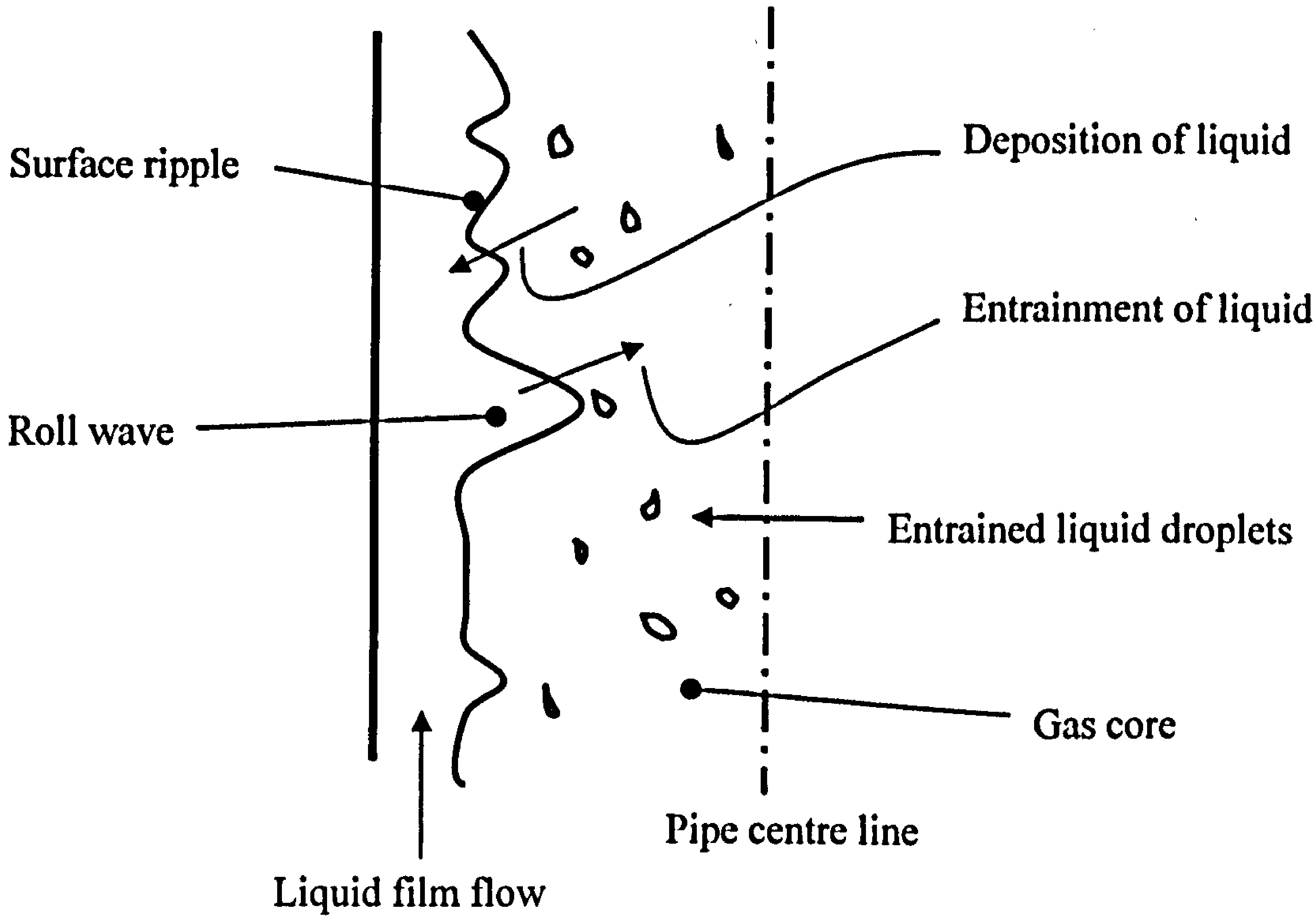

Figure 2.3: Annular flow.

The frequent occurrence of annular flow in industrial settings has resulted in the development of models particular to this flow regime. Despite the symmetrical nature of vertical annular flow, the derivation of annular flow models has not been a simple task because of the complex interaction between the forces that govern phase velocities and pressure gradient. The interdependency of these forces negates any attempt to analyse them in isolation and necessitates a specialised approach peculiar to annular flow. A complete treatment of annular flow would need to accurately represent the interplay of the following;

- The existence of ripples and roll waves on the surface of the liquid film.
- Entrained liquid drops travelling in the gas core.
- The simultaneous existence of laminar flow effects on the liquid-wall periphery and turbulent flow effects on the gas-liquid interface.
- Determination of the interfacial friction factor and its relationship to film thickness.
- The use of the correct shear stress distribution, incorporating gravitational effects.
- The entrained rate of liquid drops into the gas core from the liquid film.
- The deposition rate of liquid to the liquid film from the gas core.

The incorporation of all the above results in an annular flow model of high complexity. A common approach to this complexity is to make some simplifying assumptions such as; no liquid is entrained in the gas core, the gas-liquid interface is smooth and the gravitational and accelerational effects on both phases can be ignored. This technique can lead to models too unsophisticated to effectively represent the physical phenomena that occur, Wallis [62] (1970).

Another common approach to tackling the complexities of annular flow is to make use of the triangular relationship that exists between the film liquid flow rate, the liquid film thickness and the liquid film shear stress. This has become the basis for most annular flow models. The premise of the triangular relationship is that knowledge of any two of these quantities enables the third to be calculated. To further establish the triangular relationship it was initially found necessary to understand the variation in the shear stress across the flow as this would allow the velocity profile to be found. The least complex approach to this problem is to assume that the shear stress is linear, this approximation is justified if the liquid film is very thin in relation to the tube diameter, and that the liquid film is laminar. In practice this method under predicted the liquid film thickness and over predicted the liquid film flow rate as it does not account for turbulent effects, Hewitt & Hall-Taylor [26]. To improve on this initial assumption and to account for turbulent effects, the liquid film was treated in a similarly way to that of the boundary layer region of a single-phase flow. This allowed the application of a less complex single-phase theory to obtain the velocity profile. The triangular relationship was then obtained by integrating the velocity profile across the liquid film. The integration assumes that the liquid film was thin enough for the curvature of the tube wall to be ignored.

It was recognised that this simplistic triangular relationship was too unsophisticated to accurately represent the forces at work in annular flow. In view of this, some investigators have attempted to compensate for the inadequacies of the triangular relationships. Shearer & Nedderman [63] (1965) assumed a laminar flow throughout the liquid film and a constant shear stress. Willis [64] (1965) using an equally simplistic approach, argued that even though the film flow maybe turbulent in the region of the gas-liquid interface, laminar flow will be dominant at the pipe wall. Calvert & Williams [18] split the liquid film into two layers, one assuming a laminar flow and the second assuming a turbulent flow. Anderson & Montzouranis [65] (1960) applied the universal velocity profile but accounted for the effects of pipe wall curvature by modifying the expression for the film flow rate. Likewise Collier & Hewitt [66] (1961) applied the universal velocity profile but suggested that a laminar flow correction factor should be employed to adjust the predicted flow rate.

In practice the application of the triangular relationship was found at best to yield predictions approximately 20 per cent greater than measured values, Gill & Hewitt [67] (1968). Initial investigations using the triangular relationship were incomplete due to the assumption of a smooth gas-liquid interface. To address this deficiency investigators incorporated into models some form of interfacial roughness correlation. This was necessary because the ripples and roll waves generated at the gas-liquid interface have considerable effect especially regarding the pressure gradient, Butterworth & Hewitt [45].

To account for conditions at the gas-liquid interface, Calvert & Williams [18] defined a drag coefficient between the phases which was correlated as a function of the liquid film thickness. Anderson & Montzouranis [65] correlated the interfacial friction factor in terms of the gas Reynolds number and the ratio of the dimensionless mass flow and film thickness, obtained from the application of the universal velocity profile. Wallis [68] (1970) proposed an interfacial friction factor, based on the superficial velocity of the gas, which equated the interaction of pipe roughness, pipe diameter and film thickness. Wallis provided a simpler version of his correlation which instigated a general rule that a gas-liquid flow with a liquid fraction of one-tenth will develop a pressure drop ten times greater than that developed by the same gas flow flowing alone in a smooth dry pipe. Shearer & Nedderman [63] obtained a linear relationship between effective pipe roughness and a dimensionless film thickness, although the resulting correlation can only be applied to a very limited range of annular flows. They also identified that the interaction between gas and liquid flow rates, viscosity, density, surface tension and pipe diameter resulted in effects not yet being accounted for by annular flow theories.

An important characteristic of annular flow is the existence of waves on the surface of the liquid film. Two basic types of waves have been identified, the small amplitude *ripple* wave and the large amplitude *disturbance* or *roll* wave, see Gill *et al* [69] (1963), Hall-Taylor *et al* [70] (1963), Collier & Hewitt [66] and Shearer &

Nedderman [63]. In addition to the difference in the amplitude of the two wave types, further distinctions have been observed. The ripple type waves are always present in annular flow, they travel at a lower velocity, do not form complete rings around the pipe circumference and are separated by small distances. Individual ripple waves quickly merge with the bulk film causing them to lose their identity. In contrast, disturbance waves only appear in certain circumstances of annular flow, always form complete rings around the pipe circumference, and appear as infrequent pulses travelling the entire length of the pipe. A more recent study of the ripple and wave phenomena encountered in annular flow is given by Wolf *et al* [71] (1996).

2.5.12 Liquid Entrainment Correlations

One of the simplifying assumptions made to assist the derivation of annular flow models, and is implicit in the separate flow model, is that the gas and liquid phases flow separately. In reality this is not the case and the proportion of the liquid phase that can become entrained in the gas core can be very high. Collier & Hewitt [66] published entrainment results where, at the highest gas flows, approximately 90% of the liquid was entrained as droplets in the gas core. Several authors have commented on the significance of the entrained droplets and their effect on the overall pressure drop. Lopes & Dukler [72] (1986) remark that the inadequacies of earlier annular flow investigations were due to the assumption that the shear generated by the wavy gas-liquid interface to be solely responsible for higher annular flows having higher pressure gradients. Lopes & Dukler [72] attempted to correct this assumption by adequately allowing for additional effects arising from interaction of the entrained liquid and the slower moving liquid film. As well as Lopes & Dukler [72], Moeck & Stachiewicz [73] (1972) also concluded that the momentum exchange resulting from entrainment and deposition, and hence energy loss, contributes substantially to the observed pressure gradients.

The mechanism by which liquid droplets become entrained in the gas core, was identified by several investigators. Hall-Taylor *et al* [70] , Gill *et al* [74] (1964) and Shearer & Nedderman [63] attribute liquid entrainment to the occurrence of roll waves on the gas-liquid interface and the action of the gas flow on the tips of these waves. Although there is clear observational evidence for the mechanism of entrainment the subject became more involved when attempts were made to predict the amount of entrainment in an annular flow. Two studies by Gill *et al* [69] and Gill & Hewitt [67] attempted to quantify the rate of entrainment. The studies demonstrated that in the addition to the mechanism of entrainment other factors need to be considered when calculating liquid entrainment. This was indicated experimentally by the method of liquid injection. The settling length required for a fully developed flow and the final entrained liquid fraction were found to differ depending on whether a porous sinter or a central jet injector was used. It was found that the central jet injector under certain circumstances assimilated a greater entrained liquid fraction in the developed flow and that flows using a porous sinter injector took a significantly longer time to fully develop. Hutchinson *et al* [75] (1974) described the jet injection technique as providing an additional deposition mechanism. Experimentally there is an argument that laboratory techniques devised for the mixing of phases in order to generate an annular flow must closely resemble the physical process of industrial application being modelled.

It has been speculated that in certain circumstances the rate of entrainment will match the rate of deposition i.e., a hydrodynamic equilibrium. Whalley [17] comments that up to 400 pipe diameters are required for something approximately close to equilibrium to be established, but also suggests that equilibrium cannot really be attained. He reasons that as pressure decreases with distance, the gas density decreases altering the entrainment / deposition ratio. Collier & Hewitt [66] speculated that the deposition rate probably depends on the droplet concentration in the gas core and the re-entrainment rate may depend on the film thickness and that hydrodynamic equilibrium can occur.

Collier & Hewitt [66] and Gill *et al* [74] adopted an existing technique where a dimensional entrainment parameter R was correlated with the Lockhart & Martinelli parameter. For vertical annular flow the correlation is;

$$X = 0.069R^{0.39} \tag{2.56}$$

This method has been used successfully for high liquid flow rates but only for air-water systems.

Levy [76] (1966) proposed an annular flow model with liquid entrainment. Levy [76] evaluated the pressure drop using a shear stress term which was a combination of momentum and mass transfer effects. Reasonable success was reported by Levy [76] but for a limited range.

Hutchinson & Whalley [77] (1973) described what they termed a simple model of entrainment. They defined entrainment in terms of what they understood to be the dominant effects relevant to entrainment, namely, interfacial shear stress, film thickness and surface tension. A comparison with experimental data demonstrated some good agreement but not convincingly enough for general application. Hutchinson *et al* [75] developed this idea further constructing two new models one of which, the diffusion model, attempted to account for radial variations on the distribution of the entrained droplets.

A more recent entrainment correlation given by Govan *et al* [59] determines the onset of entrainment by defining a critical liquid film Reynolds number;

$$\mathrm{Re}_{l_{CRIT}} = \exp\left[5.8504 + 0.4249\left(\frac{\mu_g}{\mu_l}\right)\left(\frac{v_g}{v_l}\right)^{1/2}\right] \tag{2.57}$$

For liquid film Reynolds number values of less than the critical, even with high gas velocities, the entrainment is zero. The entrainment is obtained from a correlation for the rate of entraining liquid in the gas core and is solved by comparison with the rate of deposition of liquid on the liquid film, i.e., a deposition model.

Specific to annular flow is the deposition model of Pan & Hanratty [78] (2002). The correlation was developed using data for horizontal and vertical air-water flows. It was assumed that the flows were fully developed i.e., the rate of deposition of liquid from the gas core to the liquid film was balanced with the rate of liquid from the liquid film to the gas core. An entrainment correlation was defined in terms of a balance between the rates of atomisation and deposition. It is described as providing a good first approximation for entrainment in horizontal flows for liquids whose viscosity is close to water.

2.5.13 Void Fraction Correlations

Knowledge of the void fraction is of particular interest to the application of the separated flow and annular flow models described in Section 2.5.9 & 2.5.11 respectively. The void fraction is a function of the relative velocity of the two phases and consequently it is subject to changes in the gas specific volume. As the gas specific volume of a two-phase flow will vary over the length of the pipe it is travelling through so will the void fraction. In certain situations where it is impractical to measure the void fraction, such as flow through pipeline components, the void fraction is treated as a constant.

The importance of the void fraction has lead to the existence of many correlations and models to allow the void fraction to be predicted. A graphical comparison of the more commonly used void fraction correlations is given in Figure 2.4 for an air-water flow at atmospheric conditions.

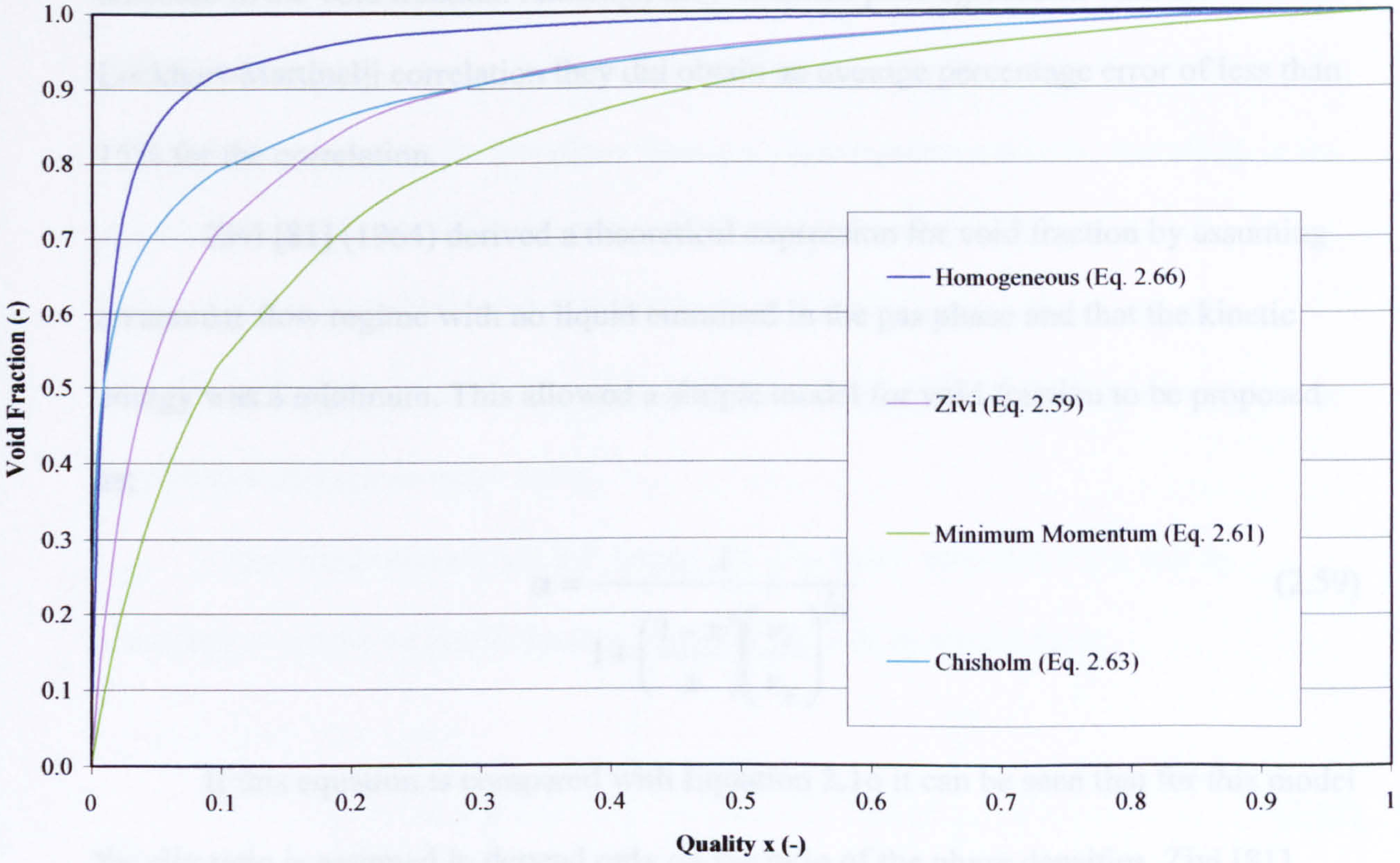

Figure 2.4: Void fraction correlations.

One of the earliest two-phase correlations is that of Lockhart & Martinelli [51] which it relates the void fraction to the Lockhart-Martinelli parameter. The experimental data from which the correlation was derived included air-oil blends with viscosities ranging from 2.3 to 1480 mPas. An approximation of this graphical correlation, is given by Butterworth [79] (1975) and allows the void fraction to be defined as;

$$\frac{1-\alpha}{\alpha}=\left(\frac{1-x}{x}\right)^{0.72}\left(\frac{v_l}{v_g}\right)^{0.4}\left(\frac{\mu_l}{\mu_g}\right)^{0.08} \tag{2.58}$$

According to Govier & Aziz [47], the best general void fraction correlation for a gas-liquid flow is that of Hughmark & Pressburg [80] (1961). Using quick closing valves and oil blends, with viscosities of 5.8 and 28.6 mPas, the void fraction was correlated for a 1" nominal bore test pipe. Increases in the viscosity were found to lead to a decrease in the void fraction. Although they obtained poor agreement with the Lockhart-Martinelli correlation they did obtain an average percentage error of less than 15% for the correlation.

Zivi [81] (1964) derived a theoretical expression for void fraction by assuming an annular flow regime with no liquid entrained in the gas phase and that the kinetic energy was a minimum. This allowed a simple model for void fraction to be proposed as;

$$\alpha = \frac{1}{1 + \left(\frac{1-x}{x}\right)\left(\frac{v_l}{v_g}\right)^{2/3}} \tag{2.59}$$

If this equation is compared with Equation 2.16 it can be seen that for this model the slip ratio is assumed to depend only on the ratio of the phase densities. Zivi [81] proposed a further modification endeavouring to discern between the bulk of the liquid phase and liquid entrained in the gas phase. The result was an expression for void fraction incorporating an entrained liquid fraction, *E*;

$$\alpha = \left\{ 1 + E\left(\frac{v_l}{v_g}\right)\left(\frac{1-x}{x}\right) + (1-E)\left(\frac{v_l}{v_g}\right)^{2/3}\left(\frac{1-x}{x}\right)\left[\frac{1 + E\left(\frac{v_l}{v_g}\right)\left(\frac{1-x}{x}\right)}{1 + E\left(\frac{1-x}{x}\right)}\right]^{1/3} \right\}^{-1} \tag{2.60}$$

Although this improved model of Zivi [81] is only applicable to steam-water flows, according to the author, if the entrained liquid fraction is assumed to be zero, it provides the lower bound for much of the available experimental data. This is not dissimilar to the minimum theoretical value for the void fraction which coincides with the maximum slip ratio;

$$k=\left(\frac{v_g}{v_l}\right)^{\frac{1}{2}} \tag{2.61}$$

A similar approach to that of Zivi [81], was taken by Smith [82] (1971). Smith [82] also includes in his correlation a factor allowing a fraction of the liquid phase to be considered entrained in the gas phase forming a homogeneous mixture travelling in the gas core. Smith [82] proposed that the momentum of the separated phases, a liquid phase and a gas phase containing liquid droplets could be assumed to be equal e.g., 'equal velocity head'. Similarly to Zivi [81], the model of Smith [82] is only applicable to air-water and steam-water flows.

Chisholm [54] uses Smiths' 'equal velocity head' model to show that by assuming an entrained liquid fraction of *E*, the slip can be shown to be;

$$k=E+(1-E)\left[\frac{1+E[(1-x)/x]v_l/v_g}{\frac{v_g}{v_l}+E(1-x)/x\frac{v_l}{v_g}}\right]^{\frac{1}{2}} \tag{2.62}$$

According to Chisholm [54] a value of 0.4 for entrainment gives good experimental agreement for air-water flows. Chishom [54] concludes that using the homogeneous specific volume, defined by Equation 2.31 in his 'equal velocity head' model gives good agreement over a wide range of steam-water conditions if the slip ratio is calculated using;

$$k=\left(\frac{v_h}{v_l}\right)^{\frac{1}{2}} \tag{2.63}$$

where v_h is given by;

$$v_h = x v_g + (1-x) v_l \qquad (2.64)$$

Equation 2.62 can also be expressed as;

$$k = \left[1 - x\left(1 - \frac{v_g}{v_l}\right)\right]^{1/2} \qquad (2.65)$$

The simplest method to predict the void fraction is to assume the slip ratio to be unity and this allows Equation 2.21 to become;

$$\alpha = \frac{x v_g}{x v_g + (1-x) v_l} \qquad (2.66)$$

This is the homogeneous assumption and by definition the void fraction determined by this model provides an upper bound for void fraction prediction. For most instances the homogeneous assumption over predicts the void fraction. However, at low qualities and high mass fluxes, a good approximation of the void fraction can be obtained using the homogeneous assumption.

One of the more sophisticated empirical correlations used to predict the void fraction is known as the CISE correlation, Premoli *et al* [58]. The correlation works well because, depending on flow conditions, it assumes either separated or homogeneous flow. For definitions of homogeneous and separated flow see Sections 2.5.5 and 2.5.9 respectively. The correlation uses Equation 2.67 to determine the slip ratio from which the void fraction can be calculated. The slip ratio is given by;

$$k = 1 + E_1\left(\frac{y}{1 + yE_2} - yE_2\right)^{0.5} \qquad (2.67)$$

where

$$y = \frac{x}{(1-x)}\frac{v_g}{v_l} \qquad (2.68)$$

$$E_1 = 1.578\,\mathrm{Re}^{-0.19}\left(\frac{\nu_g}{\nu_l}\right)^{0.22} \tag{2.69}$$

$$E_2 = 0.0273We\,\mathrm{Re}^{-0.51}\left(\frac{\nu_g}{\nu_l}\right)^{-0.08} \tag{2.70}$$

and the Weber number was determined from;

$$We = \frac{G^2 D\mu_l}{\sigma} \tag{2.71}$$

The empirical correlations for void fraction are effectively correlations for the slip ratio. All the above correlations allow the void fraction to be predicted as an average across the channel. In real two-phase systems the void fraction and relative phase velocities will vary with radial position, i.e. velocity and void fraction have non-uniform distributions. The shape of these non-uniform distributions is called the concentration profile. A model especially formulated to deal with the relative motion of phases and the radial changes is the drift flux model, discussed in more detail in Section 2.5.4. A development of the drift flux model by Zuber & Findlay [61] allowed the same approach to be used to predict void fraction. A distribution parameter, C_0 was introduced to account for the non-uniform distribution of the void fraction and its concentration profile. Although accounting for non-uniform flow had already been attempted by Bankoff [60], Zuber and Findlays' model also incorporated the effect of the local relative velocity of the phases. The model has been generally applied across flow regimes, including annular flows, but it often requires knowledge about the velocity and void fraction distribution not readily available, see Butterworth & Hewitt [45].

Stepanek & Kasturi [83] (1972) introduced a dimensionless correlation with particular reference to two-phase flow in helical coils. The correlating parameters for void fraction and pressure drop were interrelated with the view that they would better account for the complex behaviours encountered in two-phase flows than simpler correlations. Gomezplata *et al* [84] (1972) modified a correlation introduced by Brown *et al* [85] (1969). Several parameters are defined in the correlation and the void fraction must be retrieved by an iterative method.

2.5.14 The General Application of Pressure Drop Correlations

There is some disagreement in the literature as to the most appropriate correlation to apply to a given set of conditions. Several investigators advise caution when attempting to apply a correlation to flows that lie out with the original experimental conditions, Collier & Thome [48], Thom [52] and Holt *et al* [86] (1999). The general application of any correlation will inevitably lead to it being used with experimental comparisons that are out with it's derivation, where it will perform poorly. This may partly explain the differing views held by investigators. The factors identified as obstacles to obtaining true comparisons of correlations are the differences in flow regimes, operating pressures and flow rates, methods of fluid injection and fluid properties, and the length and diameter of the test pipe and settling length.

Spedding *et al* [87] (1998) and Simpson *et al* [4] observed a deterioration in the predictive ability of correlations when they were applied to larger pipe diameters. The same authors also commented on errors attributable to flow development effects which are exacerbated when applying a single correlation across the entire spectrum of flow patterns. Hewitt [36] suggests that the only way to overcome these effects is to produce models that are flow-regime related. For a recent example of a flow regime related model see Holt *et al* [86].

Despite the difficulties encountered when making true comparisons, several correlations are demonstrably superior. Among these is the Friedel [50] correlation, Section 2.5.12, recommended by Hewitt [36]. Whalley [17] also recommends Friedel

[50] but qualifies its use, as described in Table 2.2. The review by Simpson *et al* [4] on horizontal correlations, which does not include Friedel [50], remarks on the relatively good performance of the Lockhart-Martinelli correlation. Spedding *et al* [87] (1998) provided an up-to-date comparison of a large number of correlations for vertical flows. Three correlations are recommended for pressure loss, Hagedorn & Brown [88] (1965), Beggs & Brill [89] (1973) and Orkiszewski [15]. Like the review by Simpson, Spedding *et al* [87] did not include the Friedel correlation. Govier & Aziz [47] favoured the correlation of Govier *et al* [19] for air-water incompressible flows.

Viscosity Ratio (μ_l/μ_g)	**Correlation** (-)	**Mass Flux, G** (Kg/m^{2}s)
<1000	Friedel [50]	-
>1000	Chisholm [122] (1973)	> 100
>1000	Lockhart & Martinelli [51] (1949)	< 100

Table 2.2: Recommendations for Correlations, Whalley [17]

It is widely agreed that it is unlikely that a single correlation will be able to provide the best agreement across all flow conditions. Orkiszewski [15] made improvements to the application of correlations by devising a scheme that embodied several correlations, giving a combination of methods and providing means by which they can be appropriately applied. More recently, and for similar reasons, Beattie & Whalley [49] proposed a method to calculate the frictional pressure drop allowing for flow pattern influences but maintaining a simplistic form.

The method of Beggs & Brill [89] differentiates between flow patterns by allowing appropriate adjustments to the correlation. Beggs & Brills [89] intended application was inclined pipes and a mechanism for incorporating flow pattern and the inclination angle effects on the void fraction was a necessary feature. Spedding *et al* [87] recommend this method for vertical flows but Collier & Thome [48] recommend it for inclined pipes only.

Hagedorn & Brown [88] devised an entirely empirical method which was principally an extended form of the single-phase energy balance. Using a mixture density and assuming that the friction factor was related to the Reynolds number and the relative roughness of the pipe wall, in the same way as it is for single-phase flows, they were able to define a two-phase Reynolds number. Good experimental agreement has been reported using this correlation.

Manabe *et al* [90] (1997) evaluated a mechanistic model that was a combination of existing correlations. Manabe *et al* [90] reported that for inclined and horizontal flows the mechanistic model out performed all commonly used correlations when applied to any flow pattern. Ellul & Issa [91] (1989) devised a separated flow model simulating bubbly flows. Hawkes *et al* [27] provided evidence for the behaviour of the core structures of wispy-annular flows associated with high mass fluxes. Ohnuki & Akimoto [92] (1996) investigated the dependency of two-phase flows on pipe scale using a 200mm diameter test section and Ohnuki & Akimoto [93] (2000), explored the effects of gas-liquid mixing methods.

2.5.15 Summary

The most commonly used two-phase flow models are empirical correlations, the majority of which were devised to meet the demands of a particular industrial application, e.g., oil, nuclear and boiler. Investigators tend to favour empirical correlations as they are relatively easy to apply and they require little or no understanding of the prevalent phenomena occurring in the system. Analytical models have been developed but the increased sophistication with which the subject has been approached has yet to yield improved methods of prediction, see Hewitt [36] and Hewitt [1].

A choice of empirically based solutions now exists with a varying degree of sophistication. The more obvious simplifying assumptions employed when deriving two-phase models leads to the homogeneous and separated flow models. Both models have been presented in the literature incorporating various two-phase multipliers and correction factors in an attempt to improve prediction accuracy and reliability.

The separated flow model is of particular interest as it enables various adjustments to be made for phase velocity differences, knowledge of which can be obtained from void fraction data. The favoured correlation for the frictional two-phase multiplier is that of Friedel [50] but this is not applicable where the viscosity ratio exceeds 1000. A strong candidate for experimental review is the C parameter method of Chisholm [2]. Based upon the pioneering work of Lockhart & Martinelli [51] the C parameter has a simplistic but accommodating method of correlating the friction gradient.

The most likely flow regime to be encountered by this investigation is annular flow, which is governed by the complex interaction of several different phenomena. The predominant flow properties influencing these phenomena are identified by Wallis [68] as the pressure gradient, buoyancy, surface tension, inertia of the gas, inertia of the liquid, viscosity of the gas and the viscosity of the liquid. Although strongly defined boundaries exist between the phases, phase interaction is not negligible. On the contrary, the existence of ripple and roll waves on the liquid surface is evidence of interfacial frictional forces at work. In addition to the losses due to the gas-liquid interface, entrained liquid in the gas phase can also contribute substantial energy losses. The mechanism of entrainment is not yet fully understood furthering the difficulties involved in the prediction of liquid entrainment. A correlation favoured by some authors is that of Govan *et al* [59].

Annular flow models have been devised that employ the triangular relationship of film liquid flow rate, thickness and shear stress. Varying degrees of success have been experienced with the application of these models, tending to work well over limited ranges out side of which they quickly become unreliable. This is due to the inability to accurately model the gas-liquid interface and difficulties relating to acceleration, entrainment and deposition effects.

2.6 Viscosity Effects on Pressure Drop Predictions in Pipes

A study on a 500m deep $1^1/_4$ nominal bore experimental well by Hagedorn & Brown [94] (1964), specifically addressed viscosity effects in pressure drop prediction. Test liquids included mixtures of Corsicana and crude oil with viscosity ranging from 0.86 through to 110 mPas. The most notable conclusion of Hagedorn & Brown [94] was the apparent cut off point for viscosity related effects. It was found that below a viscosity of 12 mPas that all viscous effects are negligible. Above 12 mPas significant pressure losses in addition to those recorded for equivalent air-water flows were observed. The additional losses incurred by the increased viscosity were attributed to the increased slippage between the two phases and the increased friction within the test liquid itself. Hagedorn & Brown [94] make the observation that a single cut off viscosity above which viscosity effects become important does not exist as viscosity effects were found also to be functions of the velocities of the two phases.

Holt *et al* [86] have produced a generally applicable method for pressure drop prediction in vertical flows through the provision of a regime dependent mix of correlations. The flow pattern specific model was tested on data generated using 10 and 5 mm diameter test section measuring the pressure drop and void fraction. Among the test mixtures used was air-aqueous glycerol test liquid with a viscosity 14 mPas. The model first predicts the flow pattern that is present and then an appropriate model is applied to suit the flow regime. For the annular flow regime, the correlation for entrainment and deposition is based on the work of Govan & Hewitt [59], the film thickness was determined from the method of Asali *et al* [95], and a new correlation was defined for the interfacial friction factor. The model is described as accurate in predicting annular flow data.

Fukano & Furukawa [96] (1998) studied the effects of high viscosity on the structure and interaction of two-phases by measuring liquid film heights using a conductance probe. Aqueous glycerol solutions with viscosities of 4, 6.4 and 10 mPas were used in vertical 26 mm and 19.2 mm diameter 5.4 m long pipes. Fukano & Furukawa [96] found the gas-liquid interfacial structure to be significantly influenced by the liquid viscosity and that the roll wave height was found to be proportional to the mean liquid film thickness. The mean film thickness, t_{fm}, was correlated by;

$$t_{fm} / D = 0.0594 \exp\left(-0.34 Fr_{gs}^{0.25} \mathrm{Re}_{ls}^{0.19} x^{0.6}\right) \qquad (2.72)$$

where Fr_{gs} is the Froude number defined by the superficial gas velocity and, Re_{ls} is the Reynolds number defined by the liquid superficial velocity. A method of calculating the frictional pressure drop was proposed and was shown to agree with the experimental data with an accuracy of ± 20%. The interfacial shear stress was calculated to be much higher than that found by Wallis [68].

Asali *et al* [95] (1985) using aqueous glycerol solutions, viscosity varied from 1.1 to 5 mPas, measured film height and film flow rate for a vertical annular flow in pipes of 22.9 and 42 mm diameter. A correlation was developed that allowed the liquid film height and interfacial friction factor to be predicted if the liquid film flow rate was known. Asali *et al* [95] improved on the ideas of Henstock & Hanratty [97] (1976) where a dimensionless film height was correlated with the liquid film Reynolds number. A method to determine the interfacial friction factor was then devised which was independent of the film height and pipe diameter.

Using the results of other investigators, including Asali *et al* [95], Ambrosini *et al* [98] (1991) constructed an extensive data set of vertical flow data covering a range of viscosities and pipe diameters. Asali *et al* [95] was found to concur well with data for low liquid film Reynolds numbers. Ambrosini *et al* [98] used the film thickness and interfacial friction factor correlations of Asali *et al* [95] to develop their own correlation for interfacial friction factor and droplet size prediction.

2.6.1 High Viscosity Effects on Liquid Entrainment

One of the more recent publications that deals directly with the effects of high viscosity in an annular flow is that of Mori & Nakano [99] (2001). Investigating the inception of disturbance waves and entrained liquid droplets, the structure of the gas-liquid interface and the flow rates of entrained liquid droplets in the gas phase of an aqueous glycerol solutions with viscosities of 3.5, 11.4, 36 and 86 mPas. Observations were made on a vertical, 10 mm diameter, 3 m long test length using an iso-kinetic probe measuring entrainment rates, and a hold-up probe measuring liquid film thickness. Mori & Nakano [99] found that the majority of the liquid became entrained in the gas phase at high gas velocities. Increased viscosity was found to further confuse the gas-liquid interface producing a higher number of ripples between roll waves. Increased viscosity increases the superficial liquid velocity above which roll waves appear. They also concluded that roll waves were not the only mechanism of entrainment since at high viscosities the inception of entrained liquid droplets preceded the inception of roll waves.

Another work specific to high viscous flows is that of Campanile & Azzopardi [100] (2001). A 12 mm diameter, 450 mm vertical test length was used to produce downward flow of corn syrup solutions, viscosity range 5000 to 50000 mPas. An attempt was made to characterise the effects of viscosity on film thickness and atomisation. Existing correlations were compared to experimental results, namely Govan *et al* [59], Asali *et al* [95] and Fukano & Furukawa [96] for entrainment, film thickness and the interfacial friction factor respectively. Empirical correlations were then developed that related the pressure gradient to film thickness and viscosity. Agreement with experimental data was described as good at the lower viscosities but a degree of discrepancy was found at the higher viscosity.

2.6.2 High Viscosity Effects on Void Fraction

To investigate the influence of viscosity on void fraction Kasturi & Stepanek [101] used corn-sugar-water test solutions, viscosities of 7.5 to 14.8 mPas, in a 12.5 mm diameter helical coil. Aqueous glycerol solutions were experimented with but they were found to foam to a high degree. Good agreement for a wide range of qualities was observed using the Lockhart-Martinelli viscous-viscous line. An increase in viscosity was found to have a retarding effect on the liquid causing a subsequent increase in the slip ratio.

Porzhezinskiy & Sagan [102] (1971) using a sugar-solution, viscosity varying between 9.3 and 70 mPas, studied the downflow in a 32.7 mm diameter pipe. Increasing the liquid phase properties of density and viscosity were reported to increase the causes producing velocity slip, hence a decrease in void fraction.

Weiss *et al* [103] (1985), used a 15.1 mm diameter 1.3 m long vertical pipe to observe the effects of viscosity. The test viscosity range was between 0.92 to 1670 mPas using silicone fluids (poly dimethylsiloxane). Intermediate viscosities were also examined and these were obtained by blending. Weiss *et al* [103] concluded that a clear effect of viscosity was an increased void fraction, which is in opposition of other investigators. It is not clear why.

Chisholm [104] (1962) investigated correlations for effective mixture density in a view to accommodating influences of liquid flow rate and viscosity. The main incentive was to improve existing correlations for void fraction and slip ratio. Using air-oil data from the literature, Chisholm [104] formulated an effective mixture density correlation for horizontal flows that was accurate to ±20 per cent. It is not clear what the corresponding improvement in void fraction and slip ratio prediction was.

2.6.3 Summary

Several authors have recently applied annular flow models to viscous flow applications. The method of Holt *et al* [86] can be generally applied due to the flow pattern specific approach used. For the annular flow regime the work of Asali *et al* [95] was used to determine the film thickness.

Publications that focused on methods for determining the liquid film thickness, and interfacial friction factor are Asali *et al* [95], Ambrosini *et al* [98], Fukano & Furukawa [96]. Viscosity was noted as having a significant effect on the gas-liquid interface by Fukano & Furukawa [96] whom correlated an expression for the liquid film mean thickness. Asali *et al* [95] correlated a dimensionless film height with the liquid film Reynolds number. This idea was then utilised by Ambrosini *et al* [98] who developed a more extensive set of correlations.

The effects of high viscosity on entrainment and deposition rates have been investigated by Mori & Nakano [99] and Campanile & Azzopardi [100]. Much attention was given to the gas-liquid interface by Mori & Nakano [99] and they concluded that liquid entrainment was effected by at least two different mechanisms. The work of

Campanile & Azzopardi [100] reports a mixed performance when they compared an annular flow model to high viscosity data.

Several investigators have examined the effects of viscosity on the slip ratio. The majority of these are in agreement that viscosity cause an increase in slip ratio. The exception is the work of Weiss *et al* [103].

A pattern is emerging of viscosity effects on flow properties, increased slip ratio, larger friction gradients and differing patterns of liquid entrainment. A degree of success is also evident in the predictive methods for the interfacial friction factor and liquid film thickness. The performance of the more generally applied correlations in highly viscous two-phase flows has not been documented. The viscosity of some publications is limited and those that deal with the high viscosity flows have had a narrow application or have been focussed on a specific flow characteristic.

2.7 Pressure Losses Due To Flow Restrictions

Industrial needs have dictated that some types of fittings have received more attention than others. For example, attempts to derive metering methods for two-phase flow similar to those employed in single-phase flow and the examination of the geometry of nozzles and abrupt enlargements so as to obtain a better understanding of the throttling process in valves. Examples of orifice plates studies with a view to metering two-phase flows are Chisholm [105] (1977), Dickson & Wood [106] (1972), Graham [107] (1967) and more recently Ferreira [108] (1997). For nozzles see Chisholm [109] (1967), Wallis & Sullivan [110] (1972) and Martindale & Smith [111] (1982). A recent study of abrupt contractions is given by Schmidt & Friedel [112] (1997).

The different geometry of each pipeline component results in a different balance of recoverable and unrecoverable pressure change. According to Hewitt [36] and

Whalley [17], for gradual changes in cross section, where there are no separation and circulation effects, the homogeneous and the separated flow models are sufficient to describe the flow. Other pipeline components are far more flow intrusive and have downstream settling lengths of up to ten times that observed for single-phase flows.

2.7.1 Homogeneous and Separated Flow Models

The application of the homogeneous and separated flow models requires the calculation of an all-liquid single-phase pressure loss. This all-liquid single-phase pressure loss is calculated from;

$$\Delta p_{lo} = \frac{\beta G^2 v_l}{2} \tag{2.73}$$

where single-phase loss coefficient, β, is as described in Section 2.2.2.

To determine the total two-phase pressure drop across a pipe restriction, a two-phase multiplier is applied to the all-liquid single-phase pressure loss;

$$\Delta p_{tp} = \phi_{lo}^2 \Delta p_{lo} \tag{2.74}$$

From the momentum balance, as described in Section 2.5.3, Bergles *et al* [113] (1981) defines the two-phase pressure loss for homogeneous assumption as;

$$\Delta p_{tp} = \frac{A_1}{A_2}\left(1 - \frac{A_1}{A_2}\right) G^2 \left(x v_g + (1-x) v_l\right) \tag{2.75}$$

And the separated flow assumption as;

$$\Delta p_{tp} = \frac{A_1}{A_2}\left(1 - \frac{A_1}{A_2}\right) G^2 \left(\frac{(1-x)^2 v_l}{(1-\alpha)} + \frac{x^2 v_g}{\alpha}\right) \tag{2.76}$$

Figure 2.5 depicts the general trend of the homogeneous and separated flow models when plotted against quality for air-water at atmospheric pressure. A major difficulty of the application of both homogeneous and separated flow models is the effect of void fraction. For some pipeline components such as orifice plates, valves and abrupt enlargements, obtaining values for the void fraction as the flow passes through the fitting is impractical. However the assumption that void fraction remains constant across the pipeline component is invalid, Hewitt [36].

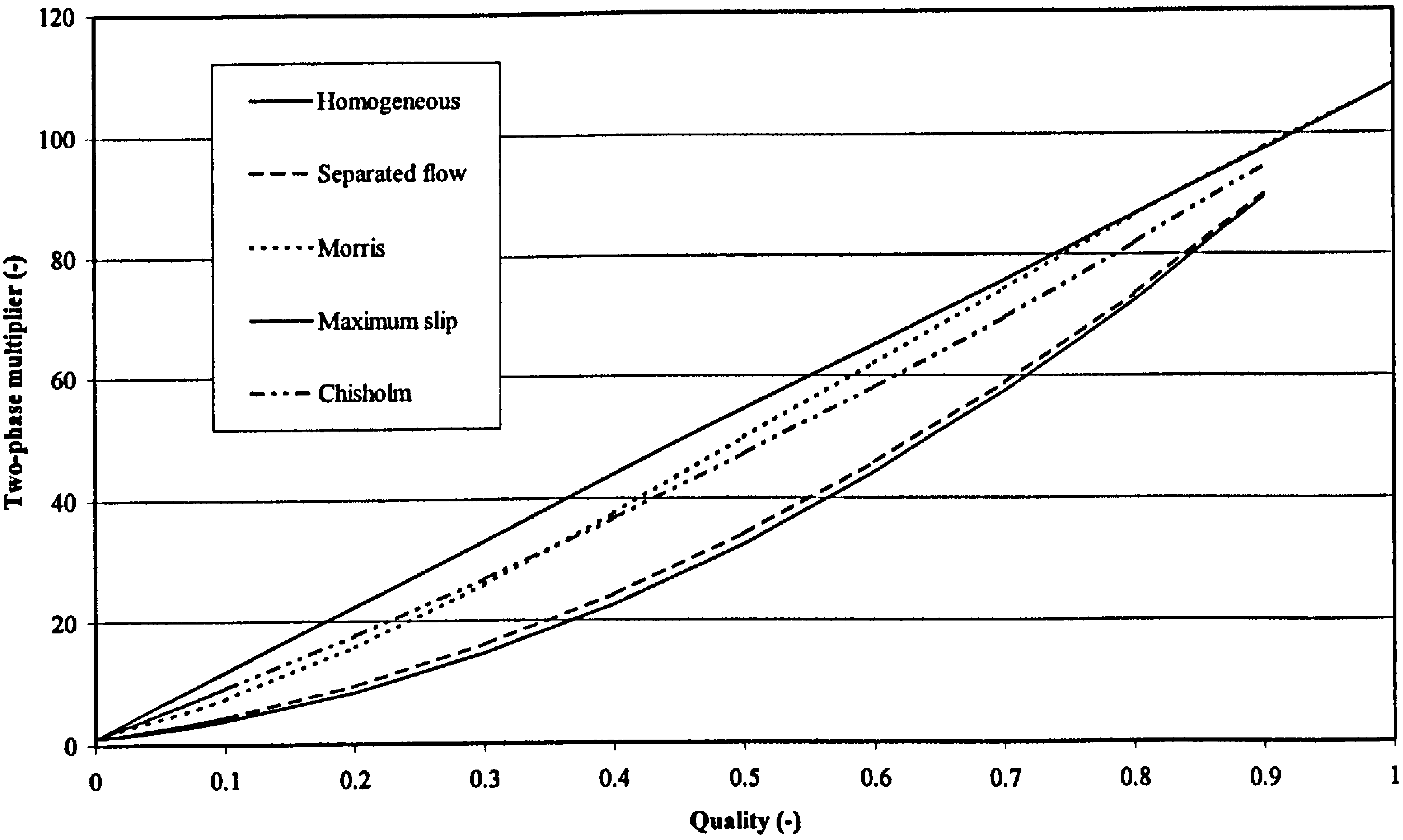

Figure 2.5: Two-phase multipliers for pipeline components.

Another deficiency of homogeneous and separated flow models is the occurrence of entrainment. This is demonstrated by the homogeneous models tendency to over predict the momentum flux in pipes and nozzles and the separated flow models tendency to do the converse. Both models fail because they represent two extreme scenarios.

The homogeneous model lumps the gas and liquid phases together, attributing them with the same velocity, when this is not physically taking place. The separated flow model attributes distinct gas and liquid velocities which is a more accurate representation of the actual flow but only for a limited range of conditions. Over most of the annular flow range, a large proportion of the liquid phase is entrained in the gas phase travelling at velocities greater than that of the liquid bulk. McNeil [57] advises that for vertical flows entrained liquid travels at up to 90 per cent of the gas velocity. A more accurate prediction of the two-phase multipliers was obtained from a model that lay some where between the two extremes of the homogeneous and separated flow models. Morris [114] (1984) used a two-phase multiplier based on an 'effective' two-phase specific volume, v_m, given by;

$$v_m = \left[x v_g + k(1-x)v_l\right]\left[x + (1-x)E + \frac{(1-E)^2}{(k-E)}\right] \qquad (2.77)$$

where the slip ratio and the entrained liquid fraction were calculated from;

$$k = \left[\frac{x v_g + (1-x)v_g}{v_l}\right]^{1/2} \qquad \& \qquad E = k\left(\frac{v_l}{v_g}\right)^{1/2} \qquad (2.78)$$

This idea was further explored by McNeil [57] for incompressible flow in nozzles and is discussed in Section 2.7.5.

2.7.2 Experimentally Obtained Two-Phase Multipliers

The difficulties of describing the void fraction and entrained liquid fraction of flows within fittings has lead investigators to generate experimental two-phase multipliers. The pressure drop attributed to a pipeline restriction is found experimentally by measuring the two-phase pressure gradient before and after the fitting. This method is demonstrated by Geiger & Rohrer [115] (1966) and Schmidt & Friedel [116] (1996) in the context of a sudden expansion. The pressure loss due to the pipeline component is then found by determining the pressure gradients to either side of the restriction and then extrapolating to the centre line of the change in area. This procedure is illustrated in Figure 2.6.

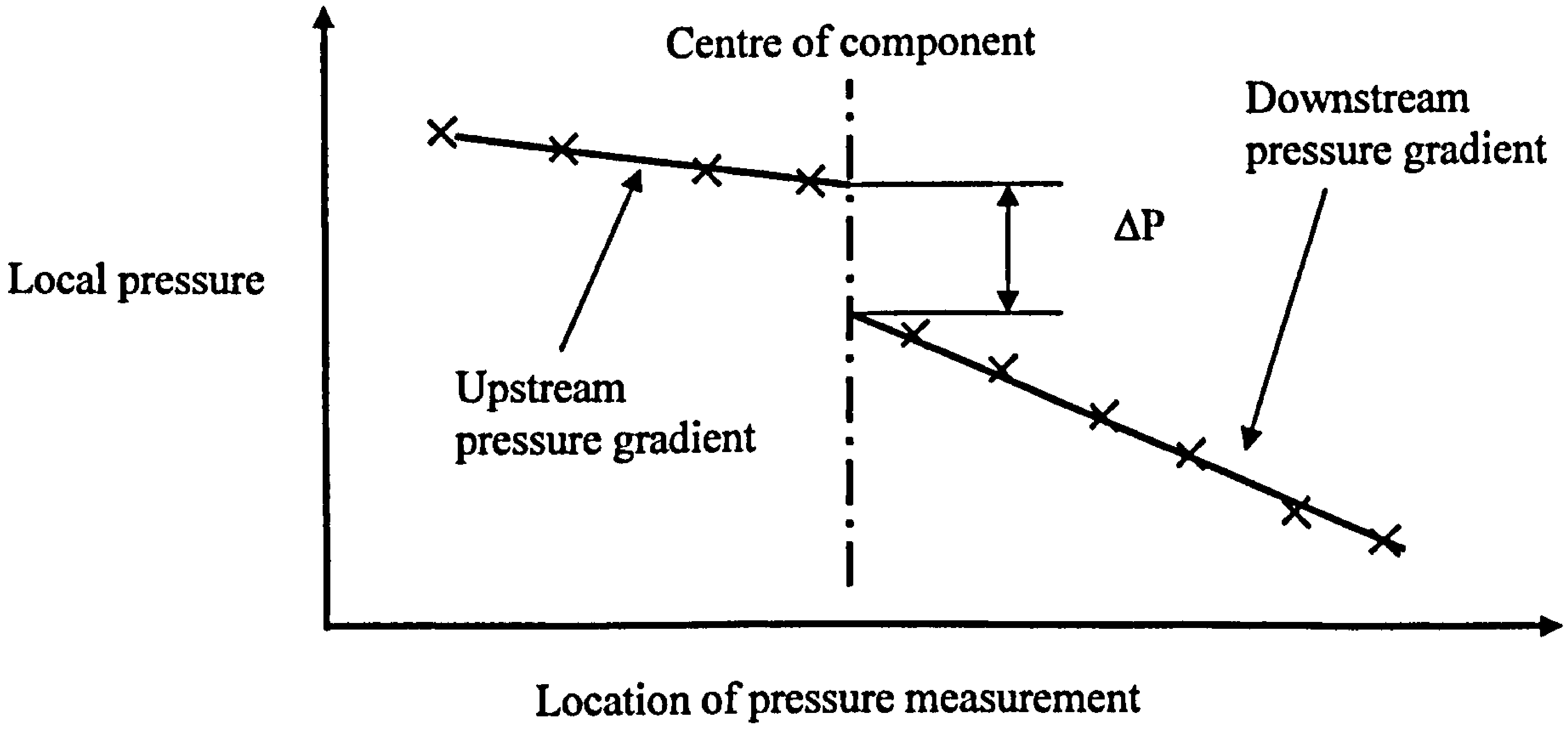

Figure 2.6: Experimental pressure drop for pipeline components.

2.7.3 Orifice Plates

In comparison to other pipeline components, the pressure recovery following an orifice plate is small. The most simplistic treatment of an orifice plate is to apply the energy equation between a plane in up stream position and a plane located at the vena contracta. If it is assumed that the flow is homogeneous and that the void fraction is constant then the pressure loss, for an orifice of area, A_o, can expressed as;

$$\Delta p_{1-2} = \frac{G_1^2 v_l}{2c_D^2}\left[\frac{A_1}{A_o}-1\right]\left[1+\left(\frac{v_h}{v_l}\right)x\right] \qquad (2.79)$$

where the discharge coefficient, c_D, is a modified contraction coefficient allowing for the effects of the velocity profile. Equation 2.79 is in practice a reasonably inaccurate model. Superior models have been derived by further examining the processes governing the interaction of the phases as they pass through the orifice plate. Early attempts at improving orifice plate models are Dickson & Wood [106] and the work of Chisholm [105].

A review of two-phase flow pressure losses in pipeline fittings given by ESDU [117] (1989), recommends the use of the two-phase multiplier of Simpson *et al* (1983). The ESDU [117] selection of correlation was based on several sources of experimental data including air-water, steam-water and air-oil, and is given as;

$$\phi_{lo}^2 = \left[1 + x \left\{ \left(\frac{v_g}{v_l} \right)^{1/6} - 1 \right\} \right] \left[1 + x \left\{ \left(\frac{v_g}{v_l} \right)^{5/6} - 1 \right\} \right] \tag{2.80}$$

The ESDU [117] advises that the accuracy of prediction for the multiplier is at best ± 20% and in some cases as poor as + 40%.

A recent publication by McNeil [118] (2000) presents a model for all expansion-contraction type pipeline components involving incompressible and compressible flows. Knowledge of fitting-specific slip and liquid entrainment at orifice plate is not required as upstream pipe flow properties are used. The momentum correction factor of McNeil [57] (1998), Equation 2.54, is used along with the single-phase loss fitting to allow pressure drops due to the fitting to be calculated.

2.7.4 Valves

Data for two-phase flow through valves was found to be the least available for pipeline components considered by this study. Hewitt [36] describes the use of an expression for the two-phase multiplier for the window-zone of a shell-and-tube heat exchanger. For a fully open globe valve the two-phase multiplier is calculated from;

$$\phi_{lo}^2 = 1 + \left(\frac{v_g}{v_l} - 1 \right) \left[1.6 x_g \left(1 - x_g \right) + x_g^2 \right] \tag{2.81}$$

The ESDU [117] publication recommends a two-phase multiplier determined by the method of Morris (1985). The ESDU [117] correlation selection was based on several sources of experimental data including air-water, steam-water and air-kerosene, and is given as;

$$\phi_{lo}^2 = \left\{x v_g/v_l + k(1-x)\right\}\left[x + \frac{(1-x)}{k}\left\{1 + \frac{(k-1)^2}{(v_g/v_l)^{1/2} - 1}\right\}\right] \qquad (2.82)$$

where the slip ratio is;

$$k = \left[1 + x\left(\frac{v_g}{v_l} - 1\right)\right]^{1/2} \qquad (2.83)$$

The globe valve two-phase multiplier correlation was derived from predominately air-water data and according to ESDU [117] will predict with an accuracy of ±20 %.

As the flow through a globe valve can be considered to be contracting and then expanding the model of McNeil [118], as discussed in Section 2.7.3, can be applied. McNeil [118] treats a globe valve as an equivalent orifice plate by assuming any losses incurred by flow direction changes in the valve can be represented as orifice plate form loss. Similarly to orifice plates the slip ratio and entrained liquid fraction upstream of the globe valve allow pressure drop predictions to be calculated using the single-phase loss coefficient.

2.7.5 Nozzles

Similarly to orifice plates, most interest in nozzles has stemmed from the need to devise metering methods for two-phase flows. Graham [107] correlated the data for the vertical flow of air-water through nozzles of diameter, 15.9, 24.5 and 35 mm for qualities mostly outside of the annular flow region.

The lesson learned from other pipeline components is the need to account for processes occurring within the fitting such as liquid entrainment and slip ratio effects.

This approach was adopted by King & Piar [119] (1999) where entrainment and deposition mechanisms were used for the determination of what they describe as multidimensional effects. The model assumed an annular displaced flow and was derived from data obtained for a vertically orientated converging nozzle with a throat diameter of 10 mm.

A publication of McNeil [57] builds upon an approach of Morris [114]. An annular flow is envisaged with some of the liquid phase travelling at a lower velocity while the rest travels as a homogeneous mixture with the gas phase, i.e., mixed with the gas and at the gas velocity. The model is advantageous as it can be applied using existing pipe flow correlations to obtain the slip ratio and entrained liquid fraction. The model compares well with air-water data provided in the literature.

2.7.6 Abrupt Enlargements

If wall shear and gravity forces are ignored, a momentum balance can be obtained for the incompressible two-phase flow through an abrupt expansion. For a homogeneous flow, where the ratio of the two areas of cross section is, *S*, the resulting pressure loss is given by;

$$\Delta p_{1\text{-}2} = -G_1^2 S(1-S)v_l\left[1+x\left(\frac{v_g}{v_l}-1\right)\right] \qquad (2.84)$$

The same difficulties are encountered with the homogeneous abrupt expansion model that are known to occur when the homogeneous model is applied to other pipeline components. The homogeneous model is invalid because entrainment and slip ratio effects are ignored and the void fraction is not constant across the abrupt expansion, Collier & Thome [48].

The two-phase multiplier recommended by the ESDU [117] publication is that of Simpson *et al* (1983) and is given as;

$$\phi_{lo}^2 = \left[1 + x\left\{\left(\frac{v_g}{v_l}\right)^{1/6} - 1\right\}\right]\left[1 + x\left\{\left(\frac{v_g}{v_l}\right)^{5/6} - 1\right\}\right] \quad (2.85)$$

ESDU [117] advise that there are no apparent inaccuracies resulting from particular ranges of inlet diameter, area ratio or mass velocity. The correlation was derived from steam-water data mostly in the annular flow regime.

McNeil [57] suggests that the pressure drop across an abrupt enlargement can be determined from the application of the momentum equation giving;

$$p_t - p_2 = G_2\left(c_{m2}G_2v_2 - c_{mt}G_tv_t\right) \quad (2.86)$$

where the subscripts t and 2 stand for throat and downstream pipe respectively and the momentum correction factor c_m, is calculated using Equation 2.54.

2.7.7 Summary

The application of either homogeneous or separated flow models to predict pressure losses due to pipeline components is insufficiently accurate in most instances. The literature contains few extensive explorations of two-phase flow through pipeline components. Enhanced correlations have been proposed by ESDU [117], which at best provide data fits of ± 20% over selected quality ranges. More ambitious models have been developed that incorporate slip ratio and entrainment effects, most notably that of McNeil [57] and McNeil [118]. Further experimental work is required to fully validate these models. There are no data sets available that contain highly-viscous two-phase flows through pipeline components.

2.8 Viscosity Effects on Pressure Losses Due To Flow Restrictions

Dickson & Wood [106] studied the downward flow of air-oil mixtures through a sharp-edged orifice plate. The behaviour of air-oil mixtures was shown to only slightly deviate from the air-water mixtures but this was for a restricted quality range and low viscosity.

Schmidt & Friedel [116] tested the flow of two-phase mixtures through an abrupt enlargement for eight different area ratios. Several liquid phases were used including air-glycerine. The maximum liquid viscosity was 31 mPas for mass fluxes of 1000, 2000 and 3000 kg/m^2/s. At the higher mass fluxes, the phases were found to foam on discharge but at the lower mass fluxes the pressure change was a strong function of liquid phase density and viscosity. The effect of the liquid viscosity on the pressure was much greater than that of the liquid density. A semi-empirical model to predict pressure change was proposed. The model incorporates liquid phase viscosity, entrainment, void fraction and surface tension and is described as being sufficiently accurate for engineering purposes.

Schmidt & Friedel [112] evaluated a model for pressure drop across a sudden contraction. Using the same experimental set up as Schmidt & Friedel [116], a range of viscosities and diameter ratios were tested. Two-phase flows were found not to contract beyond the physical edge of the fitting. Similar to the work on the abrupt enlargement, a new model incorporating the parameters of void fraction, entrainment, liquid viscosity and surface tension was proposed. The model is described as being sufficiently accurate for engineering purposes.

2.9 Summary of Review

Single-phase turbulent and laminar flows in pipes have been thoroughly explored and are well documented in the literature. This is also true for the generation of loss coefficients for turbulent flows through standard pipeline components. For laminar flows through pipeline components the influences of viscous forces leads to a strong Reynolds number dependency occurring below a critical Reynolds number. For many standard geometry's this dependence and the resulting loss coefficient has yet to be fully investigated although several publications demonstrate the peculiarities of flows at low Reynolds numbers. Most notable among theses are Alvi *et al* [9], Edwards *et al* [10], and Kitteridge & Rowley [6]. Single-phase loss coefficients at low Reynolds numbers are of particular interest as they may be necessary for the determination of two-phase multipliers for high viscosity two-phase flows through pipeline components.

Two-phase flows are characterised by flow patterns. A method of deciphering two-phase data flow to assist in interpretation and analysis is the use of flow pattern maps. Although there are many investigations of flow pattern maps little exists for high viscosity flows. Furukawa & Fukano [42] is one of the few publications that attempts to investigate the effects of high viscosity on the validity of the boundaries of existing flow maps.

A large body of work exists concerning the prediction of pressure drop of two-phase flows. Much of this work is based upon the application of two generally applicable models, the homogeneous and separated flow model. The simplifying assumptions made in order to derive these models allow them to be easily applied but these same simplifications can also leads to high margins of error. Of the two, the separated flow model has a much higher degree of adaptability, as differences in the phase velocities and liquid entrainment can be considered. Both the homogeneous and separated models require an empirical solution for the fictional pressure gradient and this is often determined using a two-phase multiplier. The C parameter method Chisholm [2] is often used for this purpose. Another widely applied correlation of the two-phase multiplier form is that of Friedel [50]. The Friedel [50] correlation was derived from an extensive data set and as a result it has proven to be the most reliable correlation for a wide range of applications. The performance of these generally applied correlations in the context of high viscosity flows has never been assessed.

The common occurrence of the annular flow regime in two-phase applications has lead to the developed of an annular flow specific model. Some recent publications contain correlations for the annular flow model derived using viscous flows. These correlations are used for determination of film thickness, interfacial friction factor and pressure drop. Key to these correlations are the mechanisms of liquid deposition and entrainment. A certain amount of insight into high viscosity effects has been provided by Fukano & Furukawa [96], Asali *et al* [95], Ambrosini *et al* [98] and Campanile & Azzopardi [100] but further exploration is required as most of these studies have only used relatively low viscosities.

A disadvantage of empirically based correlations is that they are effectively restricted to the range of conditions from which they were derived. According to Holt *et al* [86] empirical correlations should only be applied to conditions that do not lie out with the originating experimental work. The generally applied correlations of Lockhart & Martinelli [51], Chisholm [2] and Friedel [50] were not derived from high viscosity data. This means that the performance of these models when applied to high viscosity flows is unknown. A situation that is not easily remedied as very limited high viscosity two-phase data is provided in the literature.

The established practice for evaluating pressure losses due the flow of two-phase flows through pipeline components is to employ two-phase multipliers. The publication of ESDU [117] is a review of two-phase multipliers determined for standard pipeline fittings. ESDU [117] provides recommendations for the most reliable of these correlations. There are no publications, including ESDU [117], that provide two-phase multipliers derived from high viscosity data. The work of McNeil [118] is the only two-phase model for flow restrictions that includes compressibility effects. Neither the recommendations of ESDU [117] nor the slip model of McNeil [118] have been assessed using high viscosity data.

The main objective of this study is to determine the appropriate design methods to employ when evaluating the performance of pipe flows and pipeline components with respect to highly viscous two-phase flows. As demonstrated by this review there are no publications that provide an empirical verification of existing models as the literature has only limited high viscosity two-phase pipe flow data and an absence of any high viscosity two-phase pipeline components data.

Chapter 3

DESIGN & INSTALLATION OF THE EXPERIMENTAL TEST FACILITY

3.1 Introduction

A new and unique facility was developed for this study and installed in the Department of Mechanical Engineering of Heriot-Watt University. The implementation of the new facility required the identification of appropriate two-phase flow research techniques. From these techniques corresponding design criteria and system parameters were derived. Careful consideration was given to:

- Project objectives e.g. obtaining highly viscous two-phase experimental data.
- The existing knowledge base present at Heriot-Watt University due to a history of research in two-phase flow and single-phase highly viscous flows.

3.2 Design Considerations

3.2.1 Project Objectives

The purpose of the rig was the experimental testing of highly-viscous two-phase flows in the vertical orientation using a straight length of pipe and the standard pipeline components of an orifice plate, nozzle, globe valve and abrupt enlargement. The test facility was required to operate with air-water and air-glycerine two-phase mixtures i.e., water and glycerine test liquids. This flexibility in the choice of test liquids enabled the direct comparison of the behaviour of highly-viscous two-phase flows with better understood air-water two-phase flows.

3.2.2 Existing Single-Phase Test Facility

Prior to this study, the Department of Mechanical and Chemical Engineering at Heriot-Watt University had been involved in the investigation of highly viscous single-phase flows. A description of an earlier facility is given by McNeil *et al* [13] (1999). Although only a single-phase test facility, knowledge gained through its operation provided an important stepping stone for the design of the more complex two-phase facility.

In addition to the operational side of a highly-viscous test facility, the expertise gained from these earlier studies was advantageous in the selection of test liquids. First hand experience of the complications of using non-Newtonian test liquids influenced the selection of a Newtonian test liquid.

3.2.3 Test Facility Design Criteria

To fulfil experimental commitments and take advantage of existing expertise, as outlined in Sections 3.2.1 & 3.2.2 respectively, the following design criteria were identified:-

- The supply and circulation of the liquid phase with sufficient storage capacity enabling highly-viscous test liquids to be repeatedly introduced and with drawn from service.
- The generation and supply of a gas phase i.e., air at a constant supply pressure.
- A means of accurately measuring the gas phase mass flow rate.
- A means of accurately measuring the liquid phase mass flow rate.
- A test length incorporating, pressure taps for local pressure measurement and the facility to house in-line test components.
- A means by which the local pressure taps on the test length could be purged by the gas or liquid phases.

- A mixing device to introduce the liquid phase to the gas phase.
- A separation tank to assist in the re-circulation of the test liquid.
- A method to measure the momentum flux rate of the test liquid as it discharges from the test length in to the atmosphere.
- A means of measuring the void fraction of two-phase flows.
- A data acquisition system enabling the electronic logging of pressure and momentum readings.
- A method of controlling the temperature of the circulating test liquid.

3.3 General Layout of Test Facility

The layout of the test facility is given in the schematic, Figure 3.1. The experimental rig comprised of three loops around which liquid was circulated by means of a positive displacement pump. Two of the loops, the test loop and the calibration loop, were constructed from 25 mm nominal bore copper pipe and the third, a re-circulating loop, was constructed from 50 mm nominal bore copper pipe. During operation the re-circulation and one other loop were used simultaneously.

A bank of control valves on the discharge side of the pump was used to select either the test or calibration loop and appropriate flow nozzle. The pump was located on the basement floor, the lowest point on the test facility. Liquid from two 40 gallon supply tanks passed through a heat exchanger to the suction side of the pump via a 100 mm diameter PVC pipe. A large diameter pipe was used on the suction side of the pump so that the frictional pressure drop in the pipe did not exceed the gravitational pressure drop during highly viscous tests, thus avoiding cavitation problems encountered in the single-phase work of McNeil *et al* [13].

Experimental mass flow rates were regulated by the use of valve A. Adjustments made to the position of valve A to constrict the flow in the re-circulation loop diverted more of the test liquid through either the test or calibration loops.

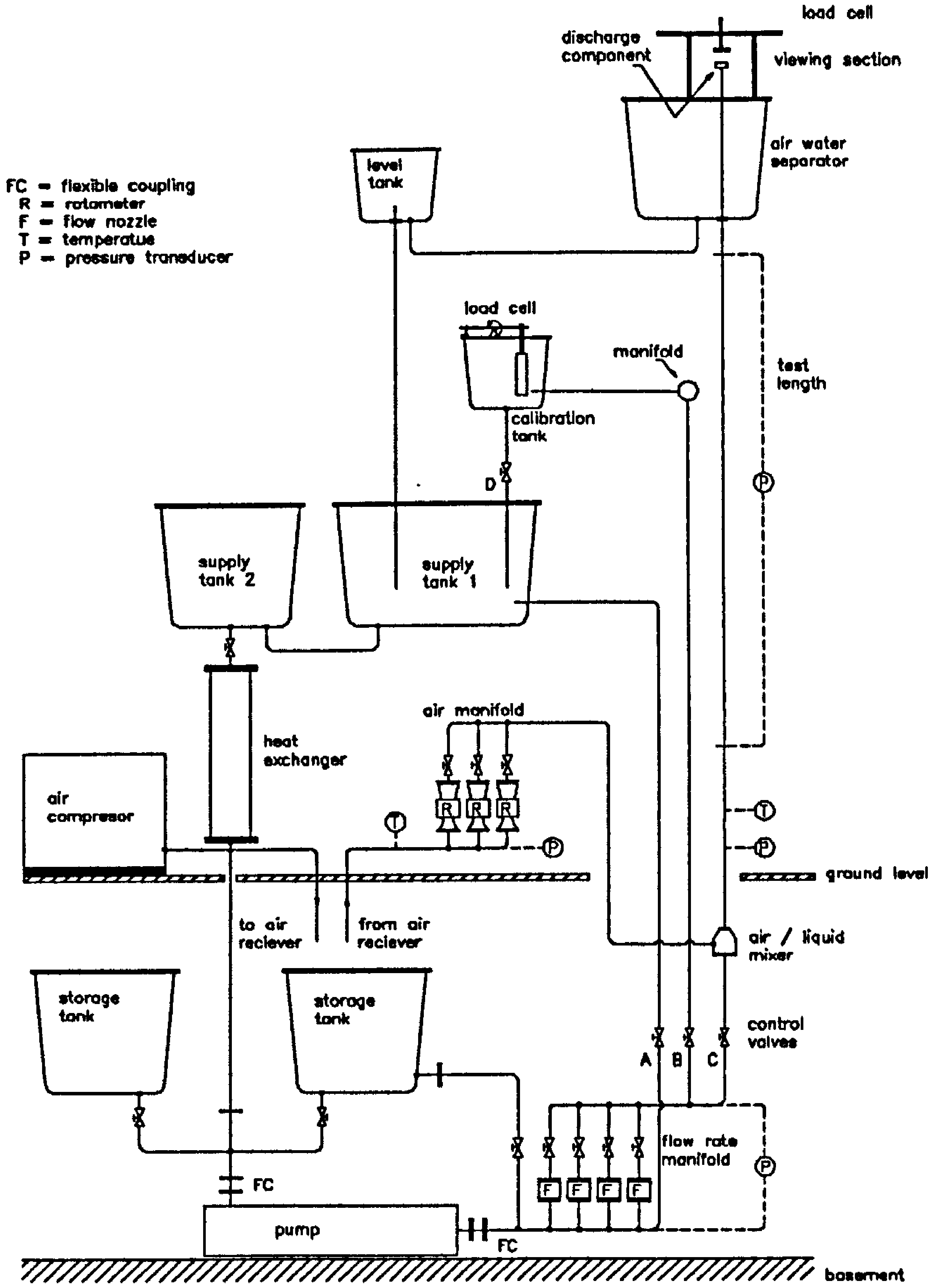

Figure 3.1: Test Facility Layout

The test loop, engaged by opening valve C and closing valve B, ran vertically from the ground to a high level and incorporated an air-liquid mixing device, a settling length and a test section. Mounted above the exit of the test section was a target, used to measure the momentum flow rate of the exiting test liquid. The target and the end of the test section were enclosed in a viewing glass to allow visualisation of the momentum exchange. The viewing glass also acted as a channel diverting the test liquid after impinging on the target into the separation tank. The test liquid was returned to the supply tanks from the separation tank. A thermocouple was placed at the beginning of the test section to allow the test temperature to be measured.

The calibration loop, engaged by closing valve C and opening valve B, ran vertically and terminated with a 2" nominal bore, horizontal manifold that evenly distributed the test liquid between two 20 gallon calibration tanks situated above the supply tanks. Liquid draining from calibration tanks into the supply tanks below was controlled by valve D. A thermocouple positioned up stream of the distribution manifold on the calibration loop gave the calibration temperature. A float connected to a load cell arrangement was inserted in each calibration tank. The rising liquid levels in the calibration tanks increased the buoyancy force acting on the float and in turn on the load cell. The calibration of the buoyancy force with the liquid level in each calibration tank is described in Section 4.5.2.

Two-phase work required the delivery of air to the air-liquid mixer. An Ingersoll-rand SSR M110 compressor was used to replenish an air receiver located in the basement. From the air receiver the test facility could draw a constant air supply at a static pressure of 7.5 bar gauge. Three Fisher-Rosemount Brooks air rotameters were installed between the air receiver and the air-liquid mixer. The rotameters allowed the continual monitoring of the mass flow rate of air flowing through the test facility, the regulation of which was achieved by the use of three gate valves located downstream of the rotameters. A thermocouple was positioned upstream of the rotameters to give the air supply temperature. Air delivered to the air-liquid mixer passed into the test loop, discharged at the test loop exit and vented to atmosphere through three 200 mm diameter exhausts on the separation tank.

3.4 Detail Description of Test Facility Components

3.4.1 Test Section

The test section, shown in Figure 3.2, was housed vertically in a purpose built scaffolding tower constructed from 25 mm square section tube. Both the test section and a preceding 2.75 m settling length were made from 25 mm diameter nominal bore copper tube. A series of twelve 2 mm diameter pressure taps were located over the full length of the test section the positions of which are given in Figure 3.2.

The mid section of the test section consisted of an interchangeable spool piece. The ability to readily remove and replace the spool piece enabled a range of test components to be inserted in-line with the test section. With the exception of a standard one inch globe valve, all test components were manufactured in-house. These were a straight length of pipe, a nozzle, an abrupt enlargement and an orifice plate, details of which are given in Figure 3.3. The globe valve, rated PN32, was manufactured in accordance with BS 5154 series B and dimensions are given in Figure 3.10. All globe valve tests took place with the valve seat in the fully open position.

The frequency with which the test components would be inter-changed necessitated the construction of a custom designed flange. The design of flange needed to ensure a leak free connection whilst maintaining the integrity of the internal surface of the test section. All flanges were machined from Brass bar as per Figure 3.4. For certain experimental work the test section and preceding settling length were required to be re-installed in 20 mm nominal bore tube e.g. to allow experimental work involving the abrupt enlargement. This difficulty was accommodated by fitting custom built flanges to all 25 and 20 mm nominal bore test section spool pieces and settling lengths, providing the necessary flexibility for any combination of assembly.

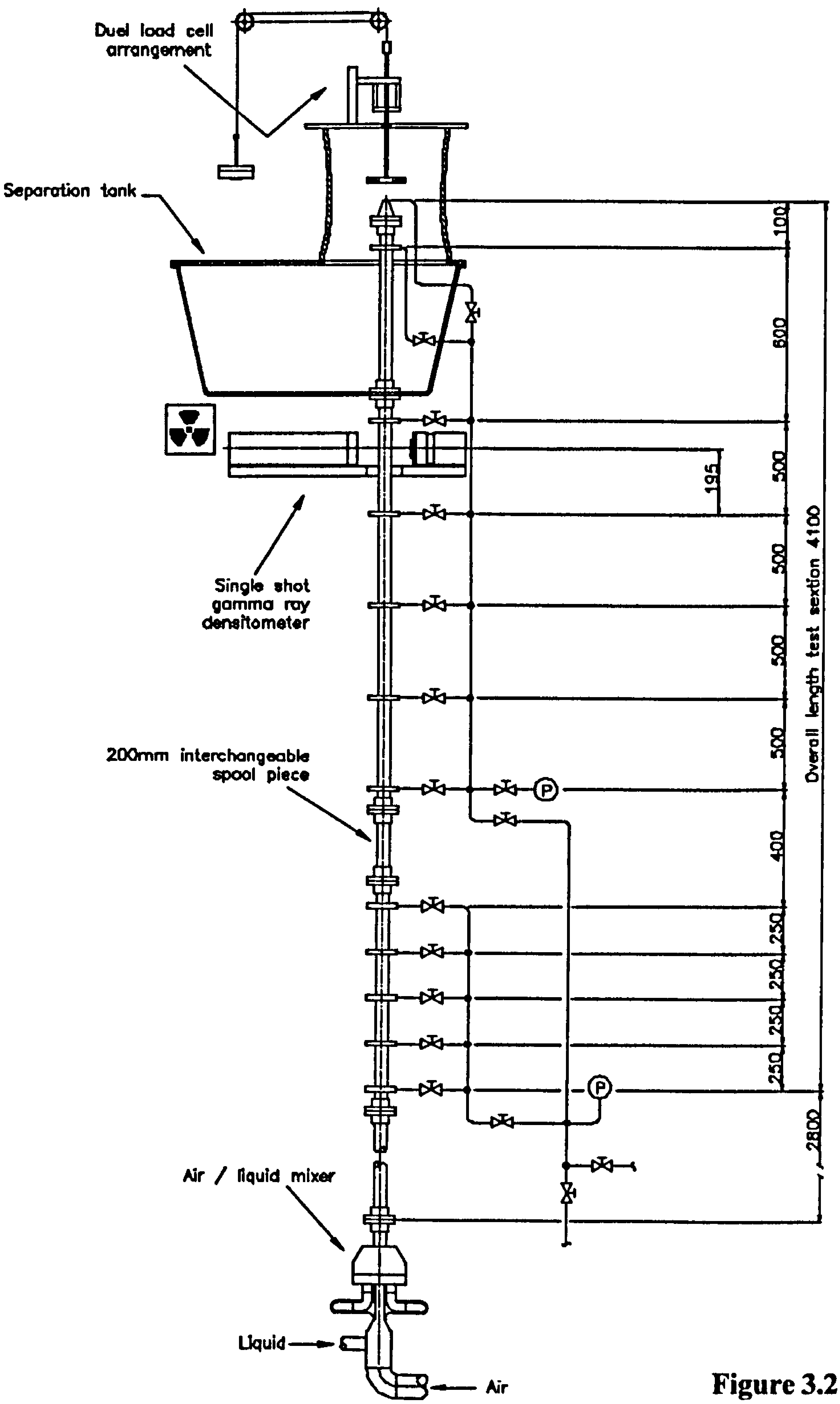

Figure 3.2: Test Section

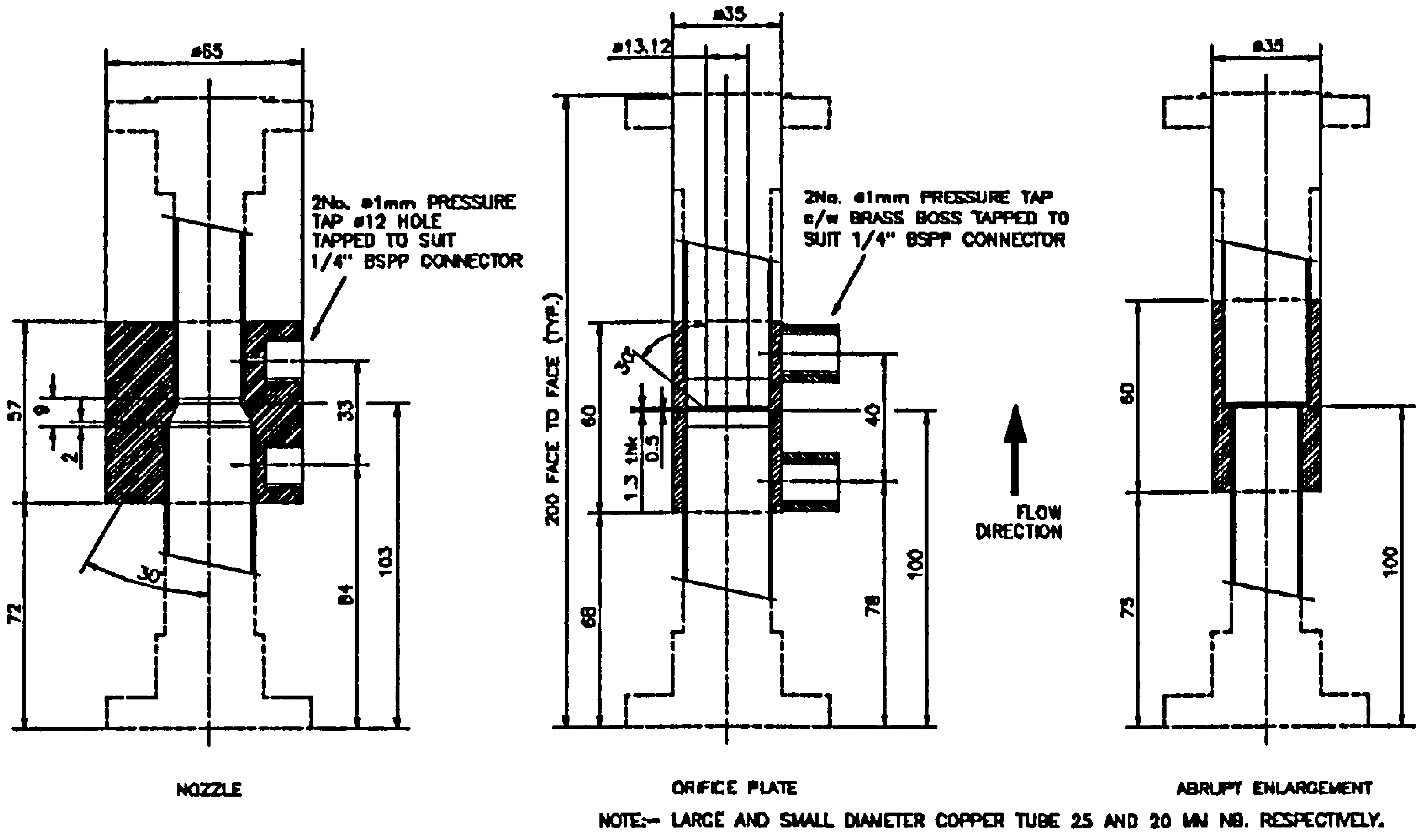

Figure 3.3: Spool Piece Test Components

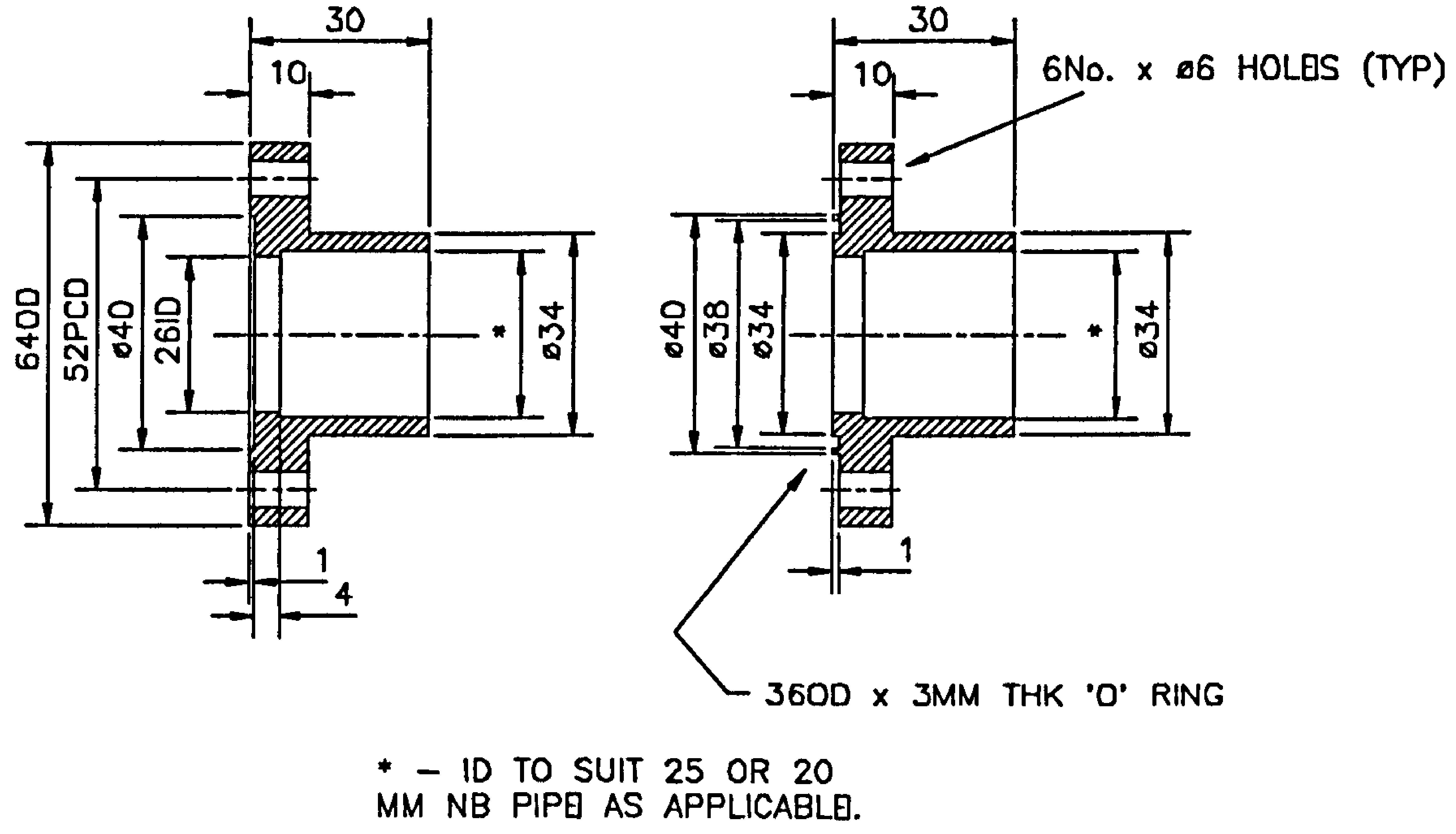

Figure 3.4: Custom Built Flange For Spool Piece Insertion

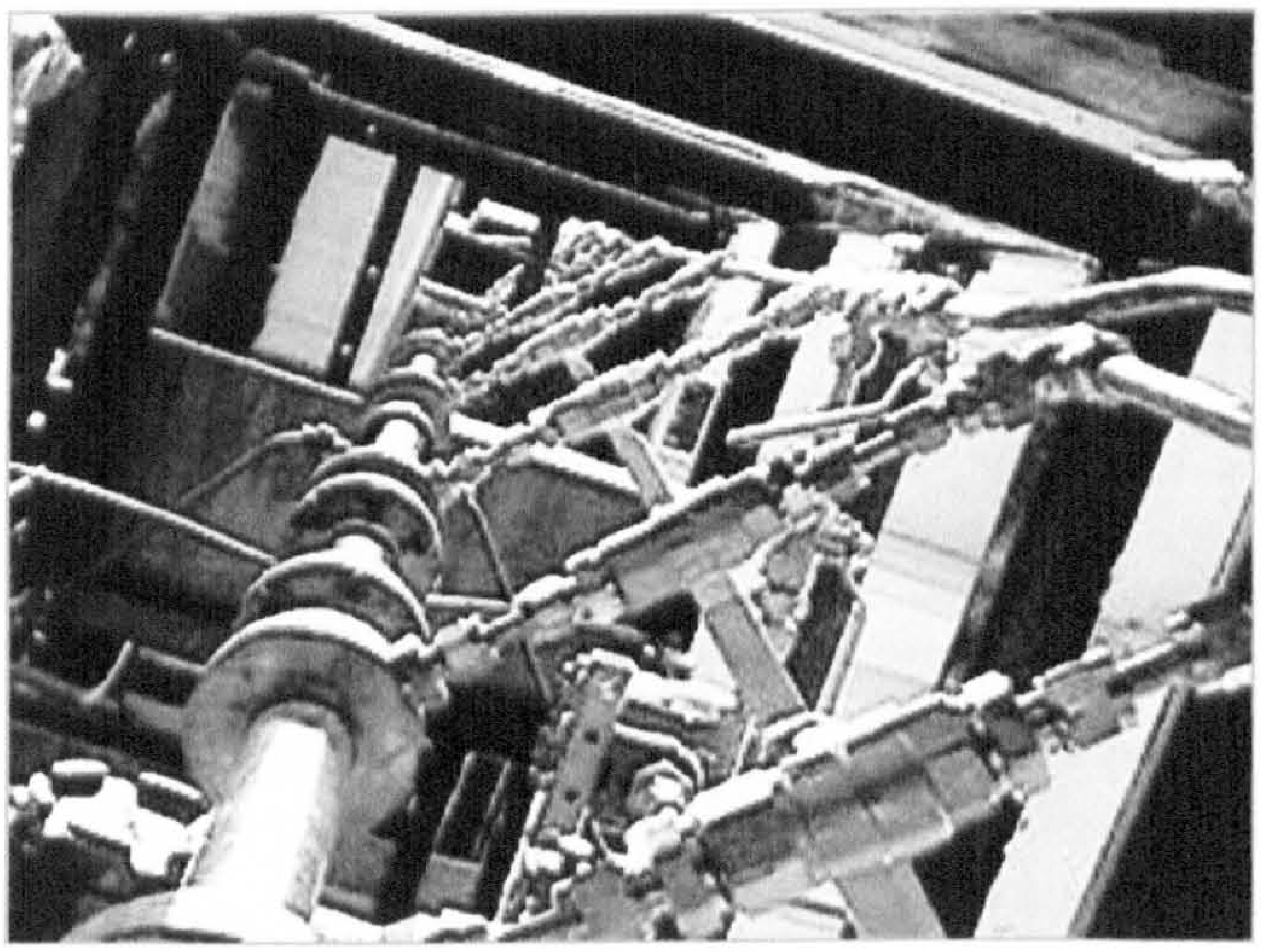

Plate 3.1: Test Section

The internal diameter of both the 25 and 20 mm nominal bore test sections was determined by filling them with water, which was then collected and weighed. By accurately measuring the length of the each test section the average internal diameter was calculated. For the 25 and the 20 mm nominal bore test sections these were 26.12 mm and 20.18 mm respectively.

A common 5 mm ID stainless steel pipe linked all the pressure taps on the test section to a single Rosemount 2088 SMART pressure transducer. A series of 6 mm ball valves allowed each pressure tap to be isolated or connected with the pressure transducer. This common line was also connected to the air and liquid supplies allowing the local pressure taps to be flushed with the gas or liquid phase. Plate 3.1 shows the pressure line branching from the pressures taps as it ascends the test section.

3.4.2 Viewing Glass & Discharge Components.

At the exit of the test length, a viewing glass was fitted to allow the visualisation of the discharging single and two-phase flows. For reasons of access, the viewing glass was mounted on a hinged 25 mm square section tube frame allowing it to tilt clear of the end of the test section. A series of discharge components, a pipe, nozzle and orifice plate, were manufactured from Brass bar as per Figure 3.5. The dimensions of the discharge and the inline orifice plates are based on BS-1042. The dimensions of the discharge nozzle were selected to allow comparison with the discharge orifice plate but the inline nozzle dimensions were selected to match the nominal dimensions of up and down stream pipe diameters. The end of the test section was completed with a custom built flange allowing the relatively quick installation of any of the discharge components.

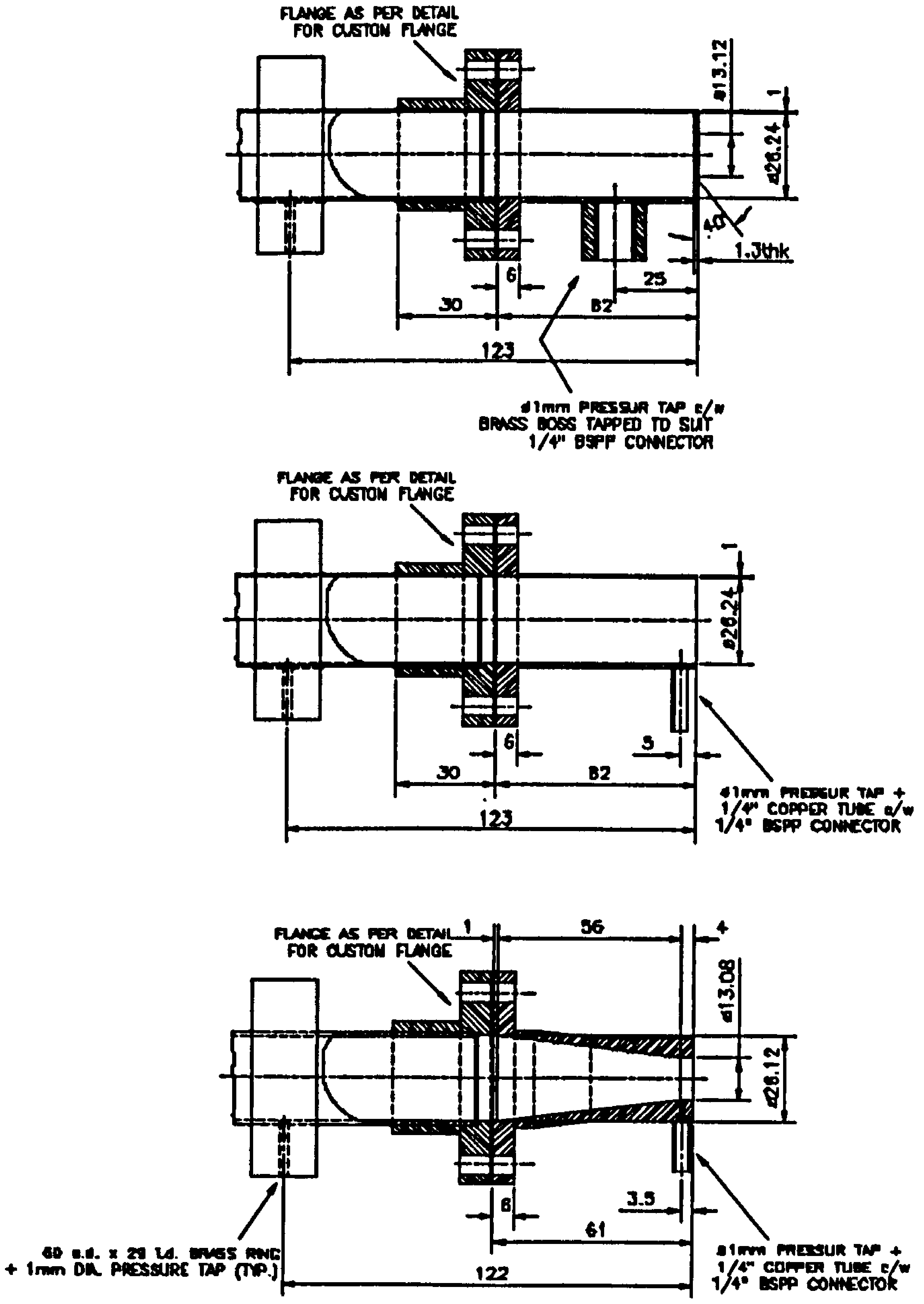

Figure 3.5: Discharge Test Components

3.4.3 Momentum Measurement

The momentum flux of single and two-phase flows was measured by locating an impingement plate, or target, above the discharge point of the test section. As the two-phase flow discharged from the test section it was turned through 90° by the target. The target was retained in place by a load cell allowing the force due to the rate of change of momentum to be directly measured. The behaviour and range of forces encountered across the single and two-phase experiments made it necessary to devise two separate load cell arrangements. A description of the momentum load cells calibration, experimental operation and construction is given in Section 4.5.7 and Figures 4.14 & 4.15.

3.4.4 Air-Liquid Separation & Disengagement

For the continuous operation of the test facility it was desirable that after discharging from the test section, the two phases be separated, allowing the liquid phase to be returned to the supply tanks for re-circulation. To assist in the separation of air-water and air-glycerine, a separation tank was installed below the viewing glass to collect the discharging mixture. The layout of the separation tank, sketched in Figure 3.6, included a number of baffles providing a large surface area to collect droplets of liquid from the air. A series of holes in the baffles and three 200 mm diameter exhausts reduced the velocity with which the air flowed through the separation tank, so as to provide more opportunity for droplets to fall out of suspension. A small level tank was used to control the liquid level of the separation tank. Adjustments made to the liquid level of the separation tank resulted in the flow path of the exiting air being effectively restricted to a route passing through all the baffles.

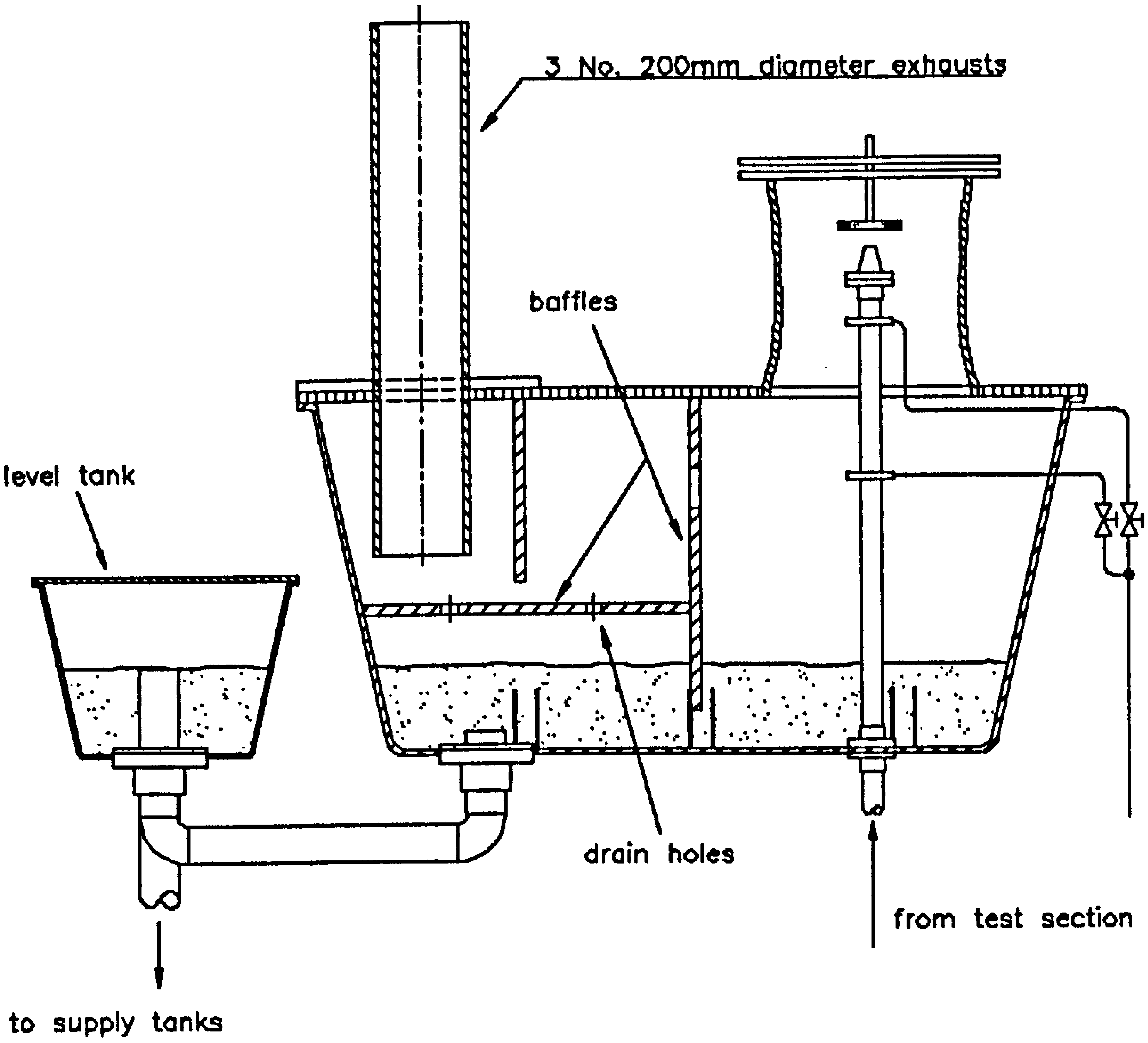

Figure 3.6: Separation Tank

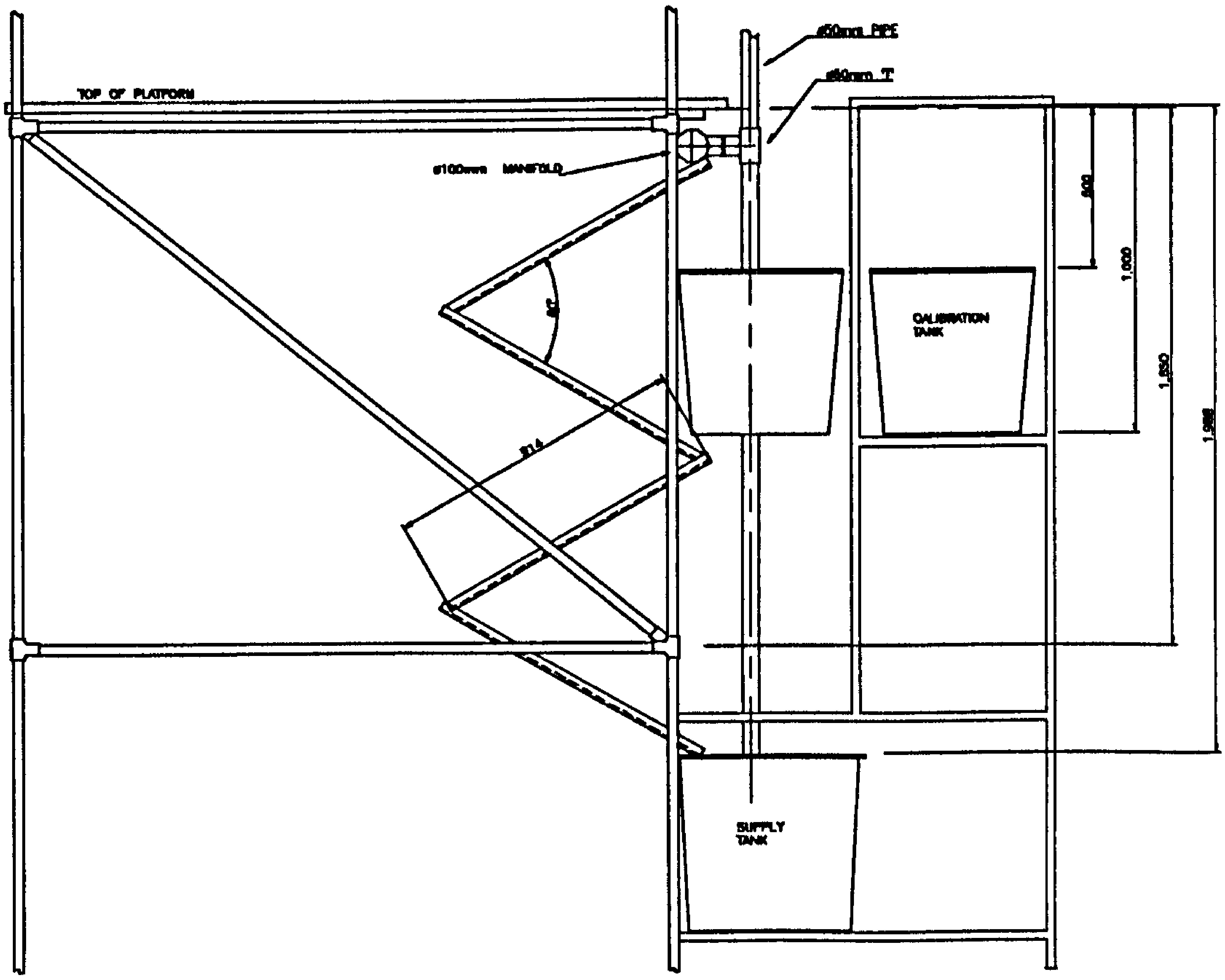

Figure 3.7: Slide Arrangement

The separation tank provided a means where by liquid droplets could be removed from the gas phase. A more difficult problem was the removal of air bubbles entrained in the bulk liquid flow of air-glycerine. It was evident from early test work that the rate of disengagement of these bubbles would be too slow for a continuous re-circulation of the test liquid with out a period of down time allowing entrained air to disengage. Initially down times as long as twelve hours were required but two modifications were made to significantly reduce this.

The first modification was the installation of a slide to smooth the delivery of test liquid from the separation tank to the storage tanks. The slide assisted in combating further air entrainment from the atmosphere, as the test liquid flowed from the separation tank to the supply tanks. The slide, shown in Figure 3.7, was constructed from four separate leaf's and formed a zigzag pattern as it made its way from high to low level between the separation tank and the supply tanks. The width and gradient of the slide was determined to assist in the thinning out the discharged mixture, enabling further air disengagement on route to the supply tanks. A manifold was devised to disperse the two-phase mixture evenly across the entire width of the slide. The manifold, constructed from a 50 mm diameter PVC tube, was placed horizontally along the top of slides top leaf. A series of elongated holes spanning the manifolds entire length, the width of which could be varied, provided a degree of control over the mixtures descent down the slide. The leaves of the slide were enclosed in Perspex to protect the mixture from being contaminated by foreign objects, such as insects and work shop dust. The transparent Perspex had the advantage of allowing visual inspection of the mixture as it flowed down the slide.

The second modification was the installation of two 3 kW immersion heaters, one in each supply tank. The viscosity of glycerine is strongly dependent on temperature. By increasing the temperature of the liquid in the supply tanks, the liquid viscosity was reduced allowing an increase in the rate of air disengagement. The immersion heaters incorporated thermostats allowing the control of the test liquids mean bulk temperature to ± 2 °C.

3.4.5 Test Liquid Storage

The test facility was operated using two test liquids, water and an aqueous glycerine solution. So that the aqueous glycerine solution could be taken in and out of service, two 40 gallon storage tanks were housed in the basement. A tee-piece and two gate valves on the pump inlet allowed the contents of these storage tanks to be sent from the basement tanks to the supply tanks. When the water test liquid was not in service it could be drained from the supply tanks to the storage tanks by gravity. To allow water to be dumped from the liquid side of the test facility, a drain valve was fitted to the lowest point of the re-circulation loop i.e., in the basement on the flow side of the pump.

3.4.6 Heat Exchanger

It was desirable to incorporate a heat exchanger in the return line between the supply tanks and the pump for two reasons. Firstly the temperature of the test liquid would rise during tests due to frictional effects in the test section. These temperature fluctuations, of about 23 or 4 degrees, were enough to significantly alter the viscosity of the glycerine test liquid. By controlling the supply of cooling water flowing through the tube side of the heat exchanger, the temperature of the test liquid entering the test section was carefully regulated.

Secondly, the heat exchanger was employed to return the glycerol test liquid back to its working temperature after the immersion heaters had been used to elevate temperatures for the speedy removal of entrained air.

3.4.7 Liquid Flow Nozzles

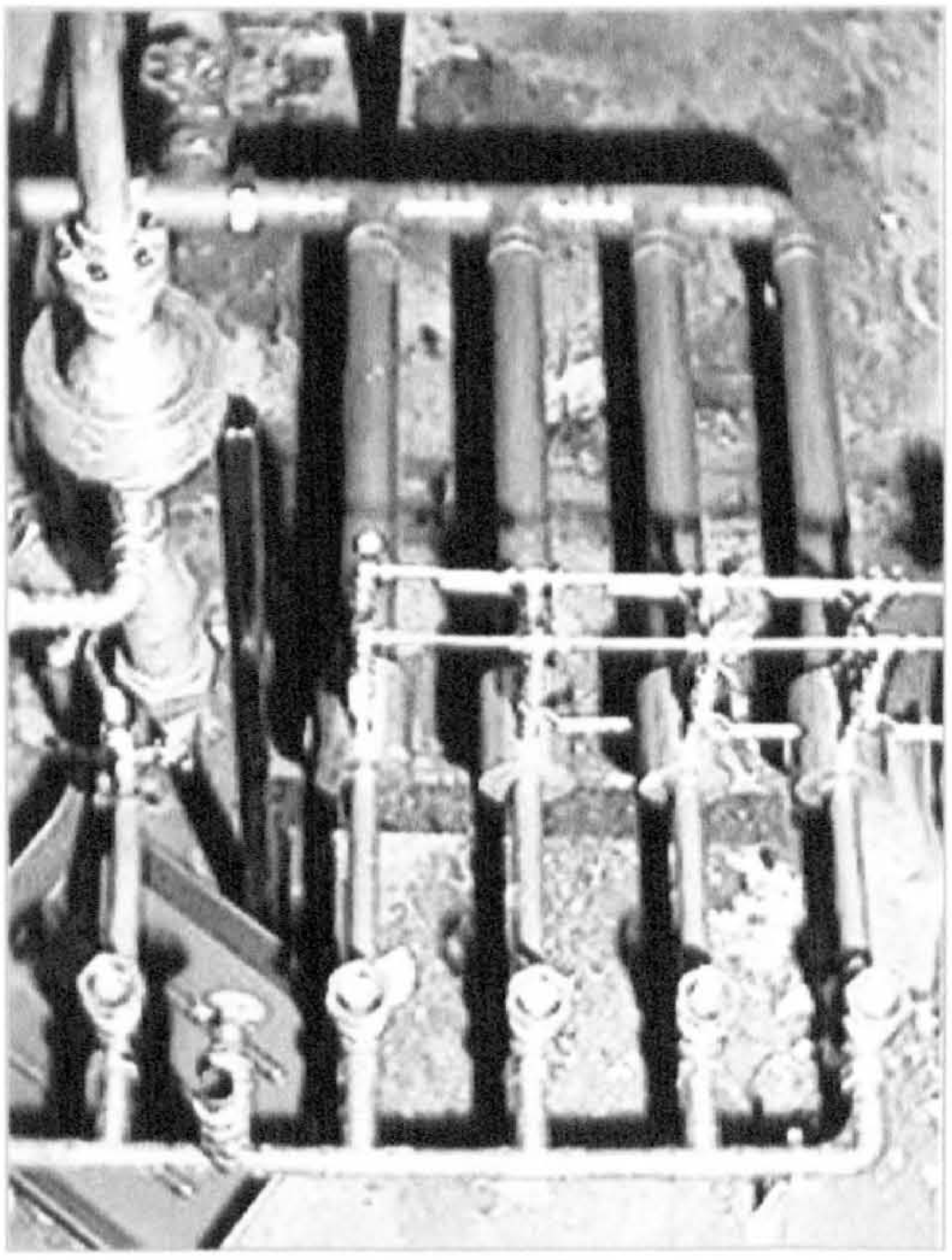

Plate 3.2: Flow Nozzles

Figure 3.8 and Plate 3.2 show the custom made flow nozzles used to measure the mass flow rate of the test liquid. These four flow nozzles located upstream of the air-liquid mixer and settling length, were arranged in parallel and connected to the pump discharge by a 50 mm nominal bore manifold. In series with each flow nozzle was a globe valve allowing their individual selection or isolation. Flow nozzle one had the largest downstream diameter of 26.02 mm and the downstream diameters of each subsequent flow nozzle reduced by a ratio of 2:1. Pressure taps, 2 mm in diameter were provided immediately up and downstream of

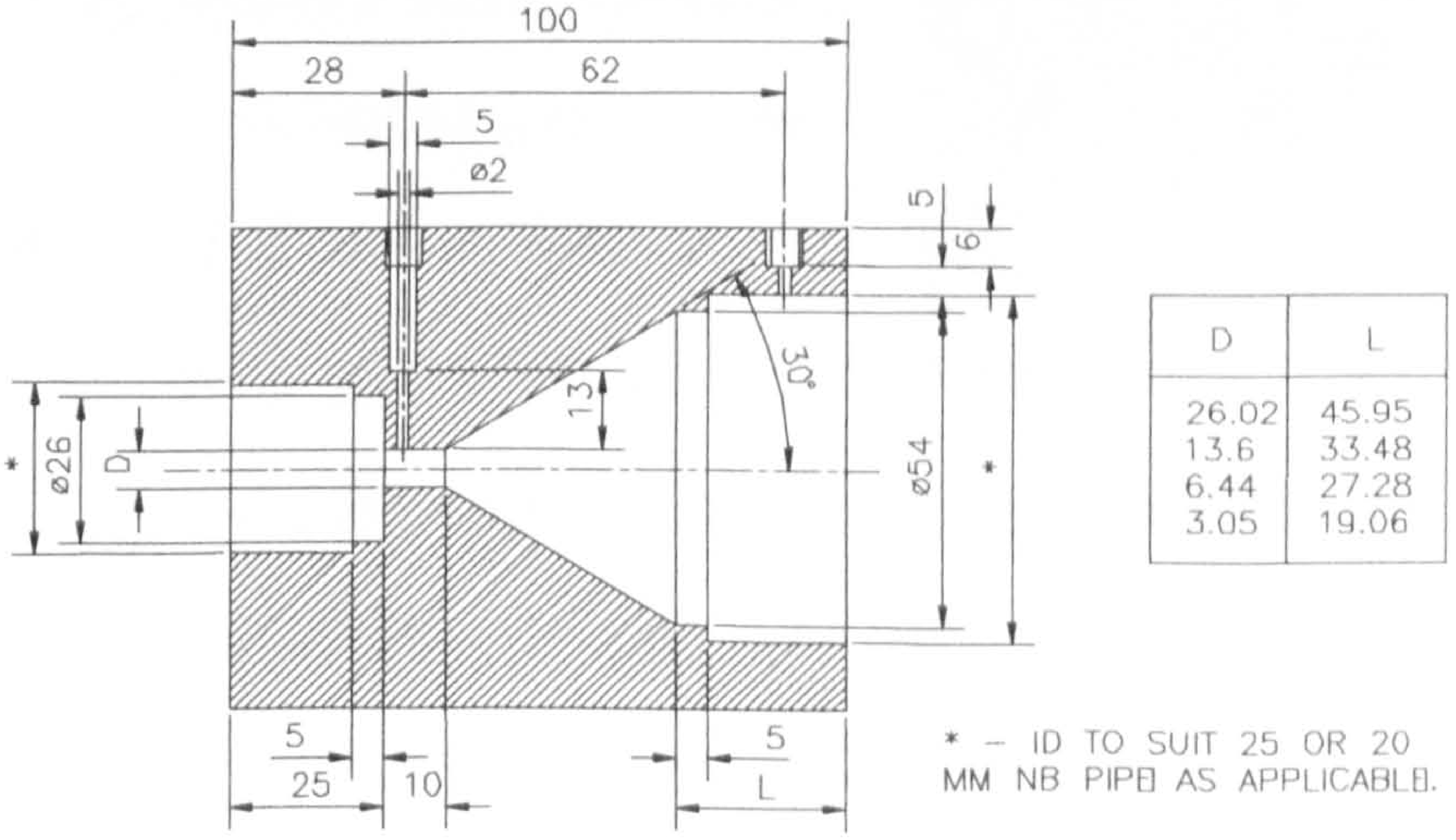

D	L
26.02	45.95
13.6	33.48
6.44	27.28
3.05	19.06

Figure 3.8: Flow Nozzles

each flow nozzle. Two common 3 mm diameter stainless steel pressure lines linked the pressure taps to a single Rosemount 3051 SMART pressure transducer. A 6 mm ball valve positioned at the juncture of each pressure tap allowed the pressure across any one of the flow nozzles to be measured in isolation by the pressure transducer.

3.4.8 Air–liquid Mixer & Non-return Valve

To combine the liquid and air phases an air-liquid mixer, shown in Plate 3.3, was custom made for this application. A detailed drawing is given in Figure 3.9. Air was supplied from the air receiver to the mixer via a 50 mm diameter pipe. Positioned on the centre line of the air-liquid mixer the air supply reduced to 20 mm in diameter before entering a mixing chamber. The liquid phase was supplied to the mixing chamber by two 20 mm diameter pipes. The conical shape of a receiving chamber through which the liquid phase first passed ensured that the liquid phase was evenly dispersed over the full circumference of the mixing chamber. A step change in diameter between a 20 mm diameter stub protruding into the mixing chamber delivering the air phase, and a 26 mm exit pipe provided an annulus through which the liquid phase mixed with the gas phase. The air-liquid mixer was constructed from Brass bar through out. Plate 3.3 shows the air-liquid mixer in situ with the 50 mm air supply and the two 20 mm diameter liquid inlets entering the mixing chamber from beneath.

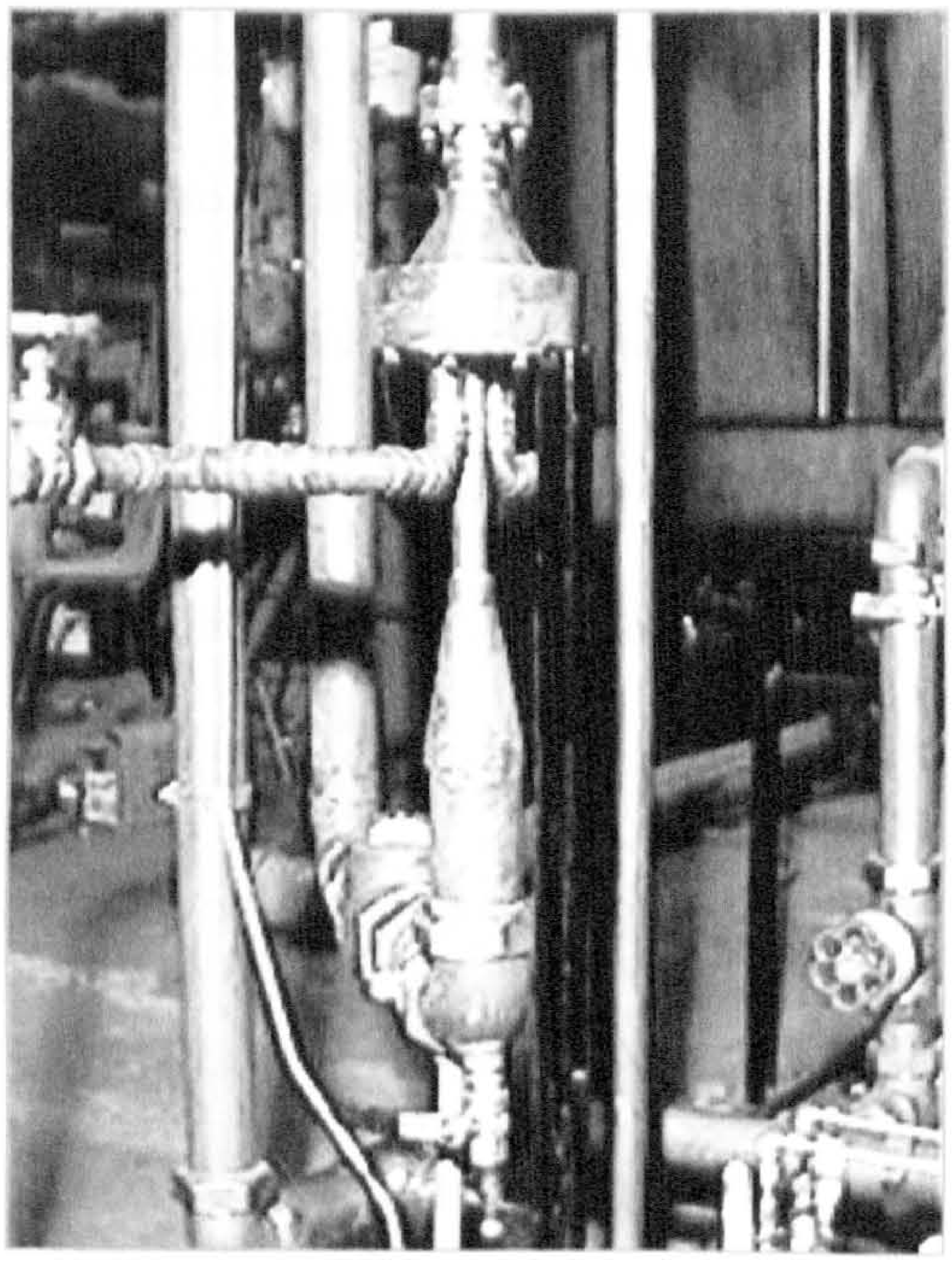
Plate 3.3: Air-Liquid Mixer

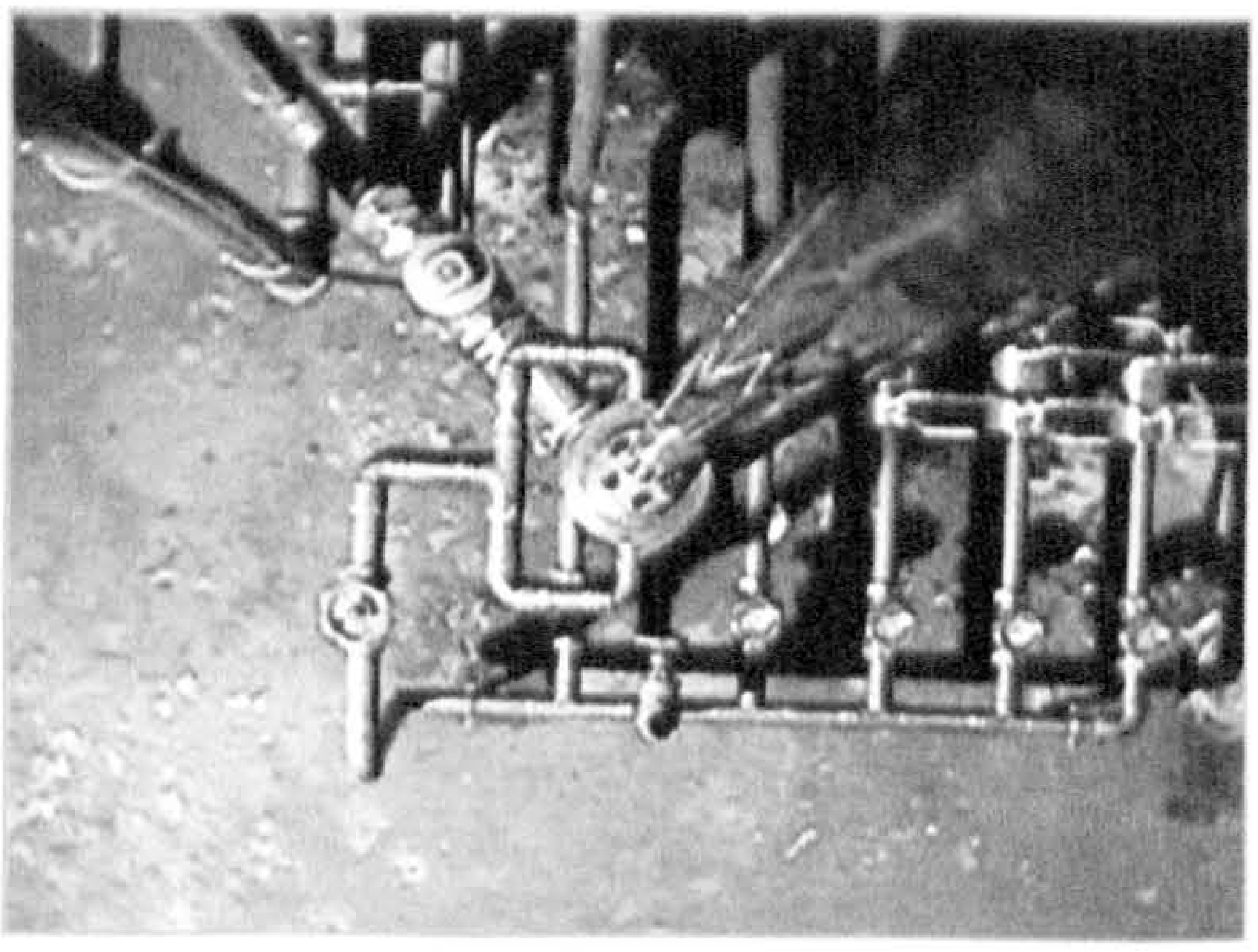
Plate 3.4: Non-return Valve

To restrict the liquid phase from entering the air supply line, a non-return valve was installed upstream of the air-liquid mixer. Plate 3.4 shows the air-liquid mixer viewed from above. The non-return valve lies top left.

3.4.9 Air Extraction & Venting

An unanticipated by-product of mixing air and glycerine to produce test mixtures was the production of a glycerine laden mists. The process generated fine droplets of glycerine suspended in the air-phase which were carried by the air stream through the separation tank and discharged to the atmosphere. Although this glycerine mist was not at high temperature, its opaque nature did interfere with fire sensors situated near to the test facility. It was necessary to install a vent pipe that could carry the discharging air to an appropriate exit point outside of the laboratory building. The vent pipe was some 12 m long so an extraction fan and rectangular hood were situated at the separation tank to assist in moving the exiting air to the discharge point. The three 200 mm diameter exhaust vents and extraction hood are shown in the foreground of Plate 3.5. The right hand side of the extraction hood contained an aperture the size of which could be adjusted enabling the extraction pressure to be balanced with the test discharge pressure.

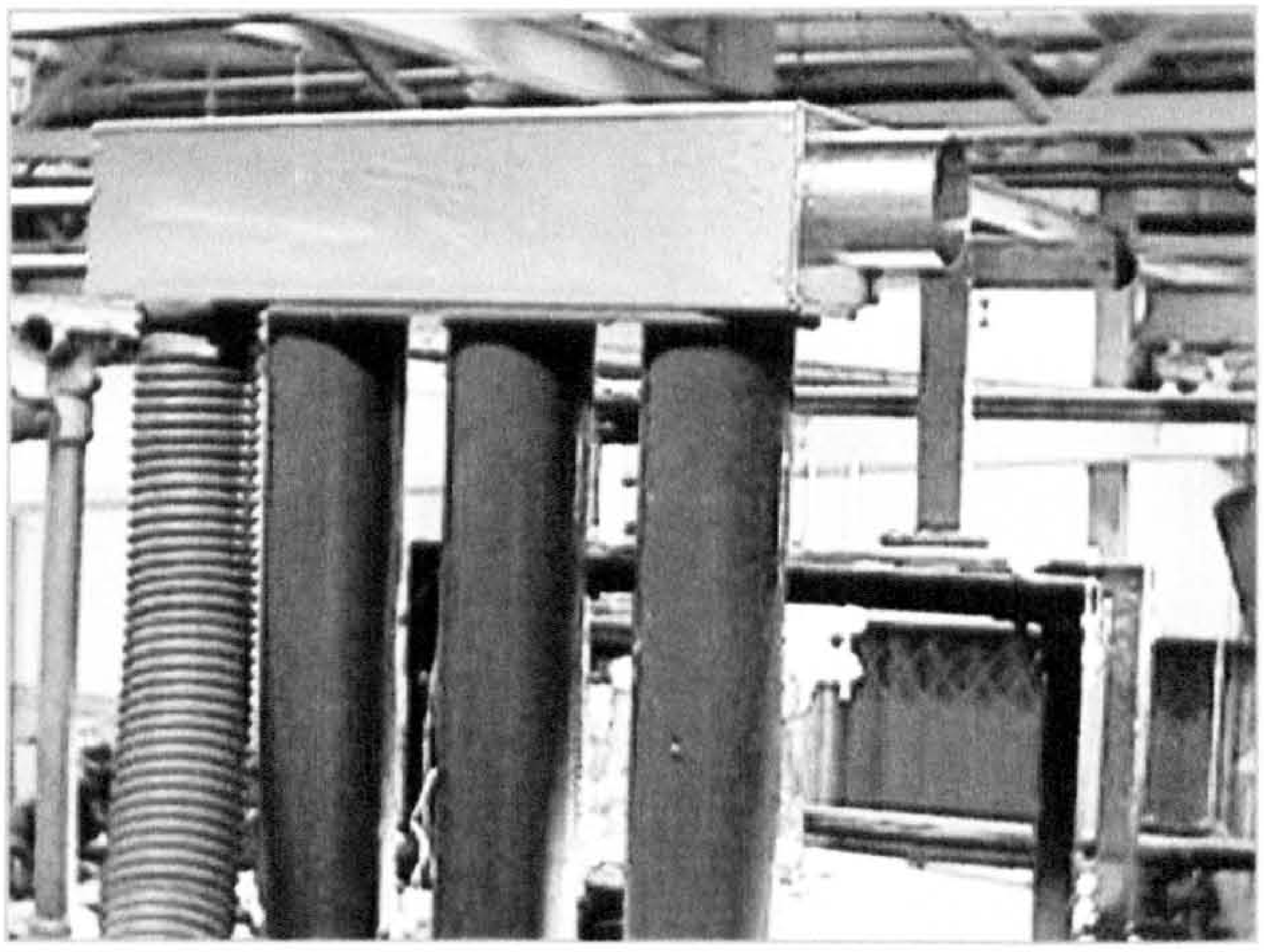

Plate 3.5: Extraction Manifold

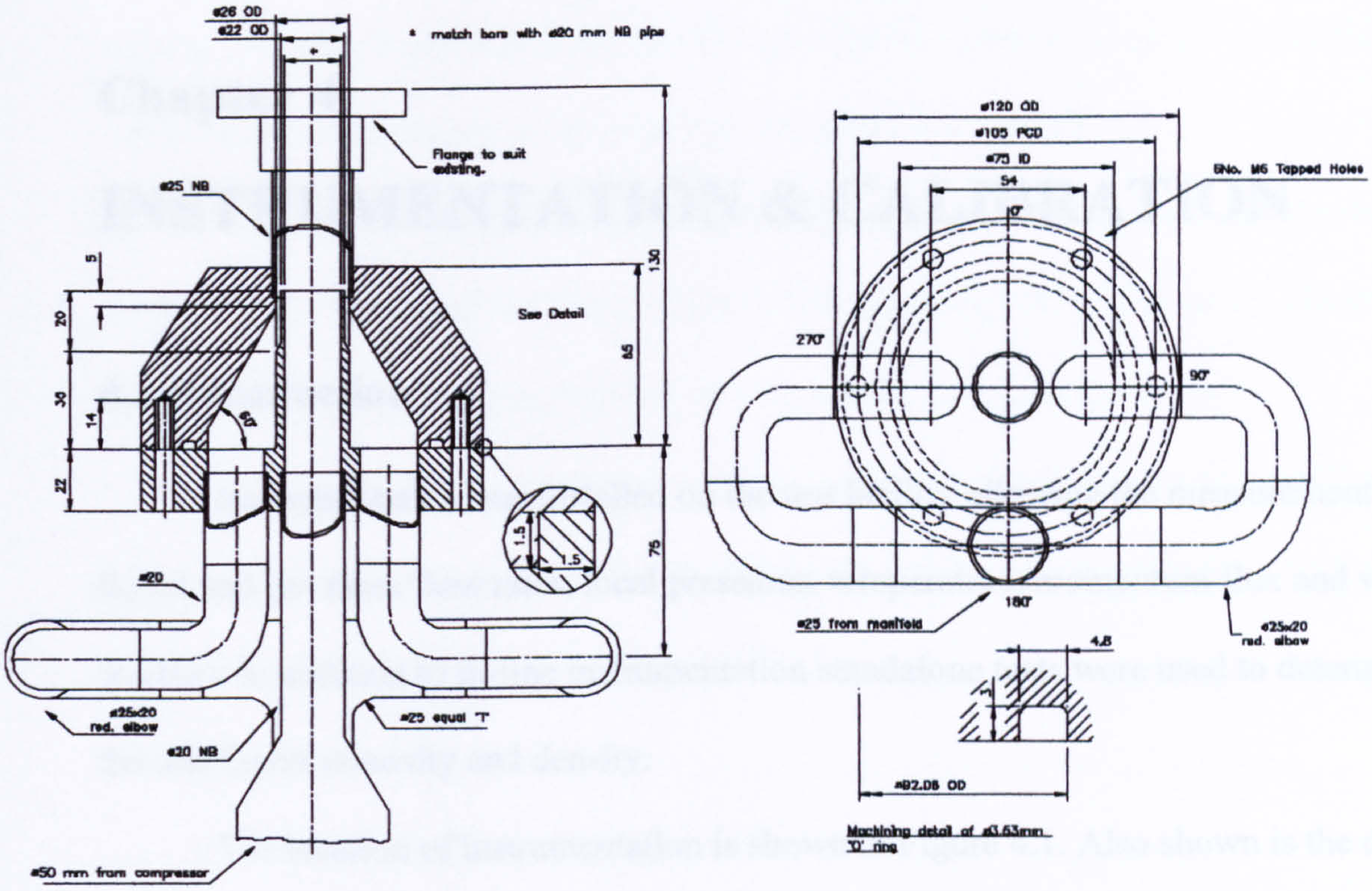

Figure 3.9: Air-Liquid Mixer

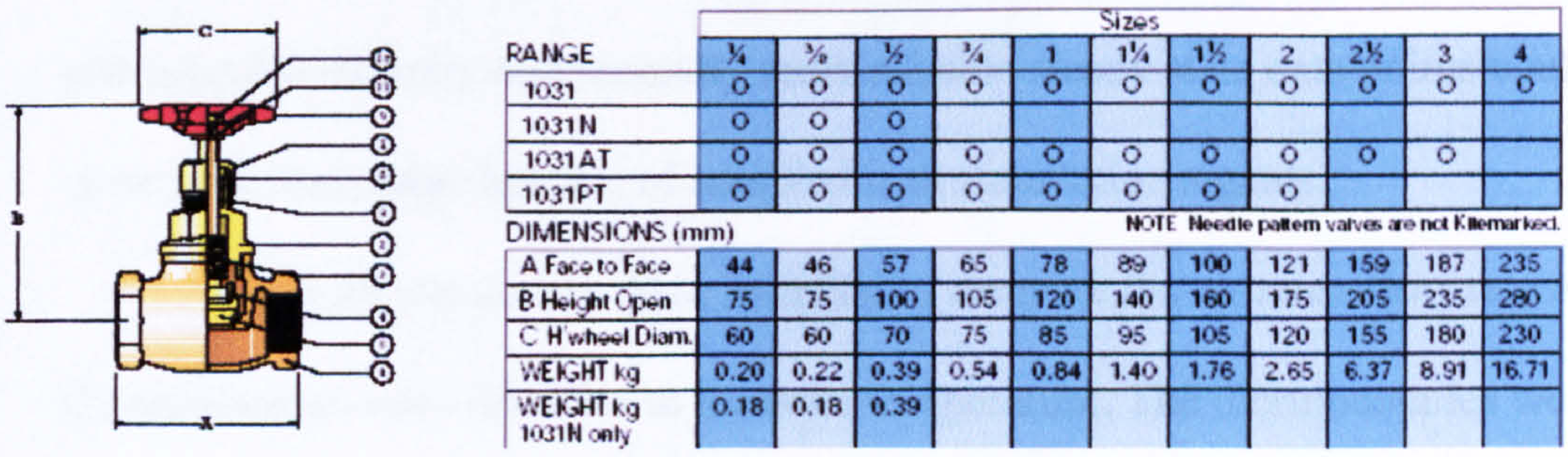

RANGE	Sizes										
	¼	⅜	½	¾	1	1¼	1½	2	2½	3	4
1031	O	O	O	O	O	O	O	O	O	O	O
1031N	O	O	O								
1031AT	O	O	O	O	O	O	O	O	O	O	
1031PT	O	O	O	O	O	O	O	O			

DIMENSIONS (mm)

NOTE Needle pattern valves are not Kitemarked.

A Face to Face	44	46	57	65	78	89	100	121	159	187	235
B Height Open	75	75	100	105	120	140	160	175	205	235	280
C H'wheel Diam.	60	60	70	75	85	95	105	120	155	180	230
WEIGHT kg	0.20	0.22	0.39	0.54	0.84	1.40	1.76	2.65	6.37	8.91	16.71
WEIGHT kg 1031N only	0.18	0.18	0.39								

Figure 3.10: Test Globe Valve

Chapter 4

INSTRUMENTATION & CALIBRATION

4.1 Introduction

Instrumentation was installed on the test facility allowing the measurement of liquid and gas mass flow rates, local pressures, temperature, momentum flux and void fraction. In addition to in-line instrumentation standalone tests were used to determine the test liquid viscosity and density.

The location of instrumentation is shown in Figure 4.1. Also shown is the data acquisition system that was used to electronically log the readings for liquid mass flow rate, local pressure and momentum flux. A substantial investment of time was made in the development of a data acquisition system and associated software. This was considered necessary primarily for two reasons. Firstly it ensured a high level of procedural continuity and secondly more reliable steady state data points could be generated from large batches of sampled instrumentation signals.

Three air rotameters were installed to measure the air mass flow rate and four thermocouples were installed to measure temperature. The thermocouples were located on the test section, calibration loop, by-pass loop and air supply. The delivery side of the positive displacement pump and the stagnation air supply pressures were monitored by Bourdon gauges. The air rotameters, thermocouples and Bourdon gauges were all read manually.

The liquid mass flow rate was obtained using four flow nozzles each sized for a different working range. Local pressures were recorded at twelve locations on the test section. Pressure transducers were used to measure the pressure drop across the liquid mass flow nozzles and the local pressure taps on the test section.

Two separate load cell transducer arrangements were employed, one for single-phase and one for two-phase tests. Housed at the discharge of the test length the load cell transducer arrangements enabled the momentum flux to be measured.

The void fraction was measured using a dedicated counter housed in a PC and a gamma-ray densitometer. The software that controlled the counter allowed count rates to be automatically logged and stored on the PC.

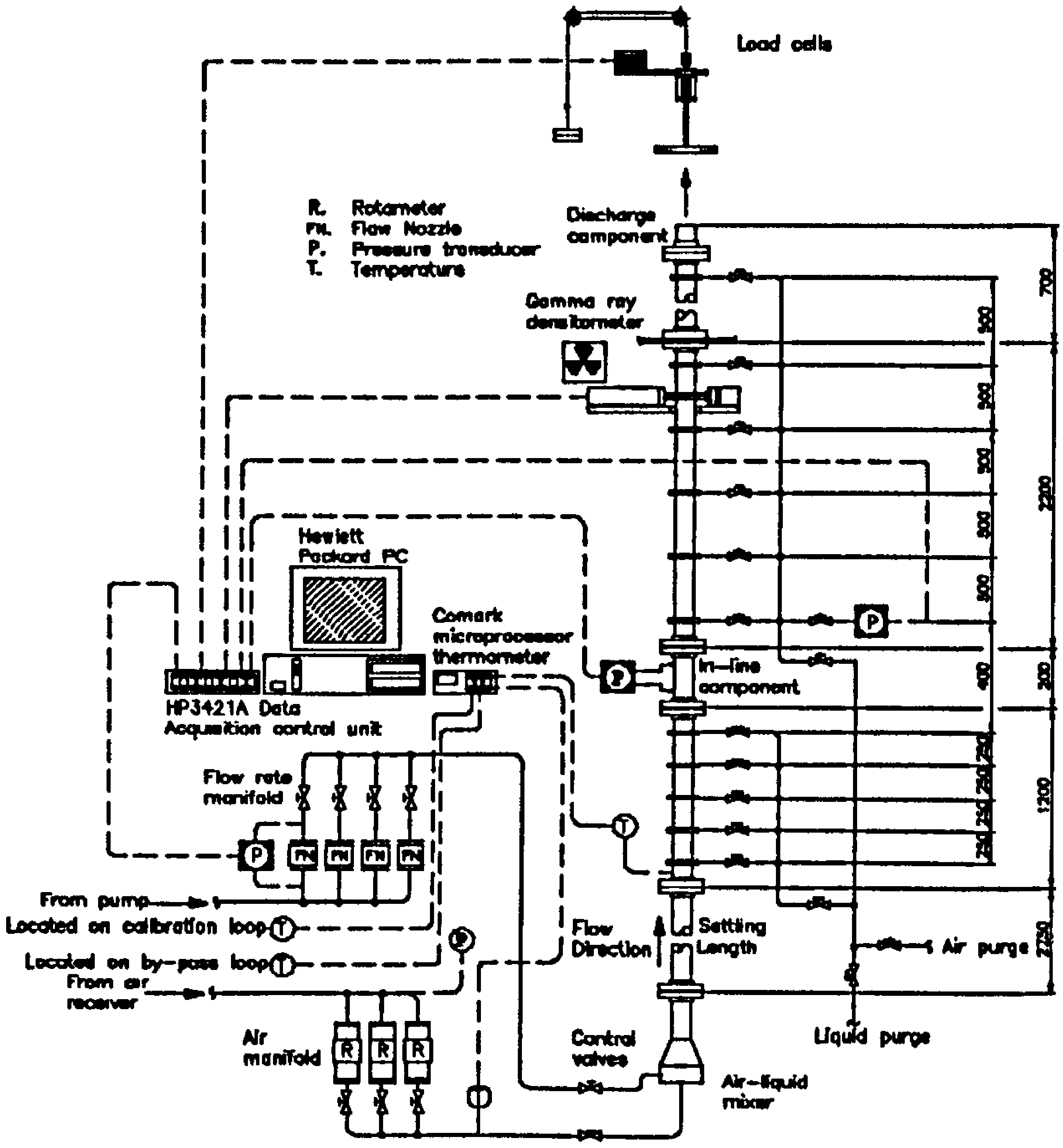

Figure 4.1: Data Acquisition and Instrumentation

4.2 Manual Readings

4.2.1 Viscosity Control & Measurement

An important aspect of this research was the influence of viscosity on the behaviour of two-phase flows. To enable control and accurate measurement of viscosity a high specification rheometer was used. The test liquids' viscosity was necessary for determining the flow nozzle calibration curves, analysing of the single-phase test data, predicting the liquid mass fluxes present in two-phase tests and the analysis of highly viscous two-phase test data. The hygroscopic nature of glycerine meant that, over a period of days, moisture drawn from the flowing air significantly altered the viscosity.

The nominal test viscosities of 550, 200 and 50 mPas were achieved by the addition of water to the glycerine test liquid. The quantity of water was determined experimentally by adding the water in two litre increments. After each addition of water the test liquid was circulated and then the viscosity was measured. This process was repeated until the desired test liquid viscosity had been reached. The properties of glycerine are given in Table C.6, Appendix C.

A Carri-Med CSL controlled stress rheometer was used to obtain the shear stress of the glycerine test liquid as a function of strain rate at specific temperatures. The Carri-Med was a stand-alone system that processed individual 30 ml samples. A syringe was used to place test liquid samples on the Carri-Med test plate. The temperature of the test plate, and thereby the sample temperature, were finely controlled by software mounted on an IBM PC. Shear stress values were obtained by driving a cone against the sample. The cone rotated on an air bearing mounted spindle. The air bearing ensured that the resistance to the rotational movement of the spindle was due to the actions of the sample against the cone. The software allowed the generation of files in ASCII format so that the shear stress temperature relationships generated by the Carri-Med could be transferred to another system for analysis.

4.2.2 Procedure for Viscosity Measurement

Shear stress responses to strain rate data were generated from samples by the Carri-Med at two degree C intervals over the temperature range of 16 to 40 °C. A typical result is shown in Figure 4.2. A straight line relationship was found between shear stress and strain rate, indicating that the aqueous glycerine test solutions were Newtonian i.e., viscosity was independent of strain rate. A temperature viscosity curve was then found by plotting the gradients of the shear stress strain rate measurements against temperature. A typical result is shown in Figure 4.3. A third order polynomial gave a good fit to the resulting curve.

The viscosity of the glycerine test liquid dropped as the moisture content of the glycerine increased. To maintain the viscosity of the test liquid at a high level during down time the immersion heaters were set to 50°C and the temperature of the test liquid elevated for extended periods of up to 48 hours. This approach inhibited further moisture ingress and assisted in the removal of the water content. A complete set of viscosity temperature curves for single and two phase tests is given in Appendix C1.1 & C2.1 respectively.

4.2.3 Density Measurement

The regular weighing of a 50 ml density flask allowed the continual monitoring of the density of the glycerine test liquid through out its use. The viscosity of the aqueous glycerine test liquids were nominally 550, 200 and 50 mPas corresponding to 1260, 1235 and 1190 kg/m^3 densities respectively.

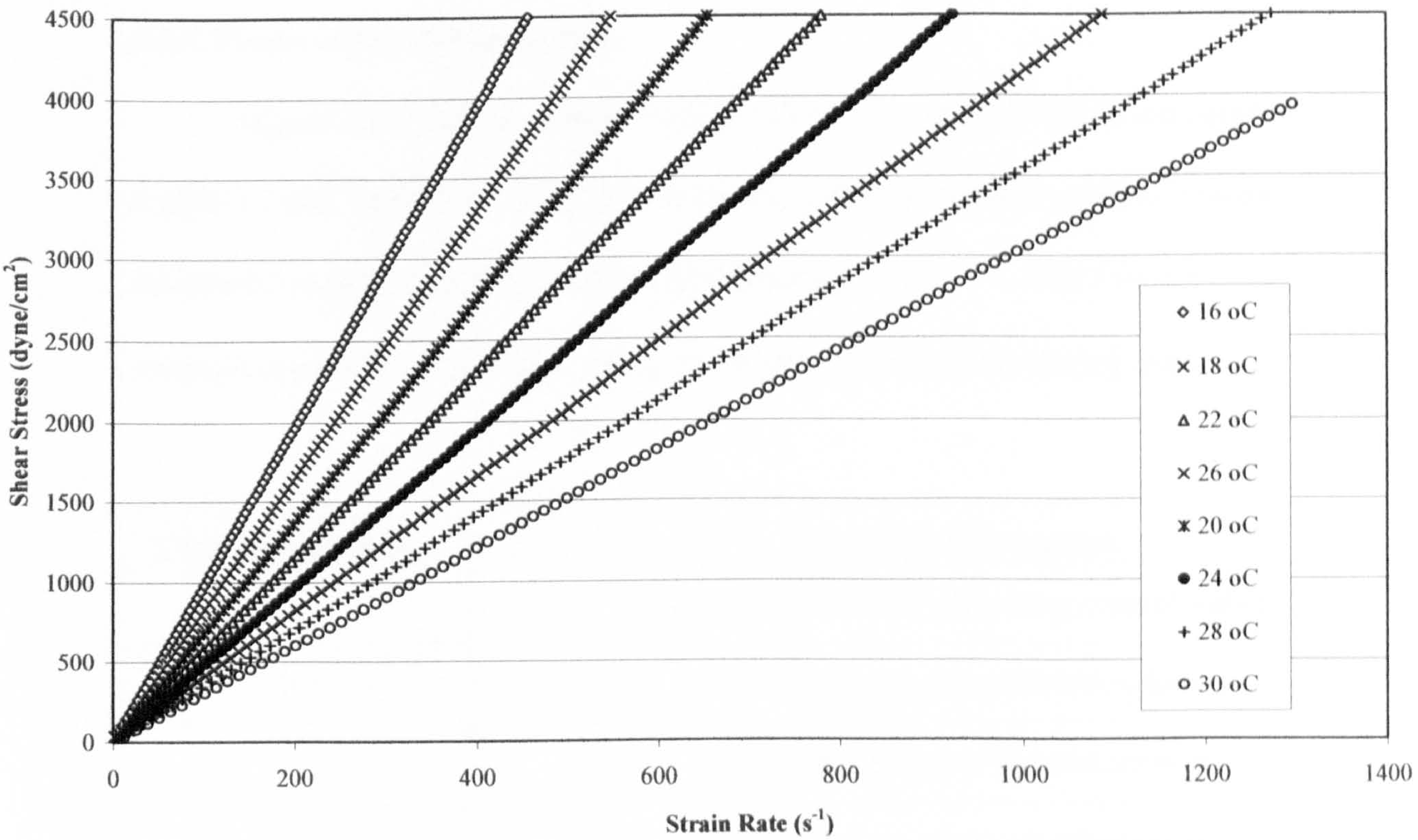

Figure 4.2: Shear Stress versus Strain Rate for Glycerine Test Liquid Sample

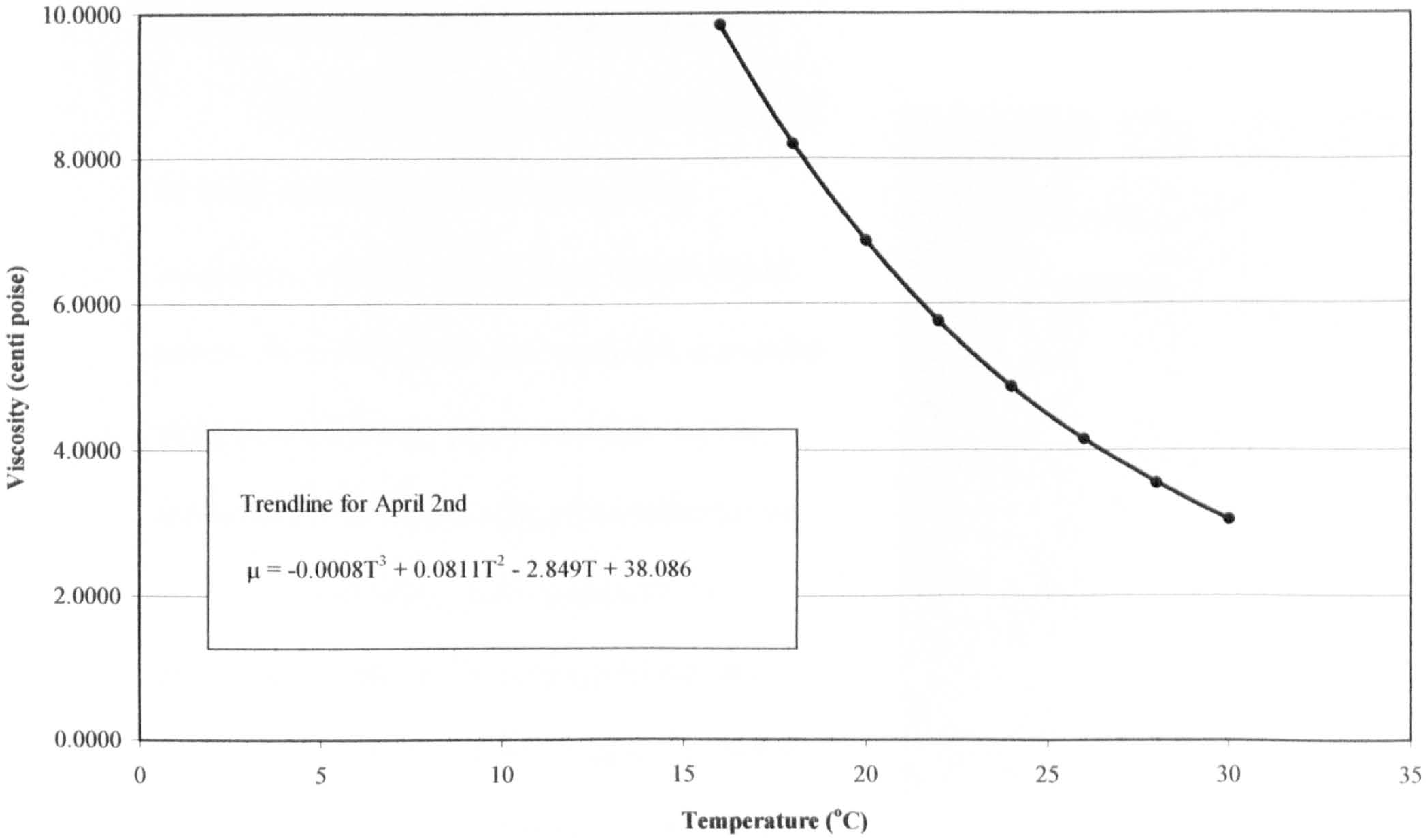

Figure 4.3: Viscosity versus Temperature of Glycerine Test Liquid Sample

4.2.4 Temperature Measurement

Four K-type thermocouples were located on the test facility as indicated in Figure 4.1 and Table 4.1. The Thermocouples were interrogated using a Comark microprocessor thermometer with a discrimination of ±0.1 °C. The Comark microprocessor thermometer readings were recorded manually during tests.

Thermocouple No.	Location Description
1	Upstream of the by-pass loop control valve
2	Midway along the calibration loop
3	At the beginning of the test section
4	Down stream of the air rotameters

Table 4.1: Thermocouple Assignment

4.2.5 Air Mass Flow Rate Measurement

The mass flow rate of air was measured by three Fisher-Rosemount Brooks air rotameters situated upstream of the air-liquid mixer. The rotameters were mounted in parallel using a manifold arrangement. Gate valves, upstream of each rotameter, controlled the air mass flow rate which was indicated as a percentage of full-scale by the position of a needle driven by a rotatable magnet located in the rear of the rotameter housing. The rotatable magnet responded to the movement of another magnet situated in the air stream and encapsulated in a float. The air rotameters were

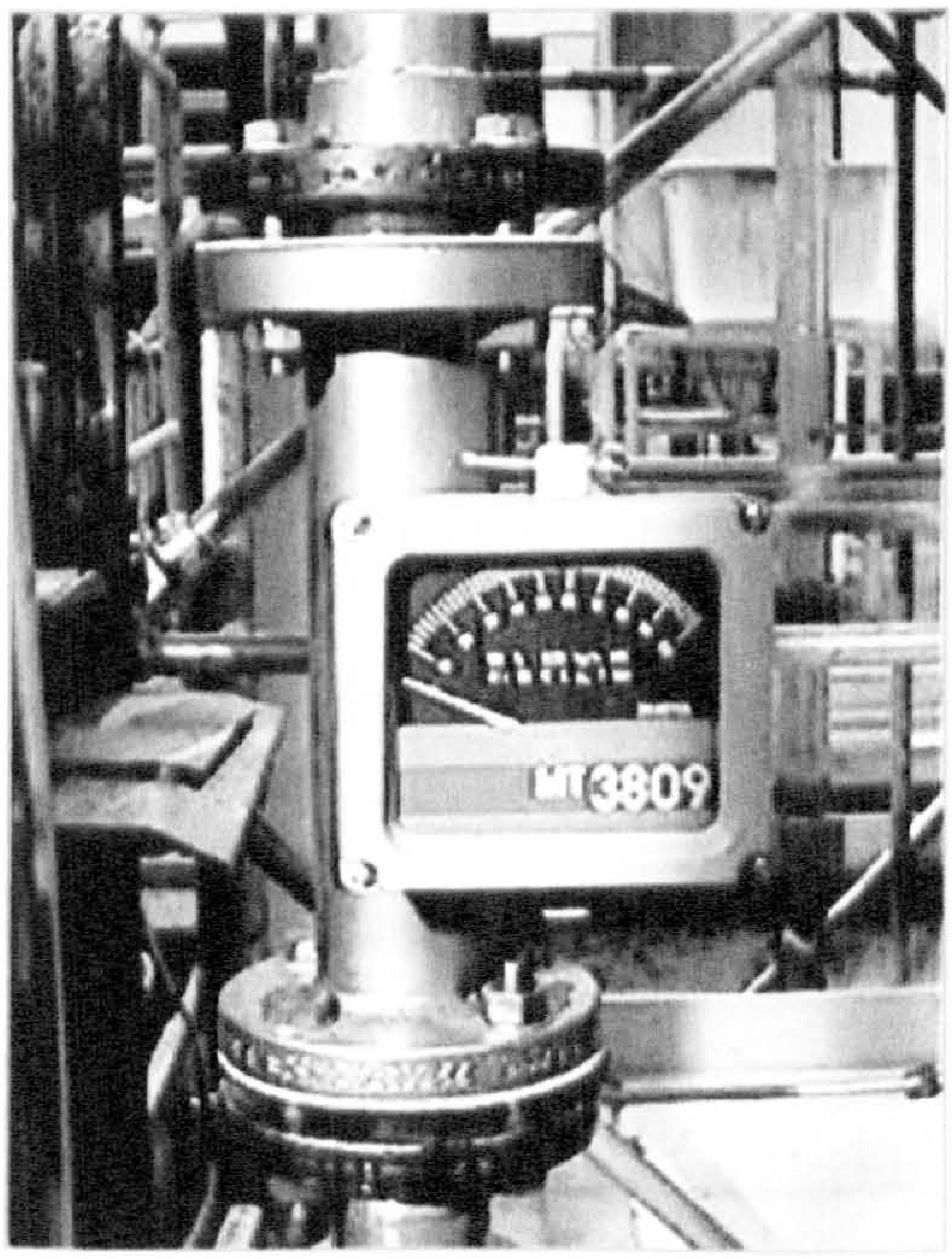

Plate 4.1: Air Rotameter three

accurate to ±1.6% of full scale and readings were recorded manually. Plate 4.1 shows rotameter three as installed.

The factory calibrations provided by the manufacturer were carried out at a temperature and pressure of 20 °C and 1.013 bar respectively. These were corrected as follows. If nominal volume flow rate for rotameter three was 3.8 m^3/h the actual flow rate, Q_{ACT}, for a test conducted at 7.5 bar G and at 20 °C would be:

$$Q_{ACT} = Q_n \sqrt{\frac{\rho_n}{\rho_t}} \tag{4.1}$$

where the nominal density, ρ_n, is:

$$\rho_n = \frac{p}{RT} = \frac{1.013x10^5}{287(0+273)} = 1.292\, kg/m^3 \tag{4.2}$$

The density for the test conditions is:

$$\rho_t = \frac{p}{RT} = \frac{8.033x10^5}{287(20+273)} = 9.524\, kg/m^3$$

The test volume flow rate from Equation 4.1 is:

$$Q_{ACT} = Q_n \sqrt{\frac{\rho_n}{\rho_t}} = 3.8\sqrt{\frac{1.292}{9.524}} = 1.4\, m^3/h$$

The test maximum, full scale, mass flow rate is then:

$$M = \rho Q_{ACT} = 13.33\, kg/h = 0.003703\, kg/s$$

The corrected full scale mass flow rates for all the air rotameters are given in Table 4.2.

Rotameter	**Serial No.**	**Manufactures Mass flow rate (kg/s)**	**Corrected mass Flow rate (kg/s)**
1	3809E11CACAA1A1	0.0039	0.003703
2	3809E12CACAA1A1	0.034	0.03295
3	3809E14CACAA1A1	0.035	0.326

Table 4.2: Manufactures and Corrected Full-scale Air Mass Flow Rates

4.3 Void fraction measurement

The void fraction was measured using a ^{241}Am (Americium) isotope as a gamma-ray source as it was readily available to the project. This collimated low-energy source projected a 10 mm diameter beam of good geometry from one end. To measure the attenuation of the gamma-ray beam as it passed through a cross section of the flow, a system was devised incorporating a photomultiplier tube (PMT) and an electronically controlled pulse counter. The final specification of the system included several components carefully matched for this application, details of which are listed in Table 4.3. An electrical configuration for the coupling of the PMT assembly output to the amplifier discriminator is given in Figure 4.4.

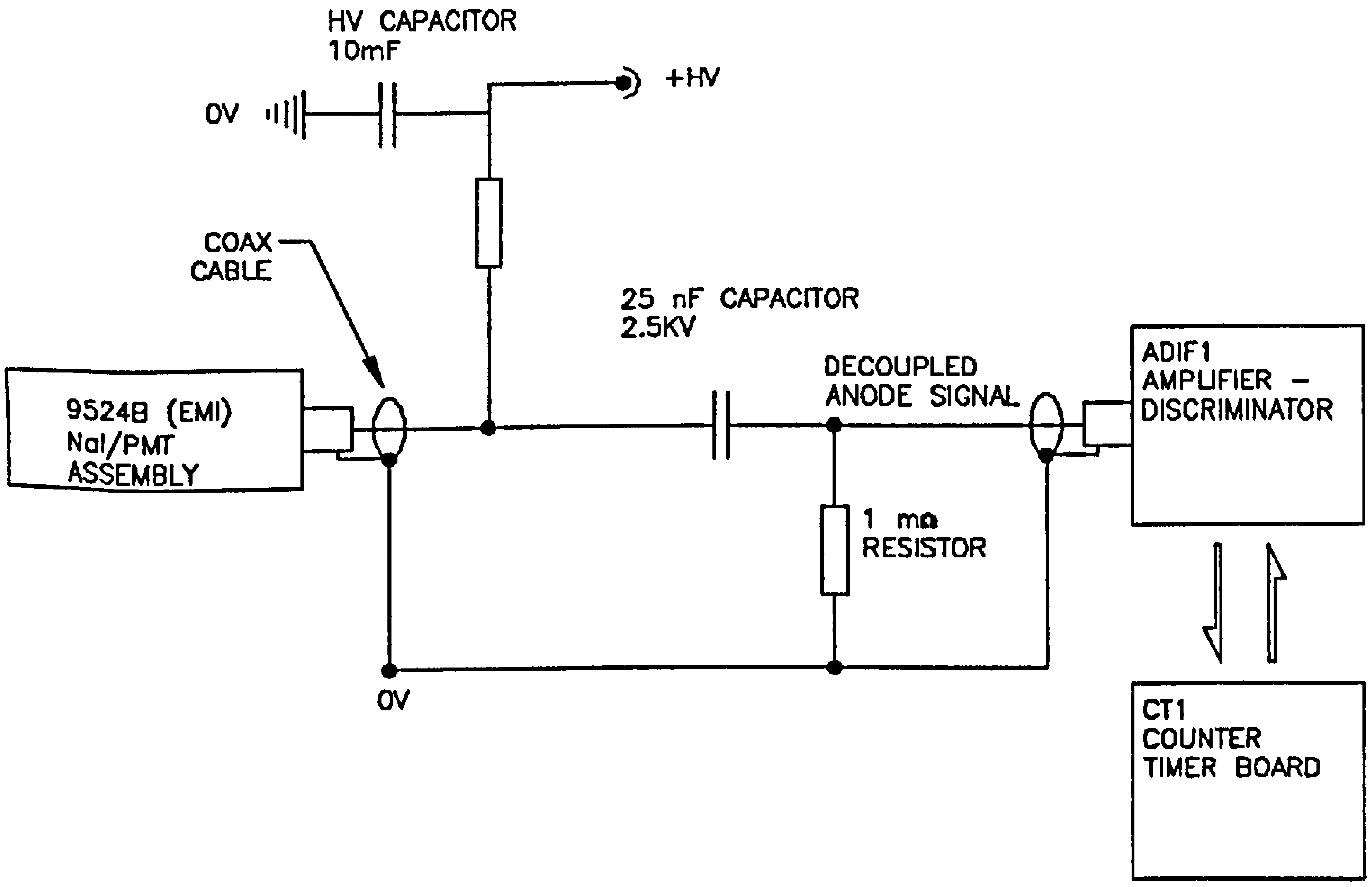

Figure 4.4: Configuration of Gamma-Ray Densitometer

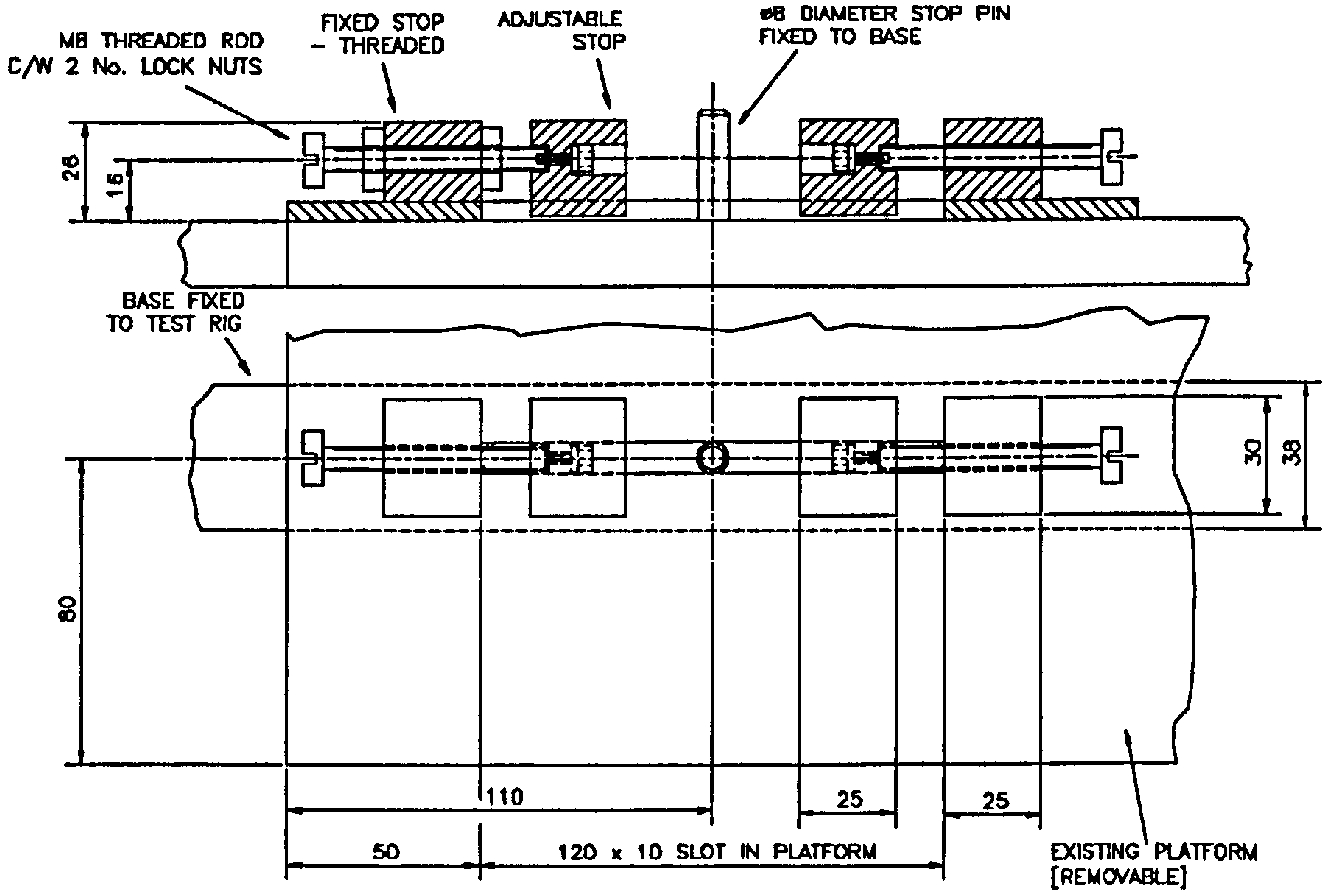

Figure 4.5: Position Locking Assembly for Gamma-Ray Densitometer Carriage

Item	Description	Manufacturer
1	NaI(TL) crystal 1" diameter x 1 mm thick assembly c/w 30 mm 9125 focused photomultiplier. Dark current 0.14 nA	Hilger Crystals ltd
2	ADIF1 Amplifier-discriminator & current to frequency module.	Electron Tubes Inc
3	CT1 Counter timer board. Counting period accuracy ±1 μs.	Electron Tubes Inc
4	PS2001/12N High voltage modular power. 20 to 2000 V.	Electron Tubes Inc

Table 4.3: List of Components, Gamma Ray Densitometer.

4.3.1 Installation of Gamma Ray Densitometer

The system detailed above, normally referred to as gamma-ray densitometer, relied on the scintillation properties of a Sodium iodide crystal [NaI(Tl)]. When exposed to gamma rays, the crystal emits photons in proportion to the incident rate of the ionising source. By counting the photons emitted by the crystal i.e. detected by the photo multiplier, the attenuation of gamma rays passing through the test section and its contents could be determined. The CT1 Counter timer housed in the Hewlett Packard (HP) PC performed the complex task of interpreting the output signals from the PMT and transforming them into a count rate.

To take void fraction data during two-phase tests the collimated ^{241}Am source, by means of a locating collar, was positioned directly opposite the PMT assembly. PMT and the ^{241}Am source straddled the test section and the integrity of their alignment was maintained by fixing them both to a carriage which was in turn mounted on a rigid base. A manually operated gear driven assembly enabled the entire carriage to traverse the test section accurately positioning it at any point.

To ensure that the carriage could be repeatedly returned to selected locations a stop pin and two adjustable blocks where added to the carriage. By locking the position of the adjustable blocks the void fraction could be read at one position, moved to the extreme of that position determined by the stop pin, and then confidently returned to the original position. The void fraction was measured for every two-phase test at the pipe centre line and an offset position halfway between the pipe centre line and outer wall. For a detail of the stop pin and blocks see Figure 4.5.

The installation of the gamma-ray densitometer was further complicated by need to adhere to several safety procedures. The biggest concern was scatter generated by the ionising radiation source to its immediate surroundings. A 10 mm thick 200 mm square section channel was machined so that it could be used as an enclosure for the entire PMT and ^{241}Am source. The box section channel was secured to the carriage and slotted providing clearance for the test section to pass through it. Plate 4.2 shows the carriage, stop pin and adjustable blocks, locating collar for the ^{241}Am source and the box section channel, in position enclosing the PMT.

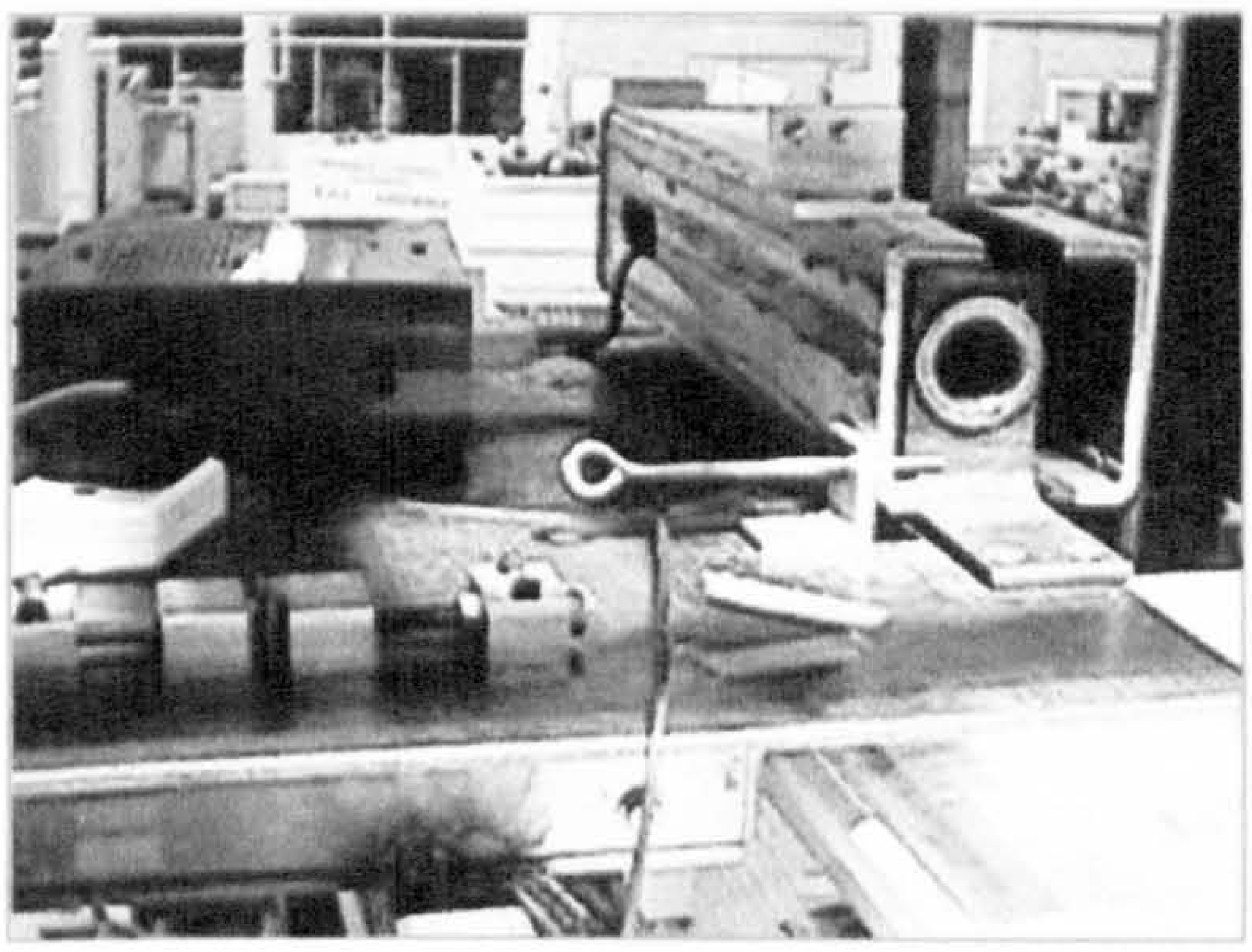

Plate 4.2: Densitometer

Safe operation of the gamma-ray densitometer required strict adherence to University health and safety policy guidelines. These were as follows:-

- A mandatory risk assessment of all working practices and a scheme of work to be submitted to the University Radiation Protection Supervisor.
- The attendance of nominated operators to an officially accredited Radiation Protection Course on the safe handling of the ionising radiation sources.

- The demarcation of a designated Controlled Area encompassing the test facility with appropriate warnings against the entrance of unauthorised personnel.
- All persons involved in the operation of the test facility allocated with film badges, worn on the outer surface of their clothing.
- The pre and post-test monitoring of radiation levels with in the control area.
- An appropriate facility for the safe storage of the ^{241}Am source when not in use.

4.3.2 Commissioning of the Gamma-Ray Densitometer

A test was devised to commission the gamma-ray densitometer. To begin with a background reading was taken using the PMT assembly. A short section of copper pipe was then positioned between the ^{241}Am source and the PMT assembly. The pipe was of the same geometry and physical properties as that used to construct the test length. Two readings were taken one with the pipe empty and one with the pipe filled with water.

A 10 mm diameter rod was then inserted into the pipe. The void fraction created by the rod was measured twice. Once with the void empty and once with the void filled with water. By measuring the internal diameter of the copper pipe the actual void fraction was calculated. If I is the incident intensity the measured void fraction can be calculated using;

$$\alpha = \frac{\ln\left[{I}/{I_l} \right]}{\ln\left[{I_g}/{I_l} \right]} \tag{4.3}$$

A derivation of Equation 4.3 is given in Appendix A.2 and a review of void fraction measuring techniques is given in Appendix A.6. Measured and actual void fraction are compared in Table 4.4.

Void Fraction (-)	Measured Void Fraction, Air in void (-)	Measured Void Fraction, Water in Void (-)
0.762	0.775	0.779

Table 4.4: Void Fraction Commissioning Test.

4.3.3 Procedure for Void Fraction Measurement

Prior to measuring the void fraction of a two-phase flow, five pre-test measurements were required. These five measurements, or 'count rates', were taken on a daily basis before any two-phase test and then used when processing all void fraction data taken that day. The five pre-test measurements were:-

1. Background radiation intensity, no source present (c/s).
2. Intensity of gamma-ray radiation with test section empty, centre-line position (c/s).
3. Intensity of gamma-ray radiation with test section empty, off-set position (c/s).
4. Intensity of gamma-ray radiation with test section full of liquid, centre-line position (c/s).
5. Intensity of gamma-ray radiation test section full of liquid, off -set position (c/s).

Having obtained the pre-test measurements two further count rates were taken during each two-phase test. One at the centre-line position and second at the off-set position.

For each of the five pre-test and the two-phase measurements taken at the centre-line and off-set positions, the count rate was recorded one hundred times. The count rates were saved to files with the extension 'PCD' and then transferred from the lab to another PC for analysis. The count rates were then averaged and the void fraction calculated using Equation 4.3.

4.4 Data acquisition System

A data acquisition system was employed to allow averaging techniques to be applied to various test signals so as to improve the reliability of data retrieved from the test facility. Shown in Figure 4.1, the data acquisition system electronically logged liquid flow pressures, local pressures and momentum values. Utilised for single and two-phase experiments the data acquisition system was advantageous in the retrieval of data points under steady-state conditions. In-house developed software allowed the user to designate sampling frequency's and time periods, manipulate stored readings and transfer data from the lab to another PC for processing.

The data acquisition system consisted of a Hewlett Packard (HP) PC and a HP3421A Data Acquisition Control Unit. The control unit provided terminals from which individual connections were made to instrument transducers. Table 4.5 identifies the channel and the associated instrumentation. Relay switches seated in the control unit allowed the computer to select channels and interrogate the voltage difference across the terminals of each channel. Channels 11 and 12 were used for both the momentum and the calibration tank load cell transducers.

Two programs were written in HP Basic to drive the data acquisition system. One for calibrating the flow nozzles and a second to record test data values generated during single and two-phase experiments. The HP Basic programming language provided special instruction sets to allow the user to easily communicate with the control unit.

The transfer of test data from the data acquisition system was achieved by using a standard file format that could be easily interpreted by other PC based software. Routines were also developed to display the test data graphically, assisting in decisions that were made in situ during test runs.

Channel No.	Signal Description & Control Unit Voltage Setting	Instrument
7	Pressure drop across flow nozzles 0 – 5v	Rosemount 3051 differential pressure transmitter (basement).
4	Local gauge pressure 0 – 30v	Rosemount 2088 gauge pressure transmitter
2	In-line component pressure drop 0 – 30v	Rosemount 3051 differential pressure transmitter (high level).
11	Jet Momentum / Front Calibration Tank 0 – 0.3v	Transducer load cell 1
12	Jet Momentum / Back Calibration Tank 0 – 0.3v	Transducer load cell 2
28	0 – 5v	Remote switch

Table 4.5: Control Unit Channel Allocation & Voltage Settings

Specifically for the use during two-phase tests, a software routine was developed that allowed the program to continuously monitor the quality of the mixture. This enabled specific air and liquid mass fluxes to be established before test data were recorded.

A feature employed in both single and two-phase tests was the remote switch. As described in Section 4.5.6, local pressure could be measured at various locations on the test section. These locations were selected manually by the operation of ¼" ball valves on the pressure line. To enable the facility to be run by a lone operator, the remote switch allowed the operator to open and close the valves located at high level whilst still co-ordinating the collection of data by the data acquisition system. Complete descriptions of the operating procedures to collect experimental data are given in Section 5.2 & 5.9 for single and two-phase tests respectively.

4.5 Automated Readings

To enable the flow nozzle pressure drop and the local pressures to be logged automatically by the data acquisition system, described in Section 4.4, pressure transducers were installed that generated industry standard process control signals. Two types of pressure transducers were employed. The Rosemount 3051 differential and the Rosemount 2088 gauge pressure transmitters, both operating on a 1-5 V dc, 4-20 mA supply. The Rosemount pressure transmitters were of a SMART type design.

4.5.1 Calibration of Rosemount SMART Pressure Transducers

The Rosemount SMART design of pressure transducer allowed the use of a HART Communicator, model 275, to interrogate and alter upper and lower pressure limits, units of measurement, and the time constant. Thus forgoing the need to manually calibrate the pressure transducer for each new pressure range that each transducer was exposed to.

The pressure reading was represented in mA and was accommodated by a Digital Signal based on HART protocol. The protocol allowed a single connection to be utilised for the pressure signal, the transducer power needs and communication with the HART Communicator.

4.5.2 Liquid mass Flow Rate Measurement

To measure the liquid mass flow rate four flow nozzles were arranged in parallel and housed in a manifold arrangement. Plate 3.2 shows the flow nozzles in situ viewed from above. The flow nozzles were manufactured from Brass bar as detailed in Figure 3.8. The upstream diameters of all the flow nozzles was 50 mm and the down stream diameters for nozzles 1, 2, 3 and 4 were 26.02, 13.6, 6.44 and 3.5 mm respectively. The pressure drop across the flow nozzles was measured using a single Rosemount 3051

Smart pressure transducer with a maximum working pressure of 250 bar, a minimum span of 12 mm of water and a maximum span of 0.56 bar. The pressures transmitted by the transducer were reliable to an accuracy of ±0.2% of full-scale reading.

The same flow nozzle calibration procedure was used for both water and aqueous glycerine test liquids. This calibration procedure involved determining the pressure drop against volume flow relationship for the working range of each nozzle. To do this, the volume of test liquid flowing through any one nozzle was collected in the two calibration tanks. The liquid levels in each calibration tank were converted into an analogue signal by a float load cell arrangement. This arrangement, shown in Figure 4.6, consisted of a cylindrical float held in position by a steel rod. As the liquid level in the calibration tank rose the buoyancy force acting on the cylindrical float increased. The buoyancy force was converted into an electrical signal by the mechanical action of a lever acting against a load cell.

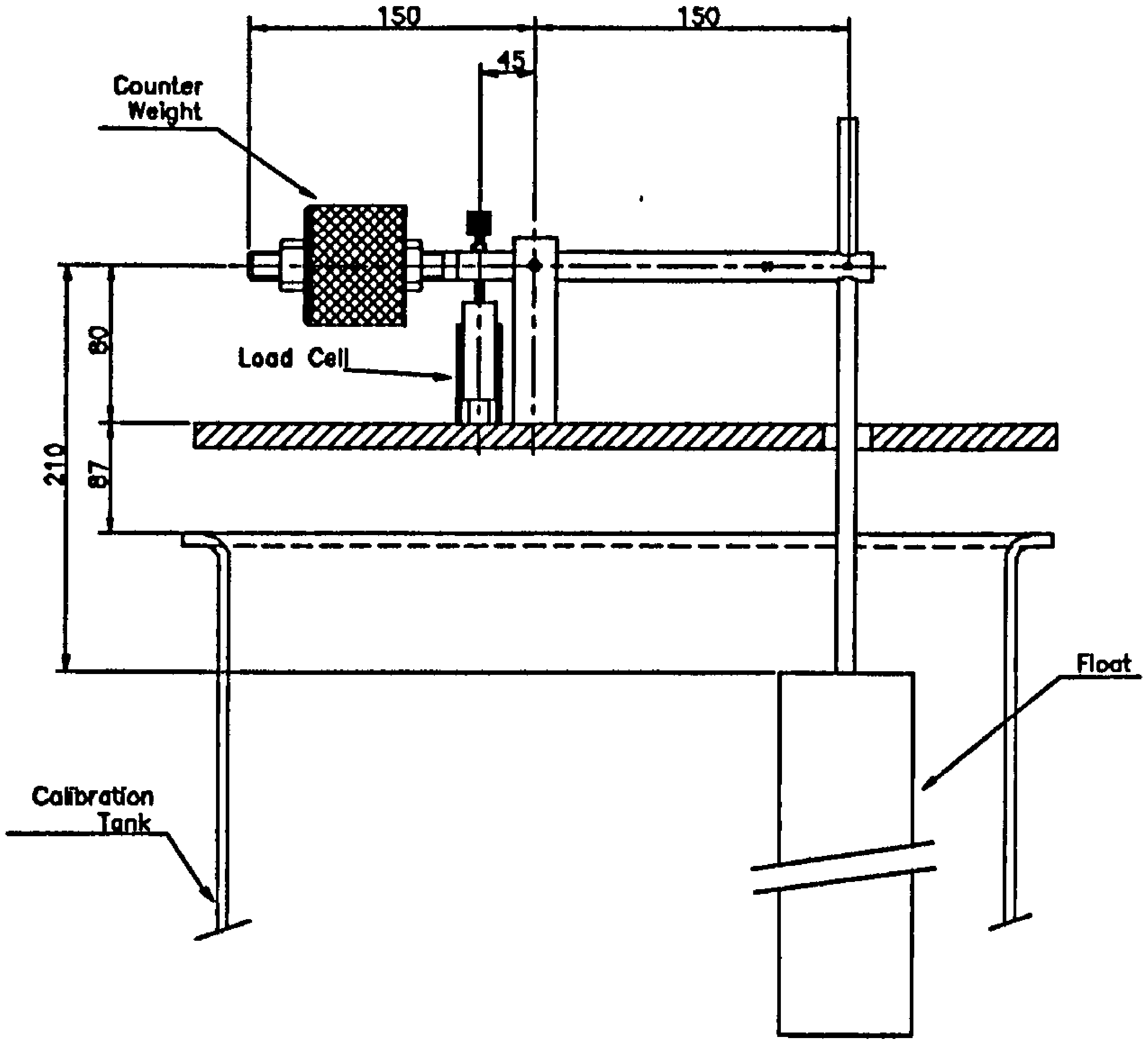

Figure 4.6: Tank Buoyancy Force Assembly

4.5.3 Calibration of Flow Nozzles

Each flow nozzle was calibrated using a software routine called LABS5, developed in HP Basic, specifically for calibration purposes. The data acquisition system, as described in Section 4.4, allowed the routines in LABS5 to record the analogue signals representing the liquid levels in the calibration tanks and the pressure drop across a selected flow nozzle.

A typical calibration, for control valves refer to Figure 3.1, began by closing control valve C and ensuring that control valves A,B and D were fully open before starting the pump. After starting the pump, the ¼" ball valves on the common pressure line and the gate valve immediately upstream of the flow nozzle being calibrated were opened. Air trapped in the pressure line was then bled by opening two M10 plugs located at the base of the Rosemount differential pressure transducer. The HART communicator was used to set the appropriate upper range value for pressure, URV, in accordance with the flow nozzle being calibrated, see Table 4.6.

The start menu of LABS5 was then used to set the sampling frequency for the tank liquid level and pressure drop signals. As the pressure drop across the flow nozzle remained relatively constant during a calibration it was not necessary to record as many pressure drop signals as liquid level signals. The sample ratio option on LABS5 allowed the user to input the ratio of liquid level samples to pressure drop samples. This sample ratio raised the resolution of the liquid level sampling to a frequency suitable for the faster flow rates. For example, a sample ratio of 1:1 resulted in 50 samples per minute of liquid level and pressure drop signals. This compares with a sample ratio of 10:1 giving 210 samples per minute of the liquid level signal and 21 samples per minute of the pressure drop signal.

To establish a flow through the flow nozzle and into the calibration loop, valve A, located on the by-pass loop was slowly closed. Once a flow rate was established LABS5 was instructed to record. Valve D was then closed so that all test liquid flowing through the flow nozzle was collected in the calibration tanks. When the liquid level in the calibration tanks reached the over flow the sampling routine was stopped. To allow the user to visually check the validity of a calibration, LABS5 generated a graph of the liquid level and pressure drop samples against time. From the graph large incidents of noise and corrupted data were easily recognised and poor calibration tests repeated. Good data was saved to file. Figure 4.7 shows a typical calibration data set as generated by LABS5.

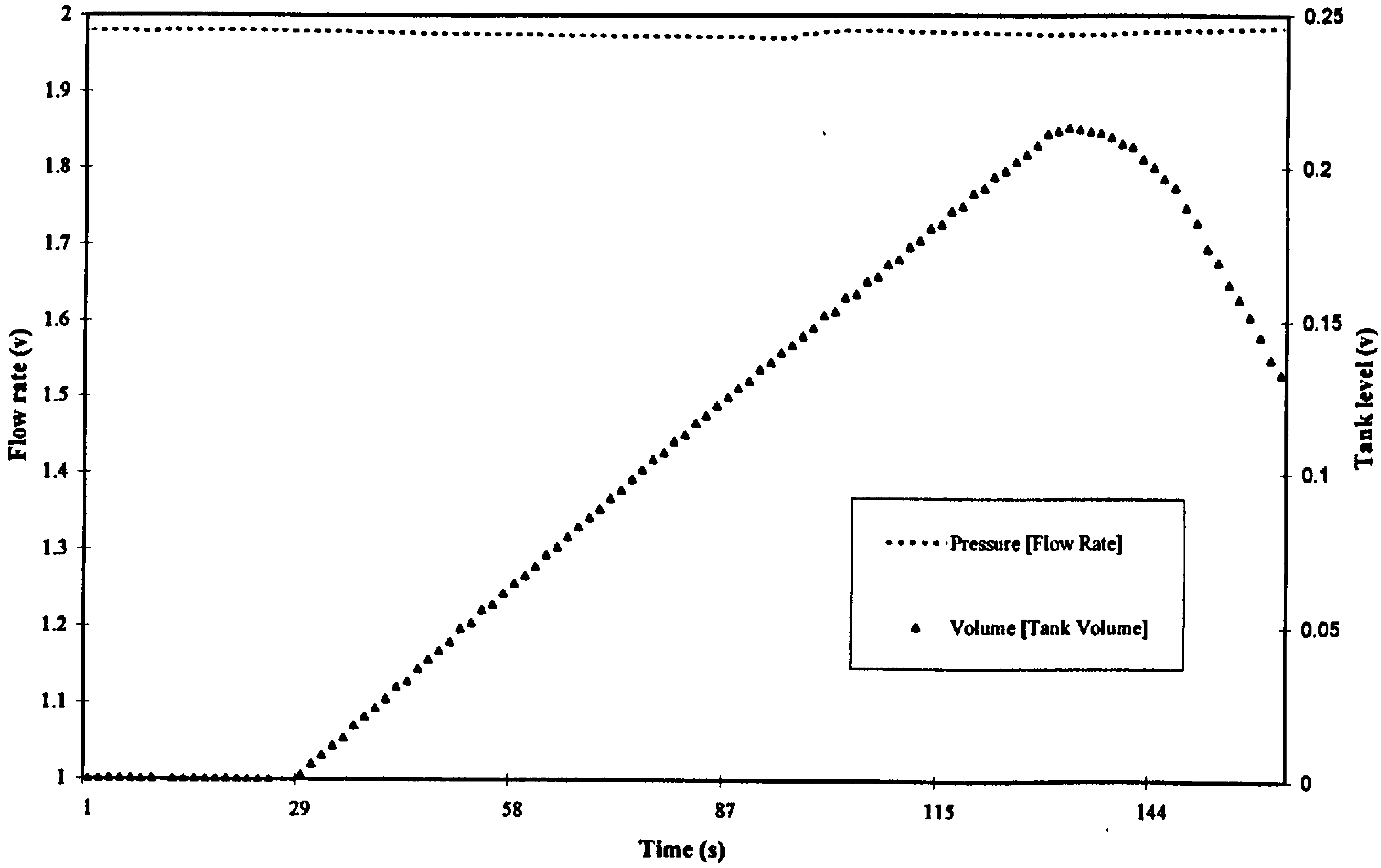

Figure 4.7: Typical Calibration Trace

4.5.4 Analysis of Water Test Liquid Calibration Data File

The above method for sampling the flow nozzle calibration using LABS5 was repeated between six and ten times for flow rates spanning the entire operating range of each flow nozzle. For analysis, the data files generated by LABS5 were transferred to a PC. A FORTRAN program called CALIB3, see Figure 4.9 for a flow diagram, was used to automatically extract the sampled data. To improve the accuracy of the calibration procedure, a routine was employed in CALIB3 to integrate the liquid level and pressure drop data using the piecewise quadratic approximation of Simpon's rule. This was necessary as the calibration tank had a tapered cross section and the flow rate slightly fluctuated over time, as can be seen in Figure 4.7. The application of Simpon's rule allowed the discharge coefficient for a flow nozzle to be defined by Equation 4.3, a full derivation is given in Appendix A.1;

$$C_D = \frac{3m}{2k}\left[\frac{V_2}{(mt_2+c)^{3/2}-(mt_1+c)^{3/2}}+\frac{V_1}{(mt_4+c)^{3/2}-(mt_3+c)^{3/2}}\right] \qquad (4.3)$$

Where;

V = the volume of fluid in the calibration tank.

k = factor derived from the physical properties of the nozzle and test liquid.

m = the gradient of the regression of the tank height data.

c = the constant of the regression of the tank height data.

$t_{1\text{-}4}$ = reference time relating to the volume set points in the calibration tank.

To apply Equation 4.3 it was necessary to measure the volume of the calibration tanks. The total volume of calibration tanks was subdivided into five volumes, each designated by a set point. The size of each of these smaller volumes was found by weighing the calibration tanks contents and recording corresponding load cell transducer values. The *k* factor in Equation 4.3 was derived from the test liquid properties and flow nozzle geometry. Discharge coefficients, pressure transducer settings and the *k* factors for the water test liquid calibrations are given in Table 4.6. To confirm the accuracy of the electronic calibration system a manual check was made. For the manual check a stopwatch was used to determine the time in which the level of the test liquid rose in a scaled sight-glass attached to the side of the calibration tanks. The increments on the sight-glasses were carefully matched to the five already determined smaller volumes. Equation 6.1 & 6.2 were used to calculate the ideal flow and the discharge coefficient.

The accuracy of the calibration of flow nozzle three was checked using a turbine meter inserted into the test section in place of the uniform diameter spool piece. The flow rate of water circulating through the test section was measured using flow nozzle three. The measured flow rates were then compared with readings from the turbine meter. Figure 4.8 shows the measured volume flow rate against the ideal values for all the flow nozzles and the 'flow check' of flow nozzle three using the turbine meter.

Flow Nozzle No.	Nozzle Diameter (mm)	Physical Constant, k (-)	URV (N/m^2)	Coefficient Manual Check (-)	Discharge Coefficient (-)
1	26.02	2.47E-05	7475	0.9542	0.9488
2	13.6	6.51E-06	50000	0.9545	0.96
3	6.44	1.457E-06	50000	0.8926	0.88
4	3.5	3.267E-07	50000	0.4387	0.46

Table 4.6: Flow Coefficients for Flow Nozzles, Water Test Liquid.

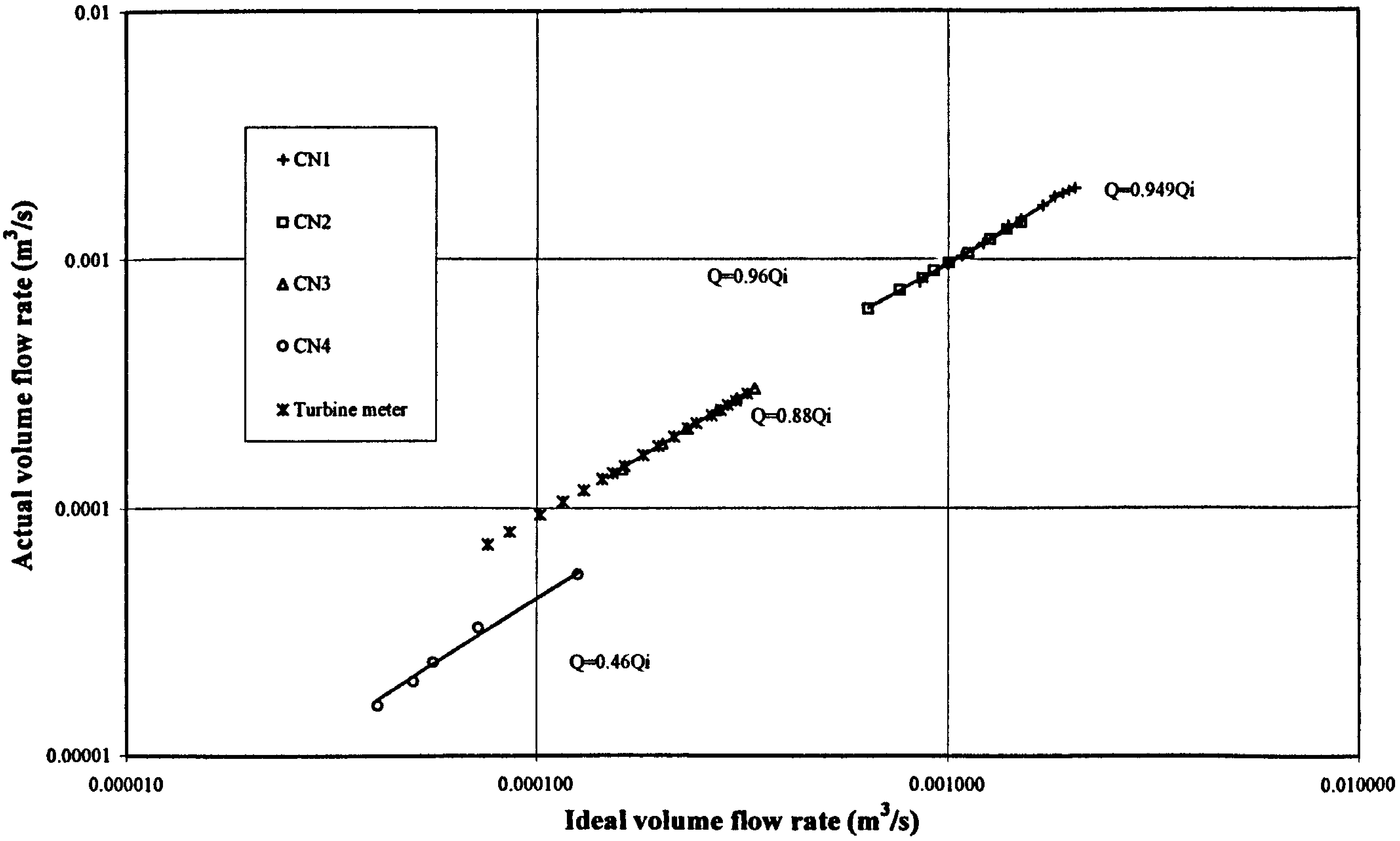

Figure 4.8: Flow Nozzle Calibrations Using Water

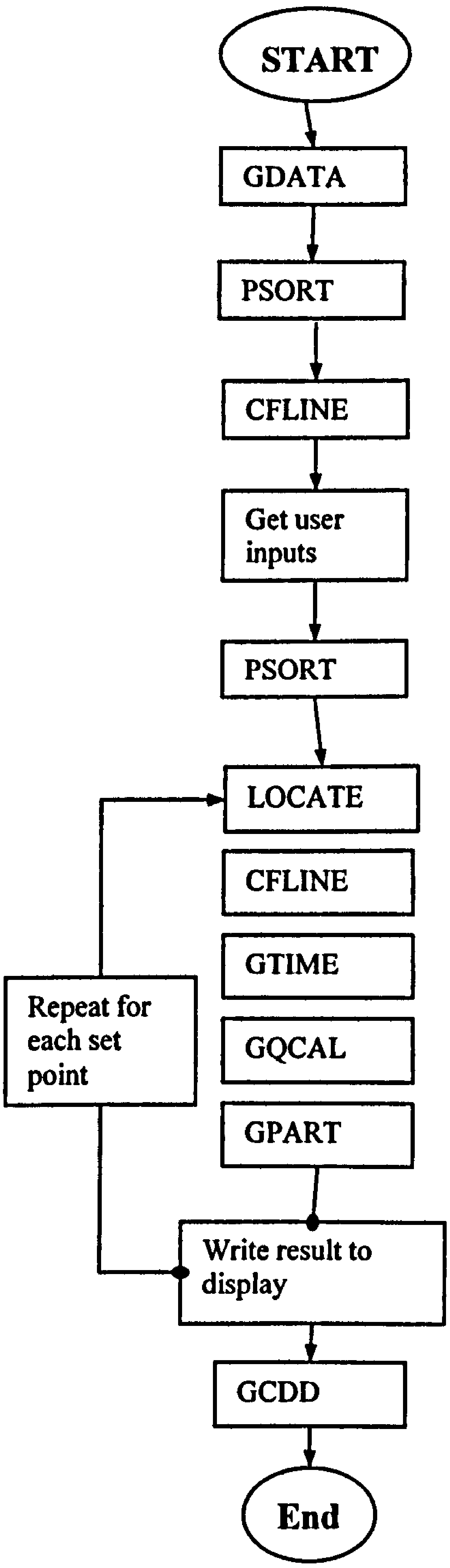

Read file –assign raw load cell signal to data variable IMPORT

Convert raw pressure transducer data to pressure drop values & average them.

Fit a line of regression to the entire sample, assigning m & c in Equation 4.3.

Size of data cluster.

No. of tanks used in calibration, tank used, TT1, TT2

Read file –assign raw data to variable IMPORT.

Fit a line of regression to the data cluster with that set point.

Calculate Q for partial volume defined by set point, assign FQ.

Use m & c to calculate equivalent *t* for set points.

Calculate first part of Simpon's rule, assign CD.

Calculate C_D for flow nozzle.

Figure 4.9: Flow Calibration Program

4.5.5 Analysis of Aqueous Glycerine Test Liquid Calibration Data File

The discharge coefficient for the water test liquid flow nozzle calibrations' was found to be constant over the full range of mass flow rates for each flow nozzle. Due to the high viscosity of the aqueous glycerine test liquids, the flow through the flow nozzles was laminar and the discharge coefficients were a strong function of the Reynolds number. The same procedure for the water test liquid, as described in Section 4.5.2, was used to calibrate the flow nozzles for the aqueous glycerine test liquids. The k, values used in the CALIB3 for the nominal viscosities of the glycerine test solution are given in Table 4.7.

Flow Nozzle (m)	**Nominal viscosity 550 mPas Density 1260 kg/m^3 (-)**	**Nominal viscosity 200 mPas Density 1235 kg/m^3 (-)**	**Nominal viscosity 50 mPas Density 1190 kg/m^3 (-)**
0.02602	2.201E-05	2.223E-05	2.265E-05
0.0136	5.803E-06	5.862E-06	5.972E-06
0.00644	1.298E-06	1.311E-06	1.336E-06

Table 4.7: ***k***, Values For Glycerine Test Solution

The discharge coefficients generated by CALIB3 were plotted for each flow nozzle against the Reynolds number calculated at the flow nozzle throat. The resulting discharge coefficient Reynolds relationship was then described using a second order polynomial. As the viscosity of the aqueous glycerine test liquids was changeable, the flow calibrations were repeated throughout the test programme using current viscosity curves. The viscosity of the aqueous glycerine test liquids were nominally 550, 200 and 50 mPas. It was not possible to manually authenticate the electronically retrieved discharge coefficients for the viscous calibrations in the same way as that of the water test liquid calibrations. For the water test liquid calibrations a sight glass on the side of each calibration tanks was used to obtain set volumes. The rate at which the aqueous glycerine test liquid rose in the sight-glass was found to be slightly less than that of the calibration tanks. To overcome this problem, two markers were inserted in each calibration tank. The volume of liquid represented by the two markers was determined by weighing the contents of the calibration tanks. A stopwatch was then used to time the rise of the liquid level between markers enabling the volume flow rates to be determined from the known volume.

Only flow nozzles CN1, CN2 and CN3 were used in the highly viscous tests and the flow calibrations for each nozzle are given in Figures 4.10 - 4.12. Also included in Figures 4.10 - 4.12 is a nozzle theory, described in McNeil *et al* [121] (2000). A complete set of flow nozzle calibrations are given in Appendix C1.2 & C2.2 for the single and two-phase tests respectively.

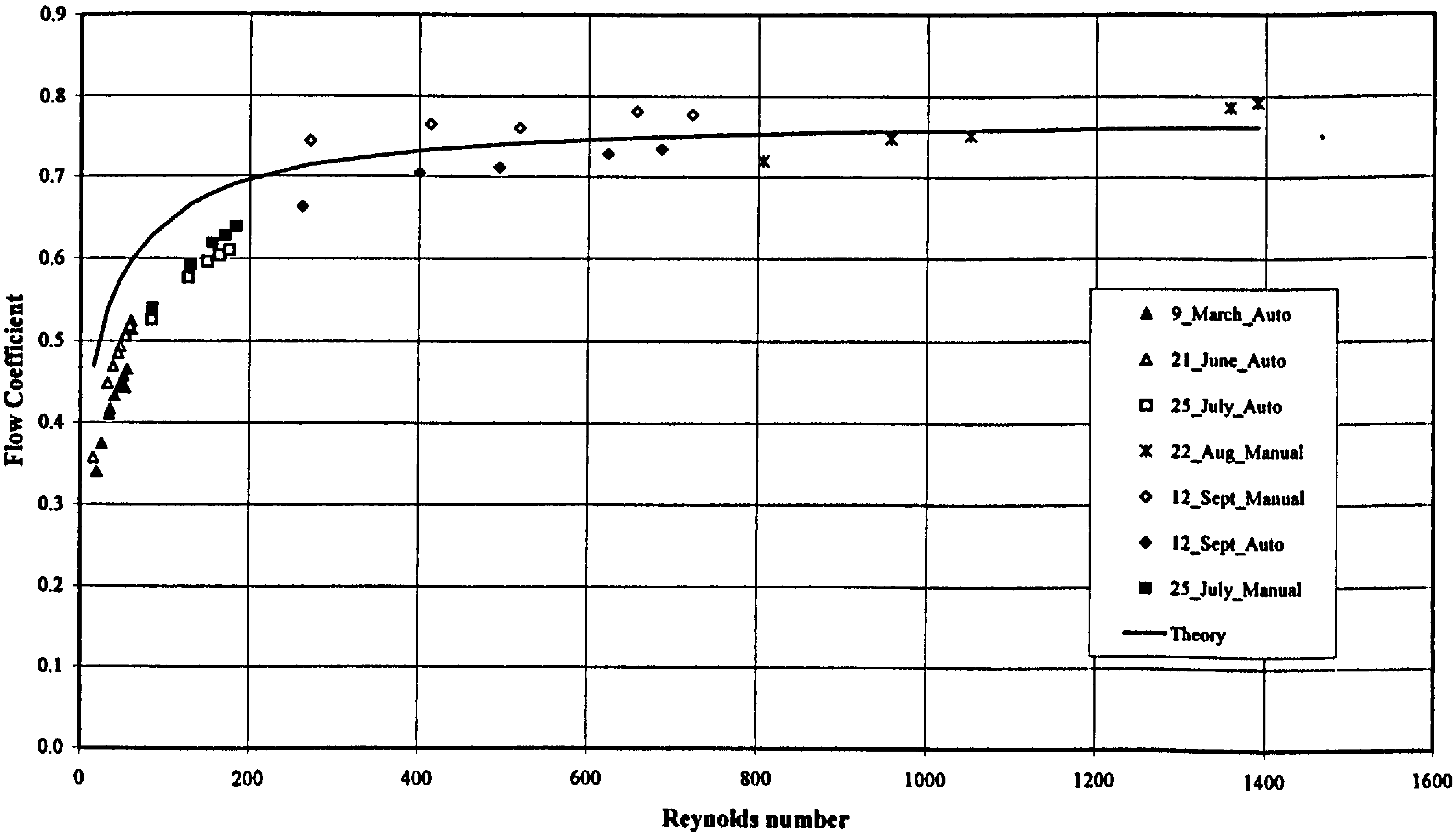

Figure 4.10: Flow Coefficients for 26.02mm Diameter Flow Nozzle 1

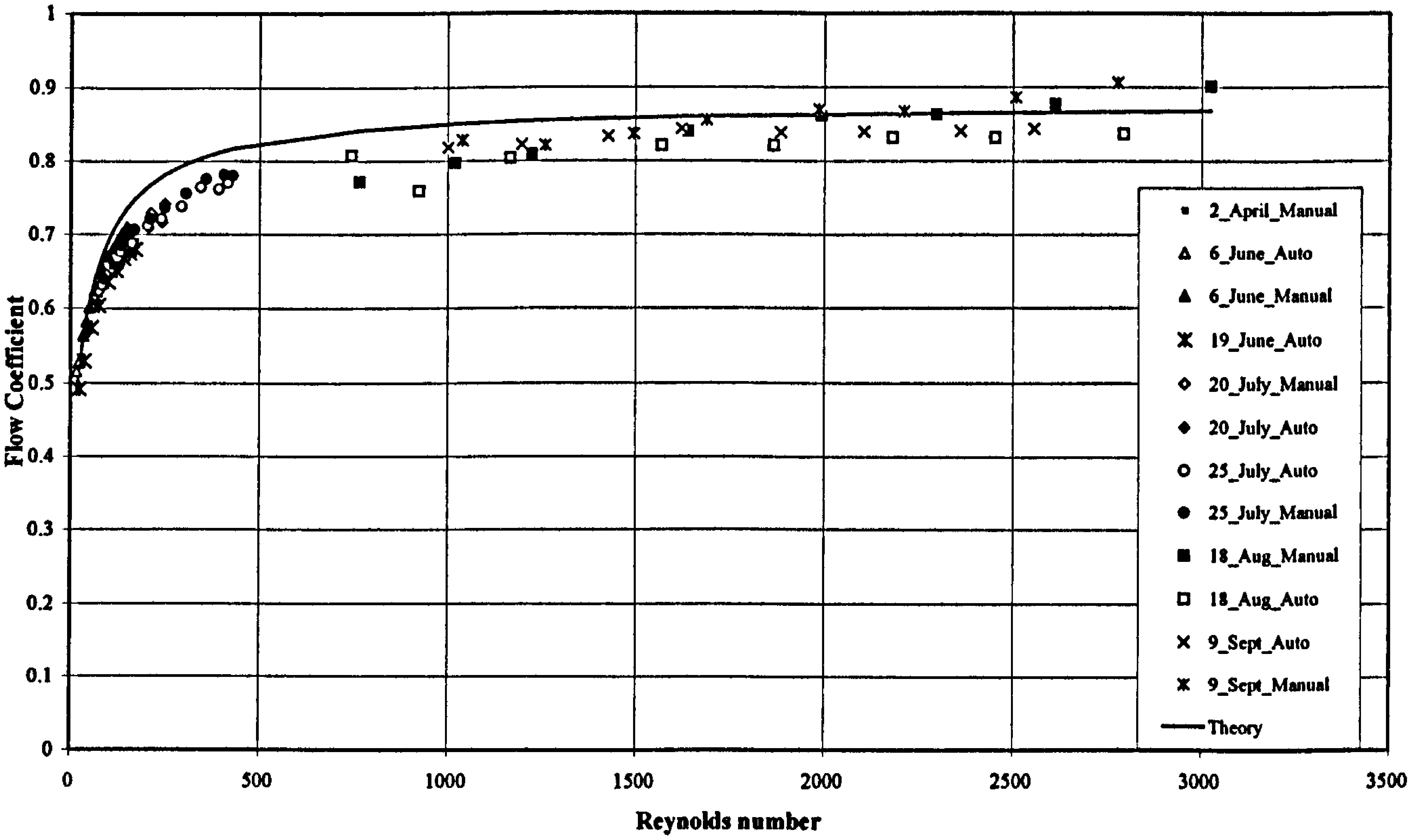

Figure 4.11: Flow Coefficients for 13.6 mm Diameter Flow Nozzle 2

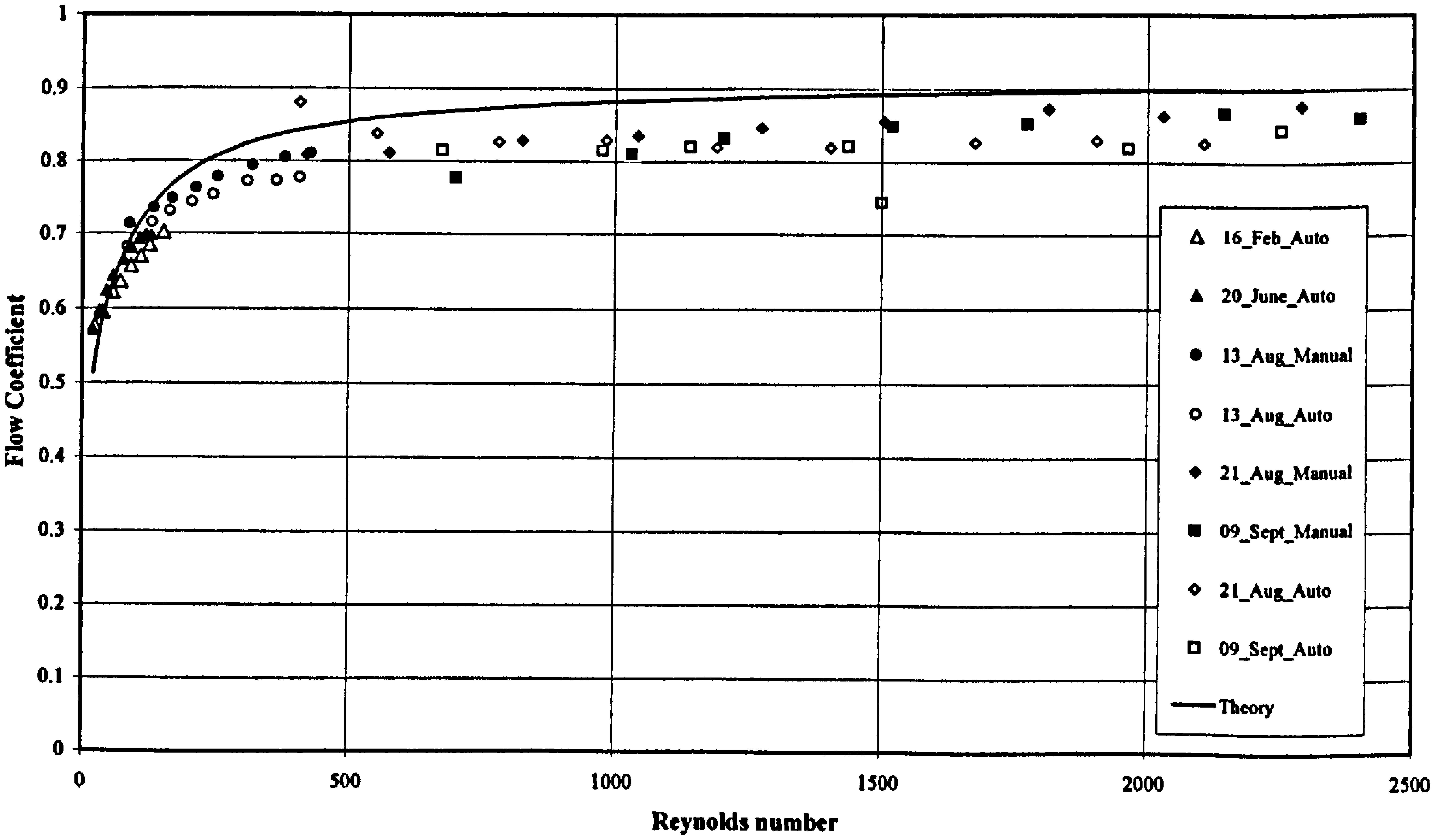

Figure 4.12: Flow Coefficients for 6.44mm Diameter Flow Nozzle 3

4.5.6 Local pressure measurement

Along the test section, a series of pressure taps allowed the local gauge pressure to be measured. The position of these pressure taps is given in Figure 3.2. The local pressure taps were connected to a common pressure line terminating, at mid level, with a single Rosemount 2088 Smart pressure gauge. This local pressure transducer had a maximum working pressure of 10 Bar and had an accuracy of ±0.2% of the full scale reading. The upper and lower pressure ranges, units of measurement and time constant for the local pressure transducer were altered as described in Section 4.5.1 using the HART Communicator.

During testing the local pressure was read using the data acquisition system as described for single and two-phase fluids in Section 5.2 & 5.9 respectively. As the local pressure fluctuated during the test, it was necessary to determine the number of samples

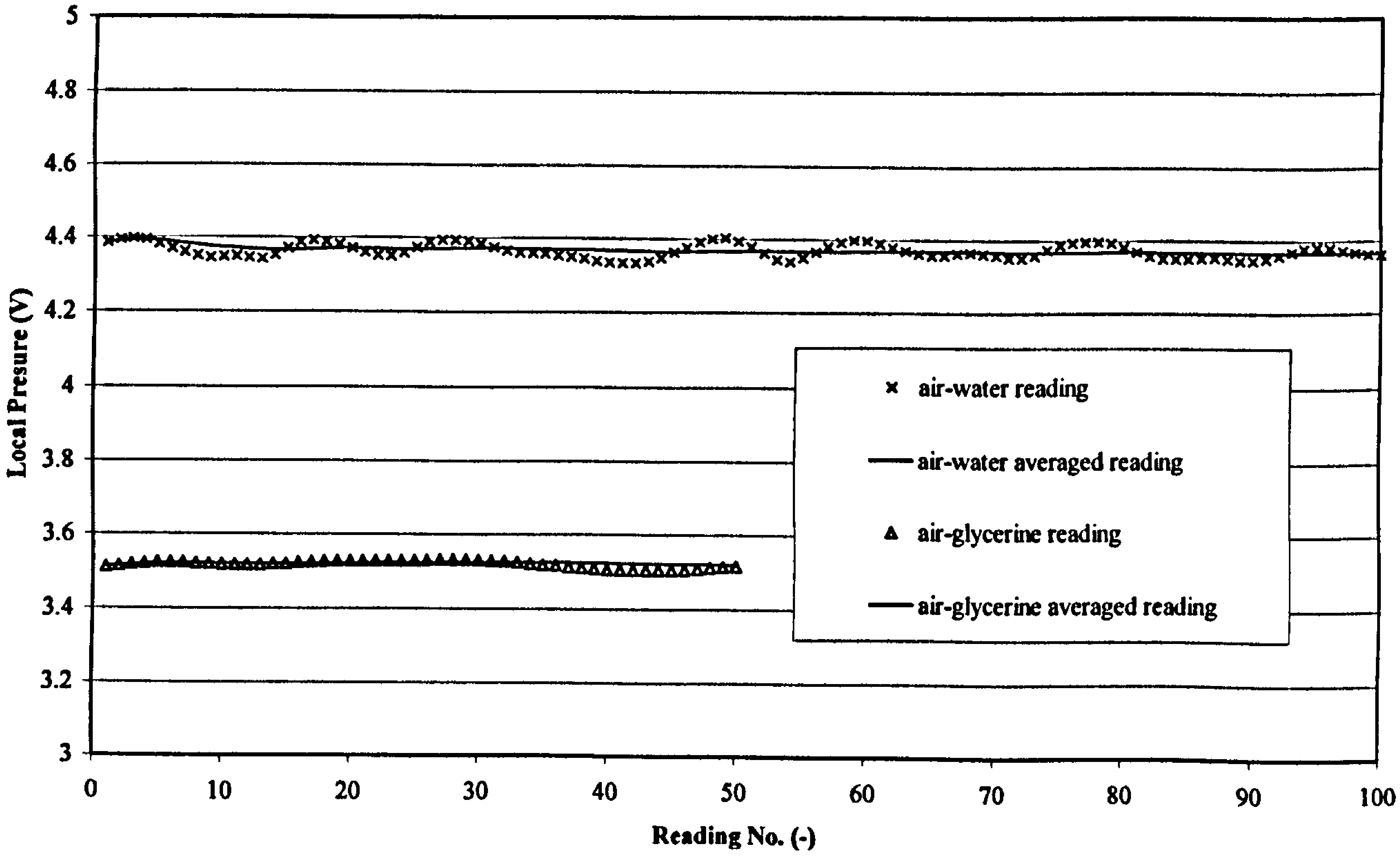

Figure 4.13: Pressure Readings

required at each local pressure tap to give a dependable average. Two traces of local pressure samples along with the corresponding running averages are given in Figure 4.13. The samples were taken for an air-water flow at a quality of 0.4 and the equivalent air-glycerine flow.

The air-water running average stabilises after fifty readings obtained in 15 seconds but the air-glycerine running average stabilises after around 25 readings. Subsequently all local pressure readings for single and two-phase flows were recorded taking the average of at least fifty readings, or sampling for at least 15 seconds.

4.5.7 Momentum Measurement

Two load cell arrangements were used for measuring the momentum flux. The smaller single-phase flow forces were measured using the arrangement shown in Figure 4.14 and the larger two-phase flow forces were measured using the arrangement shown in Figure 4.15. The single-phase flow approach utilised a fulcrum, counter weight and moment arm to multiply the forces acting on the load cell giving a working range of 0 to 2 kg.

For two-phase flows, the target was mounted directly on two adjacent load cells dispensing with the moment arm and counter weight. The more robust nature of this second arrangement limited the smallest forces it could register to 5 N but the design was considerably more stable when subjected to two-phase flows. The upper range of forces that could be measured by the duel load cell arrangement was 40 N. This was extended by the utilisation of a weight adapter as detailed in Figure 4.16. The weight adapter was fitted to the end of the targets' shaft allowing a selection of weights to be secured to the shaft and in opposition to the force of the discharging jet. This extended the maximum measurable momentum force to 100 N. For the successful application of this method, an estimate of the forces that the target would be subjected to was required, so that the system could be pre-weighted accordingly.

4.5.8 Calibration of Momentum Load Cells

The same method of calibration was used for both load cell arrangements. To calibrate the load cell, weights were placed on a cradle suspended from the shaft of the target via guide wheels. The guide wheels ensured the force of the weights was transferred to the centre line of the target and consequently acting in the same plane as that of discharging jet. The calibration required a series of weights to be applied and the corresponding load cell transducer readings recorded. A graph was then plotted of force against load cell voltage. A typical load cell calibration for the two-phase flow duel load cell arrangement is given in Figure 4.17. The curve produces a linear relationship between force and voltage.

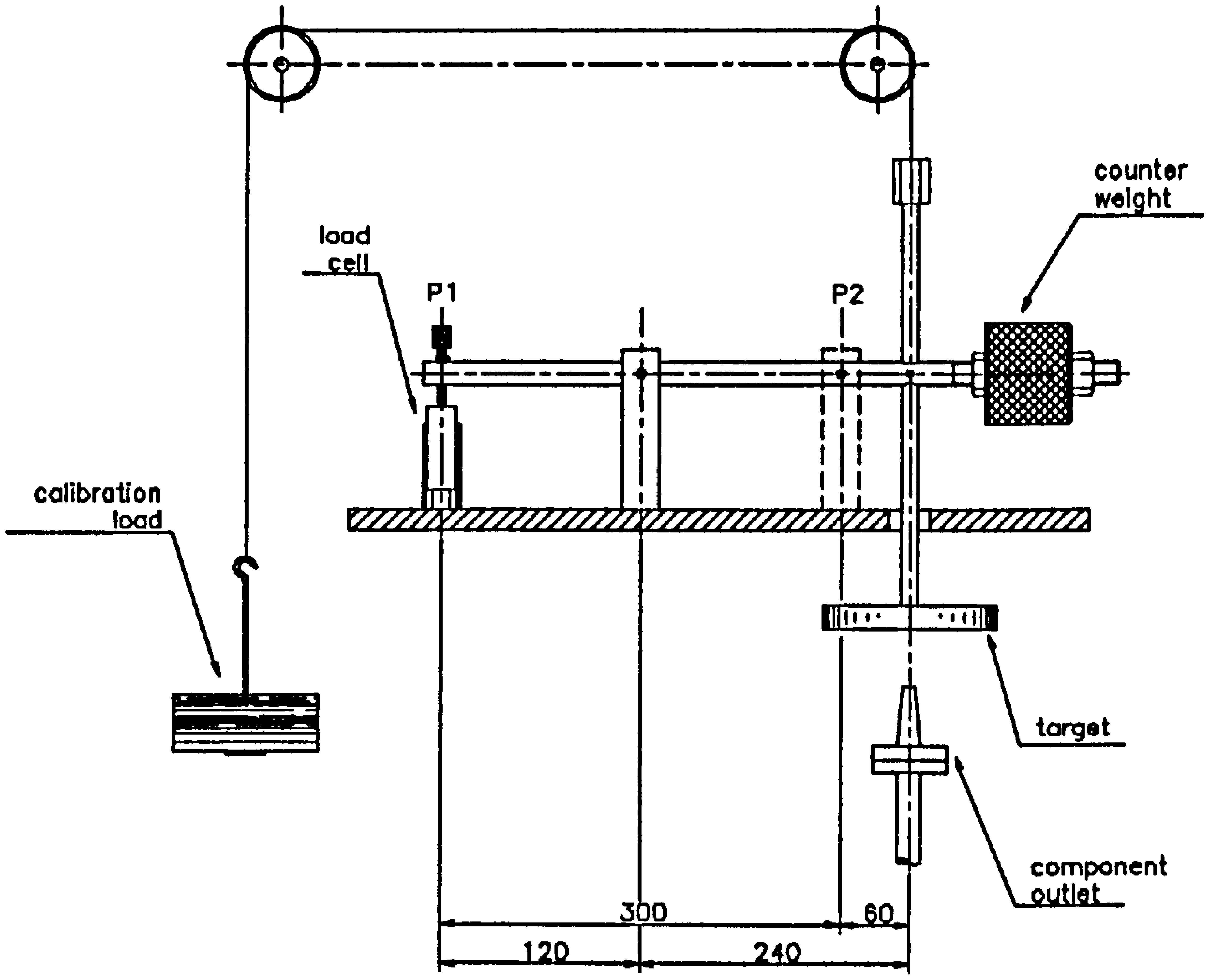

Figure 4.14: Single-phase Momentum Measurement Assembly

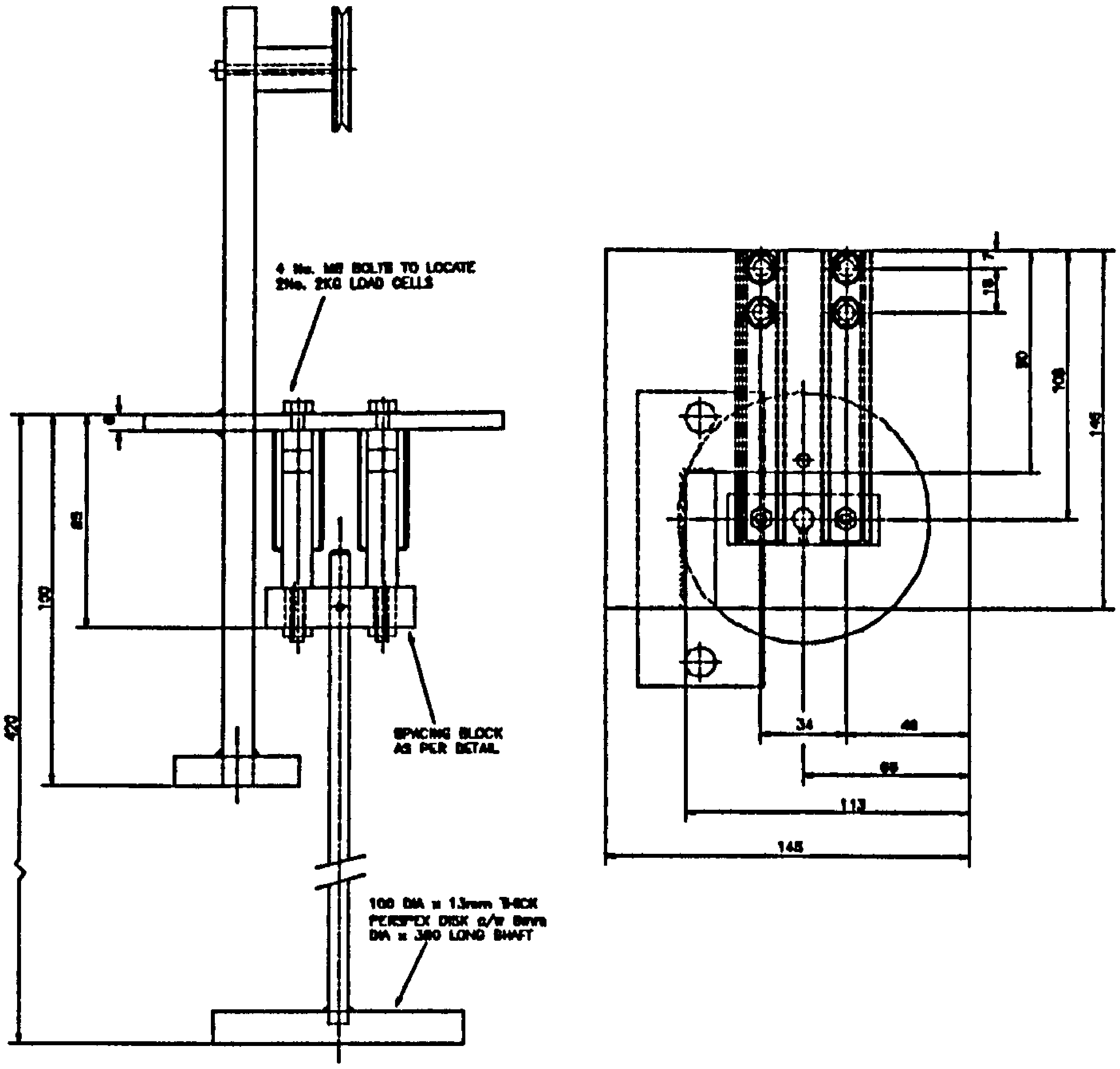

Figure 4.15: Two-phase Momentum Measurement Assembly

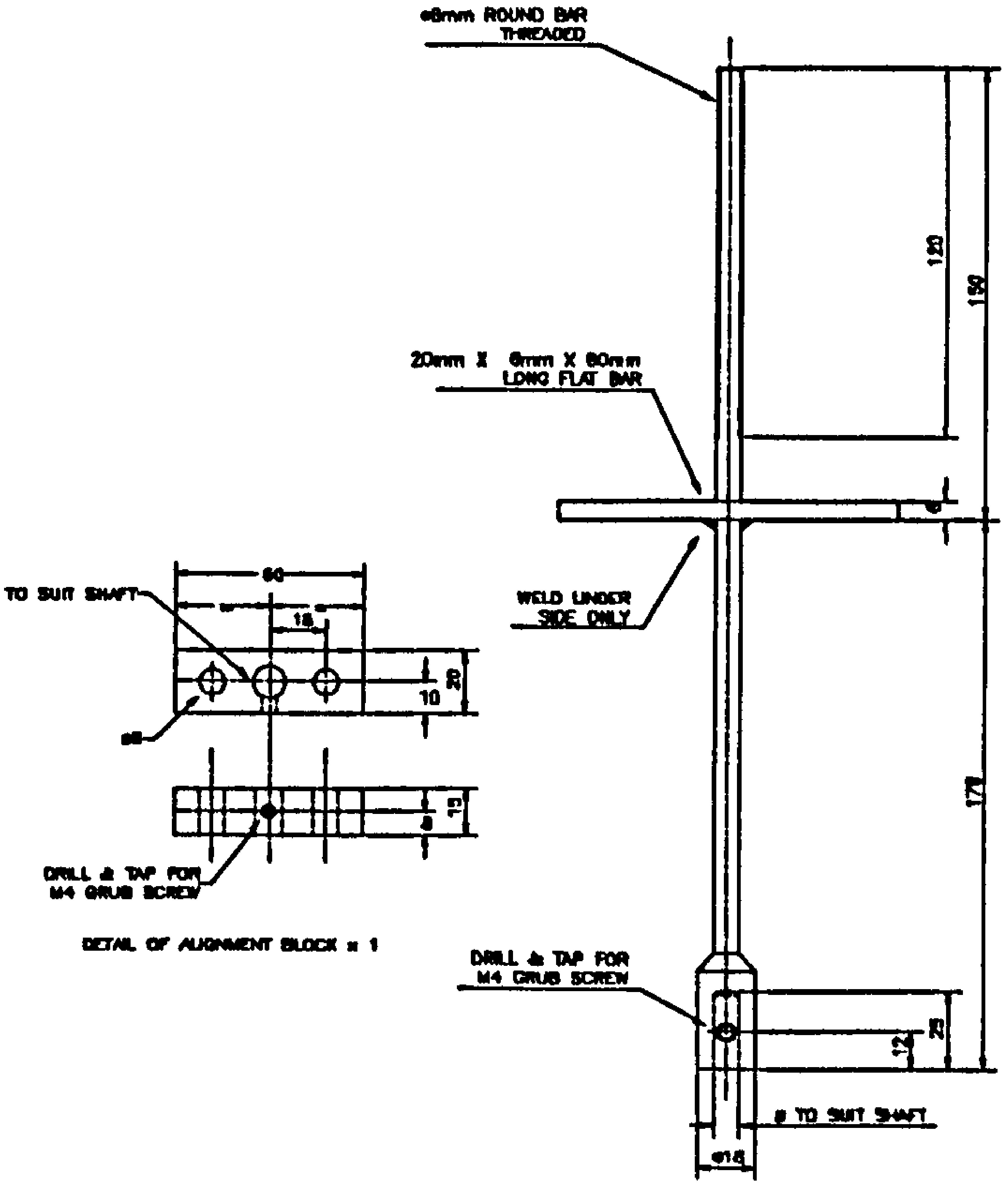

Figure 4.16: Weight Adapter

4.5.9 Experimental Recording of Momentum Data

The data acquisition system, described in Section 4.4, was used to log the experimental momentum flux results. For each experimental value of momentum flux, fifty load cell readings were recorded and averaged. A plot of momentum flux for an air-water and an air-glycerine flow at a quality of 0.4 are shown in Figure 4.18. The running averages indicate that around fifty readings are required to obtain reliable mean values.

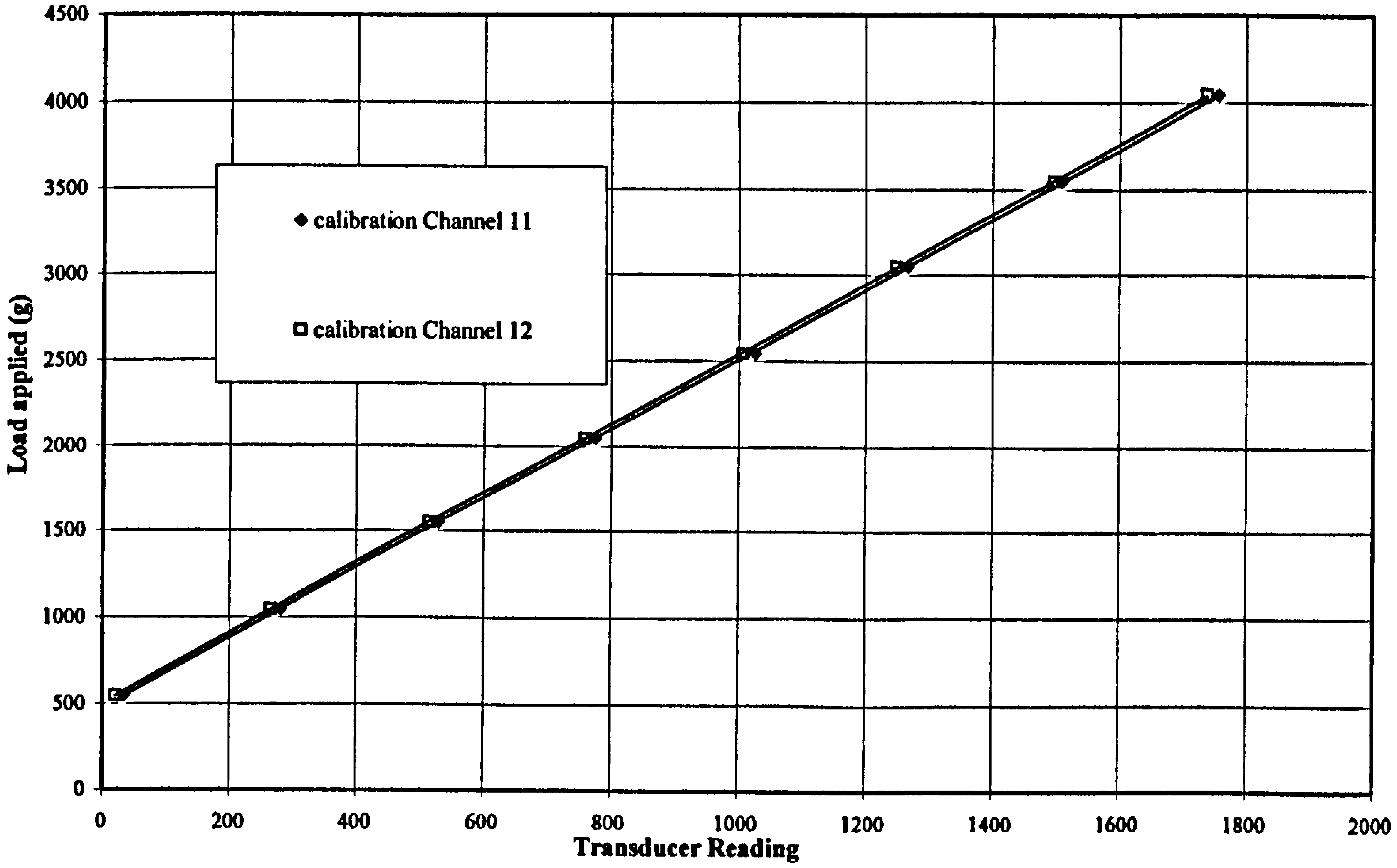

Figure 4.17: Typical Load Cell Calibration

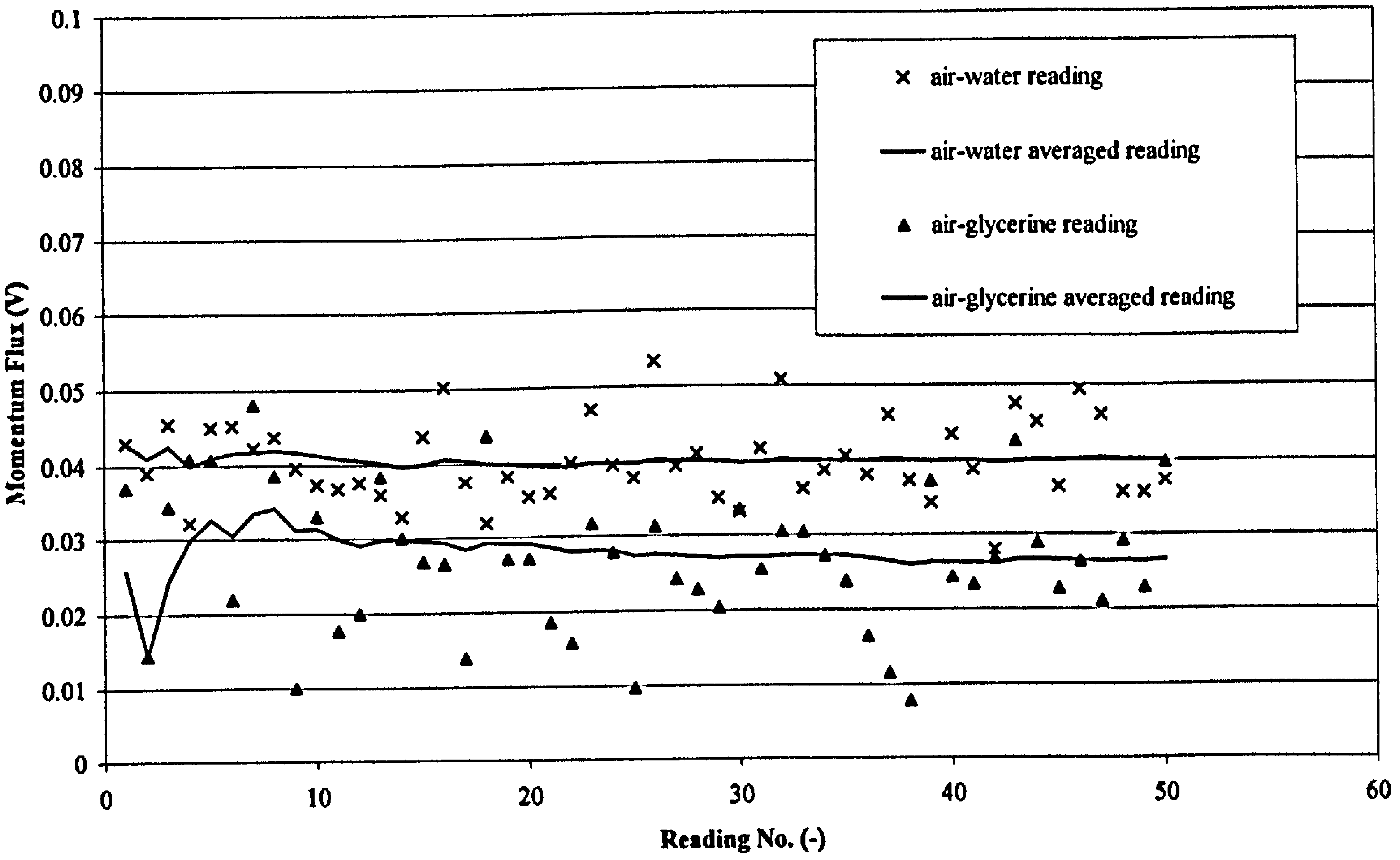

Figure 4.18: Typical Momentum Trace for a Two-Phase Flow Discharge

Chapter 5

EXPERIMENTAL PROCEDURES & COMMISSIONING TESTS

5.1 Introduction

The test facility, described in Chapter 3, and the instrumentation, described in Chapter 4, were used to obtain single and two-phase test data, the operation of which is detailed in four test procedures. The test procedures were developed in the validation stages of the test facility and were initially used to obtain single-phase air and water, and two-phase air-water commissioning test data. Modifications were then made to these test procedures to accommodate the more demanding two-phase highly viscous tests.

To drive the data acquisition system, all testing utilised a suite of software routines contained in a programme called TPF2 the flow diagram for which is given in Figure 5.1. Single and two-phase commissioning tests gave opportunity for the development of this programme allowing the validation of the test facility instrumentation when measuring local pressure, mass flow rate and momentum flux. Experimental data generated by TPF2 were reduced using a programme called Tp_Data_Creation.

5.2 Single-Phase Water Test Procedure

The single-phase water test procedure was used to record local pressures, liquid mass flow rates, momentum forces and the pressure drop across in-line components.

Test liquid temperature fluctuations were not recorded as these were considered too small to effect results.

5.2.1 Defining Test Specific Operating Parameters

Prior to any test, the user, by means of a series of menus in TPF2, selected and entered the appropriate operating parameters. These selections were choice of test liquid, water or aqueous glycerine solution, flow nozzle 1,2,3 or 4 and date of test. To instigate a test the software was then instructed, via menu three, as to what signals to record and the sampling rate to use. The options in menu three indicated the operating status of the channels on the data acquisition control unit. Figure 4.1 provides a schematic of the test facility and instrumentation. The data acquisition system channel designation is given in Table 4.5. To initiate the appropriate channels for a typical single-phase test, involving the measurement of liquid mass flow rate, momentum force, ten local pressures and the differential pressure across an in-line test component, required selections in menu three as shown in Table 5.1.

Option	Designation	Setting
1	Flow measurement (ch 7)	ON
2	Momentum measurement, load cell one (ch 11)	ON
3	Momentum measurement, load cell two (ch 12)	ON
4	No of local pressure points (ch 4)	10
5	Number of local pressure samples (ch 4)	50
6	Number of flow and momentum samples (ch 7, 11 & 12)	50
10	Read component pressure drop (ch 2)	ON

Table 5.1: Menu Three Options, TPF2 Single-Phase Tests.

Figure 5.1: Flow Diagram for TPF2

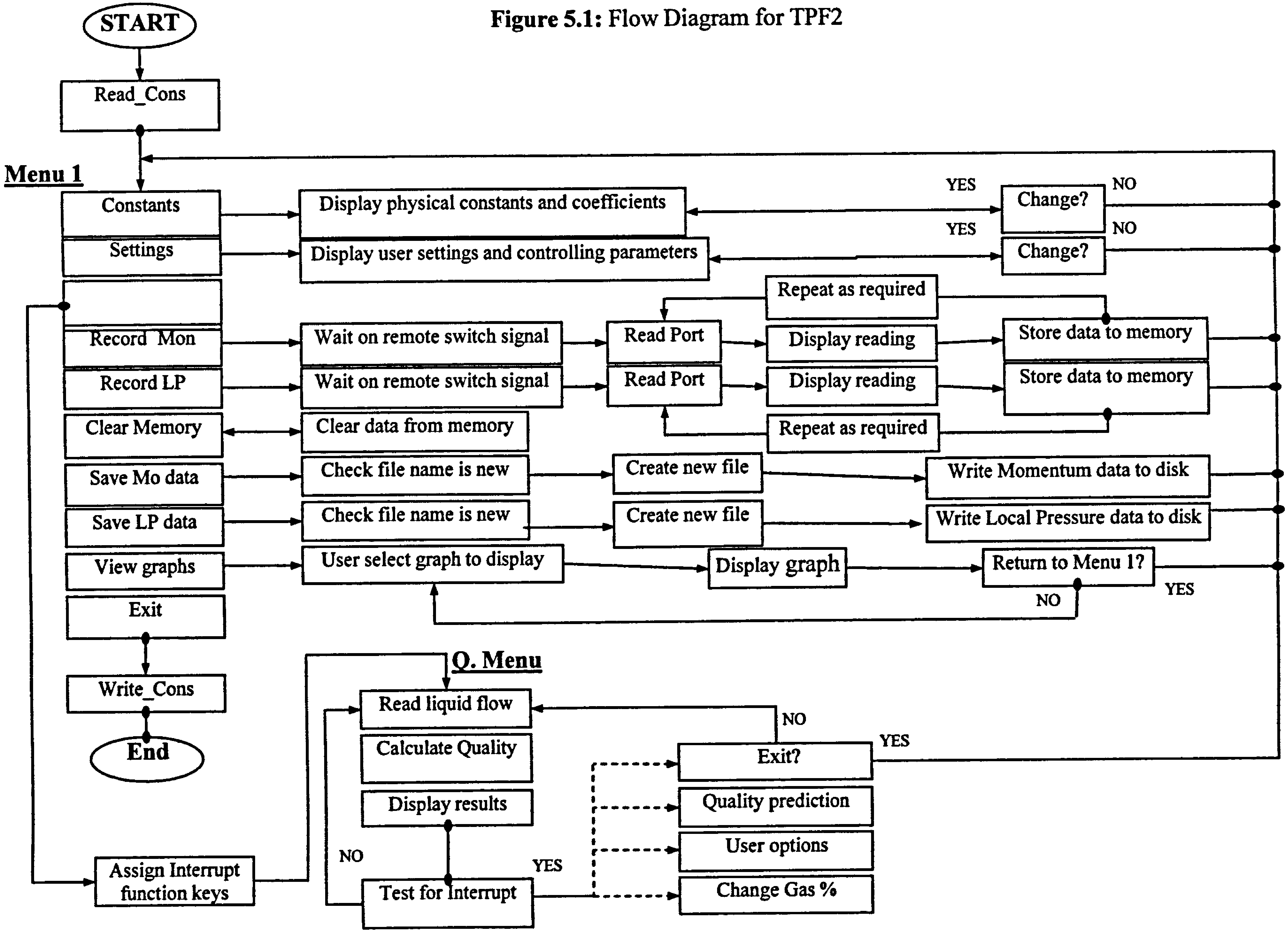

5.2.2 Establishing a Single-Phase Flow

After priming TPF2 for the single-phase test, a single-phase flow was then established in the test facility. This was accomplished by closing valve B and opening valves A, and C, see Figure 3.1. One of the four flow nozzles was selected by closing all the control valves immediately upstream of all other flow nozzles. The pump was then started and by slowly closing valve A, restricting the flow through the by-pass loop, a single-phase flow was directed into the test section. The upper range values or URVs' for the flow and the local pressure transducers were then set using the HART communicator. For the URV of the flow pressure transducer see Table 4.6. The URV for the local pressure transducer was set to 10% higher than the highest local pressure present in the test section at the time of test.

5.2.3 Recording Flow Rate and Momentum Data

After the single-phase flow was established, the flow rate pressure signal transducer was bled. The flow rate and momentum values were then recorded by selecting option four from menu one, 'Record flow & momentum data'. A minimum settling time of thirty seconds was observed to allow steady state conditions to be reached and then the sampling was started. After the flow and momentum channels were sampled all data was retained in the PC memory.

5.2.4 Recording Local Pressure Data

Option five was selected from menu one, 'Record local pressure values'. Before the sampling was started with the remote switch, the liquid purge valve on the local pressure line was opened, see Figure3.2. With this valve open every local ¼" ball valve was opened in turn flushing any air from the pressure line and taps. The purge valve was then closed and the first ¼" ball valve on the pressure line of the test section opened. The remote switch was used to instruct TPF2 routine to sample the local pressure. When the local pressure had been sampled indication was given on the PC display. This valve was then closed and the next valve on the pressure line opened and the procedure with the remote switch repeated. In this all way ten local pressure values were sampled along the test section.

5.2.5 Recording In-line Component Pressure Drop Data

The pressure drop across either the in-line orifice plate or nozzle, was recorded using option ten on menu three of the TPF2 software. In-line component pressure drops were sampled as part of the local pressures sampling routine. For example if ten local pressures and an in-line component pressure drop were required this function was set to 'ON' and the number of local pressure drops was set to eleven. See example given in Table 5.1. Once the local pressure drop sampling routine was started the eleventh sample was made from channel two instead of channel four i.e., the last local pressure sample was read from the differential pressure transducer across the in-line component at high level and not the local pressure transducer.

5.2.6 Recording Discharge Component Pressure Drop Data

When either the nozzle or orifice plate discharge components, were fitted to the end of the test section the local pressure was read at a location 122 mm upstream of the discharge component exit. This pressure tap was connected to the common pressure line in the same way as all the pressure taps on the test section. Subsequently the pressure at this location was measured in the same way as the pressure at all other locations on the test section as described in Section 5.2.4.

Similarly an additional pressure tap on the discharge orifice plate, located at 25 mm upstream of the orifice, was connected to the common pressure line and the local pressure measured as per Section 5.2.4.

5.2.7 Creating a Data File for Test Data Transfer

To write accumulated test data to file, option eight from menu one, 'Save data', was selected. The user was prompted for a data tag for the file. The tag was three characters in length. The save routine automatically generated a file name using the data tag and the test date. The file was saved in ASCII format suitable for transfer to another PC based system for analysis.

5.3 Processing Test Data

5.3.1 Extracting Data from Test Files and Calculating Mean Values

The data files generated by TPF2 were transported from the lab computer to another PC for processing. A programme called Tp_Data_Creation was developed in FORTRAN. This extracted the experimental data from the TPF2 generated files and automatically calculated the mean value of liquid mass flow rate, local pressures, and in-line test component differential pressures, from the sampled values. A flow diagram is given in Figure 5.2 for Tp_Data_Creation. The test conditions and mean values were written to a master file by Tp_Data_Creation, the contents of which were interrogated by various Microsoft Excel based spreadsheets during analyses.

5.3.2 Converting Voltage Pressure Data to Pascals

The mean local pressure and liquid mass flow rate values sampled by the data acquisition system were stored as voltages. After extracting the data from TPF2 test files using Tp_Data_Creation, these voltages were converted to their Pascal equivalents by using Equation 5.1:

$$p = \tfrac{1}{4}URV(V-1) \tag{5.1}$$

where 'V' is the mean pressure value in volts and the URV is the upper range value that was set on the pressure transducer used to record the pressure. For the liquid mass flow rate readings, URV values are given in Table 4.6. For the local pressure transducer readings the URV values were recorded along with the test data by the TPF2 program. A derivation of Equation 5.1 is given in Appendix B.

5.3.3 Correcting Local Pressure for Vertical Orientation

The pressure transducer used to measure the local pressures along the test section was located near the in-line test component just over one metre from the start of the test section. The vertical orientation of the test section meant that the recorded local pressure values needed to be corrected for the effect of the gravitational pressure gradient.

Local pressure values were corrected by adding the product of the height difference between the local pressure transducer and the location of the local pressure tap and gravitational pressure gradient. The gravitational pressure correction was calculated from the gravitational constant and the test liquid density. Table 5.2 gives the test liquid densities for water, and the three nominal viscosities of the aqueous glycerine solution. For local pressure taps located below the local pressure transducer the gravitational pressure correction was positive and for local pressure points located above the local pressure transducer the gravitational pressure correction was negative.

To assist in the processing of the test data, local pressure taps were identified by their relative position to the lowest or first local pressure point on the test section. Figure 3.2 gives the positions of all the local pressure taps. Table 5.3 gives the relative positions of all local pressure taps to the first local pressure tap. The 'PT' value in Table 5.3 is the relative position of the pressure transducer to the first local pressure tap.

	Water	**Glycerine 550 mPas**	**Glycerine 200 mPas**	**Glycerine 50 mPas**
Density (Kg/m^3)	1000	1260	1235	1190

Table 5.2: Test Liquid Density

	1	**2**	**3**	**4**	**5**	**6**	**PT**	**7**	**8**	**9**	**10**	**11**	**12**
Position (m)	0.00	0.25	0.50	0.75	1.00	1.40	1.49	1.90	2.40	2.90	3.40	3.96	4.098

Table 5.3: Positions for Local Pressure Correction

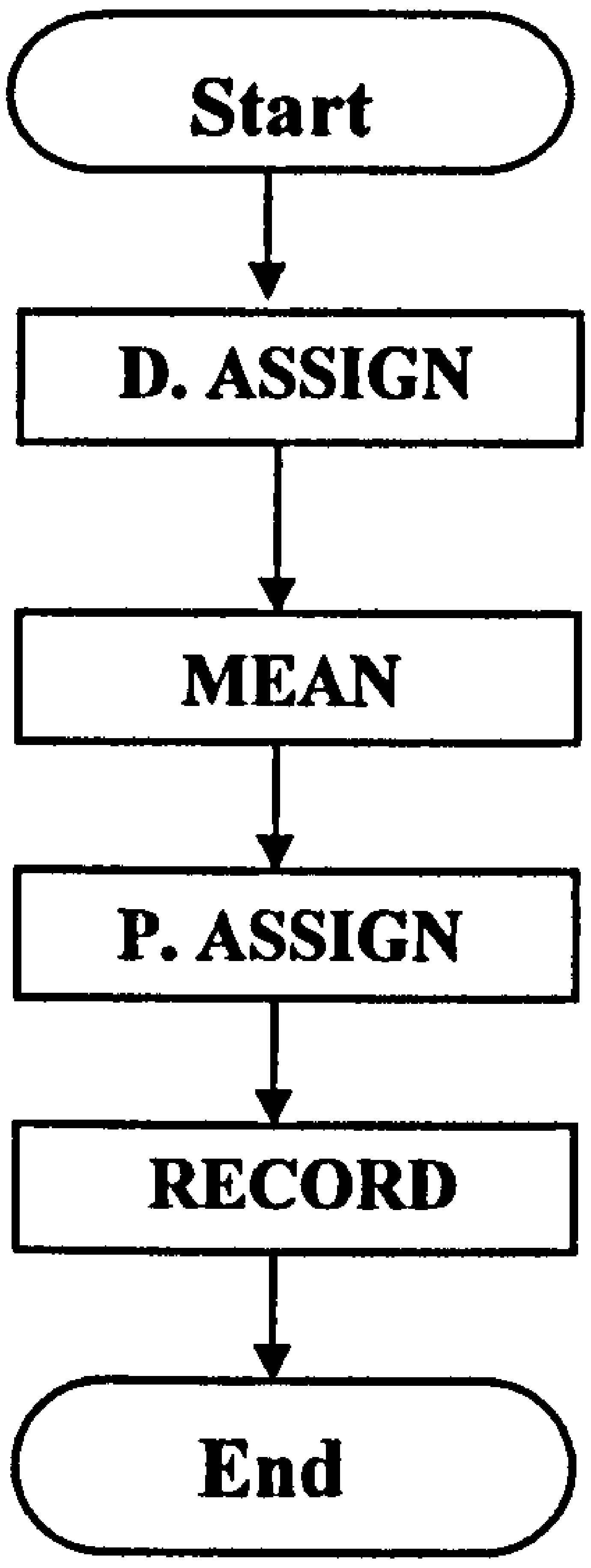

Read test data file and assign to an array

Calculate mean values for liquid mass flow, momentum, local pressure values and void fraction data.

Read test data file and assign test operating parameters to an array

Save mean and values and test operating parameters to data file.

Figure 5.2: Flow Diagram for TP_Data_Creation

5.4 Single-Phase Water Commissioning Test

Two single-phase water commissioning test were completed using the data acquisition system as described in Section 4.4 and the single-phase test procedure described in Section 5.2. Before analyses, the data was processed using the methods described in Section 5.3.

5.4.1 Single-Phase Water Pipe Friction

Ten local pressures were measured along the test section for a range of liquid mass flow rates. The friction factor, f_l, of a highly turbulent flow was calculated from the Reynolds number using the Blasius equation:

$$f_l = \frac{0.079}{\mathrm{Re}_l^{0.25}} \tag{5.2}$$

The experimental friction factor was found from the pressure gradient developed in a uniform length of pipe. From Equation 2.2 the experimental friction factor is related to the pressure gradient and volume flow rate by:

$$f_l = -\frac{\pi^2 D^5}{32 Q_l^2}\left(g + \frac{1}{\rho_l}\frac{dp}{dz}\right) \tag{5.3}$$

Experimentally the pressure gradient was found from a 'best fit' line to the local pressures measured in the test section. Figure 5.3 shows a typical example of local pressure plotted against position along the test section, for a water only flow.

To verify the ability of the test facility to accurately measure the liquid mass flow rate and local pressures along the test section, the friction factor was determined experimentally for a range of volume flow rates. As can be seen in Figure 5.4 reasonable agreement, to with in ±10%, was obtained when comparing the Blasius correlation against experimental friction factors.

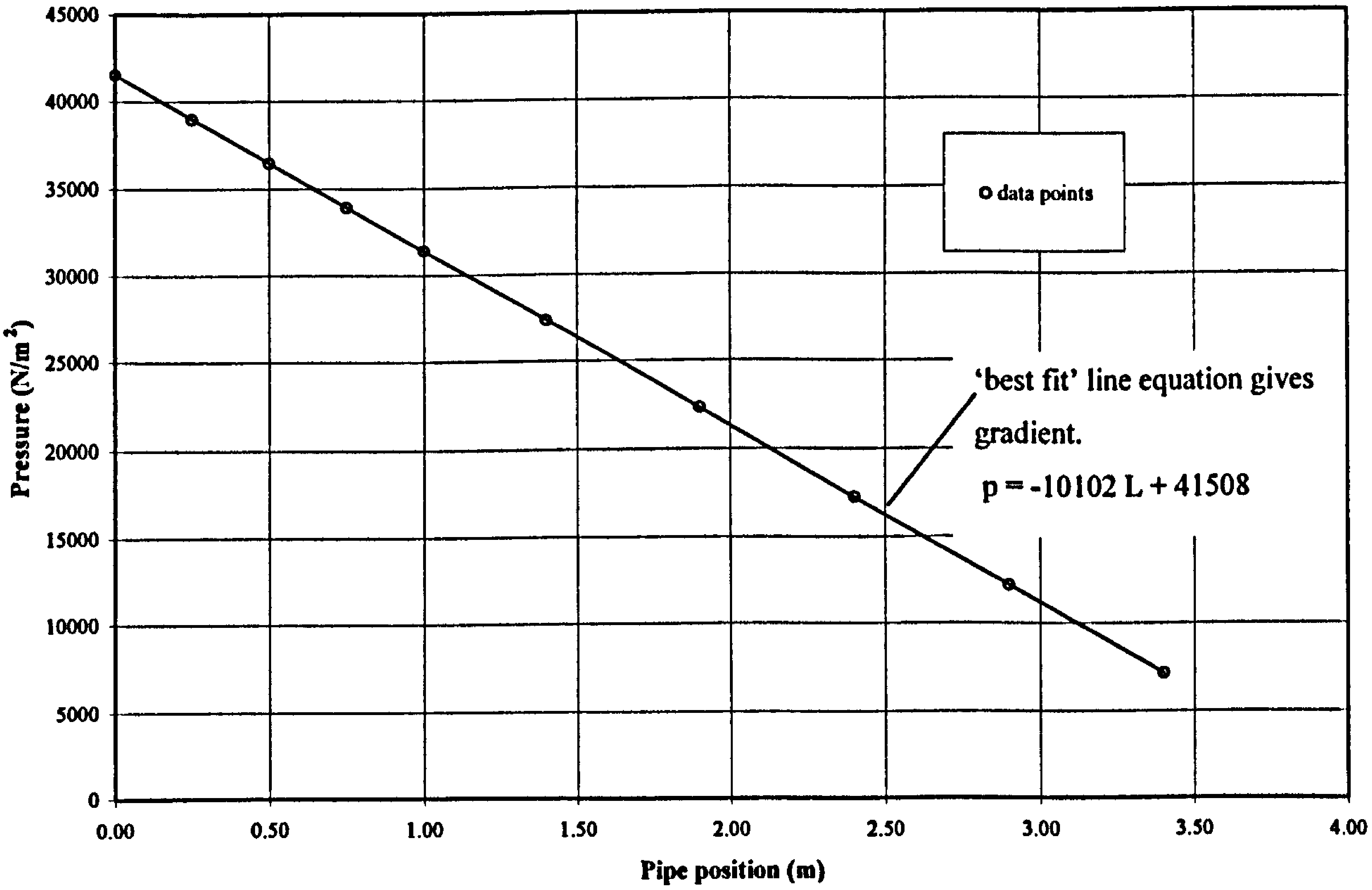

Figure 5.3: Typical Water Only Pressure Distribution

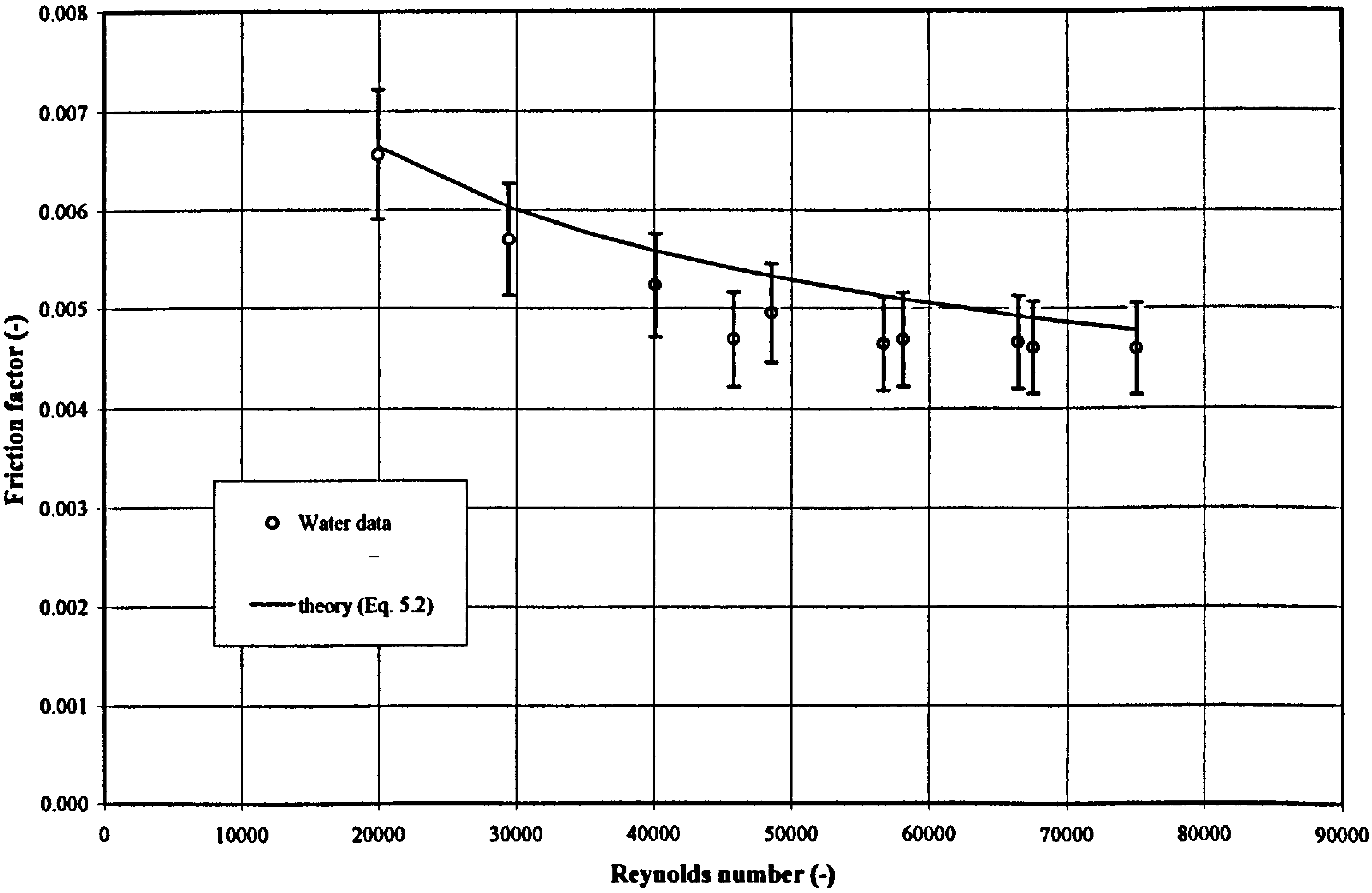

Figure 5.4: Comparison of Water Friction Factor with Blasius Correlation

5.4.2 Single-Phase Water Pipe Discharge

To test the reliability of the system devised to measure the momentum flux of jets discharging from the test length, as described in Section 4.5.2, a second water only commissioning test was carried out. With the pipe discharge component in place, the force on the discharge plate was recorded for a range of flow rates. The theoretical momentum correction factor C_m for turbulent flows is 1.02. The apparent jet force was calculated from;

$$J_{AP} = Mu_l \qquad (5.4)$$

where M and u_l are the mass flow rate and velocity of the discharge jet respectively. The experimental C_m was found to be 1.03 and is depicted in the graph of Figure 5.5.

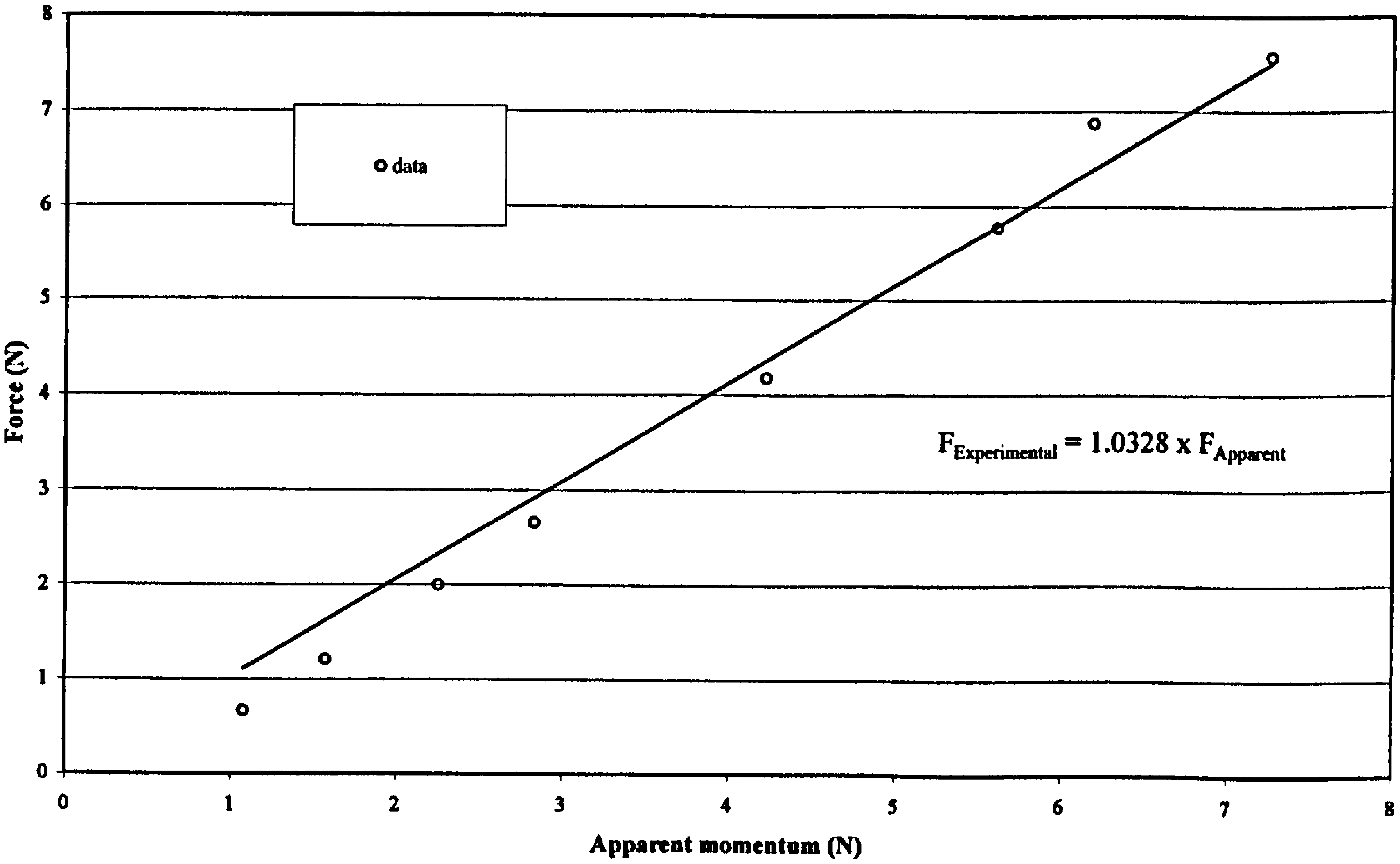

Figure 5.5: Water Momentum Measurements

Difficulty was experienced in obtaining good experimental agreement with theory for the momentum correction factor. It was discovered that the distance to the target upon which the discharging jet impinges from the pipe exit was an important factor. The target also needed to be carefully aligned with the centre line of the pipe exit. A series of pipe discharge tests were performed in order to establish the appropriate position of the target. For single-phase water tests the target position was determined to be 80 mm above the discharge component exit.

5.5 Single-Phase Aqueous Glycerine Solution Test Procedure

The single-phase aqueous glycerine solutions were tested using the same procedure that was used for the single-phase water tests, as described in Section 5.2. When the single-phase water only procedure was used for aqueous glycerine solutions, three further operations were required:

1. Prior to running the single-phase test a sample from the test liquid was taken and the viscosity of the test liquid was measured, as described in Section 4.2.2.
2. The density of the test liquid was measured, as described in Section 4.2.3.
3. During single-phase tests the temperature of the test liquid was monitored. The heat exchanger was used to control the test liquid temperature to an accuracy of ± 2 C^{o}.

5.6 Single-Phase Aqueous Glycerine Solution Commissioning Test

Three single-phase aqueous glycerine solution commissioning tests', at the nominal viscosities of 550, 200 and 50 mPas, were completed. The data acquisition system as described in Section 4.4, the single-phase aqueous glycerine test procedure described in Section 5.5 and the data reduction methods described in Section 5.3 were used. Momentum flux was not measured for glycerine single-phase tests as the forces involved were too small.

5.6.1 Single-Phase Aqueous Glycerine Solution Pipe Friction

Ten local pressures were measured along the test section for a range of liquid mass flow rates. The theoretical friction factor of a laminar flow can be calculated from the Reynolds number using:

$$f_l = \frac{16}{\mathrm{Re}_l} \tag{5.5}$$

Similarly to the turbulent flows, described in Section 5.4.1, the experimental friction factor was found from the pressure gradient developed in the test section using Equation 5.3. The friction factor as a function of the Reynolds number for the aqueous glycerine solution tests is shown in Figure 5.6. The variation of experimental with theoretical friction factor was ±5%.

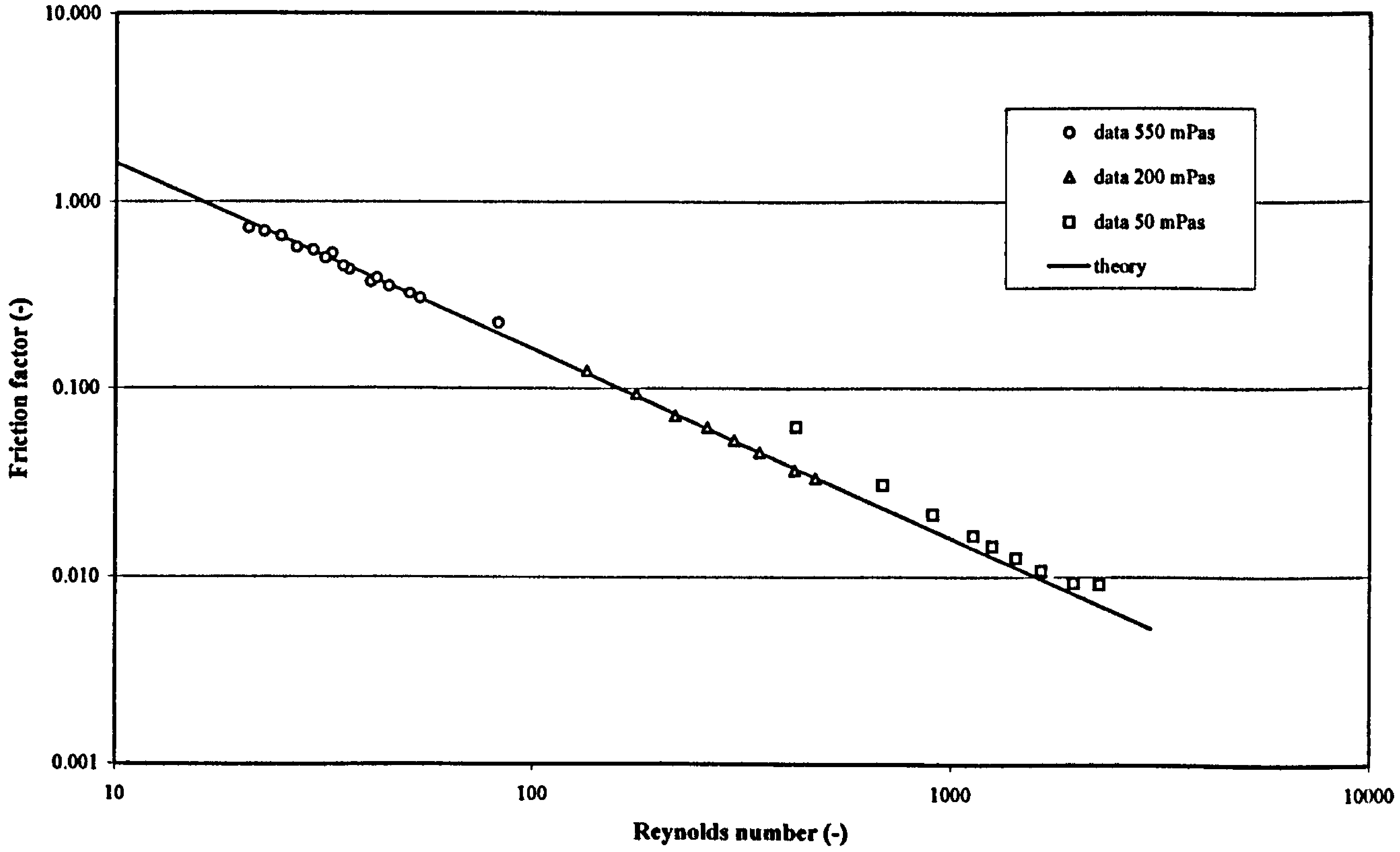

Figure 5.6: Comparison of Glycerine Friction Factors with Laminar Theory

5.7 Single-Phase Air Test Procedure

The single-phase air tests were made using the procedure described in Section 5.2 for water tests. The procedure differed only in the requirement to record the test temperatures at the air rotameters and at the beginning of the test section.

5.8 Single-Phase Air Commissioning Tests

For the air commissioning tests, the data acquisition system as described in Section 4.4, the single-phase air test procedure described in Section 5.7 and the data reduction methods described in Section 5.3 were used.

5.8.1 Single-Phase Air Pipe Friction

For the single-phase air tests the test section was isolated from the by-pass and calibration loop by closing valve C, Figure 3.1. All water was drained from the test section and air from the air receiver was passed through the test loop for a drying period of 30 minutes.

A Fanno flow test was then conducted by passing air through the test loop, recording the air mass flow rate registered by the air rotameters and measuring the local pressure at each of the ten pressure taps on the test section. This was repeated for a range of air mass flow rates. To ensure that the air flows discharging from the test section were under sonic conditions, a pressure transducer was connected to a pressure tap located 5 mm from the end of the pipe discharge component. Air mass flow rates were adjusted accordingly so that the exit pressure of the discharging air was substantially above atmospheric.

Fanno flow theory allows the Mach number, Ma, at any point, L_c, upstream of a sonic discharge to be related through:-

$$4\frac{f_g L_c}{d_t}=\frac{\left(1-Ma_u^2\right)}{\gamma Ma_u^2}+\frac{(\gamma+1)}{2\gamma}\ln\left[\frac{\left(\frac{\gamma+1}{2}\right)Ma_u^2}{1+\left(\frac{\gamma-1}{2}\right)Ma_u^2}\right] \tag{5.6}$$

where f_g is the gas friction factor, γ is the isentropic index for air and subscript u denotes the upstream properties. As the stagnation conditions at the entrance of the test length were known, it was possible to solve Equation 5.6 for the Mach number using a Newton-Raphson derived iterative process. Assuming that the local pressure measured at the most upstream point is accurate, all subsequent local pressures, p_u, were calculated using:-

$$p=p_u\frac{Ma}{Ma_u}\left[\frac{1+\frac{(\gamma-1)}{2}Ma^2}{1+\frac{(\gamma+1)}{2}Ma_u^2}\right]^{\frac{1}{2}} \tag{5.7}$$

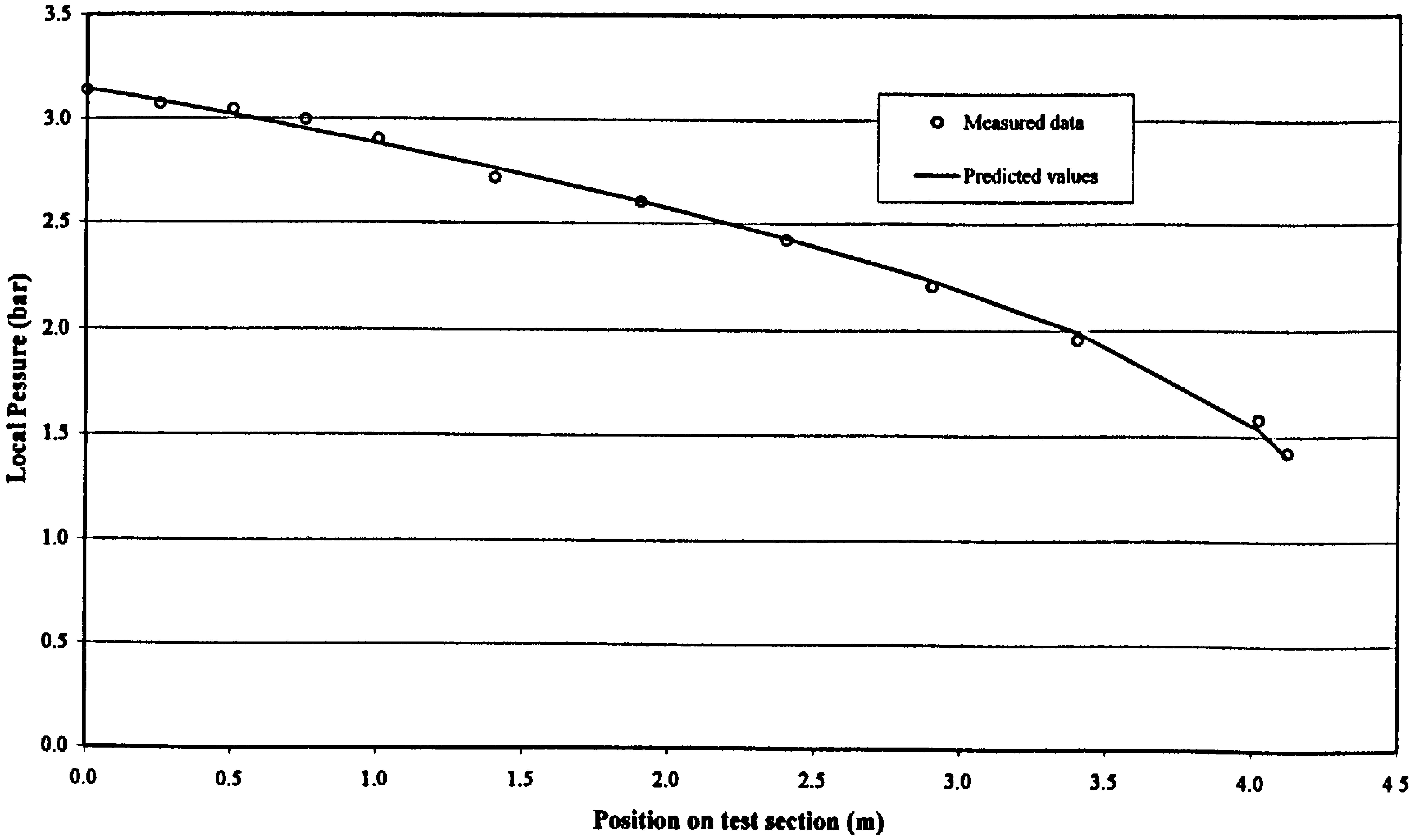

Figure 5.7: Air-Only Pressure Distribution

Figure 5.7 shows a graph of local pressure against distance along the test length. The predicted values were obtained by fitting Equations 5.6 & 5.7 to the experimental data. This involved determining friction factors that resulted in the minimum root mean square errors between the measured and predicted local pressures. Good agreement was obtained with the sonic test data when the empirical value of the friction factor, 0.00391 gave an upstream Mach number and pressure of 0.39 and 314 kN/m^2 respectively. To further validate the test data and justify the use of the iterative process, a comparison of experimental and predicted air mass flow rate was made. The predicted mass flow rate was found from:-

$$M = P_u \frac{\pi}{4} D_t^2 Ma_u \sqrt{\frac{\gamma}{RT_u}} \tag{5.8}$$

Good agreement was found between the measured mass flow rate of 0.267 kgs^{-1} and the predicted mass flow rate using Equation 5.8 of 0.266 kgs^{-1}.

5.9 Two-Phase Test Procedure

The method of logging test data for two-phase flows was similar to that of the single-phase procedure described above in Section 5.2. The procedure for two-phase tests was more complex as it involved monitoring the phase mass fluxes before and during tests, and collating both manually and electronically logged data. Although the two-phase tests shared the same data acquisition routines of TPF2 as the single-phase test procedures, additional test parameters were required so that the liquid and air mass fluxes could be monitored.

5.9.1 TPF2 Test Parameters Specific to Two-Phase Flows.

In addition to those test parameters described in Section 5.2.1 for single-phase flows, two-phase tests also required the user to supply the rotameter or rotameters in use, the nominal quality being measured, the temperature of the liquid and air phases, the test liquid being used, and the upper range value for the local pressure transducer. For a description of temperature measurement and the air rotameters see Sections 4.2.4 and 4.2.5 respectively.

5.9.2 Establishing a Two-Phase Flow

The range of two-phase flows encountered in this research were predominately in the annular flow regime. As a result, the procedure described here lead to the quick establishment of an annular flow regime in the test section minimising the length of time spent in the slugging regime. This was desirable since slugging forces can be destructive.

The same method described in Section 5.2.2 was used to establish the required nominal liquid flow rate required. All valves downstream of the air-rotameters on the air supply were closed when the compressor was started. An important check made prior to turning on the compressor was that the flow from the compressor to the air receiver was clear and all valves on route to the air receiver were open. If the test liquid was an aqueous glycerine solution the extraction fan, described in Section 3.4.9, was switched on before any air was allowed to flow through the test section. With the compressor running the air-receiver was charged to a working gauge pressure of 7.5 bar. The gate valve controlling the air flow rate through rotameter two was then opened to give a reading of approximately 30% of maximum flow. If smaller flow rates of air was introduced, or if the valve was opened too slowly, slugging occurred. After a flow of air was established in the test section, a back-pressure was generated against the delivery of the liquid phase. This was compensated for by further closure of valve A, increasing the pressure on the liquid side. By gradually increasing the air flow rate, while maintaining the liquid flow with the operation of valve A, the desired mass flow rate of air and liquid was achieved.

Once a two-phase flow was present in the test section, the flow pressure transducer was bled to allow any air that had worked its way into the liquid side to escape.

5.9.3 Monitoring Two-Phase Flow Mass Fluxes

As the majority of two-phase test required specific test qualities and mass fluxes to be present, it was important that these test parameters could be monitored prior to recording test data. A routine, option three from menu one of TPF2, 'Monitor Quality', was developed for this purpose. This routine relied on the user supplying discharge coefficients for the flow nozzles and viscosities for the test liquids. For a description of viscosity measurement and the calibration of flow nozzles see Sections 4.2.2 & 4.5.3 respectively. A menu invoked through the routine was used to instruct the software as to the percentage flows on the air rotameters. This menu also allowed the user to enter the air-phase temperature and select the flow nozzle in operation. With this information, the routine proceeded to sample the flow pressure transducer and calculate the liquid and air phase mass fluxes. These values were displayed and the user could instruct the software to calculate the required changes in air or liquid mass flow rates to achieve the desired quality. When aqueous glycerine test liquids were used this routine also incorporated an iteration process to resolve the viscosity, Reynolds number and discharge coefficient relationship.

Once the desired quality and mass fluxes had been achieved the monitoring routine was exited.

5.9.4 Recording Void Fraction Data

The data acquisition programme, TPF2, automatically recorded all user defined operating parameters on exit. This feature enabled the user to exit TPF2 after establishing the desired two-phase mass fluxes, and record the void fraction using the procedure described in Section 4.3.3. After recording the void fraction TPF2 was re-invoked and all user parameters were reinstated from file.

5.9.5 Recording Flow Rate, Momentum and Local Pressure Data

The methods for recording liquid flow rate, momentum force and local pressure for two-phase flows, were the same as those described in Sections 5.2.3 & 5.2.4 for single-phase flows. An additional complication of recording two-phase local pressure drops was the need to purge the pressure taps between recording the local pressure values. This was achieved by opening the purge valve to the liquid side to flush the pressure tap between every local pressure reading.

5.9.6 Recording In-line & Discharge Component Pressure Drop Data

The same procedures, as described in Sections 5.2.5 & 5.2.6 for the recording of in-line and discharge component pressure drops for single-phase water tests, were used for two-phase tests.

5.9.7 Creating a Data File for Test Data Transfer

At the end of a two-phase test, option eight from menu one was used to save the test operating parameters and test data to file, see Section 5.2.7.

5.10 Complications Specific to the Recording of Highly-Viscous Two-Phase Data

The use of an aqueous glycerine test liquid presented difficulties that were not wholly predicted on the outset of this research. These difficulties effected the methodology adopted to retrieve experimental data, and dictated to some extent the speed at which data could be generated. Broadly speaking, there were three major issues associated with the use of the aqueous glycerine test liquid. These were:-

1. The continually changing viscosity due to the hygroscopic nature of glycerine.
2. The production of fine mist during two-phase glycerine tests, possibly due to the water content of the compressor air.
3. The entrainment and disengagement of air from the aqueous glycerine test liquid during two-phase tests.

5.10.1 Controlling the Viscosity of the Aqueous Glycerine Test Liquid

In order to remove unwanted moisture from the glycerine test liquid, immersion heaters were used to elevate the test liquid temperature for extended periods, usually over night. This process of moisture removal conflicted with the operating requirements of the test facility. A fifty minute cooling period was required, after the over night use of the immersion heaters, to return the test liquid to the test temperature prior to experimental work. Despite the use of immersion heaters the control of the test liquid viscosity was not entirely satisfactory as only a limited quantity of moisture could be removed from the test liquid. As a result the viscosity of the test liquid altered significantly over the course of the highly viscous tests. For example the 550 mPas nominal viscosity test liquid varied from 750 through to 420 mPas.

5.10.2 Extraction of Glycerine Laden Air

For reasons not completely understood, the mixing of air with the aqueous glycerine test liquid generated a glycerine mist at the separator discharge. The presence of the mist was difficult to observe at the test section discharge as the view through the sight glass was obscured by the discharging liquid-phase. The mist was clearly evident in the air phase as it exhausted from the three vents on top of the separation tank. The modifications, described in Section 3.4.9, were made so that the air-phase could be extracted to outside the building. Subsequently the range of liquid and air mass fluxes available that could be tested was limited by the performance of the venting system. The maximum mass fluxes that could be tested became subject to the maximum volume of air that the extraction fan could handle.

5.10.3 The Entrainment and Disengagement of the Air-phase

Many technical difficulties were encountered over the course of this project. The most challenging of these was the problems resulting from the entrainment of air in the viscous test liquid. These difficulties incurred the biggest time penalties, further protracting an already demanding test programme.

The biggest difficulty arose from the tendency of the air-phase to become entrained in the viscous liquid phase as this resulted in a down time to allow the entrained air to disengage. Section 3.4.4 describes the measures that were taken to minimise the opportunity for air to become entrained, and to accelerate the disengagement process i.e., the leaf slide and the immersion heaters. Despite these modifications, significant limitations were imposed on the length of time available to log data during a two-phase test. The test liquid could only be circulated once during a two-phase test after which it was required to stop the test and allow the entrained air to disengage. A window of about 15 minutes existed with in which all local pressures, mass flow rates, momentum flux values and void fraction measurements needed to be made. The time frame available for recording data was slightly longer for tests at higher qualities as the liquid mass fluxes were lower.

To accommodate the finite test time available to retrieve two-phase data, test procedures were optimised to speed up their execution. An optimum order of data recording was devised and a procedure that minimised the number of trips an operator made up the experimental stack during any one test was implemented, thus saving more time. Good practice was to establish the desired two-phase test conditions, record flow rate and momentum values, exit TPF2, record the void fraction readings, return to TPF2 and record local pressures and component pressure drops.

The settling out time allowing air to disengage from the test liquid was in the region of twelve hours. The installation of the immersion heaters in the two supply tanks, described in Section 3.4.4 reduced this disengagement time to around three hours. The immersion heaters in combination with the use of the heat exchangers, enabled a maximum of three tests a day to be completed.

5.11 Two-Phase Air-Water Commissioning Tests

Several two-phase air-water commissioning tests were done using the data acquisition system as described in Section 4.4, the two-phase test procedure described in Section 5.9 and the data reduction methods described in Section 5.3. To ensure that a subsonic process path was followed by all two-phase tests it was necessary to determine mass flow rates in advance that would give exit Mach numbers of about 0.4. Mass flow rates were calculated via application of the homogeneous flow model using air-water properties for the nominal qualities of 0.04, 0.06, 0.08, 0.1, 0.2, 0.4, 0.6 and 0.8.

5.11.1 Two-Phase Air-Water Local Pressure Recording Repeatability

To verify the methodology of Section 5.9 devised for recording two-phase test data, ten local pressures were recorded along the test length for air-water flows for the eight qualities noted above. The same water and air mass fluxes were then used to obtain a further two data sets for the same qualities.

By assuming the air-water pressure drop pipe data to be incompressible, acceleration effects could be treated as negligible, allowing the two-phase multiplier to be calculated from:

$$\frac{dp}{dz}=-\frac{g}{v}-\frac{2f_l}{D}(1-x)^2G^2v_l\phi_l^2 \tag{5.9}$$

where, *dp/dz* is the measured pressure gradient, v is the mixture specific volume. The liquid friction factor, f_l, was calculated from Equations 5.2 & 5.5 depending on the liquid only Reynolds number. The liquid only Reynolds number was evaluated using the properties of the test liquid and assuming that the test liquid travelled alone in the test section. Assuming a constant temperature for the gas i.e., the gas temperature measured at the air rotameter exit, the perfect gas law was used to calculate the air specific volume at the ten local pressure tap locations on the test section. This allowed a mean value for the air specific volume to be calculated, and therefore the air density, to be determined. Using the measured void fraction, α, the mixture specific volume was calculated from Equation 2.31.

A two-phase multiplier was calculated using the Friedel [50] correlation as given in Section 2.5.8 and is shown in Figure 5.8 along with the two other air-water data sets recorded to demonstrate repeatability. At the high qualities there is a large discrepancy between the experimental and correlated data but for the majority of the data Friedel [50] correlation describes the experimental data well.

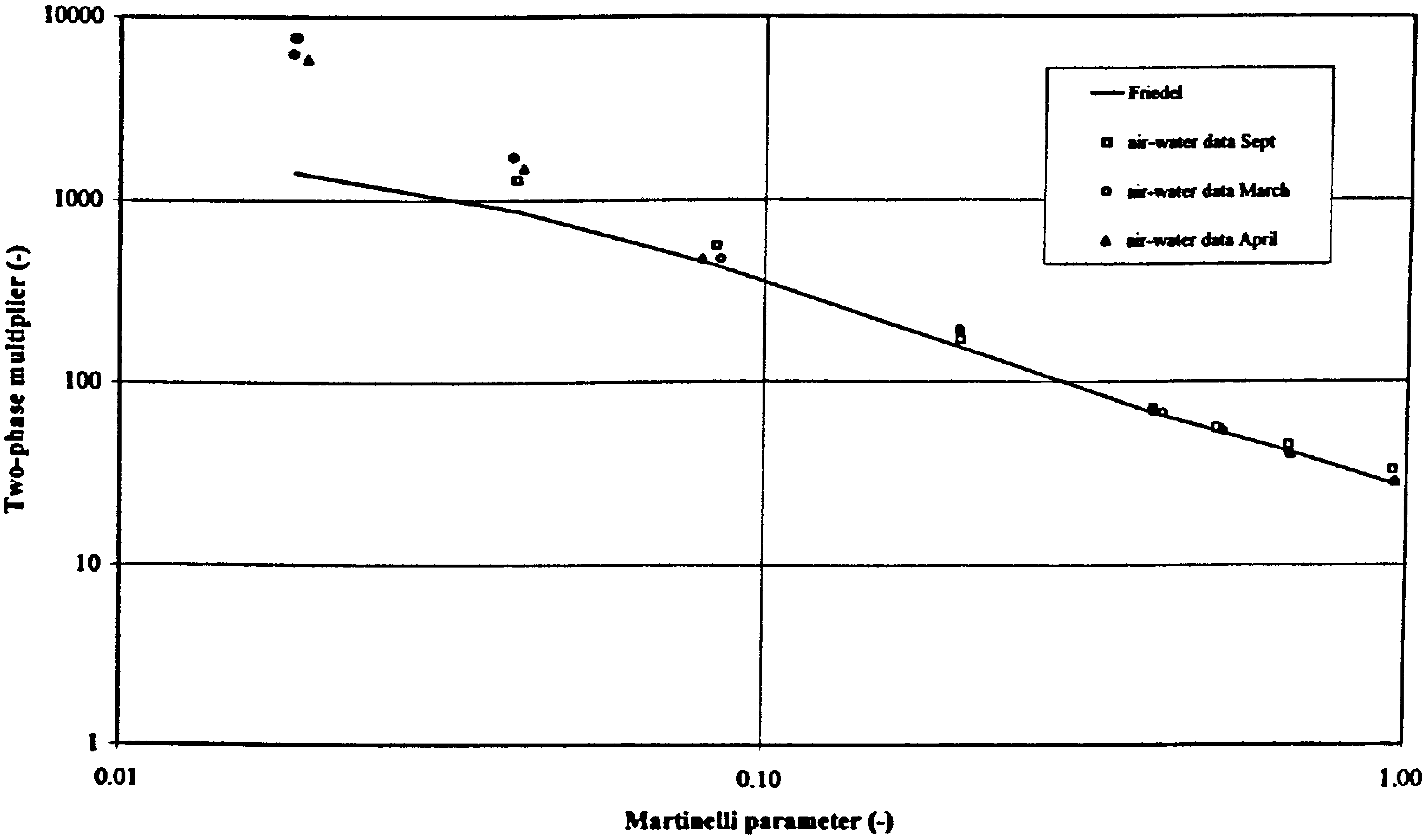

Figure 5.8: Comparison of Air-Water Data with Friedel [50] Correlation

To compare the experimental two-phase multiplier with the Chisholm [2] correlation given by Equation 2.40 and Table 2.1, the Martinelli parameter, X, was calculated using Equation 2.39. The air friction factor, f_g, was calculated from Equation 5.2 by evaluating a gas only Reynolds number using the properties of air and assuming that the air travelled alone in the test section, allowing the Martinelli parameter to be determined using:

$$X = \frac{(1-x)}{x}\sqrt{\frac{\rho_g f_l}{\rho_l f_g}} \tag{5.10}$$

As shown in Figure 5.9 reasonable agreement was found between the experimental two-phase multiplier and the Chisholm [2] correlation using a C value of 21.

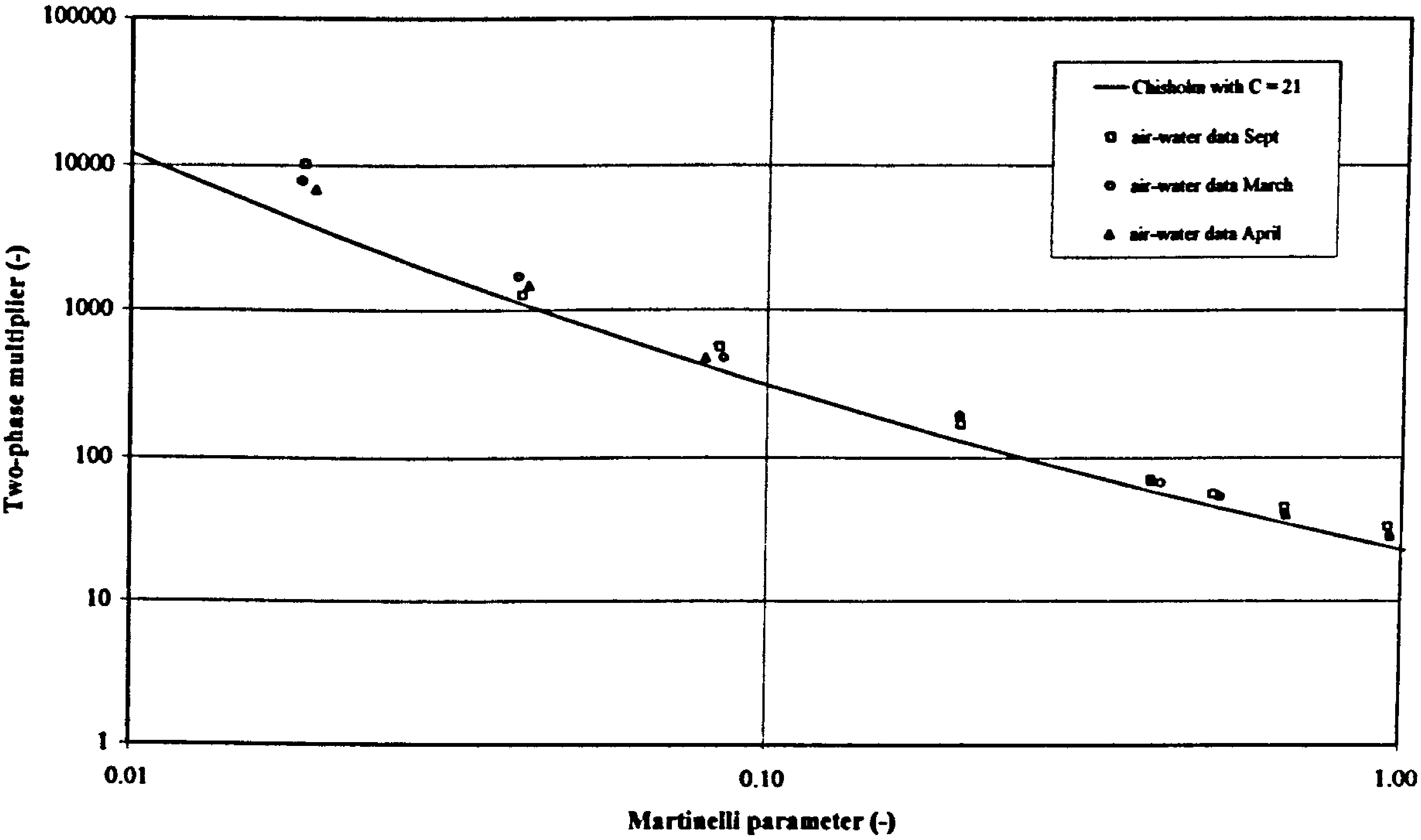

Figure 5.9: Comparison of Air-Water Data with Chisholm [2] Correlation

5.11.2 Two-Phase Air-Water Void Fraction Measurement

Void fraction measurements were made during the two-phase air-water tests of Section 5.11.1 the data are shown in Figure 5.10. Equation 4.3 was used to evaluate the measured void fraction from the test data. The homogeneous data was calculated using Equation 2.66 and the maximum slip data was calculated from Equation 2.21 using the value for maximum slip given by Equation 2.61.

As expected the measured void fraction data tends towards the homogeneous theory at the higher qualities and falls some where in middle of homogenous and the maximum slip values at the lower qualities.

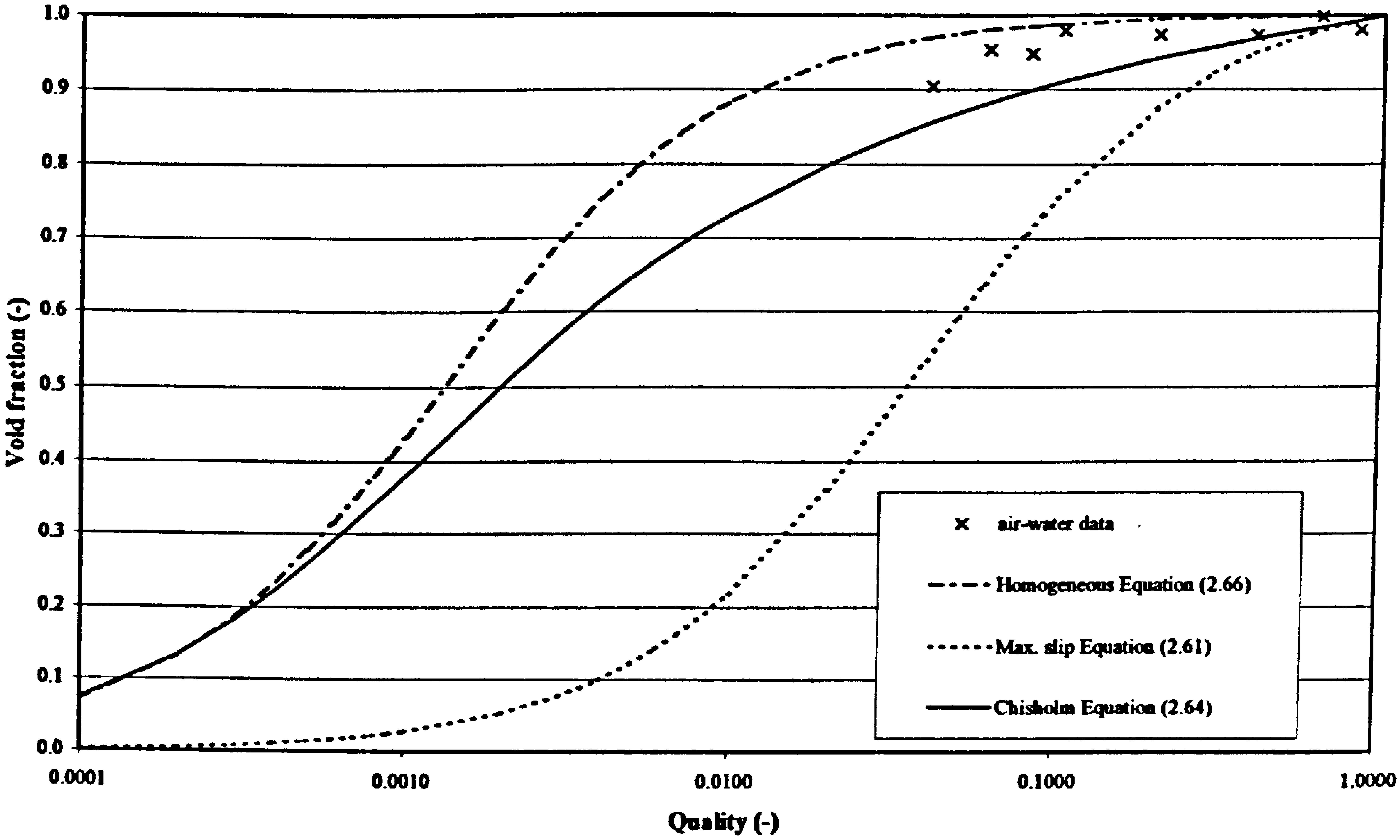

Figure 5.10: Air-Water Void Fraction Data

Chapter 6

EXPERIMENTAL DATA

6.1 Introduction

Single-phase experiments were performed to allow the determination of single-phase discharge loss coefficients. The procedure described in Section 5.2 was used for all single-phase tests.

Two-phase experiments were performed for a pipe length, in-line and discharge component geometries. In every instance of two-phase testing, the nominal qualities of 0.04, 0.06, 0.08, 0.1, 0.2, 0.4, 0.6 and 0.8 were used. All two-phase aqueous glycerine solution tests were repeated using air-water equivalent mass fluxes. The two-phase test procedure described in Section 5.9 and the void fraction method described in Section 4.3.3 were used for two-phase tests. Two-phase test data were processed as per the procedure described in Section 5.3.

6.2 Pipe Length Experiments

Two-phase pipe length experiments were carried out with the pipe spool piece installed in the test section and the pipe discharge component at the test section exit, Figure 3.2. Mass fluxes were selected to ensure subsonic process paths as per Section 5.11. In addition to air-water flows, three nominal viscosities of 550, 200 and 50 mPas were tested using aqueous glycerine solution.

6.2.1 Pipe Pressure Drop

The ten pressure taps along the test section were used to record the local pressure for the range of nominal qualities noted in Section 6.1. Figure 6.1 shows the local gauge pressure at each pressure tap location along the test length. All data start at a maximum pressure at the test length entrance and then tend towards atmospheric pressure at the test length exit. A marked difference can be seen between the pressure gradients of the low and high viscosity data. As the viscosity of the test liquid increases, so does the pressure gradient. This difference is most pronounced when comparing the air-water to the 550 mPas nominal viscosity test liquid data, where the difference in test length entrance pressures is in the region of 500%.

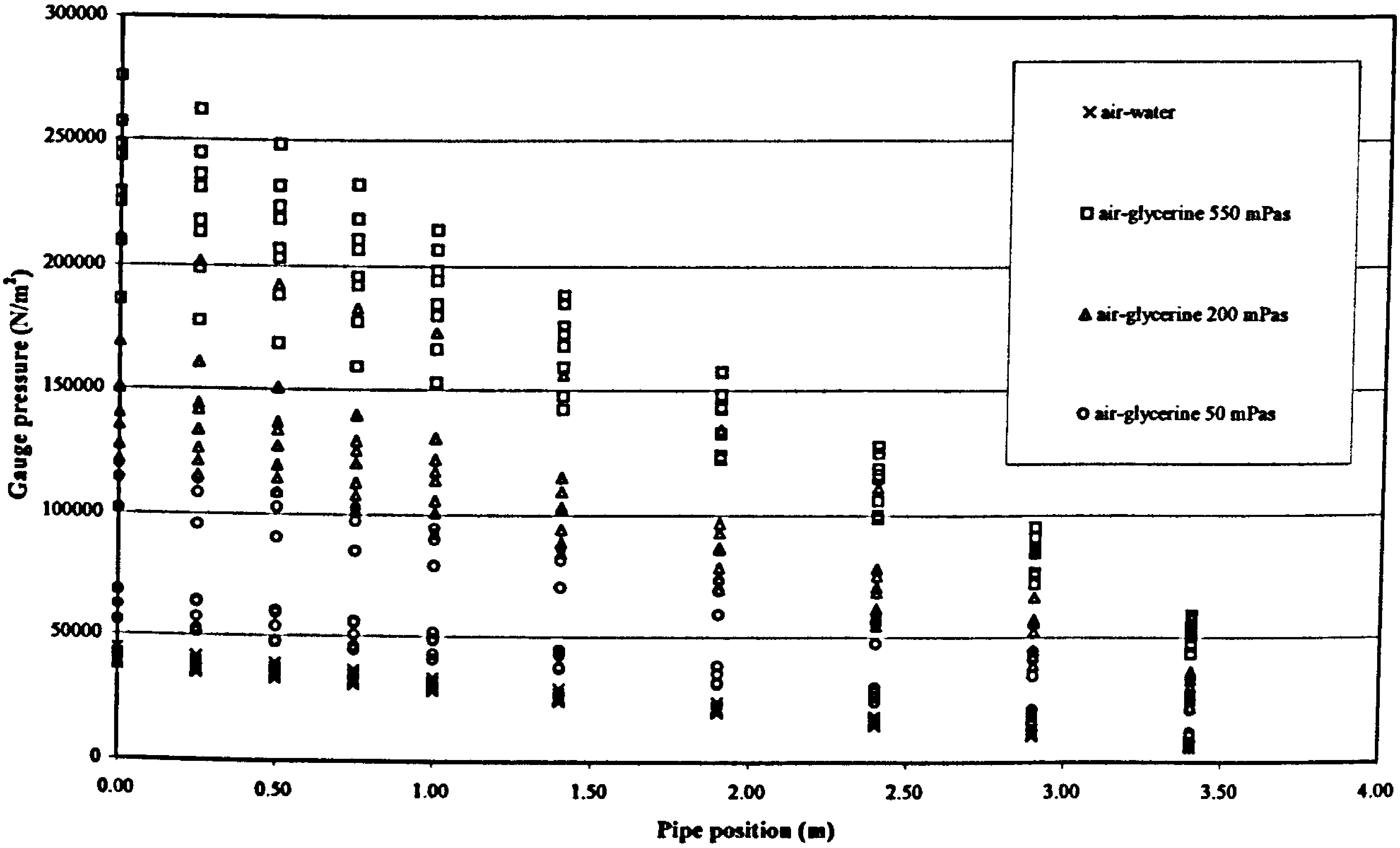

Figure 6.1: Pipe Length Two-phase Test Data

6.2.2 Void Fraction Data

The void fraction was measured for all the two-phase pipe length tests at the position indicated in Figure 3.2. The measured void fraction was calculated using Equation 4.3 and is shown against quality in Figure 6.2. For reference the

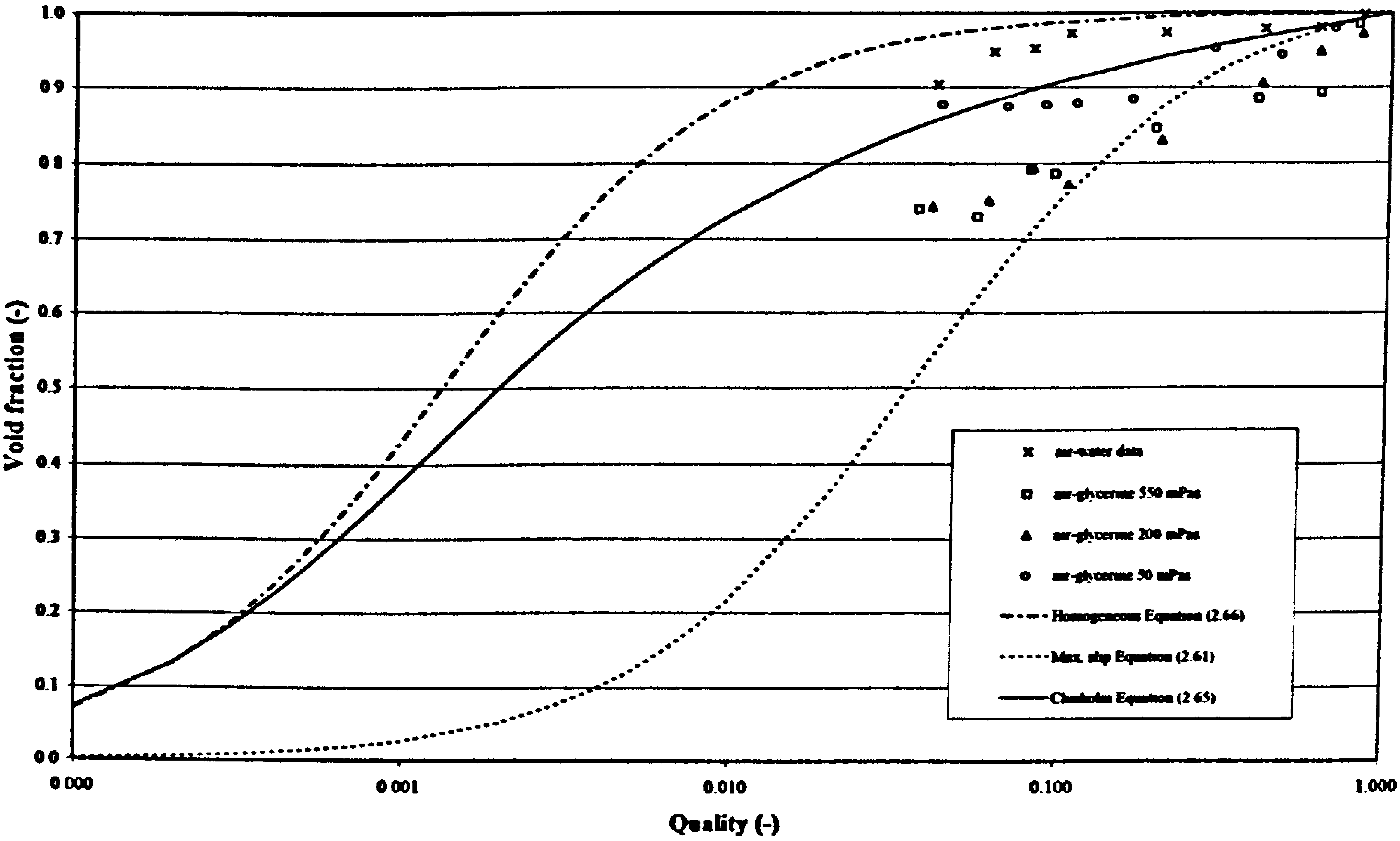

Figure 6.2: Experimental Void Fraction

homogeneous, maximum slip and Chisholm [54] (1972) values are also shown. The void fraction is at a minimum at the lower qualities and rises to a maximum at the high qualities. This trend is followed by all four test liquids. In addition to the void fraction increasing with quality, a second trend is also evident. Across the viscosity range the void fraction decreased with viscosity. The air-water tests have the highest void fraction and the 550 mPas nominal viscosity test liquid have the lowest void fraction.

6.3 In-line Components

In-line components were tested for single-phase water and viscous conditions to allow the evaluation of single-phase discharge and loss coefficients. In every instance the pipe discharge component was installed at the test section exit. The nominal viscosity of the aqueous glycerine test liquid for both the single and two-phase tests was 550 mPas. Both the in-line nozzle and orifice plate required the measurement of the differential pressure drop across the component. This was achieved using the pressure taps located as per Figure 3.3.

6.3.1 Orifice Plate Single-Phase Tests

Over a range of mass flow rates, the local pressures up and down stream of the in-line orifice plate, and the differential pressure drop across the orifice plate were measured. The discharge coefficient for the in-line orifice plate was calculated from;

$$c_D = \frac{Q_A}{Q_I} \tag{6.1}$$

where Q_A is the actual liquid volume flow rate measured, and Q_I is the ideal liquid volume flow rate. The differential pressure drop was used to calculate the ideal liquid volume flow rate from;

$$Q_I = \frac{0.25\pi D_d^2 \sqrt{2\Delta p_{lo}}}{\left[\rho_l\left(1-\left(\frac{D_d}{D_u}\right)^4\right)\right]^{1/2}} \tag{6.2}$$

Figure 6.3 shows the discharge coefficients for the aqueous glycerine and water test data. The water discharge coefficient has been extrapolated to the lower Reynolds numbers to allow comparison. The high viscosity discharge coefficient over this range is not constant and the trend is in agreement with that found by Alvi *et al* [9] (1978).

Loss and pressure drop coefficients, β, were calculated using Equation 2.4 and these are shown in Figure 6.4. The loss coefficient was calculated from the overall pressure drop obtained using the method illustrated by Figure 2.6 and the pressure drop coefficient was calculated from the differential pressure measured across the orifice plate. Below a Reynolds of around 60 the aqueous glycerine test liquid loss & pressure drop coefficients vary with Reynolds number. Above this Reynolds number they are constant. The glycerine loss and pressure drop coefficients were obtained from these trend lines using a power law and are given in Figure 6.4. The water loss and pressure drop coefficients, with values of 26.09 and 34.83 respectively, were constant and have been extrapolated to the lower range Reynolds number flows for comparison.

For both high and low viscosity data there is a significant difference between the loss and pressure drop coefficients. Measuring the differential pressure drop across the flow disruption registered a greater pressure drop than obtained from the up and down stream pressure gradients. This is due to an area of pressure recovery directly down stream of the orifice plate. In both cases the viscous data starts above the water data and ends below it.

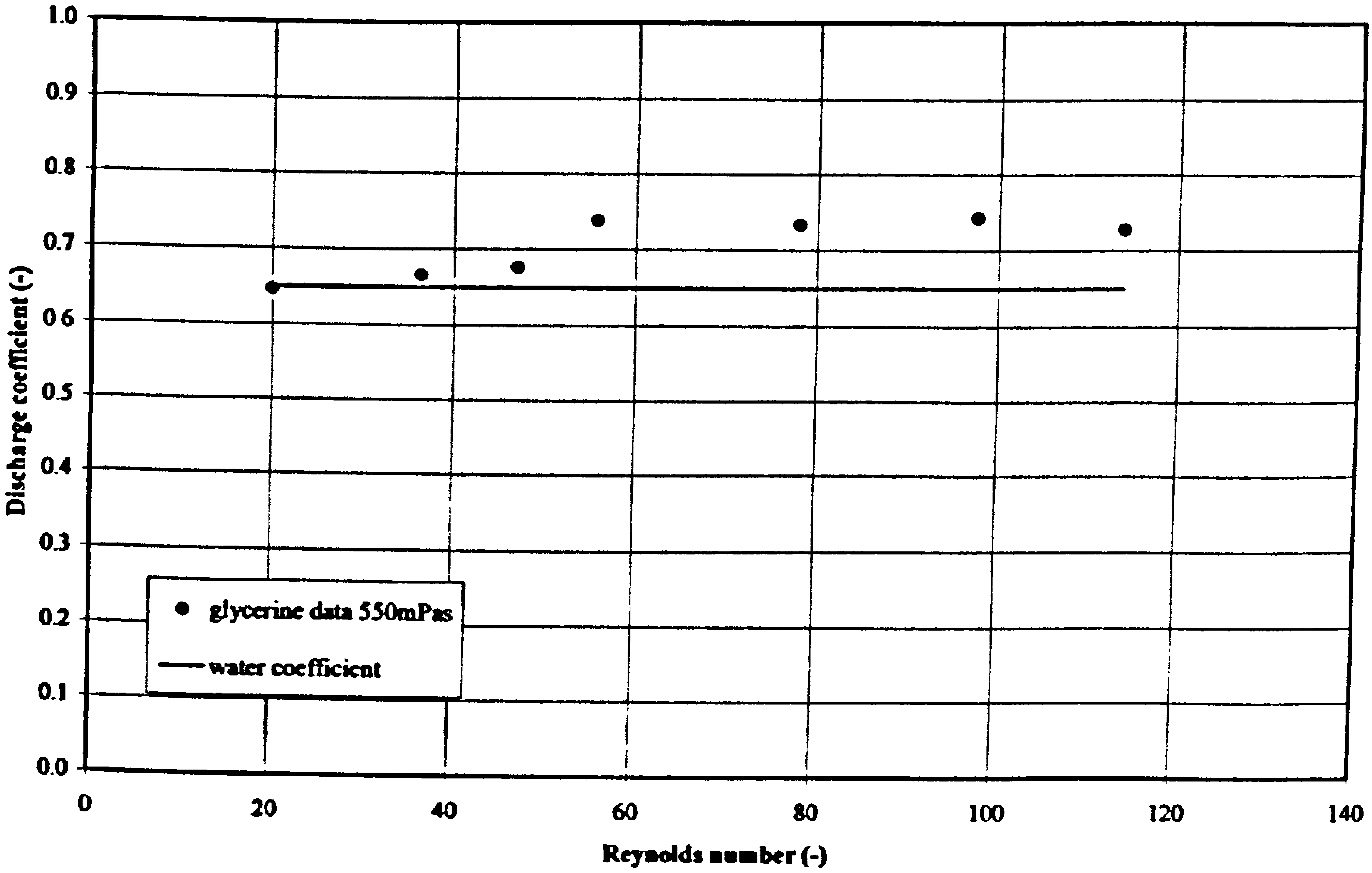

Figure 6.3: In-line Orifice Plate Single-Phase Discharge Coefficients

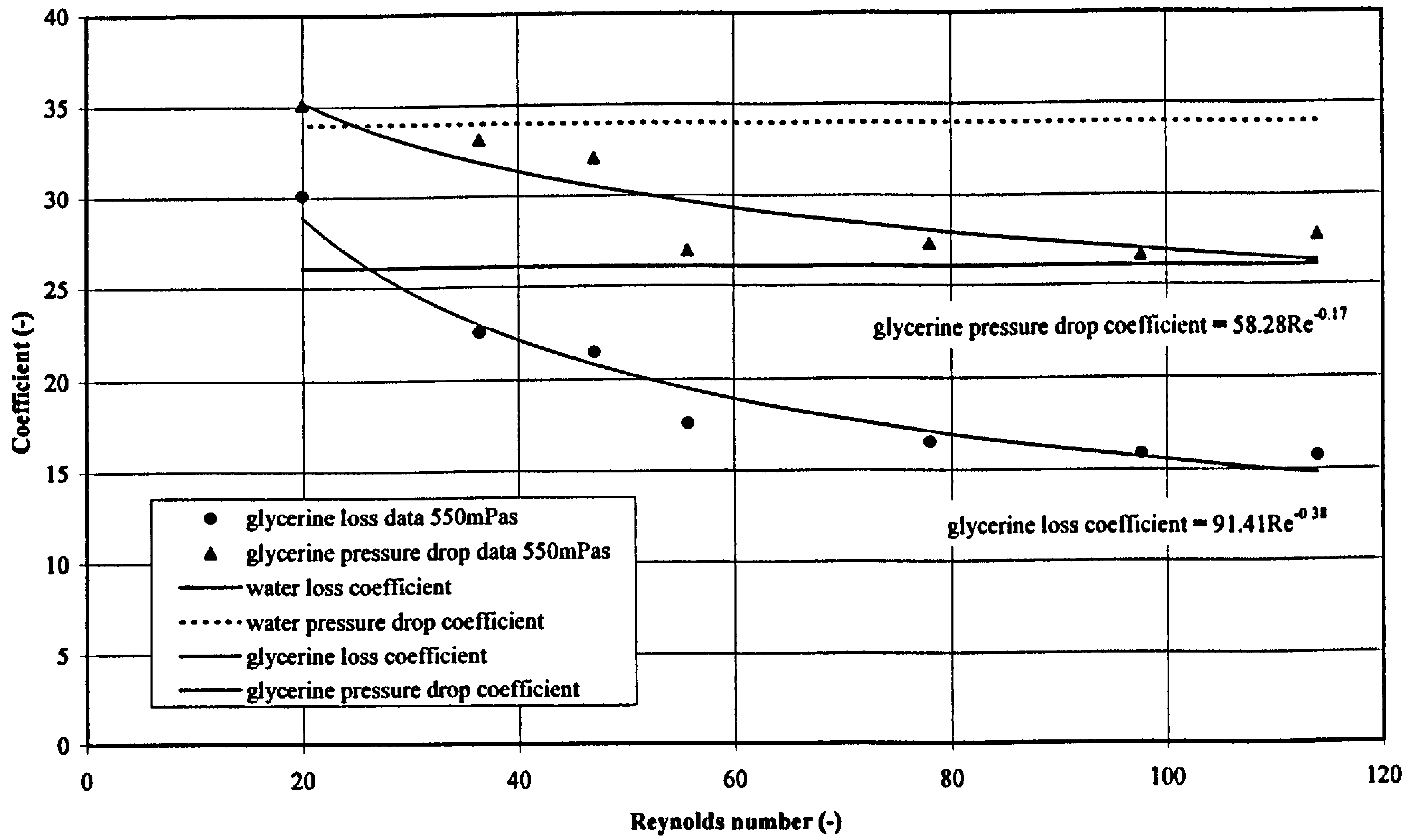

Figure 6.4: In-line Orifice Plate Single-Phase Loss & Pressure Drop Coefficients

6.3.2 Orifice Plate Two-Phase Tests

Two-phase tests with air-water and air-glycerine were performed with the in-line orifice plate. The local pressures up and down stream of the in-line orifice plate and the differential pressure drop across the orifice plate were measured over the range of nominal qualities noted in Section 6.1

The all-liquid air-water and air-glycerine single-phase pressure drop, Δp_{lo}, was calculated using the single-phase water and glycerine loss and pressure drop coefficients obtained in Section 6.3.1. The all-liquid single-phase pressure drop is given by:

$$\Delta p_{lo} = \frac{\beta G^2}{2\rho_l} \tag{6.3}$$

The two-phase pressure drop was obtained in two ways. An overall two-phase pressure drop was found from the pressure gradients given by the local pressure up and down stream of the orifice plate i.e. the method of Figure 2.6. A contracted two-phase pressure drop was obtained from the differential pressure measured across the in-line orifice plate. Overall and contracted two-phase pressure drops were used to calculate overall and contracted two-phase multipliers for air-water and air-glycerine using Equation 6.4;

$$\Delta p = \phi_{lo}^{2} \Delta p_{lo} \tag{6.4}$$

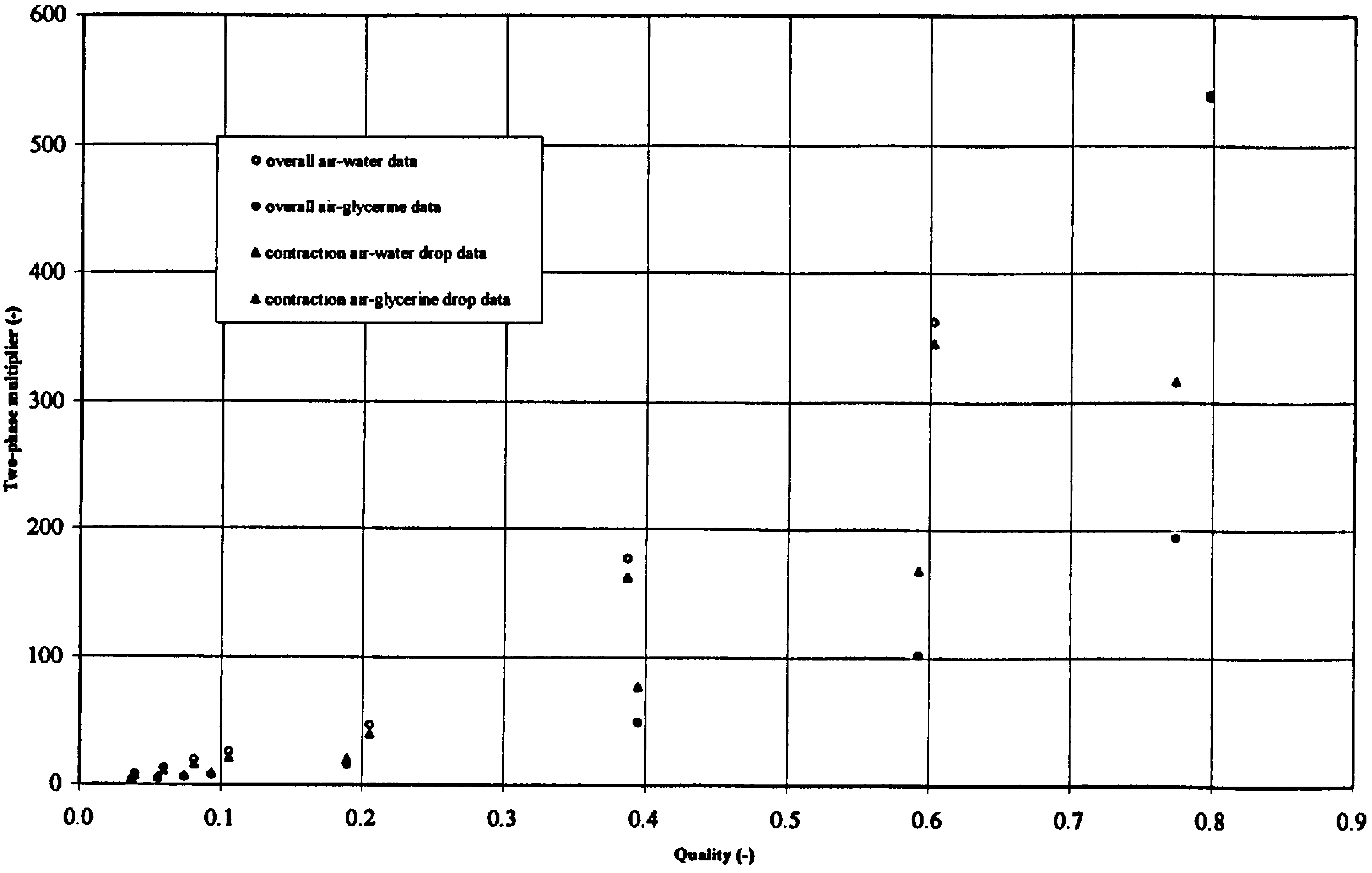

Figure 6.5: In-line Orifice Plate Two-Phase Data

Figure 6.5 shows two-phase multipliers plotted against quality for both test liquids. There is little difference between the overall and contracted two-phase multipliers for the air-water flows. Towards the higher qualities, the air-water multipliers are significantly greater than the air-glycerine multipliers. The all-liquid single-phase losses determined using the glycerine single-phase pressure and loss coefficient are greater resulting in the two-phase losses attributable to the air-glycerine flows decreasing in comparison with the corresponding air-water flows.

6.3.3 Nozzle Single-Phase Tests

The local pressures up and down stream of the in-line nozzle and the differential pressure drop across the in-line nozzle were recorded for a range of mass flow rates. The overall pressure drop was obtained using the method illustrated in Figure 2.6. Equations 6.1 & 6.2 were used to determine the discharge coefficient for the aqueous glycerine test liquid shown in Figure 6.6.

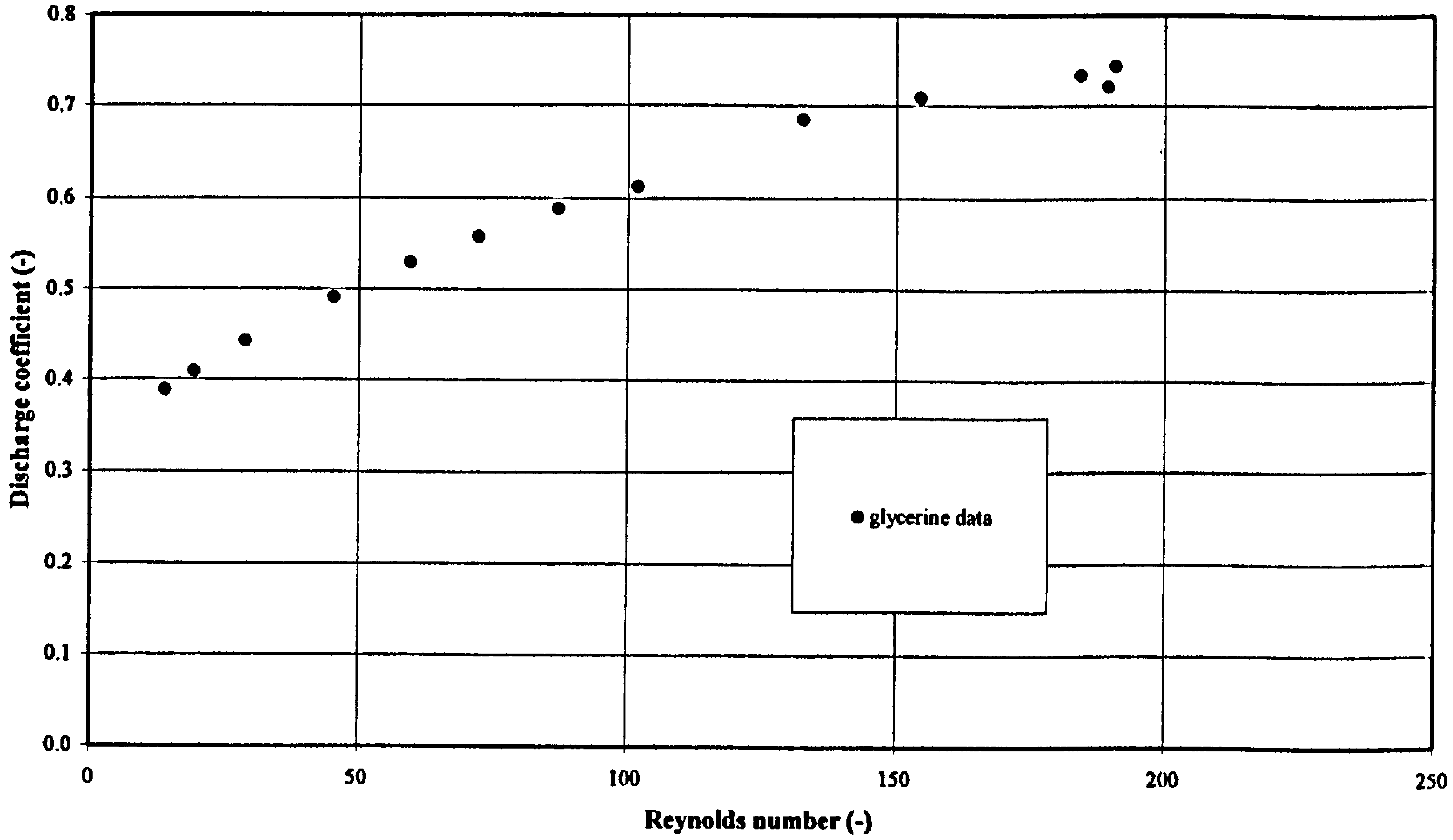

Figure 6.6: In-line Nozzle Single-Phase Discharge Coefficients

The loss and the pressure drop coefficients were calculated using the overall and differential pressure drops and Equation 2.4. For water tests these were 0.83 and 1.7 respectively and are shown in Figure 6.7. The glycerine loss and pressure drop coefficients, shown in Figure 6.7, were obtained from a power law. Similar to the in-line orifice plate, the glycerine loss and pressure drop coefficients vary strongly with Reynolds number below a Reynolds number of about 70 and then tend to a constant. Unlike the in-line orifice plate, the value of the glycerine loss and pressure drop coefficients do not fall below the value of the water pressure and loss coefficients.

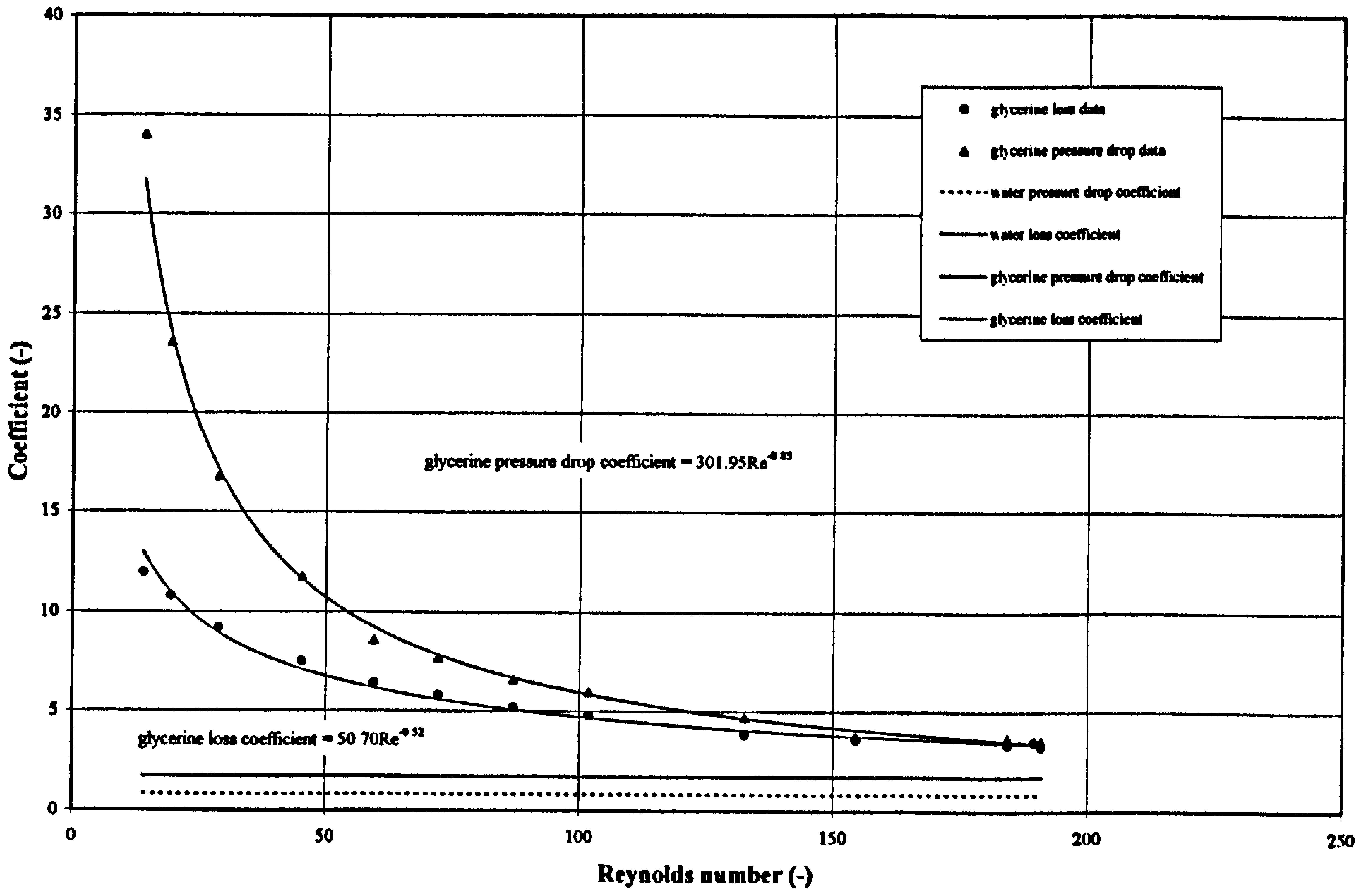

Figure 6.7: In-line Nozzle Single-Phase Loss Coefficients

6.3.4 Nozzle Two-Phase Tests

Two-phase tests with air-water and air-glycerine were performed with the in-line nozzle. The local pressures up and down stream of the in-line nozzle and differential pressure drop across the in-line nozzle were measured for the range of nominal qualities noted in Section 6.1. As per the single-phase test, an overall pressure drop was obtained using the method illustrated in Figure 2.6.

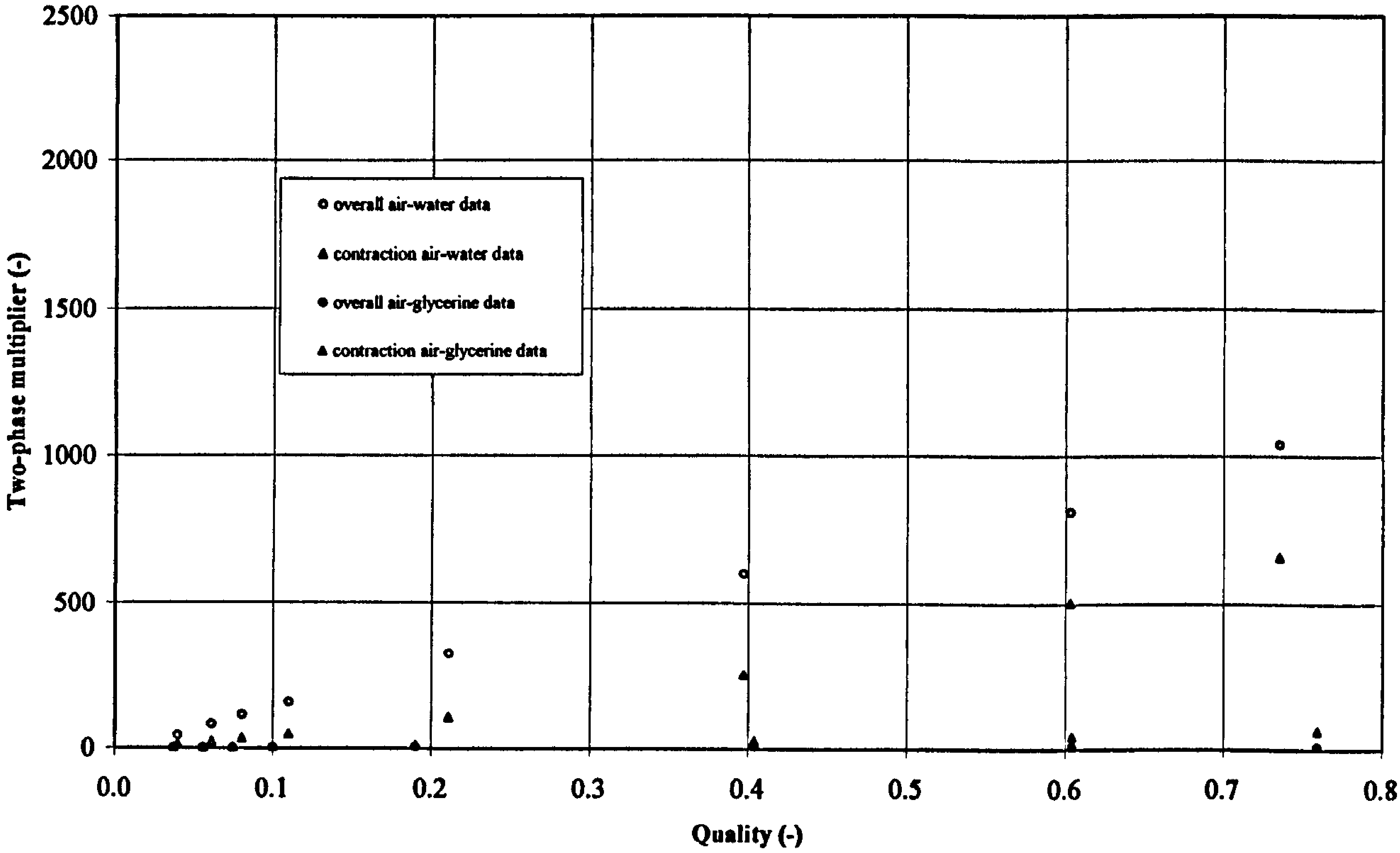

Figure 6.8: In-line Nozzle Two-Phase Data

The water and glycerine single-phase loss and pressure drop coefficients obtained in Section 6.3.3 were used with Equation 6.3 to calculate the all-liquid pressure drop. Equation 6.4 was used to determine an overall and contracted two-phase multipliers which are shown in Figure 6.8. Unlike air-water two-phase multipliers determined for the in-line orifice plate there is a notable difference between overall and contracted values. The overall multipliers are larger than the contracted multipliers especially at the higher qualities. The air-glycerine two-phase multipliers are much smaller than the corresponding air-water multipliers. Over the range of low Reynolds numbers that the two-phase multipliers were obtained the single-phase glycerine loss and pressure drop coefficients are very large, resulting in all-liquid single-phase pressure drops also being very large.

6.3.5 Globe Valve Single-Phase Tests

The local pressures up and down stream of the globe valve were recorded for a range of mass flow rates. An overall pressure drop was obtained using the method illustrated in Figure 2.6. Loss coefficients for the water and the aqueous glycerine test liquid were determined using Equation 2.4. The water loss coefficient was 8.67 and this has been extrapolated for the lower Reynolds number flows and compared to the aqueous glycerine solution loss coefficients in Figure 6.9. From the trend line of the high viscosity data the glycerine loss coefficient was obtained using a power law and is given in Figure 6.9. Similar in behaviour to that of the in-line nozzle, the glycerine loss coefficient is a strong function of the Reynolds number at the very low Reynolds number flows and then tends to a constant as the Reynolds number increases.

6.3.6 Globe Valve Two-Phase Tests

Two-phase tests with air-water and air-glycerine were performed with the globe valve. The local pressures up and down stream of the globe valve were recorded for the range of nominal qualities noted in Section 6.1. An overall pressure drop was obtained using the method illustrated in Figure 2.6.

The single-phase loss coefficients obtained in Section 6.3.5 were used along with Equation 6.3 to calculate the all-liquid pressure drop and Equation 6.4 was used to determine the air-water and air-glycerine two-phase multipliers. The two-phase multipliers are shown in Figure 6.10. At low Reynolds number, the magnitude of the air-glycerine two-phase multipliers is significantly smaller than equivalent air-water flows. This is due to the high value of the all-liquid single-phase pressure losses predicted using the single-phase glycerine loss coefficient.

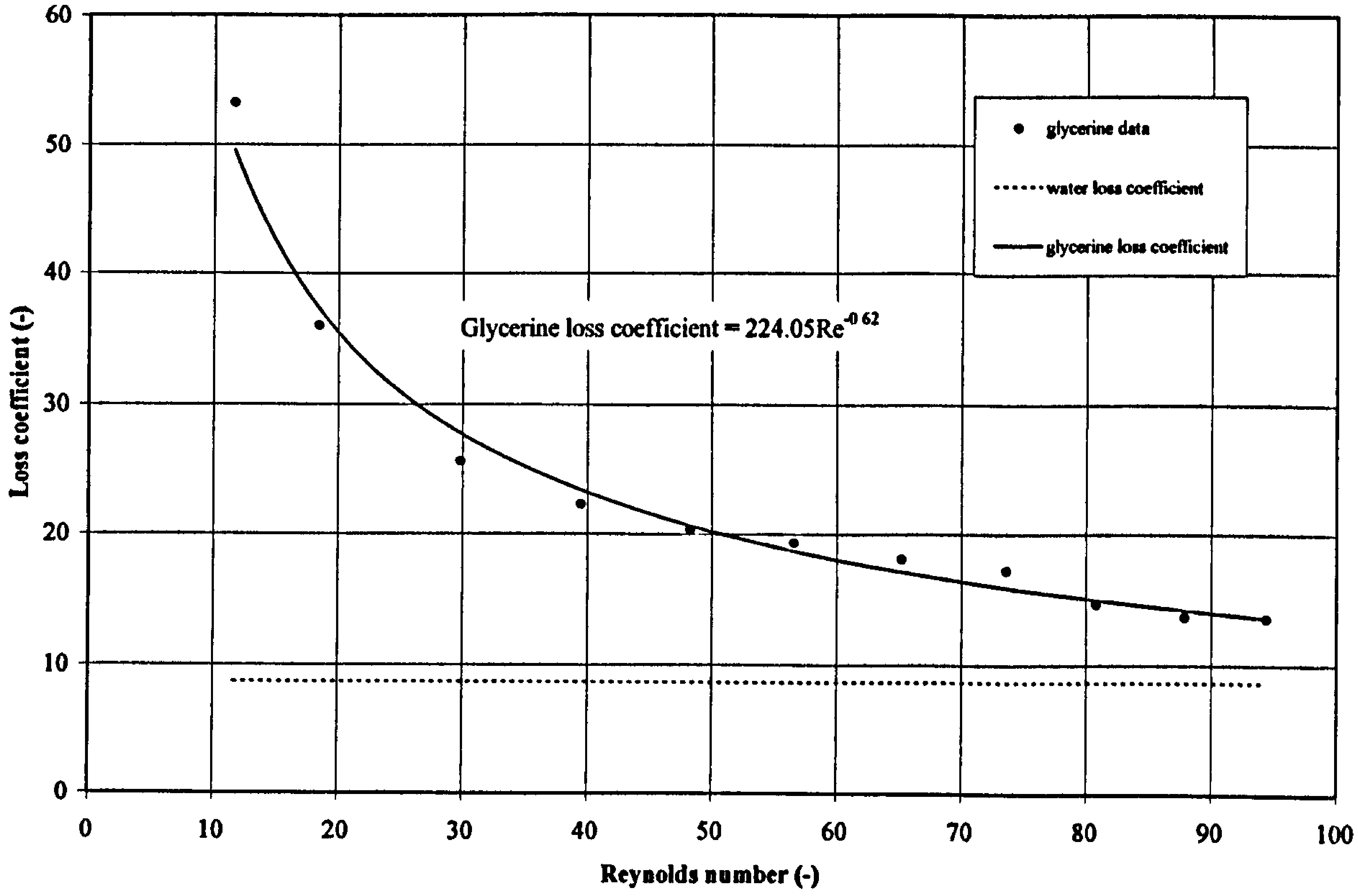

Figure 6.9: Globe Valve Single-Phase Loss Coefficients

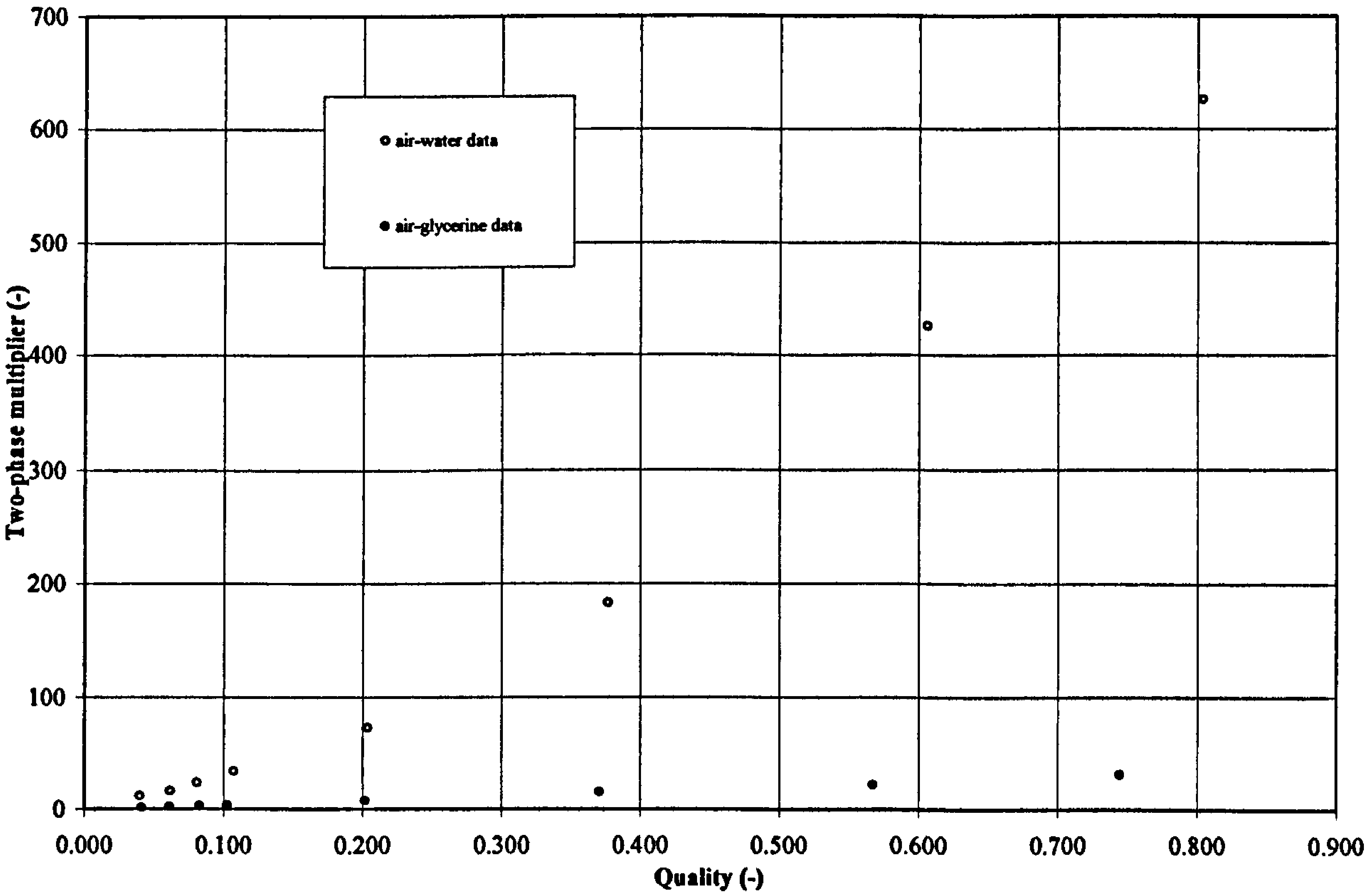

Figure 6.10: Globe Valve Two-Phase Data

6.3.7 Abrupt Enlargement Single-Phase Tests

For the abrupt enlargement tests the 25 mm nominal diameter settling length and test section upstream of the abrupt enlargement were replaced with 20 mm nominal diameter equivalents. An abrupt enlargement spool piece was installed in the test section and the pipe discharge component at the test section exit. The local pressures up and down stream of the abrupt enlargement were recorded for a range of mass flow rates and pressure drops were obtained using the method illustrated in Figure 2.6. The single-phase loss coefficient, K_c, was calculated from;

$$\frac{p_u}{\rho_l} + c_E \frac{u_u^2}{2} = \frac{p_d}{\rho_l} + c_E \frac{u_d^2}{2} + K_c \frac{u_u^2}{2} \qquad (6.5)$$

where c_E, is the kinetic energy correction factor, taken as 1 and 2 for turbulent and laminar flows respectively, and *u* and *d* subscripts refer to the up and down stream pipe diameter. The water only loss coefficient, calculated from Equation 6.5, was found to be

0.27 and is shown extrapolated to the lower Reynolds number flows with the high viscosity data in Figure 6.11.

6.3.8 Abrupt Enlargement Two-Phase Tests

Two-phase tests with air-water and air-glycerine were performed with the abrupt enlargement. The local pressures up and down stream of the abrupt enlargement were recorded for the range of nominal qualities noted in Section 6.1. An overall pressure drop was obtained using the method illustrated in Figure 2.6.

Two-phase multipliers were determined from Equations 6.3 and 6.4 and are shown in Figure 6.12. They follow a similar trend to that of the in-line orifice plate and globe valve. Some air-glycerine data points have been omitted, qualities 0.04 - 0.1. These data points are questionable as they suggest the pressure drop is negative.

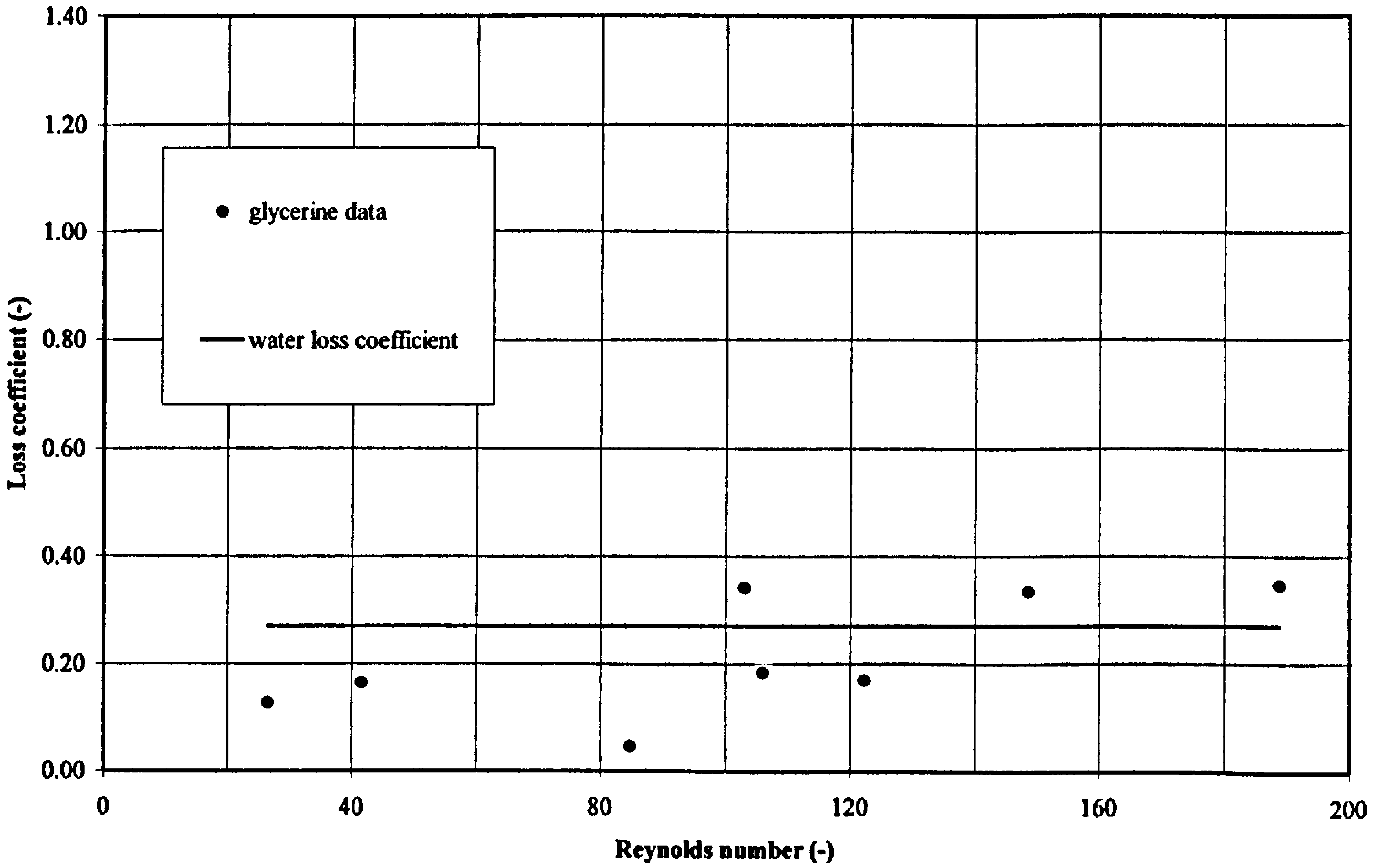

Figure 6.11: Abrupt Enlargement Single-Phase Loss Coefficients

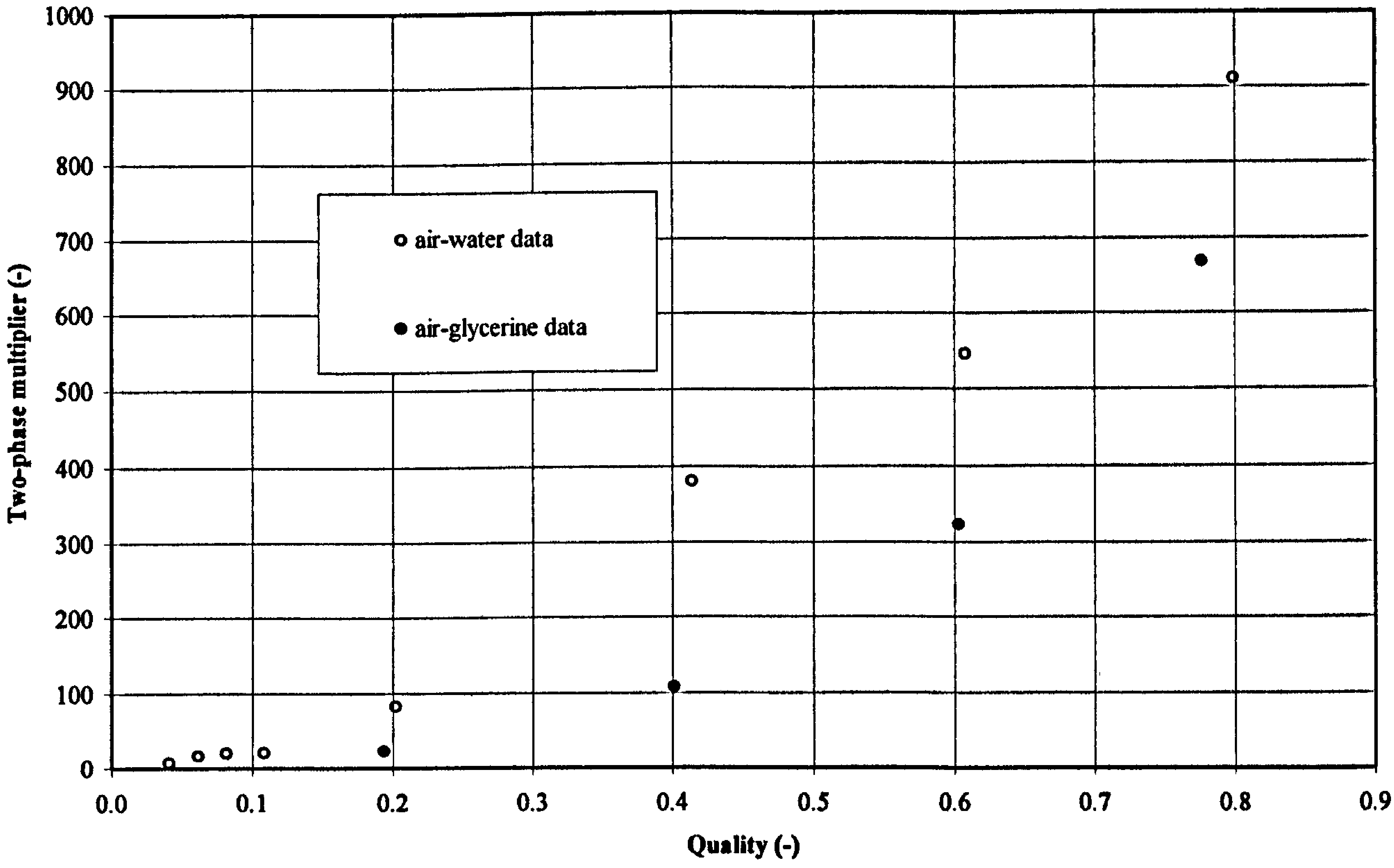

Figure 6.12: Abrupt Enlargement Two-Phase Data

6.4 Discharge Components

Discharge components were tested for single-phase water and viscous conditions to allow the evaluation of single-phase discharge coefficients.

Single and two-phase tests were carried out with the pipe spool piece installed in-line and the discharge nozzle component fitted at the test section exit.

6.4.1 Discharge Nozzle Single-phase Tests

The static pressure, located at a point 123 mm from the discharge nozzle exit, was recorded over a range of mass flow rates using glycerine solutions with nominal values of viscosity of 550, 400, 200 & 40 mPas. The discharge coefficients were calculated using Equations 6.1 & 6.2 and are shown in Figure 6.13. The water only test discharge coefficient was found to be 0.955, where as the glycerine solution discharge coefficients were found to vary with Reynolds number. The behaviour of glycerine flows was similar to the behaviour observed during the calibration of the flow nozzles described in Section 4.5.5.

Over the full range of glycerine solution viscosities, the discharge coefficients can be seen to adhere to the same trend line as they climb towards the value of the water discharge coefficient. There is a discrepancy in the 40 mPas nominal viscosity data. Difficulties experienced with the monitoring and controlling of the test liquid viscosity, described in Section 5.10, may have lead to a mismatch of the flow nozzle calibration data and viscosity readings. With out an opportunity to repeat the 40 mPas single-phase test it was not possible to confirm this as the cause of the error. This error is isolated to the single and two-phase 40 mPas nominal viscosity data.

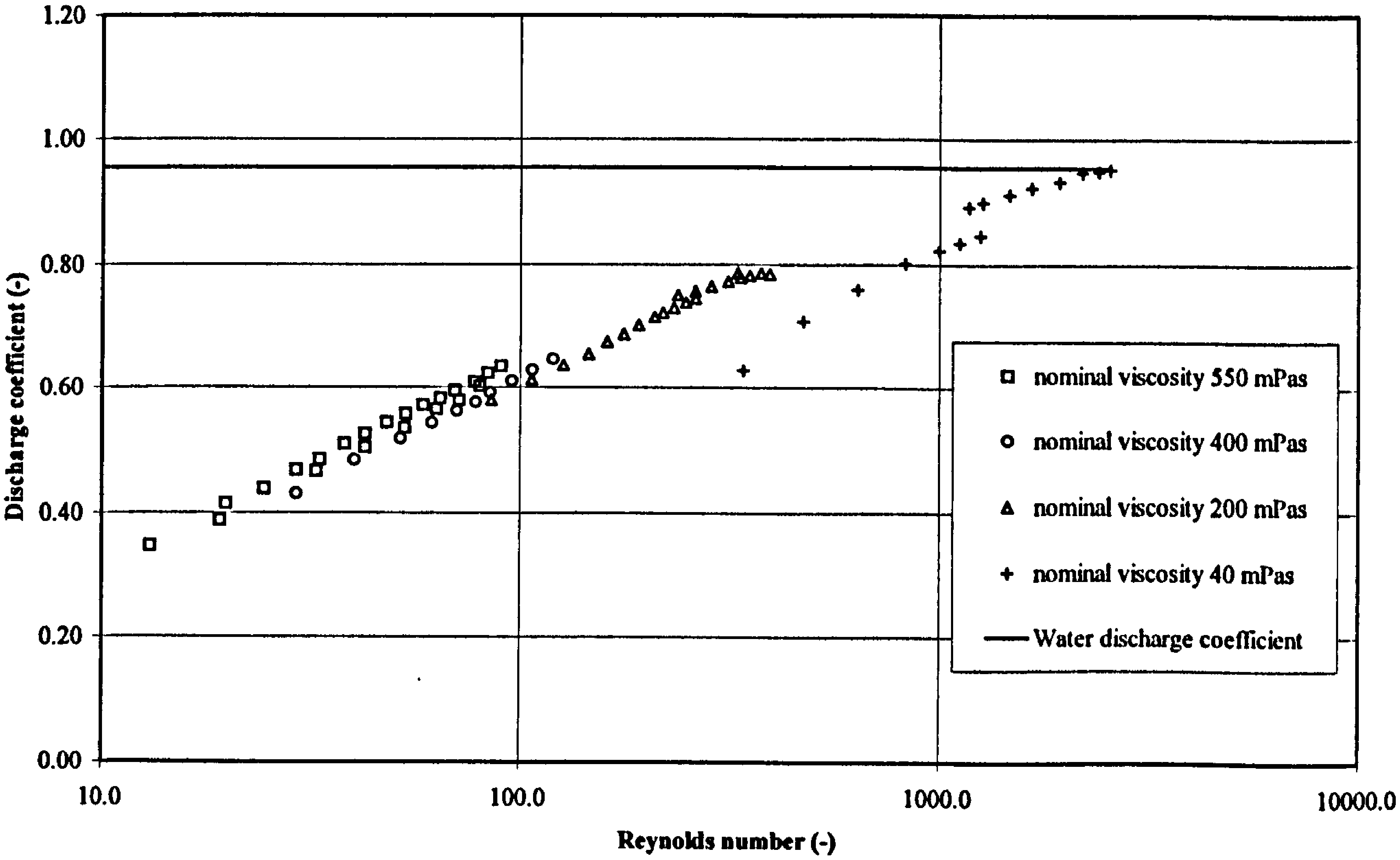

Figure 6.13: Discharge Nozzle Coefficient versus Reynolds Number

6.4.2 Discharge Nozzle Two-phase Tests

Two-phase nozzle discharge tests were performed and like the single-phase tests, the static pressure was measured at the pressure tap3.5 mm from the discharge nozzle exit. To ensure that the two-phase flows remained in the subsonic region the pressure was monitored at a pressure tap located 3 mm from discharge nozzle exit. An atmospheric pressure reading at this location indicated a subsonic discharge. Subsonic data were recorded for three nominal values of the glycerine solution viscosity, 550 200 & 100 mPas, over the range of qualities noted in Section 6.1. The measured two-phase multipliers of Figure 6.14 were calculated using Equation 6.3 & 6.4 using the turbulent single-phase loss coefficient for both air-water and air-glycerine flows. At the higher qualities the two-phase multipliers can be seen to increase with increasing viscosity.

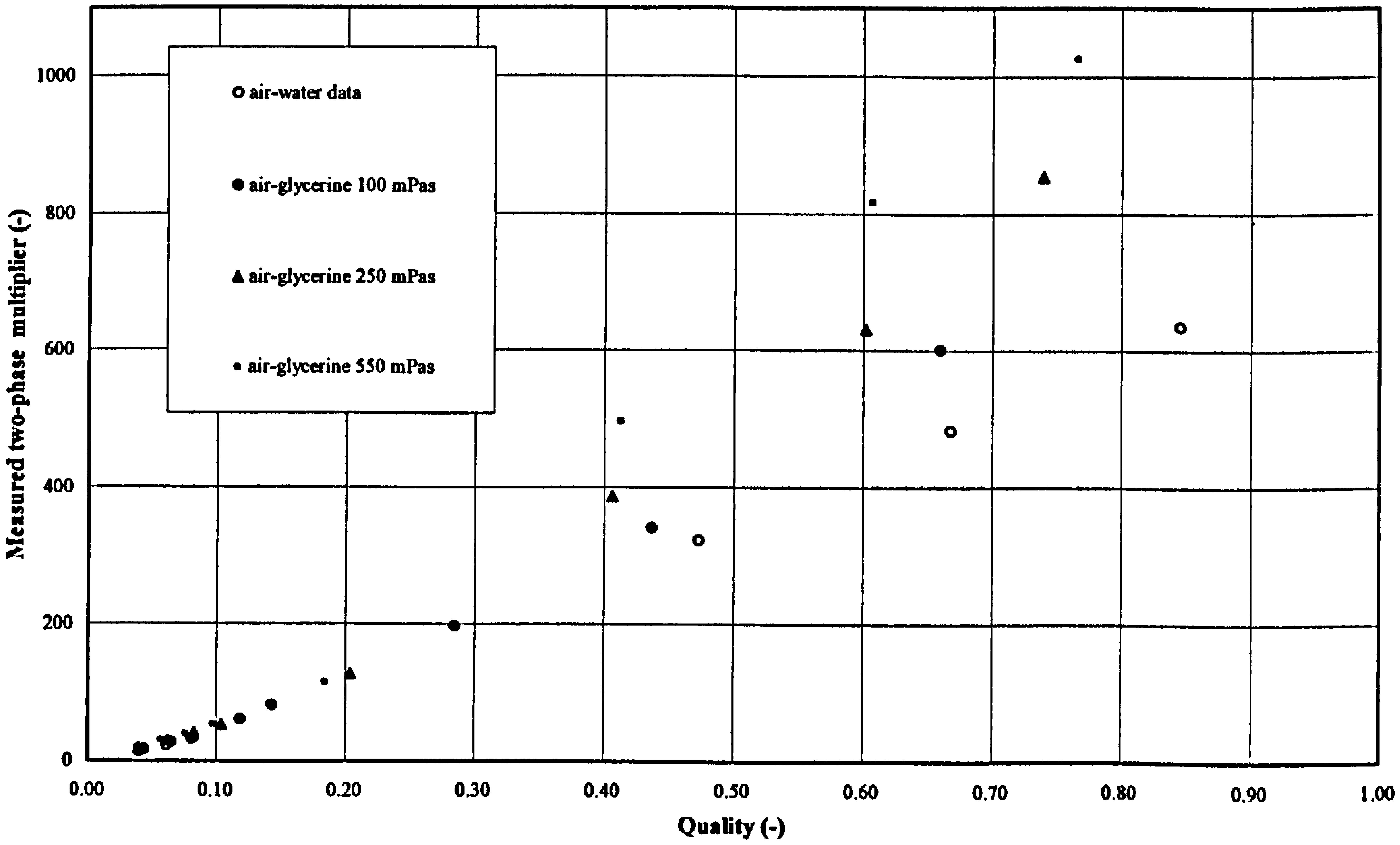

Figure 6.14: Discharge Nozzle Two-Phase Data

6.4.3 Orifice Plate Single-phase Tests

With the discharge orifice component fitted at the test section exit, single and two-phase orifice discharge tests were performed. The static pressure, located at a point 25 mm from the discharge orifice exit, was recorded over a range of mass flow rates. The discharge coefficient was calculated using Equations 6.1 & 6.2. For the water only test the discharge coefficient was calculated as 0.644 and is shown as the solid line in Figure 6.15 extrapolated to the lower Reynolds numbers of the glycerine data. The glycerine discharge coefficients are not constant. They start below the value of the water discharge coefficient and appear to climb to a value slightly above it as the Reynolds number increases. This is a different trend to that obtained for the in-line orifice plate in Figure 6.3. This is probably due to the in-line discharge jet interacting with the other fluid and the formation of the vena-contract being delayed.

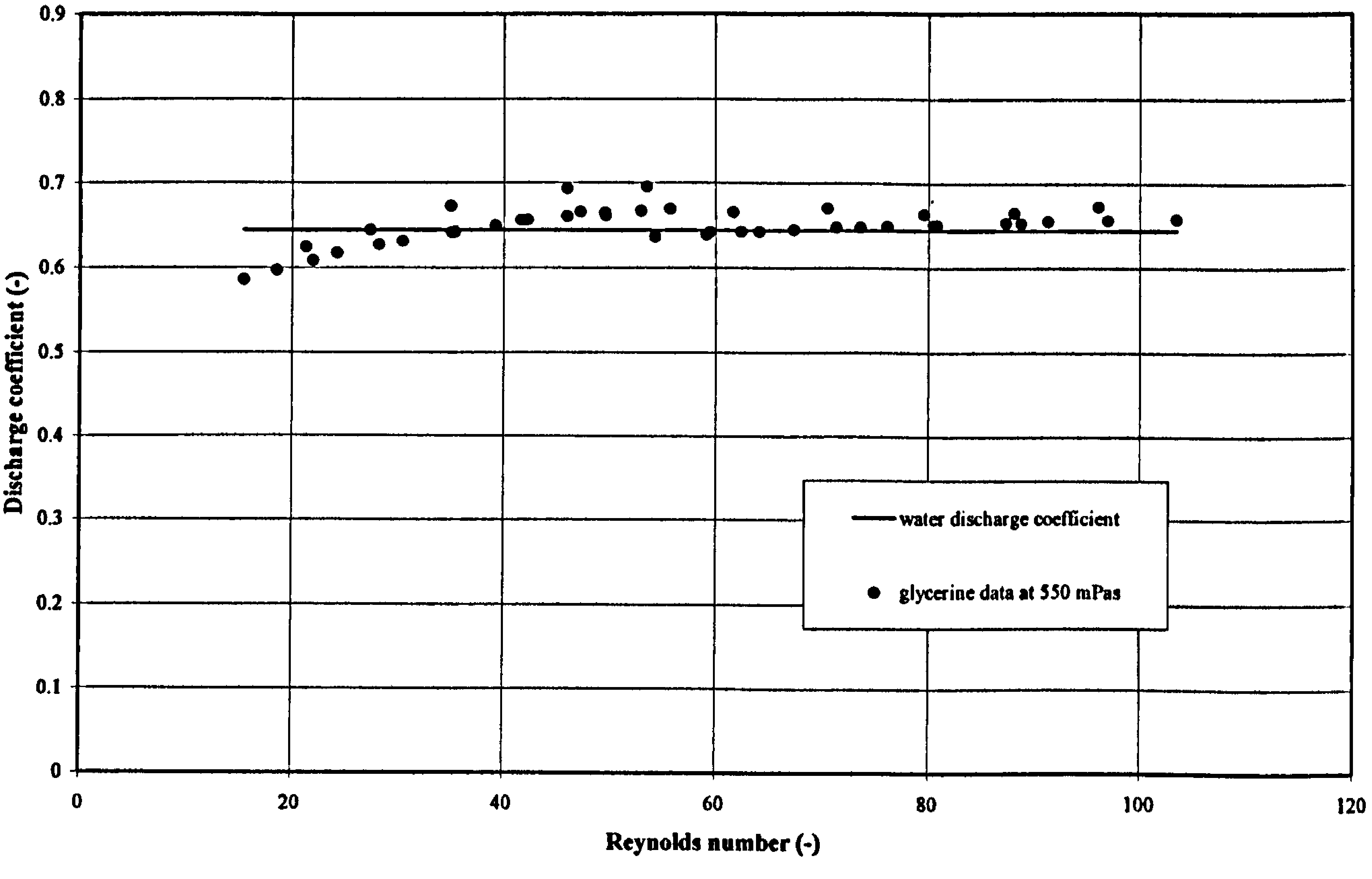

Figure 6.15: Comparison of Discharge Orifice Plate Water & Glycerine Data

6.4.4 Orifice Plate Two-phase Tests

For a glycerine solution with a nominal viscosity of 450 mPas, two-phase orifice discharge tests were performed for the range of nominal qualities noted in Section 6.1. The static pressure was measured at the pressure 25 mm from the discharge orifice exit. The measured two-phase multipliers of Figure 6.16 were calculated using Equation 6.3 & 6.4 using the turbulent single-phase loss coefficient for both air-water and air-glycerine flows. The magnitude of the air-glycerine two-phase multipliers is greater than that of the air-water two-phase multipliers. However, it should be noted that the air-water mass fluxes are between 60 and 50% less than that of the air-glycerine mass fluxes.

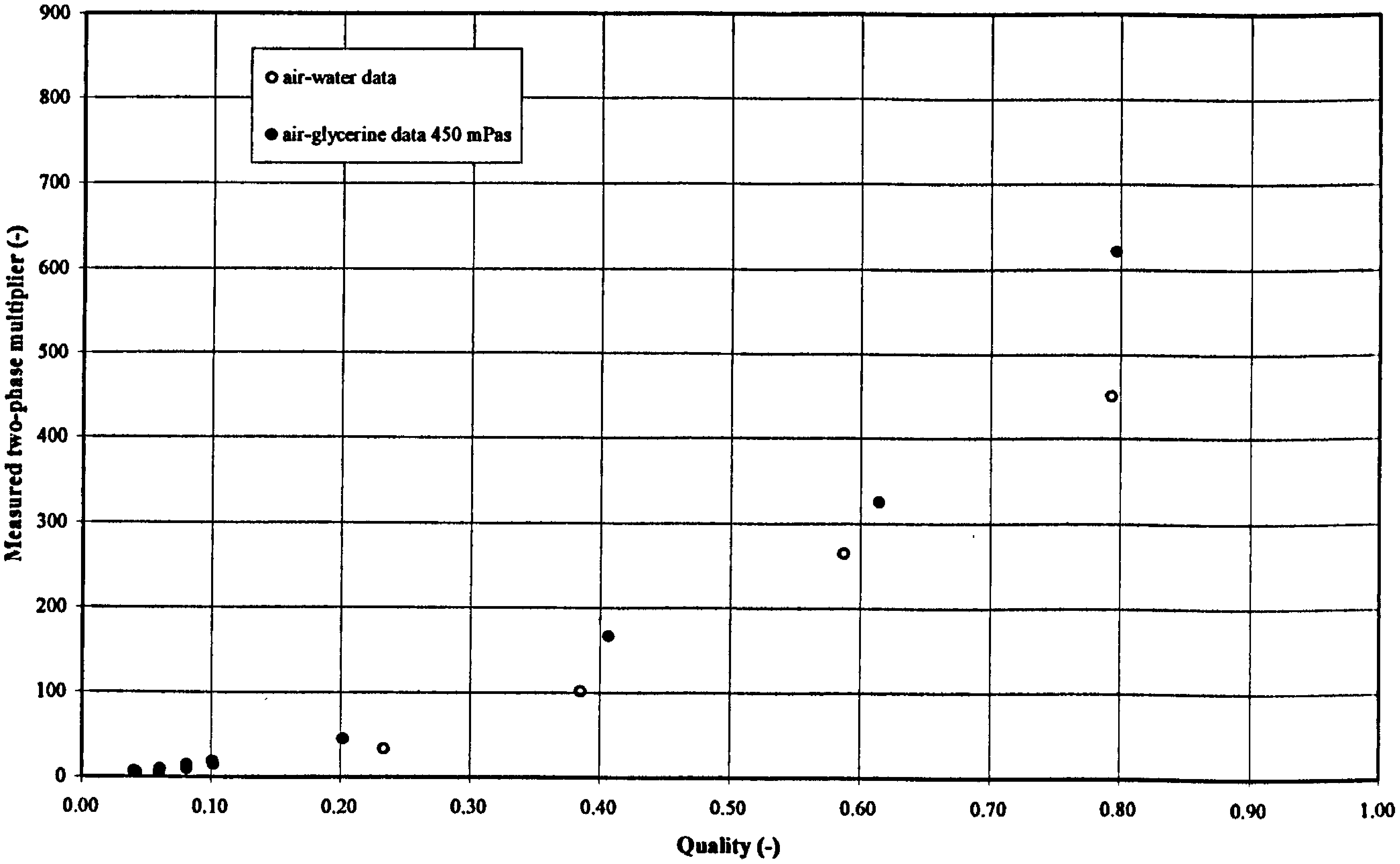

Figure 6.16: Orifice Discharge Two-Phase Data

Chapter 7

DATA ANALYSIS & MODEL COMPARISON

7.1 Introduction

An initial assessment of the data presented in Chapter 6 has been made using flow pattern maps. This relatively simple method gives an indication of the flow regime that the high viscosity data may have been obtained in. Experimental data was subdivided into two data groups; flow through a straight pipe and flow through pipeline components. They were analysed separately.

The analysis of the data taken for flow through a straight pipe required the evaluation of local film properties. This was achieved by assuming that all the flows could be adequately described by an annular flow model and applying a data reduction procedure that enabled the evaluation of the experimental values of wall shear stress, interfacial shear stress, liquid film thickness and interfacial friction factor. Comparisons have been made between the experimental film properties obtained for air-water and air-glycerine flows with nominal viscosities of 50, 200 and 550 mPas and established correlations. Experimental pressure drops were compared to the Chisholm [56] (1983), C & B coefficient methods and the correlation of Friedel [50] (1979). Also applied were publications particular to the annular flow regime produced by Asali *et al* [95] (1985), Fukano & Furukawa [96] (1998) and Ambrosini *et al* [98] (1991).

The data for the in-line components were compared to correlations recommended by ESDU [117] (1989) and the homogeneous and maximum slip flow models. Also, the annular flow model derived for the pipe flow data was applied to the in-line and discharge components data to assist in the application of the compressible flow method of McNeil [118] (2000). For the discharge nozzle and orifice plate the effects of wall shear stress were investigated.

7.2 Flow Pattern Maps

Although visualisation of flow patterns was not an objective of this study, it was important to ascertain the nature of the two-phase flows. Experimental data for the inlet and outlet of the pipe length tests were plotted on the flow pattern maps of Hewitt & Roberts [37] (1969) and Baker [43] (1954) in Figures 7.1 & 7.3 respectively. Only inlet conditions were used for the in-line and discharge components data plotted on the flow pattern map of Hewitt & Roberts [37] (1969) in Figure 7.2.

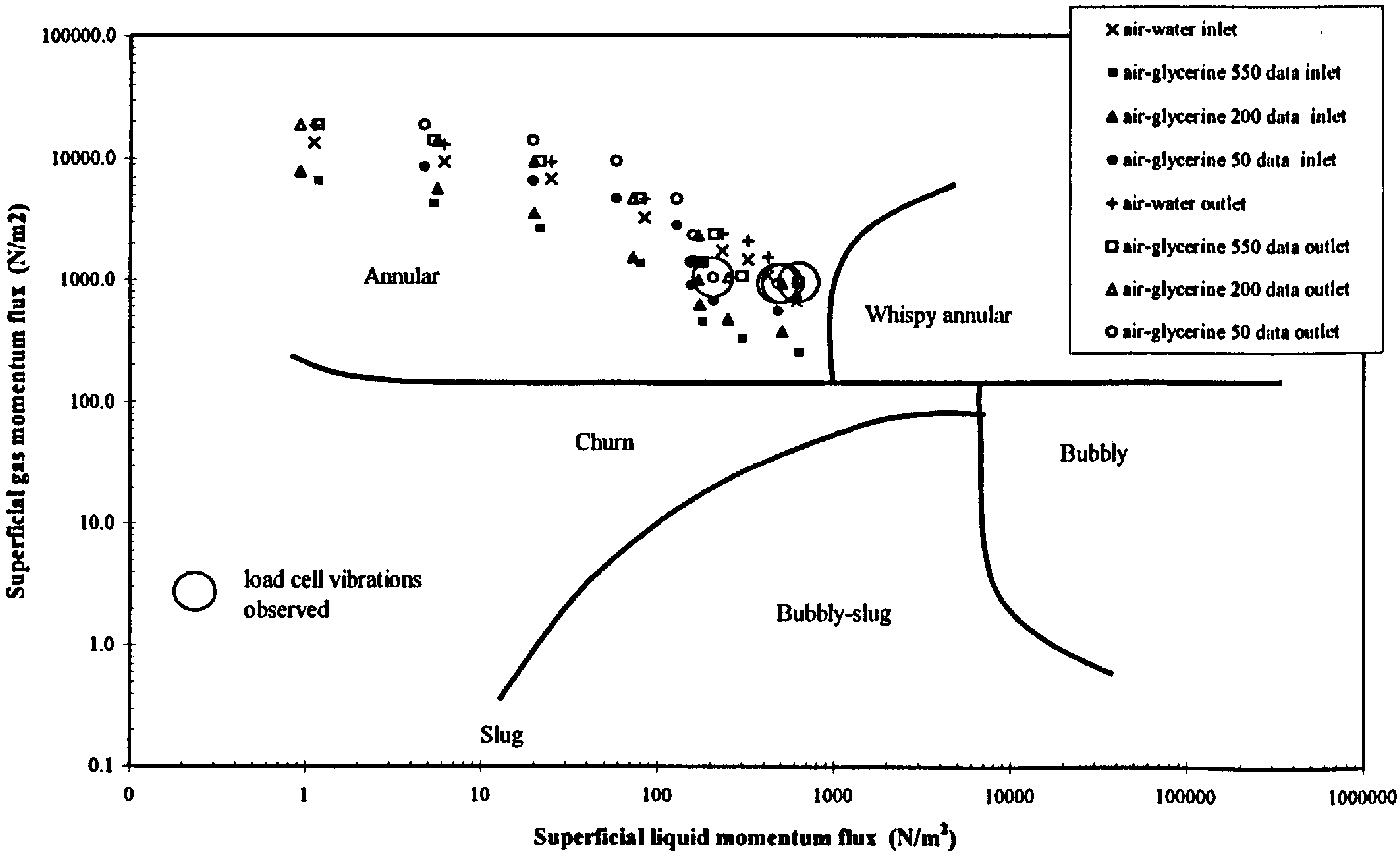

Figure 7.1: Flow Map of Hewitt & Roberts [37], Pipe Length Data

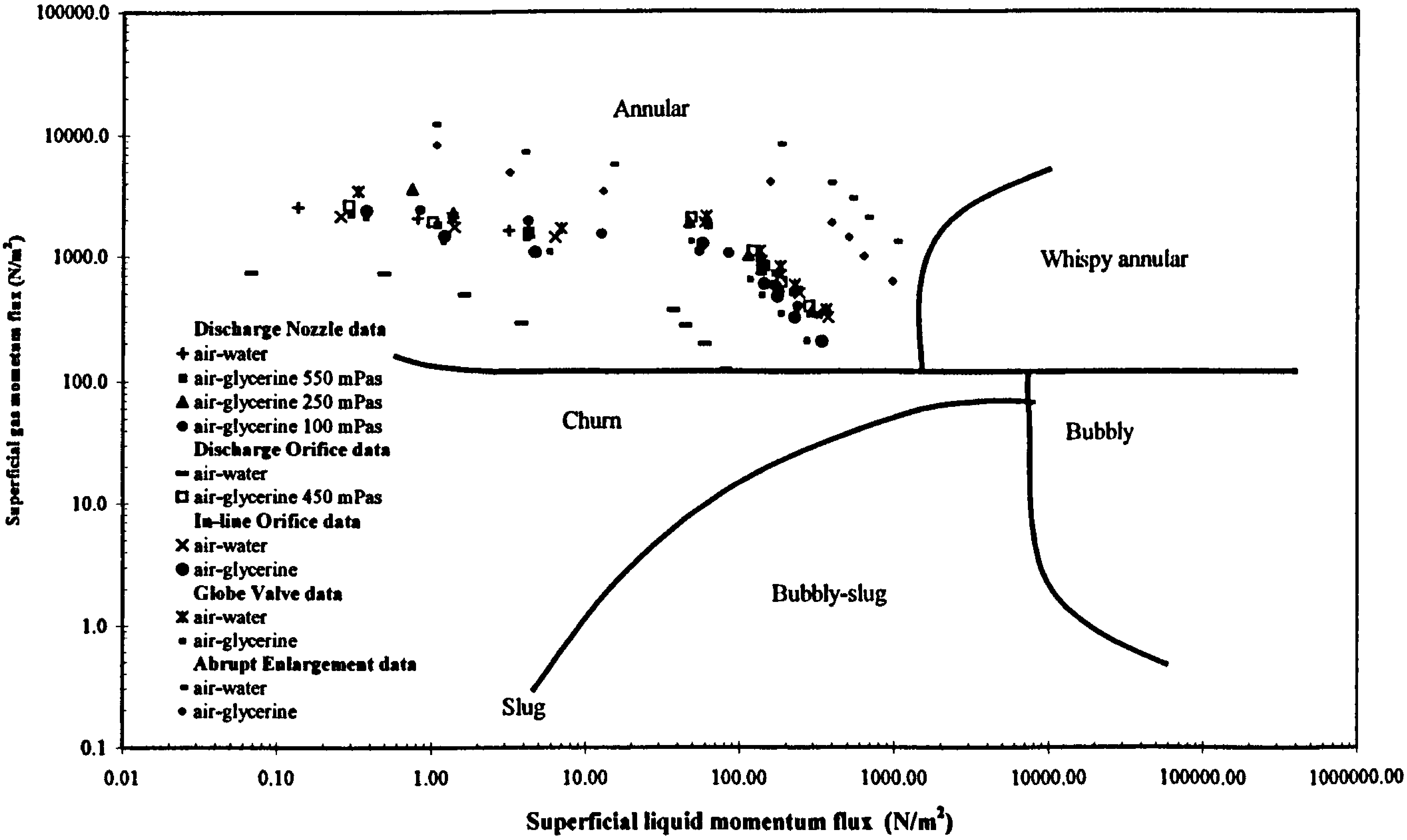

Figure 7.2: Flow Map of Hewitt & Roberts [37], Pipeline Components Data

The noticeable displacement between inlet and outlet data of the pipe length data, Figures 7.1 & 7.3, is greatest with the highest viscosity i.e., 550 mPas. This displacement is attributable to the large pressure drops that occur in the high viscosity tests, resulting in equally large changes in gas velocity and density. Encircled data points indicate conditions where the load cells were subjected to a high degree of vibration. All of the encircled data ought to be located within the slugging regime. Some of them fall in the annular flow regime, suggesting a movement or shift in the regime boundaries due to high viscosity effects. This is more evident on the Hewitt & Roberts [37] flow pattern map, Figure 7.1, where all data are located in the annular flow regime.

Furukawa & Fukano [42] (2001) found that there were no flow pattern maps derived for high viscosity vertical flows and evaluated the applicability of the Baker [43] flow pattern map, originally derived for horizontal flows. Furukawa & Fukano [42] concluded that the froth-annular boundaries of the Baker [43] flow map to be reasonably reliable, irrespective of the pipeline orientation. Data plotted on the flow pattern map of Baker [43] Figure 7.3, does generally adhere to the prescribed regime boundaries. A certain amount of discrepancy is evident where the location of data points at the lower qualities span the bubbly and dispersed boundaries. Considering that the viscosity of the test liquid used by Furukawa & Fukano [42] when assessing the Baker [43] flow map was in the region of 15 mPas, this discrepancy demonstrates that high viscosity fluids produce flow boundaries that are different to their low viscosity counterparts. It is not possible from this study to accurately determine the degree to which high viscosity alters the flow pattern boundaries. What is illustrated by these flow pattern maps is that the majority of test data were recorded in the annular flow regime.

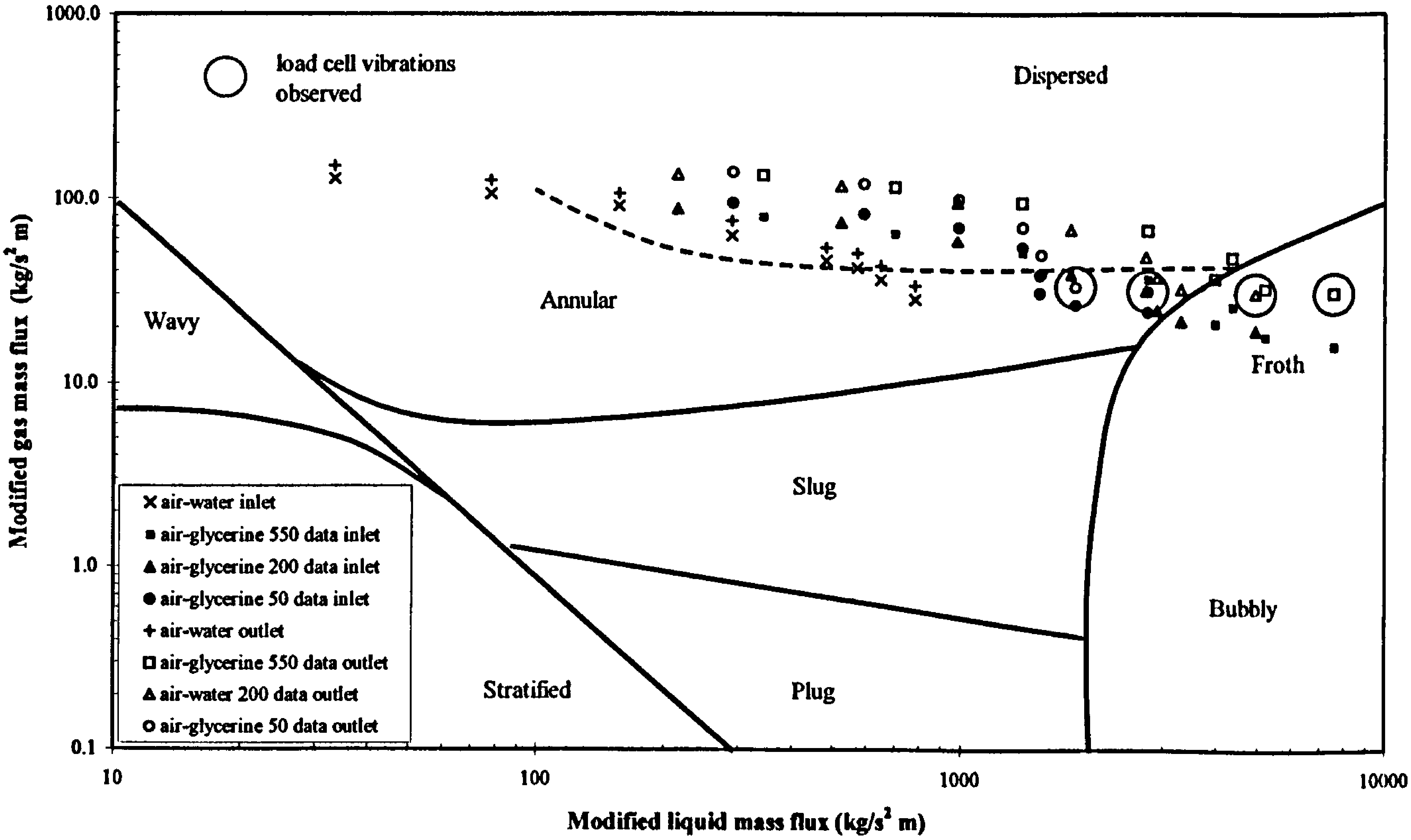

Figure 7.3: Horizontal Flow Map of Baker [43], Pipe Length Data

7.3 Analysis of Pipe Length Data

The data reduction and analysis procedures described in this section were applied to the data obtained for the pipe length experiments detailed in Section 6.2. This is the same procedure employed in McNeil & Stuart [122] (2003).

7.3.1 Data Reduction Procedure

To evaluate the local properties of wall shear stress, interfacial shear stress, liquid film thickness and interfacial friction factor, a data reduction procedure was devised. The procedure was based upon four assumptions;

1. The fluid flow could be described by an annular flow model that involved entrained liquid travelling at the gas velocity.
2. Acceleration effects in the liquid film could be neglected.
3. The method of Ambrosini *et al* [98] could be used to evaluate the liquid film thickness.
4. The gas-phase flowed isothermally and could be treated as a perfect gas.

Describing the fluid flow using an annular flow model enabled local film properties to be determined once the corresponding values of the entrained liquid fraction had been set. For a given value of entrained liquid fraction, all corresponding local flow properties at a given position in the test length could be determined using an iterative procedure. Film properties were evaluated by finding the values of the wall and interfacial shear stress, τ_w and τ_i, that provided a solution to nine simultaneous equations.

From an initial guess of the wall and interfacial shear stresses and the film thickness, the characteristic shear stress, τ_c, was calculated from;

$$\tau_c = \frac{(\tau_i + 2\tau_w)}{3} \tag{7.1}$$

The pre-set entrained liquid fraction, '*E*' was then used to calculate the specific volume of the core flow, v_c;

$$v_c = \frac{\left(x v_g + E(1-x) v_l\right)}{\left(x + E(1-x)\right)} \tag{7.2}$$

the core mass flux, G_c;

$$G_c = \frac{4\left(M_g + EM_l\right)}{\pi(D-2\delta)^2} \tag{7.3}$$

and the liquid film Reynolds number, Re_{lf};

$$\mathrm{Re}_{lf} = \frac{(1-E)(1-x)GD}{\mu_l} \tag{7.4}$$

Assumption number three allowed the non-dimensional film thickness, δ^+_l, to be found from liquid film Reynolds number using the correlation of Ambrosini *et al* [98];

$$\delta_l^+ = B\,\mathrm{Re}_{lf}^n \tag{7.5}$$

where the coefficients B and n are defined for film Reynolds numbers less than 1000, i.e., laminar flows, as 0.34 and 0.6 respectively and for film Reynolds numbers greater than 1000, i.e., turbulent flows, as 0.0512 and 0.875 respectively. The liquid film thickness, δ, was then calculated from;

$$\delta = \frac{\mu_l}{\delta_l^+}\sqrt{\frac{v_l}{\tau_c}} \tag{7.6}$$

Compressible flow effects ensured that the pressure gradient was not linear so a second order quadratic was used to provide a 'best-fit' of the ten local pressure readings taken along the test length. Figure 7.4 shows a typical curve and 'best fit' equation for the air-water values for a nominal quality of 0.04. Appendix E contains the constants for all other air-water and air-glycerine tests. The pressure gradient, *dp/dz*, was obtained at any pipeline location by differentiating the quadratic equation.

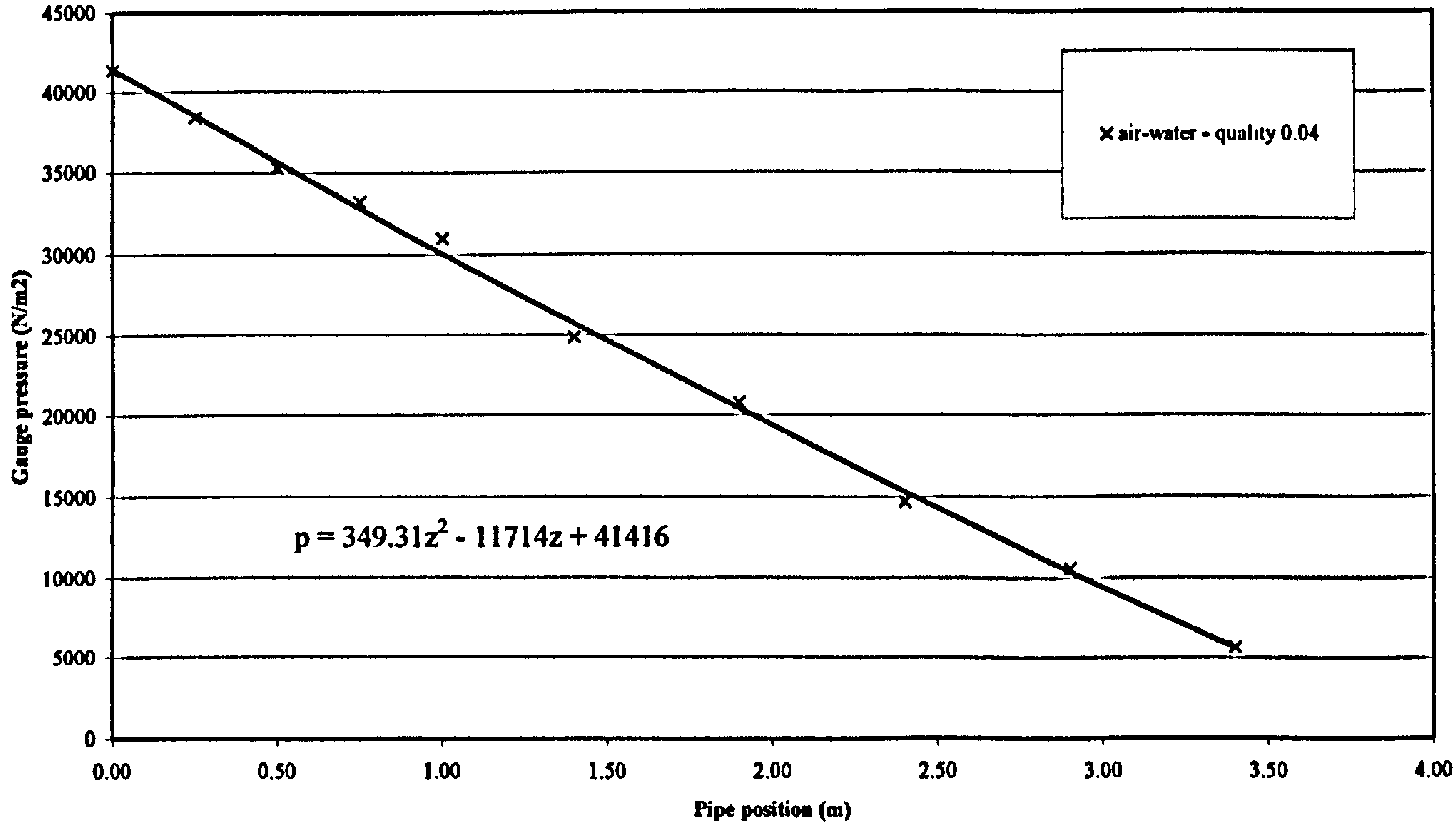

Figure 7.4: Variation of Local Pressure Along Test Length

Following assumption number four, the differential of the perfect gas law gave;

$$\frac{dp}{dv_g} = -\frac{p}{v_g} \tag{7.7}$$

Using the pressure gradient and Equation 7.7, and assuming the axial variation in the entrained liquid to be negligible, the specific core volume gradient, dv_c/dz, could then be defined by;

$$\frac{dv_c}{dz} = \frac{x}{(x+E(1-x))}\frac{dv_g}{dp}\frac{dp}{dz} \tag{7.8}$$

By neglecting the acceleration effects in the film flow, assumption number two, the momentum equation for the film can be written as;

$$\tau_i = \tau_w + \left(\frac{dp}{dz} + \frac{g}{v_l}\right)\delta \tag{7.9}$$

The corresponding momentum equation for the core flow is;

$$\tau_i = \left(\frac{dp}{dz} - \frac{g}{v_c} - G_c^2\frac{dv_c}{dz}\right)\frac{(D-2\delta)}{4} \tag{7.10}$$

Derivations of Equations 7.9 & 7.10 are given in Appendix A.3 & A.4 respectively.

A solution to Equations 7.1 to 7.10 was found by an iterative process that systematically altered the value of the wall shear stress until the outcomes of Equations 7.9 & 7.10 agreed.

7.3.2 Determination of Entrained liquid Fraction

The iterative process defined in Section 7.3.1 can only be employed to generate local conditions from the data if the entrained liquid fraction for the point of application is known. The entrained liquid fraction for each pipe length test was determined at the test length discharge by considering the measured momentum flow rates. An initial guess of the entrained liquid fraction allowed the liquid film thickness to be determined using the iterative process of Section 7.3.1 applied to the pipe exit. The calculated liquid film properties where used to solve Equations 7.14 to 7.17, allowing the momentum force to be calculated from Equation 7.13. A further iterative loop was devised that consequentially altered the value of entrained liquid fraction and recalculated the liquid film properties, by resolving Equations 7.1 to 7.10, until the values of the calculated and measured momentum forces agreed.

The values of entrained liquid fraction used to initialise this loop were either, for the air-water flows determined from the correlation of Govan *et al* [59] (1988), or for the air-glycerine flows assumed to be zero. The entrained liquid fraction at the test length discharge for the air-water and all three air-glycerine flows are plotted against the superficial gas velocity in Figure 7.5. The entrained liquid fraction for the viscous liquid is represented by;

$$\sqrt{\frac{E}{1-E}} = He^{Gu_g} \tag{7.11}$$

Table 7.1 contains the constants G, and H, for each of the three glycerine nominal viscosities.

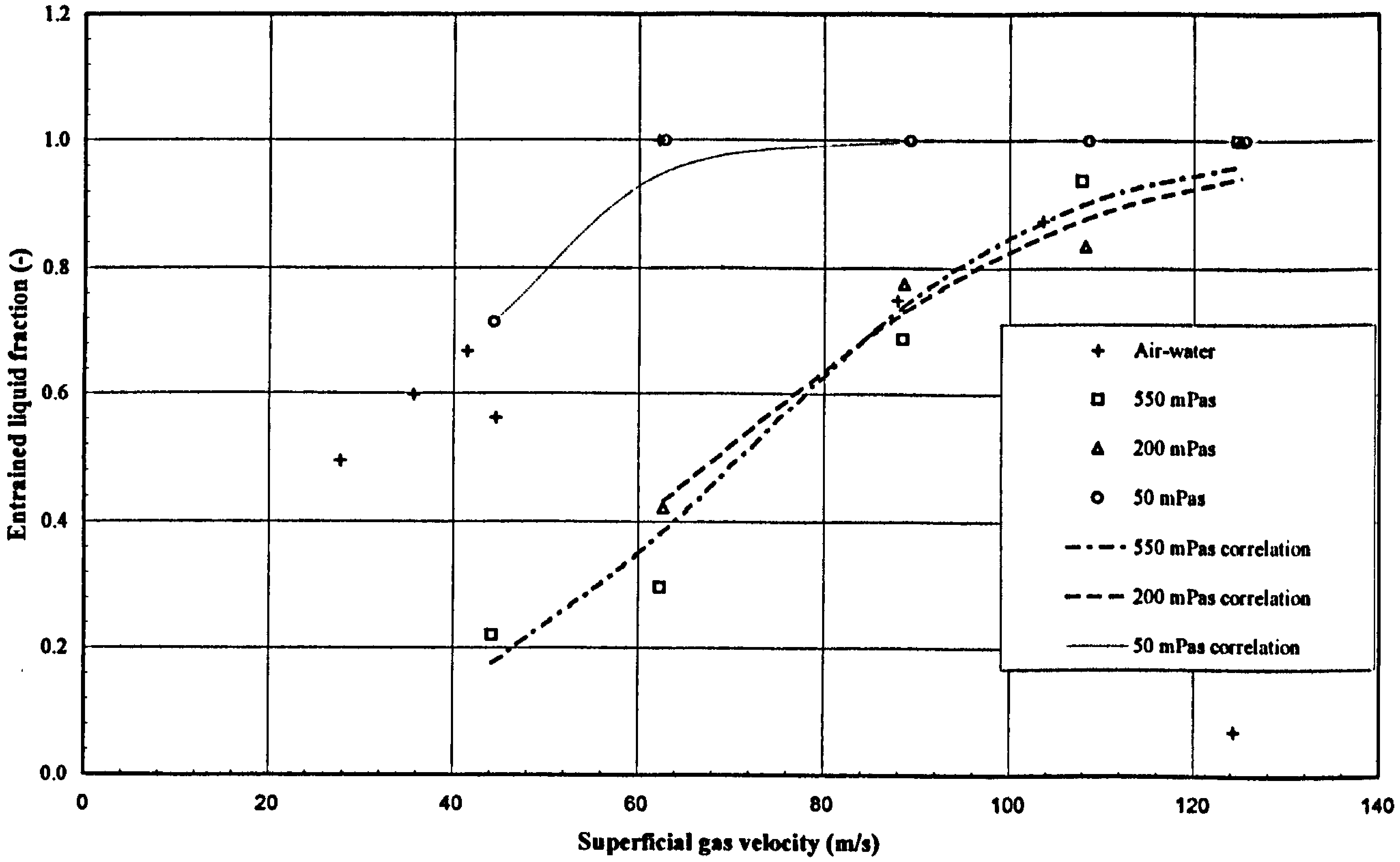

Figure 7.5: Entrained Liquid Fractions.

Viscosity (mPas)	G (-)	H (-)
50	0.0546	0.141
200	0.0245	0.188
550	0.0292	0.127

Table 7.1: Entrained Liquid Fraction Extrapolating Coefficients

7.3.3 Validation of Entrainment Correlation

The determination of the entrained liquid fraction is reliant on the assumption that Equation 7.11 and Table 7.1, based on pipe discharge data, can provide meaningful values for the entrained liquid fraction at any position in the test length. The validity of this assumption was tested using air-water entrained liquid fractions predicted at the pipe exit from correlations and extrapolated to locations along the test length. The same correlations were used at the test length locations to evaluate the procedure. A modified version of the correlation of Govan *et al* [59] allowed the comparison to be made.

Mori & Nakano [99] (2001) noted that one of the effects of viscosity was that the onset of liquid entrainment was not singularly dependent on the occurrence of disturbance waves. Although liquid entrainment certainly increased with the occurrence of disturbance waves, entrainment was present at all liquid velocities, suggesting that the inception of droplets into the gas phase could not be attributed to a critical liquid velocity. To better represent the behaviour of the entrained liquid fraction for the range of mass fluxes tested when applying the Govan *et al* [59] correlation, the critical Reynolds number was set to zero. Setting the critical Reynolds number to zero allowed, in accordance with Pan & Hanratty [78] (2002), the ratio $E/(E-1)$ to be used as a modelling parameter. This ratio is shown in Figure 7.6 as a function of the superficial gas velocity for the values obtained from the Govan *et al* [59] correlation. If a second order quadratic is fitted to the curve, the resulting entrained liquid fraction equation based on the test length exit properties of the air-water data is;

$$\sqrt{E/(1-E)} = 0.247 + 0.0451u_{gs} - 0.0001 1u_{gs}^2 \tag{7.12}$$

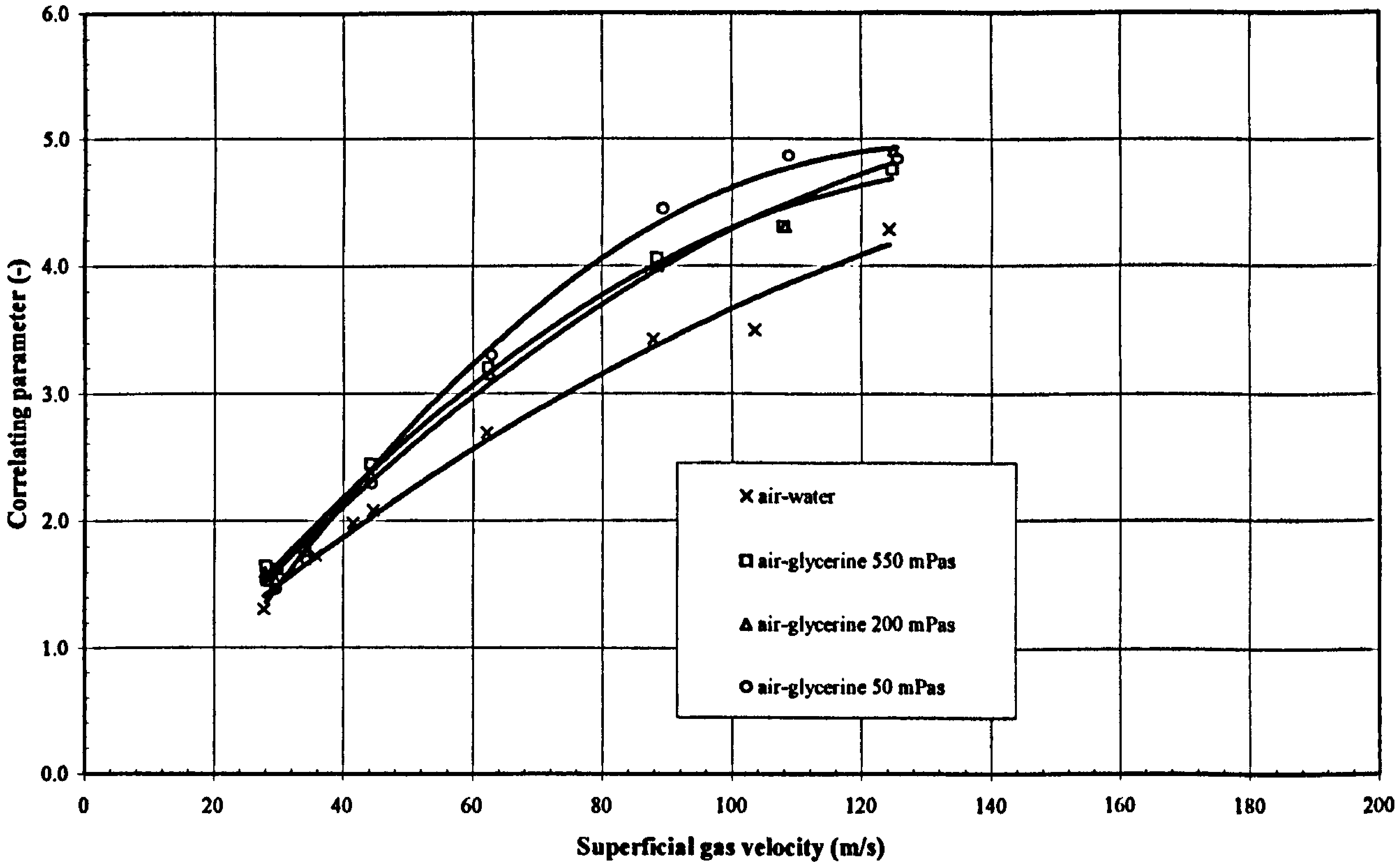

Figure 7.6: Correlations of Exit Liquid Entrainment

For the ten local pressure measurement locations on the test length, the entrained liquid fraction was evaluated using the Govan *et al* [59] correlation with the critical Reynolds number set to zero. For these same ten locations, the gas superficial velocity was calculated and used in Equation 7.12 to obtain extrapolated values for the entrained liquid fraction. Figure 7.7 is a comparison between these extrapolated values and those obtained in-tube using the Govan *et al* [59] correlation. It can be seen from the graph that all the entrained liquid fractions at any position on the test length are predicted to within ± 10%. As the overall pressure drop of the highly-viscous flows is largely dominated by the frictional pressure gradient, the effect that the entrained liquid fraction has on the determination of the wall shear stresses is limited. Thus, this level of error was considered acceptable.

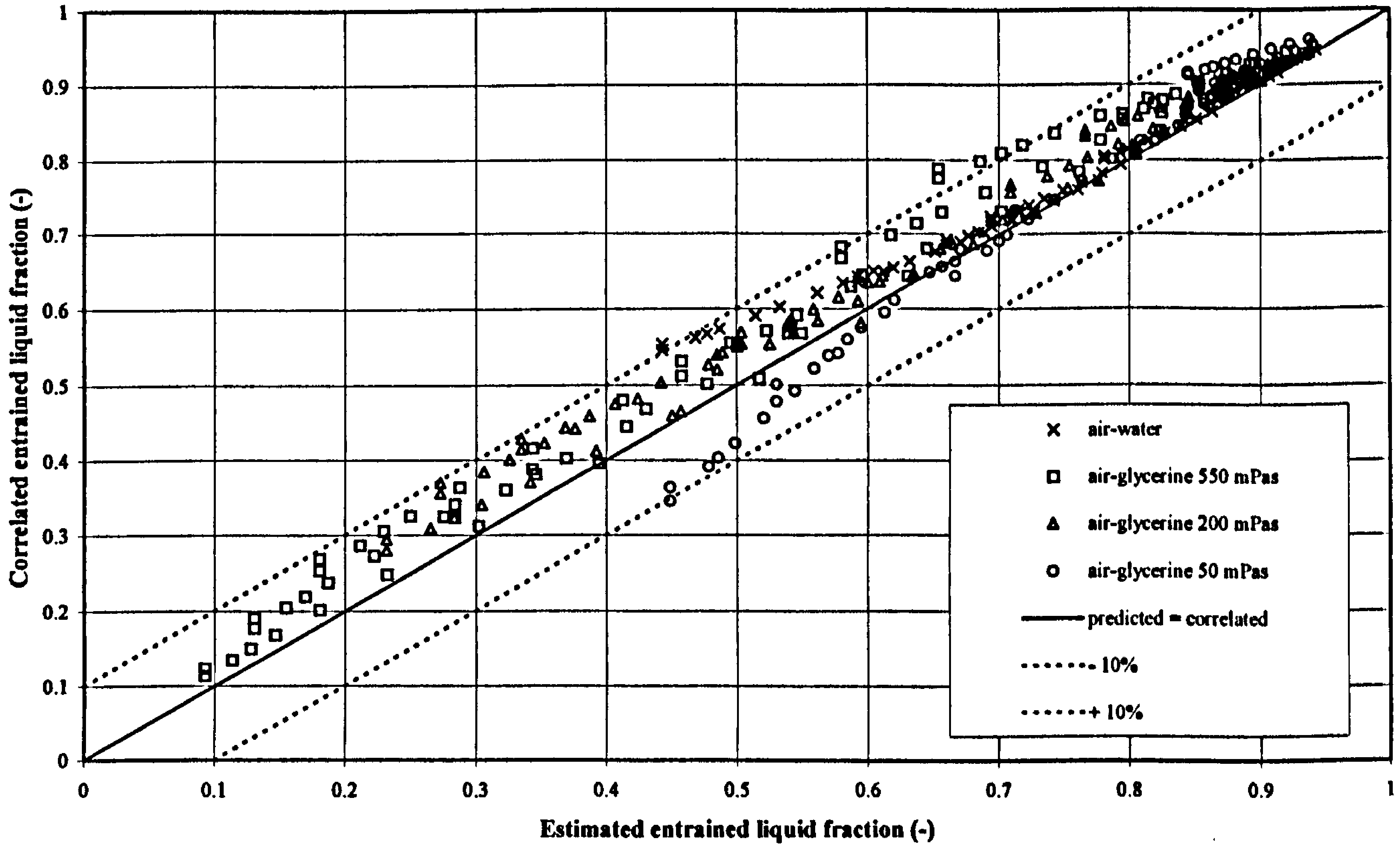

Figure 7.7: Variation of Predicted with Correlated Entrained Liquid Fraction

7.3.4 Calculation of Local Film Properties

Having devised a data reduction procedure and a modelling equation for the entrained liquid fraction, it was possible to evaluate liquid film properties at the ten local pressure positions on the test length. For the air-glycerine flows, the coefficients given in Table 7.1 were used to calculate the entrained liquid fraction from the superficial gas velocity. For the air-water flows the correlation of Govan *et al* [59] was used to calculate the entrained liquid fraction. The data reduction process of Section 7.3.1 was employed using these values for the entrained liquid fraction to obtain all other liquid film properties.

Figures 7.8 to 7.15 show the liquid film properties as they vary along the test length for all four test liquids. The highest wall and interfacial shear stresses are found in the 550 mPas nominal viscosity tests. At the lowest qualities of the air-water flows the shear stresses can be seen to decrease along the test length. The opposite is true for 550 and 200 mPas nominal viscosity where the shear stresses increase towards the test length exit. A significant difference in wall and interfacial shear stress is found at the high viscosities which decreases at the higher qualities. There is almost no observable difference in the wall and interfacial shear stress of the air-water and 50 mPas flows.

As would be expected, the highest gas velocities are found at the qualities where the gas mass flux is greatest and thus producing the highest slip ratio. The gas velocity can be seen to increase as the gas phase travels along the test length towards the exit and this is most pronounced at the high viscosity flows due to the far greater pressure gradients. An increased gas velocity will incur greater interaction at the gas-liquid interface and in turn the opportunity for more liquid to become entrained in the gas stream will also increase.

Conversely the effect of increased viscosity on the gas-liquid interface is to reduce the interaction of the two-phases and retard the motion of the liquid film leading to an increase in the liquid film thickness. It can be seen from Figure 7.5 that the glycerine liquid film is less susceptible to becoming entrained in the air phase than the water liquid film. This increase in liquid film thickness due to increased viscosity is in keeping with Figure 6.2 where the void fraction was observed to decrease with viscosity.

A liquid film property that was not recorded along the test length was the test liquid temperature. Temperature was only recorded at the beginning of the test length based on the assumption that the two-phase mixture temperature would not fluctuate significantly as it flowed along test length. It can be seen from Figure 4.3 that as little as a half degree change in temperature would lead to over a 6% rise in the test liquid viscosity. Given that this relatively small change in temperature will have a significant effect on viscosity it is then important to establish the temperature changes that may occur along the test length.

If an all-liquid flow is assumed the temperature increase can be calculated from the pipe wall friction using the all-liquid pressure drop. For the liquid phases this produces at worst a temperature rise of 0.08°C translating to a 1.5% decrease in viscosity. This estimate for the change in test temperature is not conclusive as it does not allow for the temperature changes in the gas-phase nor the interaction of the two-phases.

Figure 7.8: Local Film Properties, Air-Water , Qualities 0.04 to 0.1

Figure 7.9: Local Film Properties, Air-Water , Qualities 0.2 to 0.8

Figure 7.10: Local Film Properties, Air-Glycerine, 550 mPas, Qualities 0.04 to 0.1

Figure 7.11: Local Film Properties, Air-Glycerine, 550 mPas, Qualities 0.2 to 0.8

Figure 7.12: Local Film Properties, Air-Glycerine, 200 mPas, Qualities 0.04 to 0.1

Figure 7.13: Local Film Properties, Air-Glycerine, 200 mPas, Qualities 0.2 to 0.8

Figure 7.14: Local Film Properties, Air-Glycerine, 50 mPas, Qualities 0.04 to 0.1

Figure 7.15: Local Film Properties, Air-Glycerine, 50 mPas, Qualities 0.2 to 0.8

7.3.5 Prediction of Momentum Flux

It was not possible to obtain the momentum flux of the discharging jet for all qualities. Some qualities exhibited a degree of vibration due to slugging which masked the true value of the force being measured by the load cells. Data points where significant vibrations were observed are marked on Figures 7.1 & 7.3.

The momentum force was predicted using the method of McNeil [57] (1998). This employs a momentum correction factor, c_m, to correct for the assumed velocity distribution of the phases. The force J, is calculated from;

$$J = c_m \frac{\pi}{4} D^2 G^2 v \tag{7.13}$$

where the specific volume,v, is calculated from;

$$v = \frac{\left(x v_g + k(1-x) v_l\right)}{\left(x + k(1-x)\right)} \tag{7.14}$$

and the momentum correction factor is given by;

$$c_m = \left(x + k(1-x)\right)\left(x + (1-x)\left(E + \frac{(1-E)^2}{(k-E)}\right)\right) \tag{7.15}$$

and the slip ratio, k, and core area fraction, α_c, are given by;

$$k = \frac{E}{\alpha_c} + \frac{(1-\alpha_c)}{\alpha_c} \frac{x}{(1-x)} \frac{v_g}{v_l} \tag{7.16}$$

$$\alpha_c = \left(1 - \frac{2\delta}{D}\right)^2 \tag{7.17}$$

An experimental all-liquid two-phase multiplier was calculated from the measured force using;

$$J = \phi_{lo}^2 \frac{\pi}{4} D^2 G^2 v_l \tag{7.18}$$

In Figure 7.16 the experimental all-liquid two-phase multiplier is compared to the homogeneous and separated flow theories defined by Equations 2.77 & 2.78 respectively. The value of the slip ratio used in Equation 2.78 for the separated flow theory was assumed to be that of maximum slip, i.e., an entrained liquid fraction of zero and a slip ratio given by Equation 2.62.

For all the qualities above 0.1 the air-water data of Figure 7.16 is represented well by the homogeneous flow theory. Below this quality the homogeneous theory over predicts the two-phase multiplier. Similarly the 50 mPas data also follows the homogeneous theory except for the lower qualities. The data of the 200 & 550 mPas flows set a slightly different experimental trend indicating an effect attributable to the increasing viscosity of the test liquid. The high viscosity data sits below the homogeneous theory values for all the qualities except the very highest, suggesting that

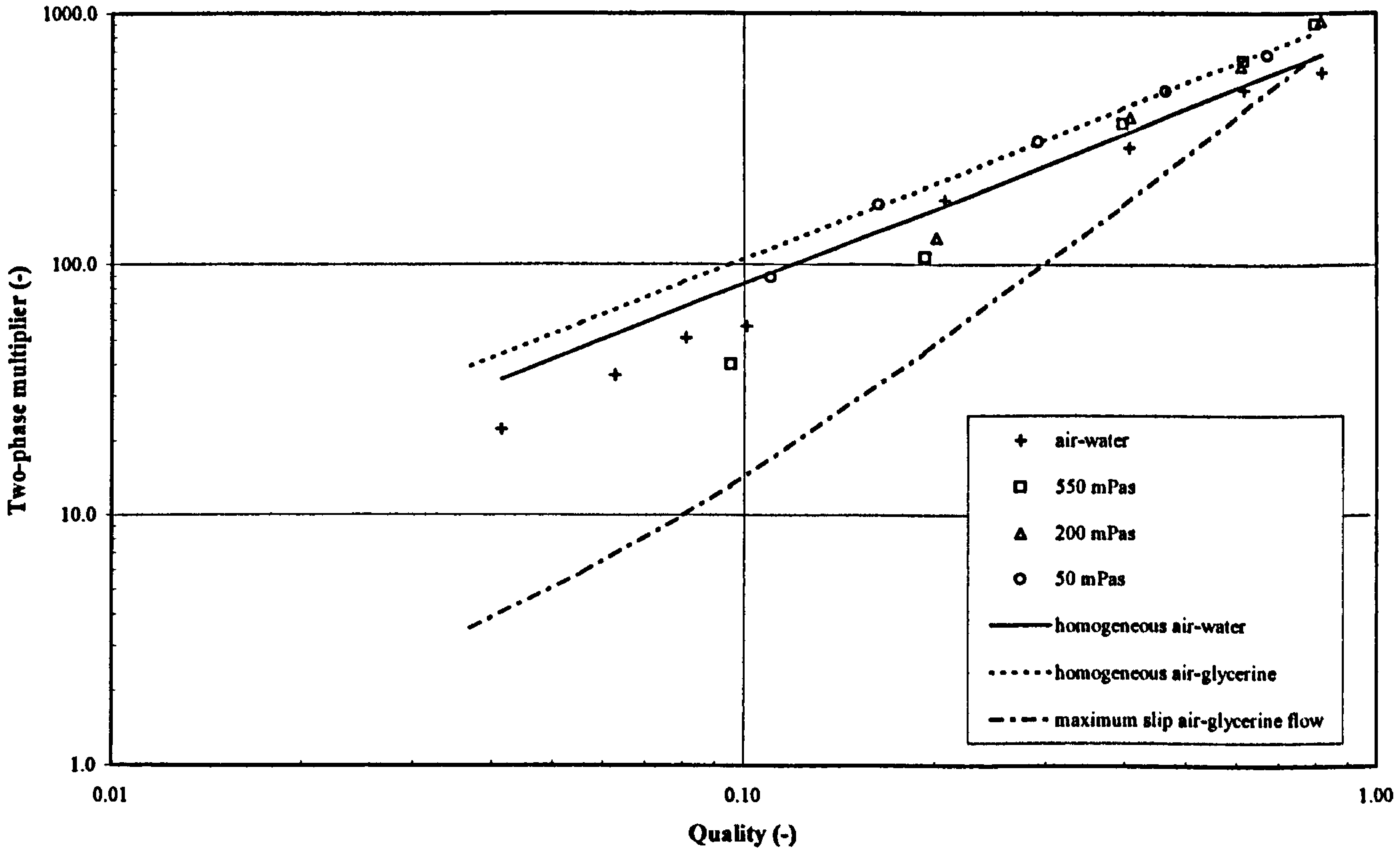

Figure 7.16: Comparison of Momentum Two-phase Multipliers

the air-glycerine has a lower entrained liquid fraction than that of the equivalent air-water flows. This is confirmed in Figure 7.6.

7.3.6 Void Fraction

The annular flow model adopted in Section 7.3.1 is based on the work of Ambrosini *et al* [98]. In Figure 7.17 the void fraction as determined in Section 7.3.1, labelled as Ambrosini *et al,* demonstrates good agreement with the measured void fraction. A common method used to predict void fraction is the correlation of Premoli *et al* [58] (1970) which was derived from low viscosity data. As can be seen from Figure 7.18, the Premoli *et al* [58] correlation does not perform well for the high viscosity flows. Void fraction can also be calculated using the C parameter method of Chisholm [56] (1983), Equation 2.38. The 'multiplier' data shown in Figure 7.19 is for a C parameter value of 25 and was calculated using;

$$\alpha = 1 - \frac{1}{\sqrt{\phi_l^2}} \qquad (7.19)$$

Agreement with the experimental data is again poor.

The void fraction correlations of Chisholm [104] (1962) and Fukano & Furukawa [96] (1998) were derived from viscous data sets. A comparison of these two correlations is given in Figure 7.20. The Chisholm [104] correlation poorly predicts the void fraction for the high viscosity flows but does perform well over the viscosity range from which it was derived i.e., 1 - 267 mPas. The Fukano & Furukawa [96] model performs markedly better than the correlations of Premoli *et al* [58] and Chisholm [104] but is less convincing when applied to the highest viscosity data.

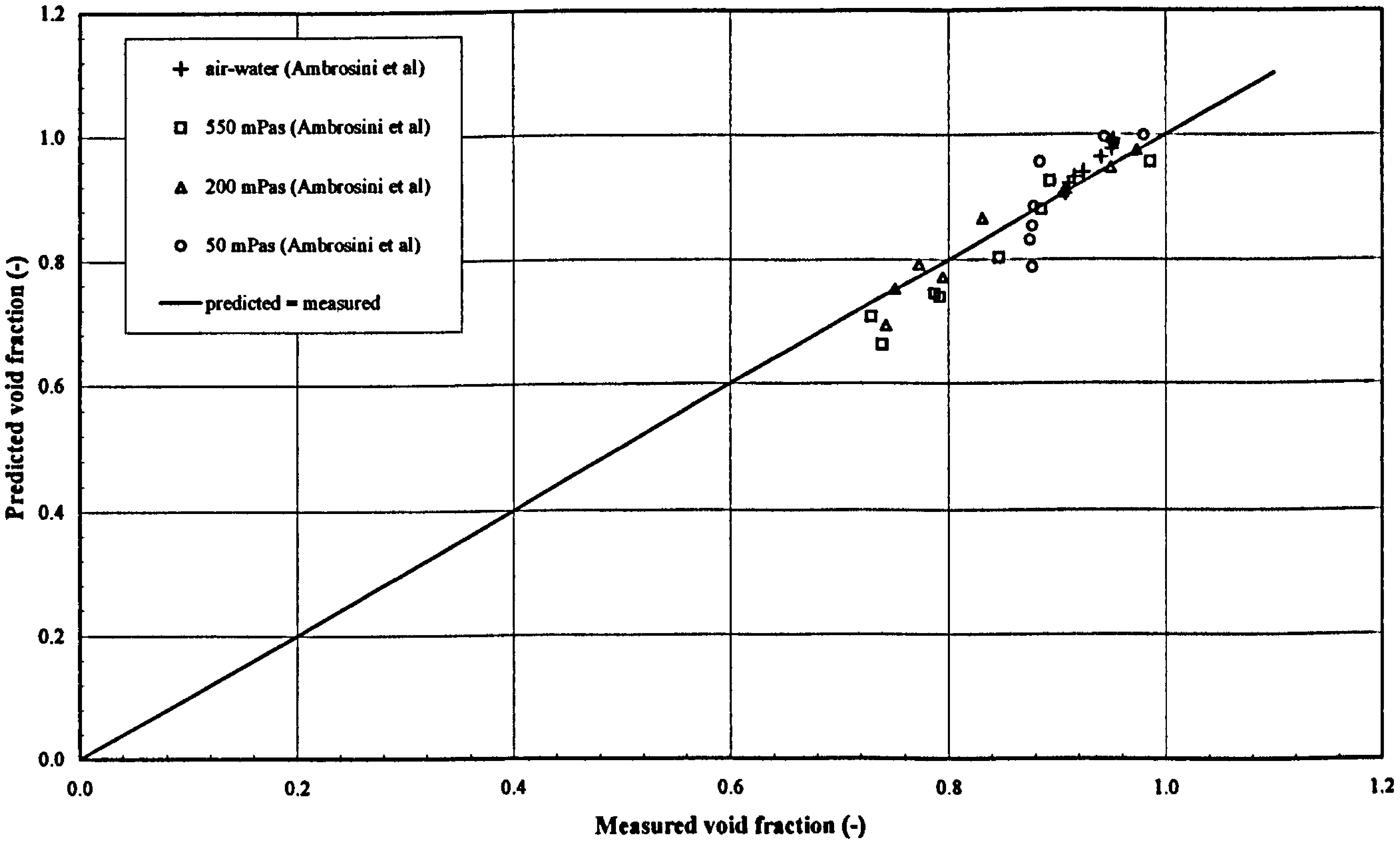

Figure 7.17: Variation of Predicted & Measured Void Fraction (Ambrosini *et al* [98])

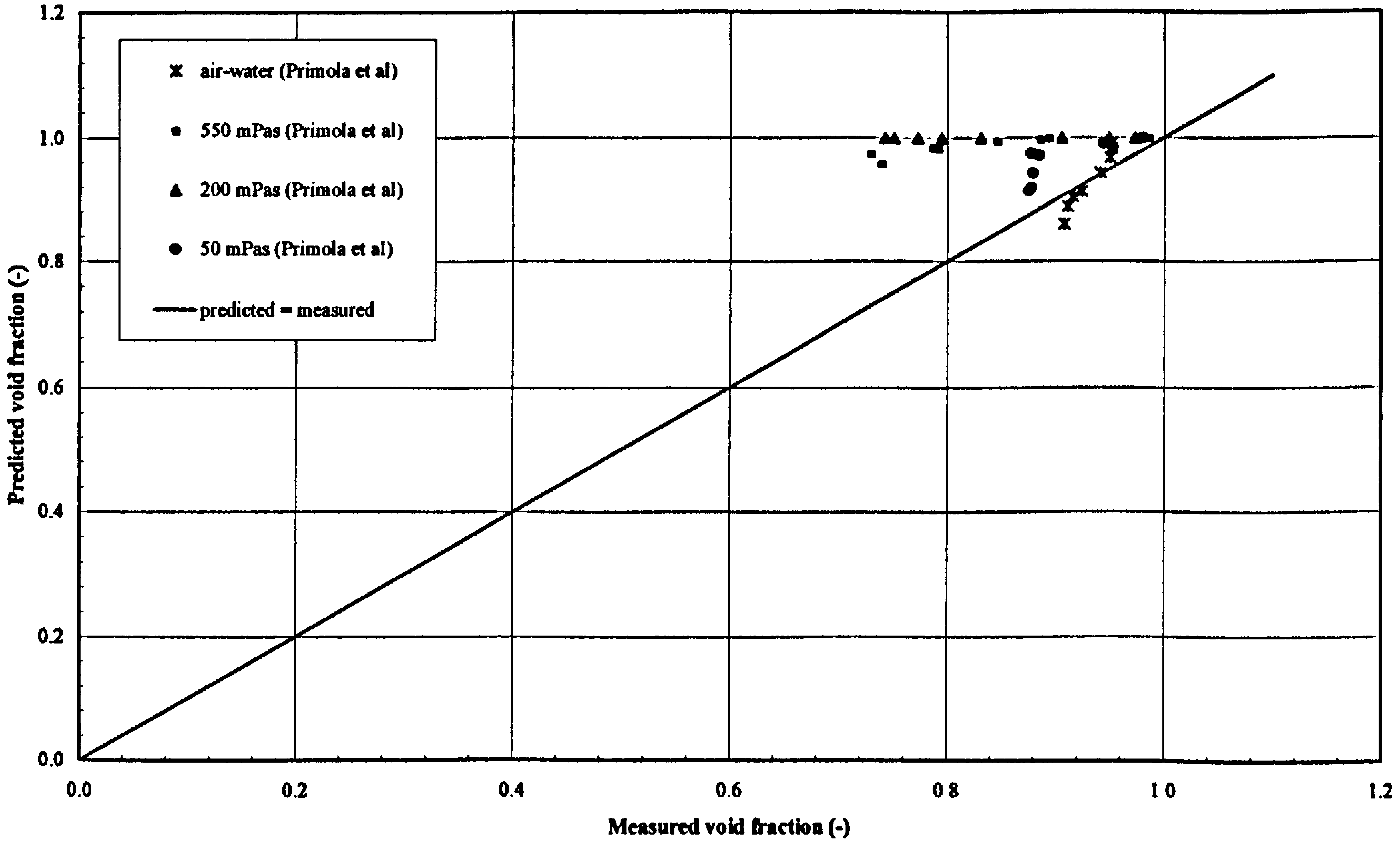

Figure 7.18: Variation of Predicted & Measured Void Fraction (Premoli *et al* [58])

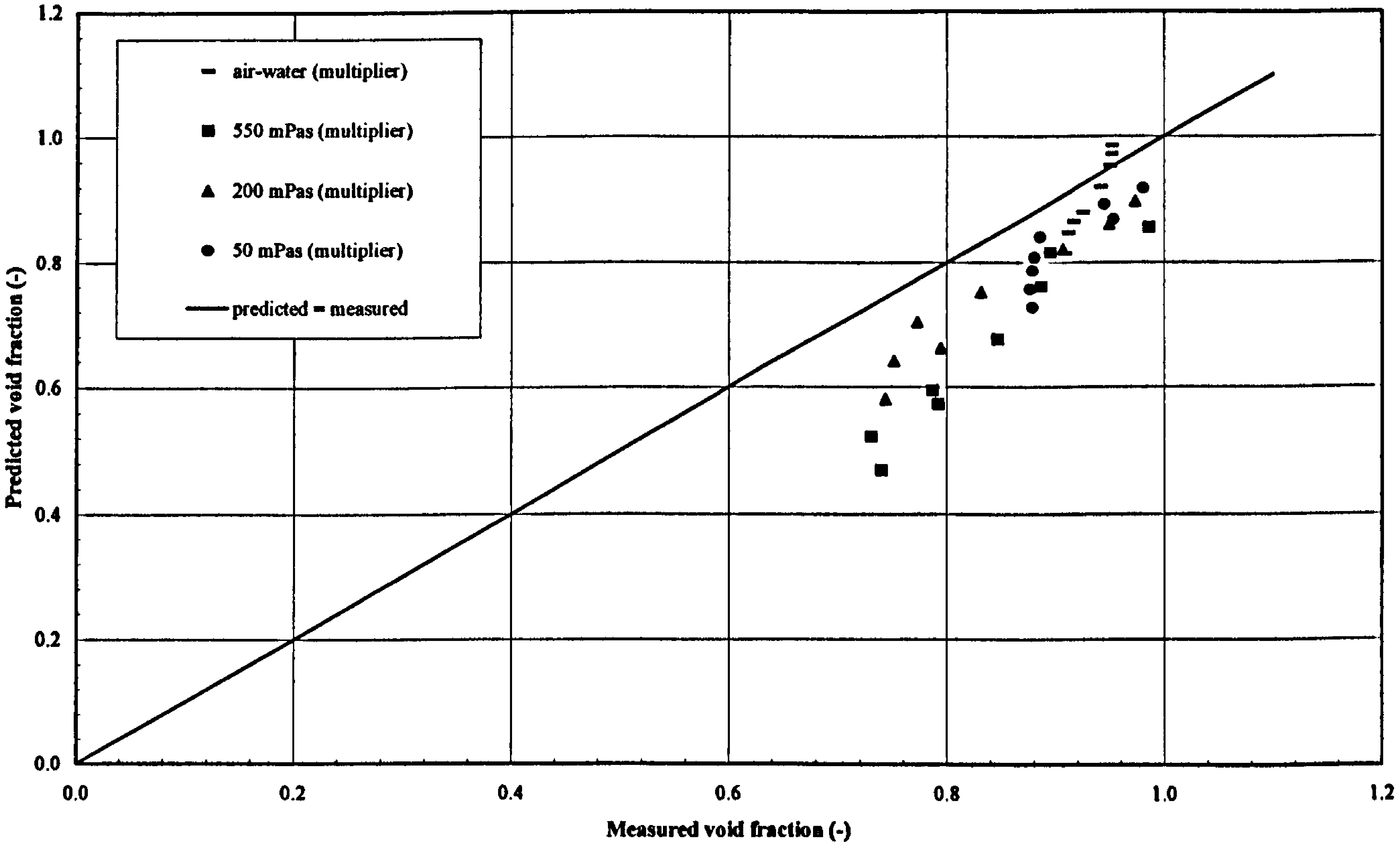

Figure 7.19: Variation of Predicted & Measured Void Fraction (Chisholm [56])

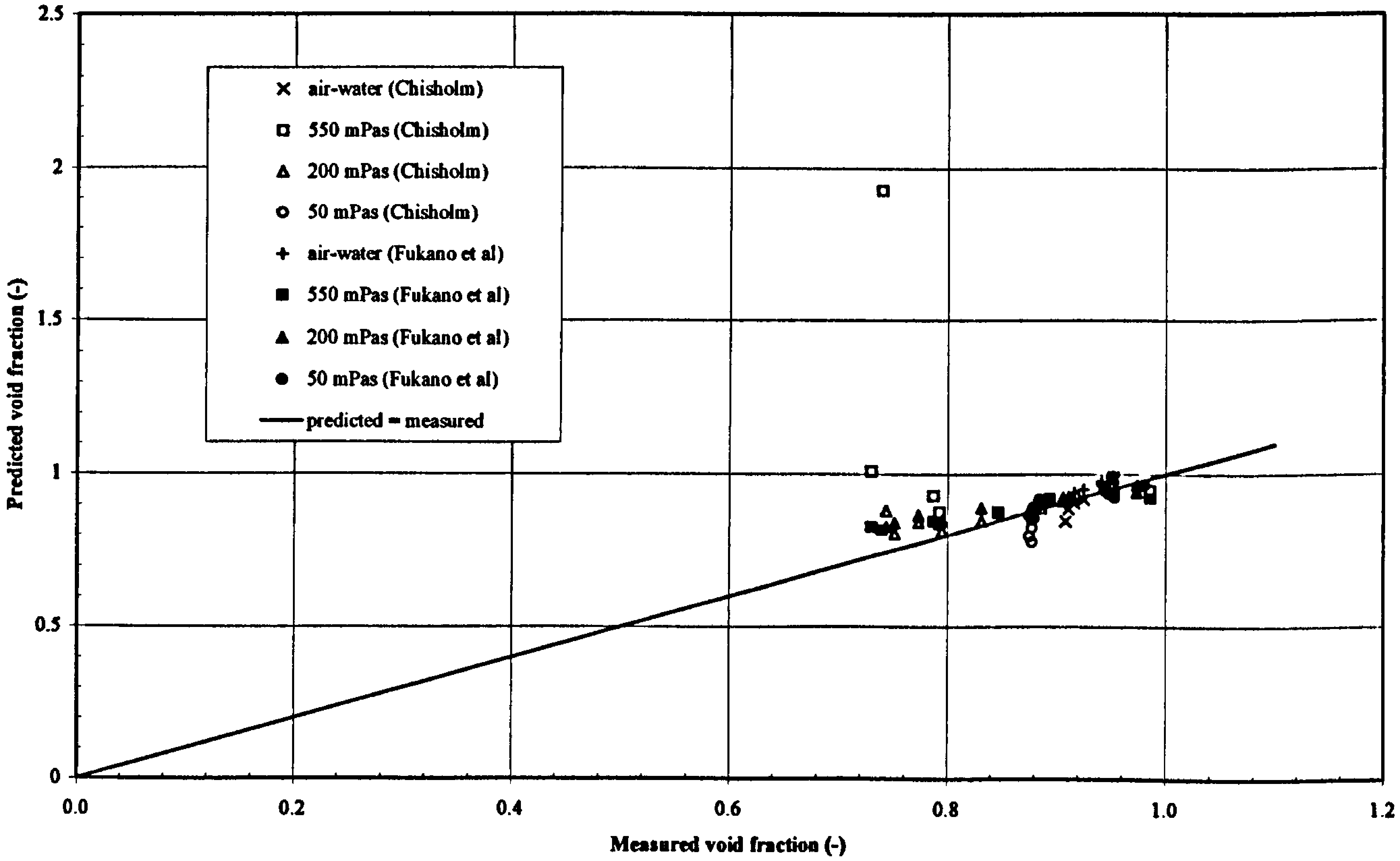

Figure 7.20: Variation of Predicted & Measured Void Fraction

7.3.7 Pressure Drop Measurements

The C parameter is a common method of two-phase pressure drop prediction and is given by Chisholm [56] (1983) and discussed in Section 2.5.11. To compare this method with the experimental data, the Martinelli parameter and the liquid-only two-phase multiplier were calculated from Equation 2.39 & 2.40 respectively. Figure 7.21 contains data evaluated using three values of the C parameter, 10, 21 and 25. The experimental values for the liquid-only two-phase multiplier shown in Figure 7.21 were calculated using the wall shear stress values determined using the method of Section 7.3.1. For the liquid phase flowing alone in the pipe the corresponding two-phase multiplier is given by;

$$\phi_l^2 = \frac{2\tau_w}{f_l(1-x)^2 G^2 v_l} \tag{7.20}$$

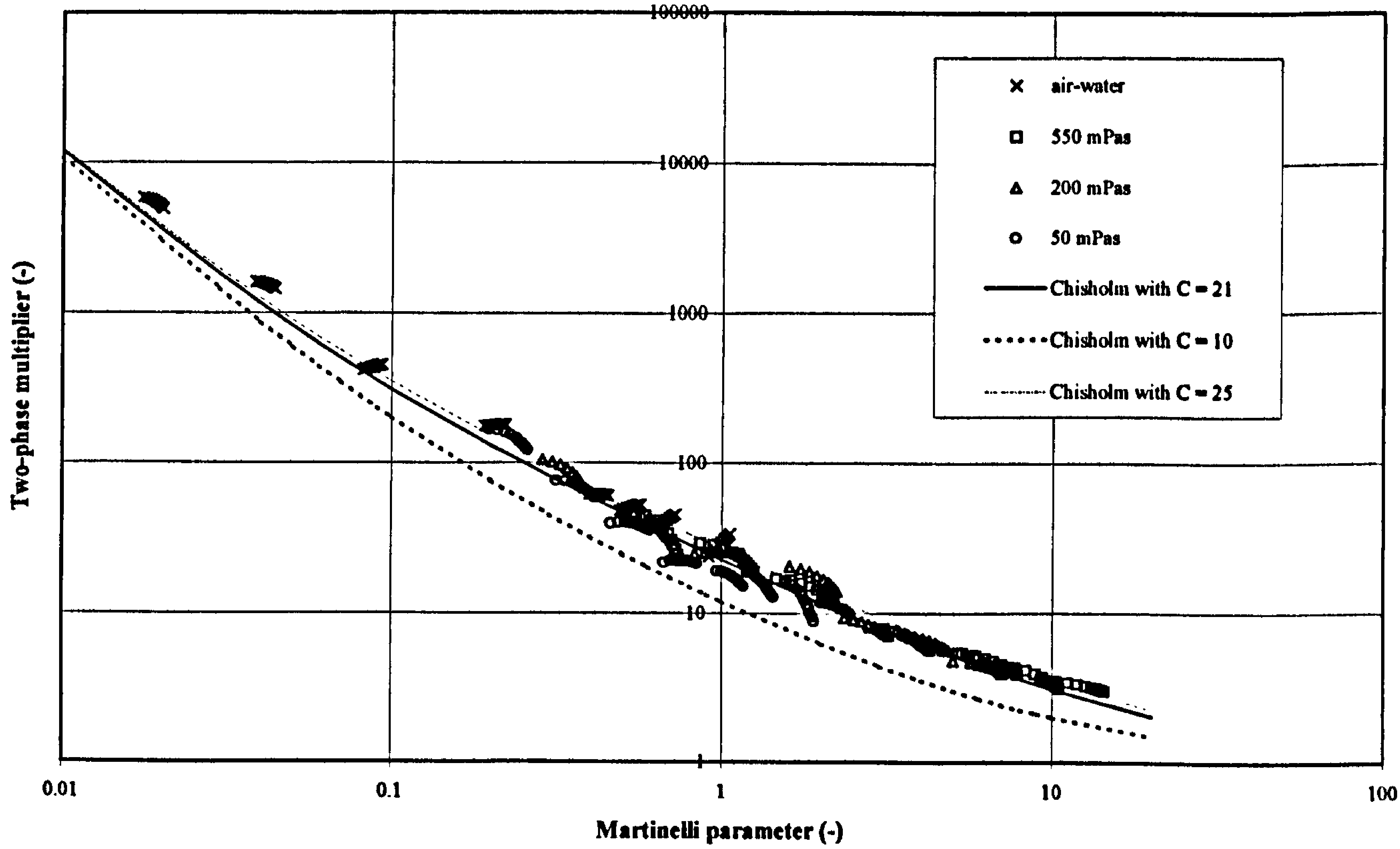

Figure 7.21: Comparison of Predicted & Measured Two-phase Multiplier

Recommended values for the C parameter are given in Table 2.1. Figure 7.21 shows that the air-water data, which is all turbulent-turbulent, is mostly correlated by a C parameter value of 21 as expected. Good agreement is also observed for air-water data by using a C parameter of value 25. This is not unexpected as Chisholm & Laird [123] (1958) reported correlating air-water flows in a 27 mm diameter vertical pipe using a C parameter value of 26.

The viscous data, which is all turbulent-laminar, is not correlated by the advised C parameter value of 10, Table 2.1, but is better correlated with a value of 25. The poor correlation of the air-glycerine data suggests that the C parameter method only extrapolates to high viscous flows if the C value is not altered. A further method of Chisholm [121] (1973) is the B coefficient method. The B parameter, defined by Equations 7.21 & 7.22, is compared with the experimental data in Figure 7.22.

$$B=\frac{C\Gamma-2^{2-n}+2}{\Gamma^2-1} \tag{7.21}$$

$$\Gamma=\left(\frac{\Delta p_{go}}{\Delta p_{lo}}\right)^{\frac{1}{2}} \tag{7.22}$$

The experimental values of Figure 7.22 were calculated by considering all the fluid as having the physical properties of the liquid phase giving the equivalent single-phase frictional pressure gradient as;

$$\left(\frac{dp}{dz}\right)_s=\frac{2f_{lo}}{Dv_l}u_{los}^2 \tag{7.23}$$

Also shown in Figure 7.22 is the correlation of Friedel [50] (1979) which is discussed in Section 2.5.8 and recommended as the best generally applicable correlation by Whalley [17] (1987). The air-water data is predicted well but the correlation significantly over-predicts the magnitude of the two-phase air-glycerine multiplier with the size of the error increasing with test liquid viscosity. This is not unexpected as the

Friedel [50] correlation is not recommended for flows where the ratio of the liquid to gas viscosity is greater then 1000, Whalley [17].

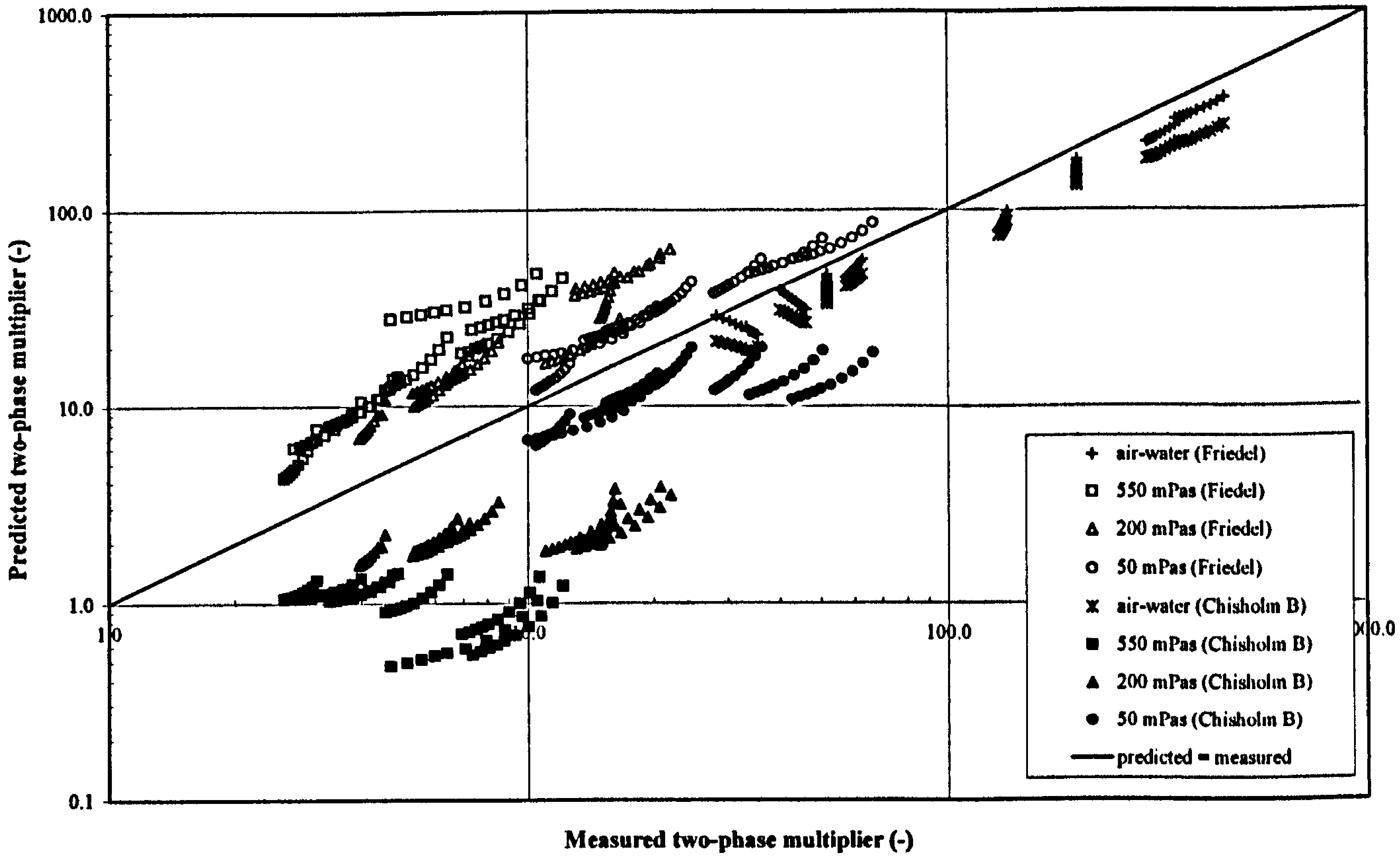

Figure 7.22: Comparison of Predicted & Measured Two-phase Multiplier

7.3.8 Interfacial Friction Factor

The values for the measured interfacial shear stress evaluated in Section 7.3.1 were used to determine an experimental value for the interfacial friction factor. The experimental interfacial friction factor was calculated from;

$$\tau_i = \frac{f_i}{2}\left(\frac{xG}{\alpha}\right)^2 v_g \tag{7.24}$$

The experimental interfacial friction factor is compared to the methods of Fukano & Furukawa [96] (1998) and Ambrosini *et al* [98] in Figure 7.23. The Fukano & Furukawa [96] method successfully mirrors the trend of the measured values and compares well for the air-water data, but it becomes less reliable as the viscosity of the test liquid increases. The method of Ambrosini *et al* [98] is prone to over prediction but performs considerably better than Fukano & Furukawa [96] method over the higher viscosity range.

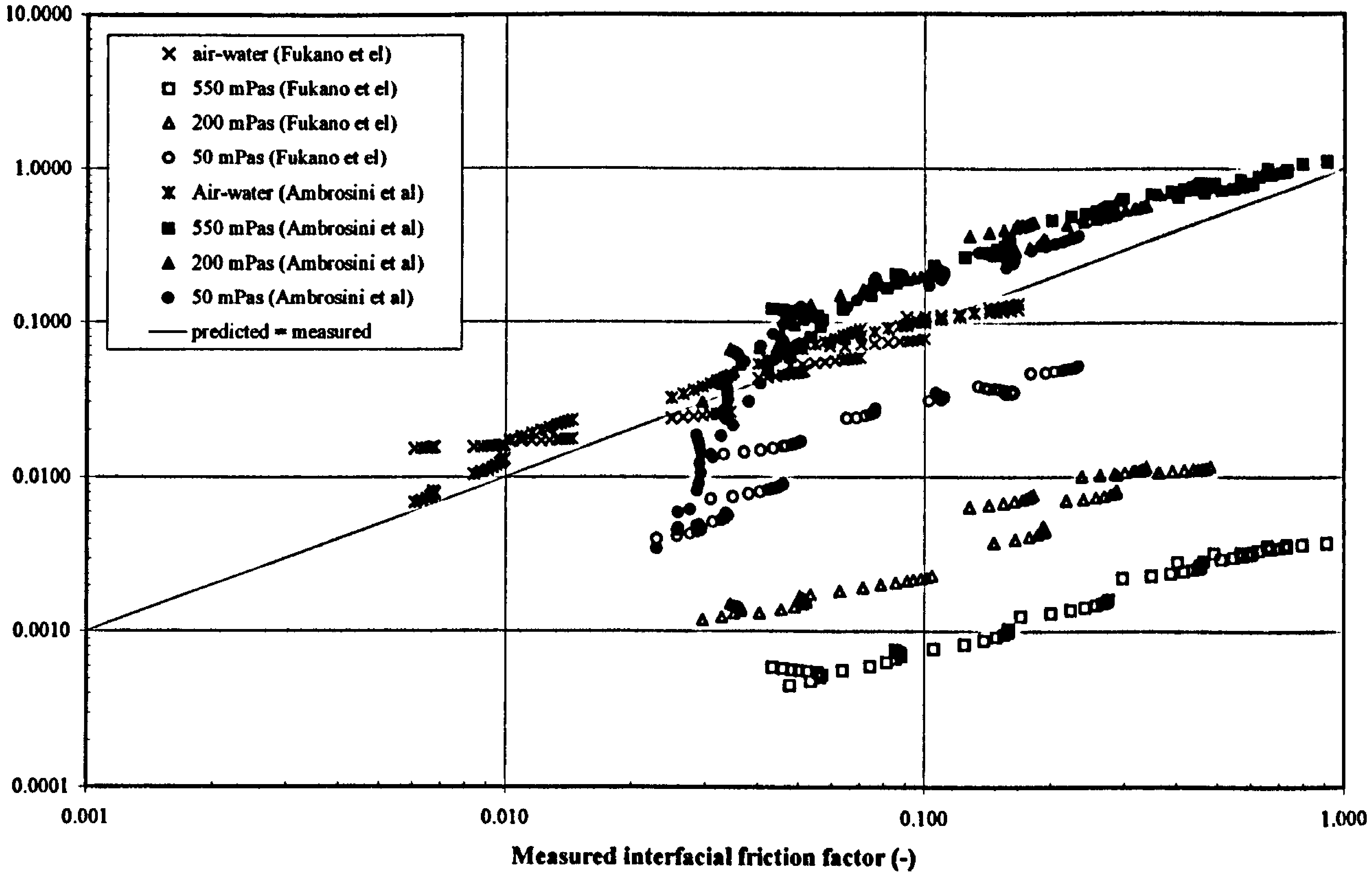

Figure 7.23: Predicted & Measured Interfacial Friction Factor

7.3.9 Conclusions

The inclusion of viscous liquids, 50 mPas viscosity or greater, in a two-phase pipe flow will have significant and observable effect. The viscous nature of the liquid phase leads to appreciably higher shear stress and pressure drops. The degree to which these properties increase is directly related to the viscosity of the liquid component. When applied to viscous flows, methods normally employed to predict the flow properties for air-water flows become inaccurate and unreliable.

It was necessary to establish the liquid entrainment fraction of the high viscosity flows from the experimental data using the annular flow model. Although the derived values were verified, the resulting entrainment correlations are specific to these tests and cannot be generally applied. The mechanisms of entrainment are not clear and none of the existing approaches are sufficient to accommodate the gas-liquid interactions present in a viscous flow.

Levels of liquid entrainment were found to decrease with increased viscosity, and this observation was supported by the momentum flux two-phase multipliers. The experimental values were located below that of the homogeneous model indicating decreasing values of liquid entrainment. The homogeneous model provided the best fit for the majority of the momentum flux data.

Void fractions were best predicted by the film method, based on the work of Ambrosini *et al* [98] and used in the annular flow model. When predicting the frictional pressure drop of high viscosity flows the best agreement was obtained by using the Chisholm [56] method with a C parameter of 25. Interfacial friction factor was most consistently predicted by the correlation of Ambrosini *et al* [98], although the agreement was poor.

7.4 Pressure Loss Due to In-Line Components

Existing correlations were compared with the in-line components, experimental data. Two-phase multipliers were determined using ESDU [117] (1989) recommendations, homogeneous and separated flow assumptions and the method of McNeil [118] (2000).

To apply the method of McNeil [118] film properties were evaluated upstream of the in-line components at a location of 1.2 m, Figure 3.2. These film properties were obtained using the annular flow model described in Section 7.3.1. The application of the annular flow model data reduction procedure required knowledge of the wall shear stress and the entrained liquid fraction. Wall shear stresses were obtained from the experimental pressure gradient. The entrained liquid fraction for the air-water flows was determined using the correlation of Govan *et al* [59]. It was assumed that pipe length constants, 'G' & 'H' of Table 7.1, could be used to obtain the entrained liquid fraction for the air-glycerine flows. This assumption was justified on the basis that the constants of Table 7.1 were evaluated under similar flow conditions to those of the in-line components.

7.4.1 Void Fraction

Equation 2.21 was used to determine the void fraction from the calculated film properties. Figure 7.24 shows the predicted against measured void fraction for all the in-line components and discharge components. The agreement is good.

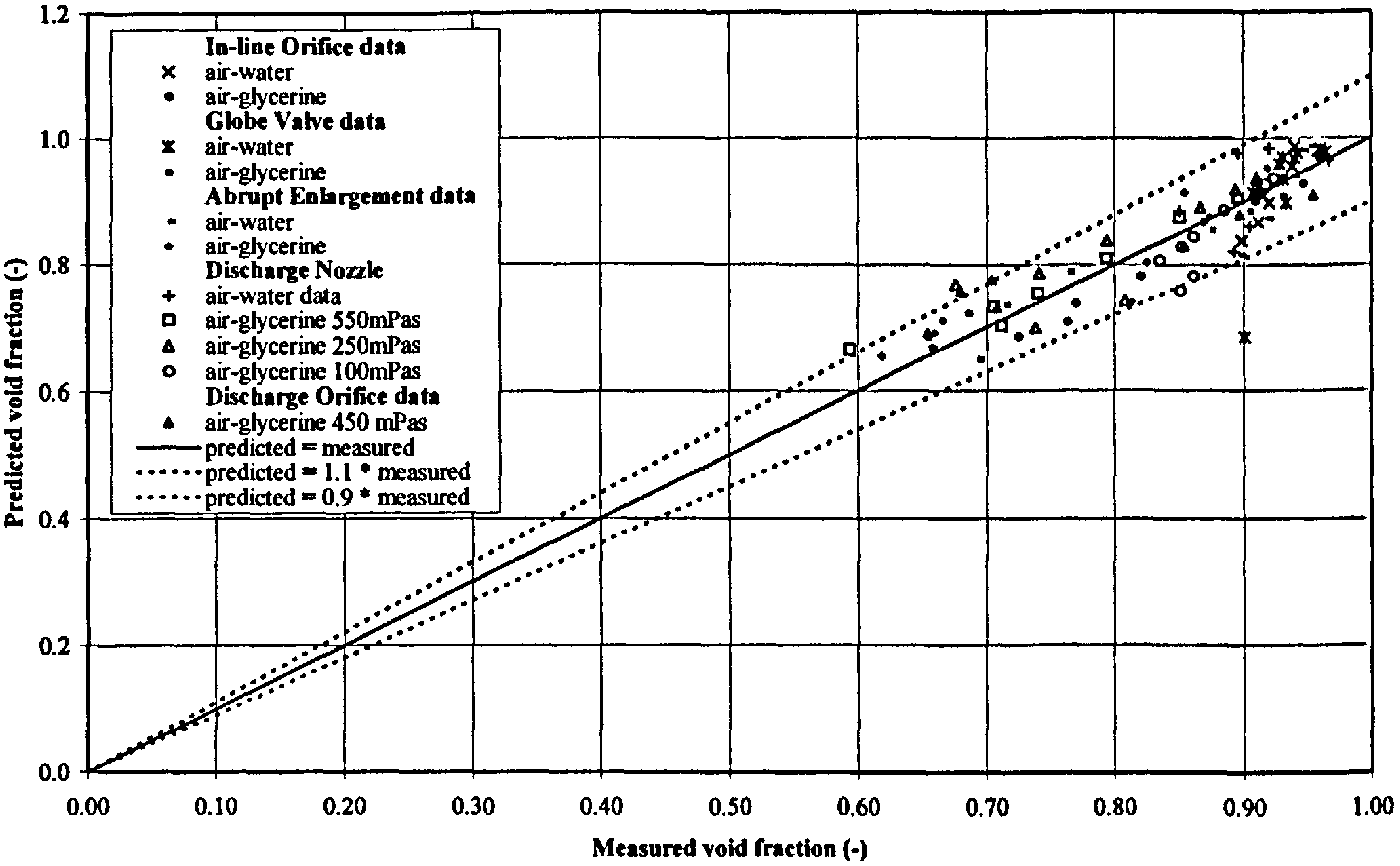

Figure 7.24: Variation of Predicted & Measured Void Fraction

7.4.2 In-line Orifice Plate

The single-phase loss coefficient data of Section 6.3.1 was compared to the method of Hooper [7] (1981), Equation 2.5. Figure 7.25 shows that the correlation of Hooper [7] produces the correct trend but the magnitude is far too great. When compared to the work of Edwards *et al* [10] (1985), the turbulent and laminar experimental loss coefficients of Figure 7.25 show some disagreement. Edwards *et al* [10] found loss coefficients to become independent of the Reynolds number at 60 and

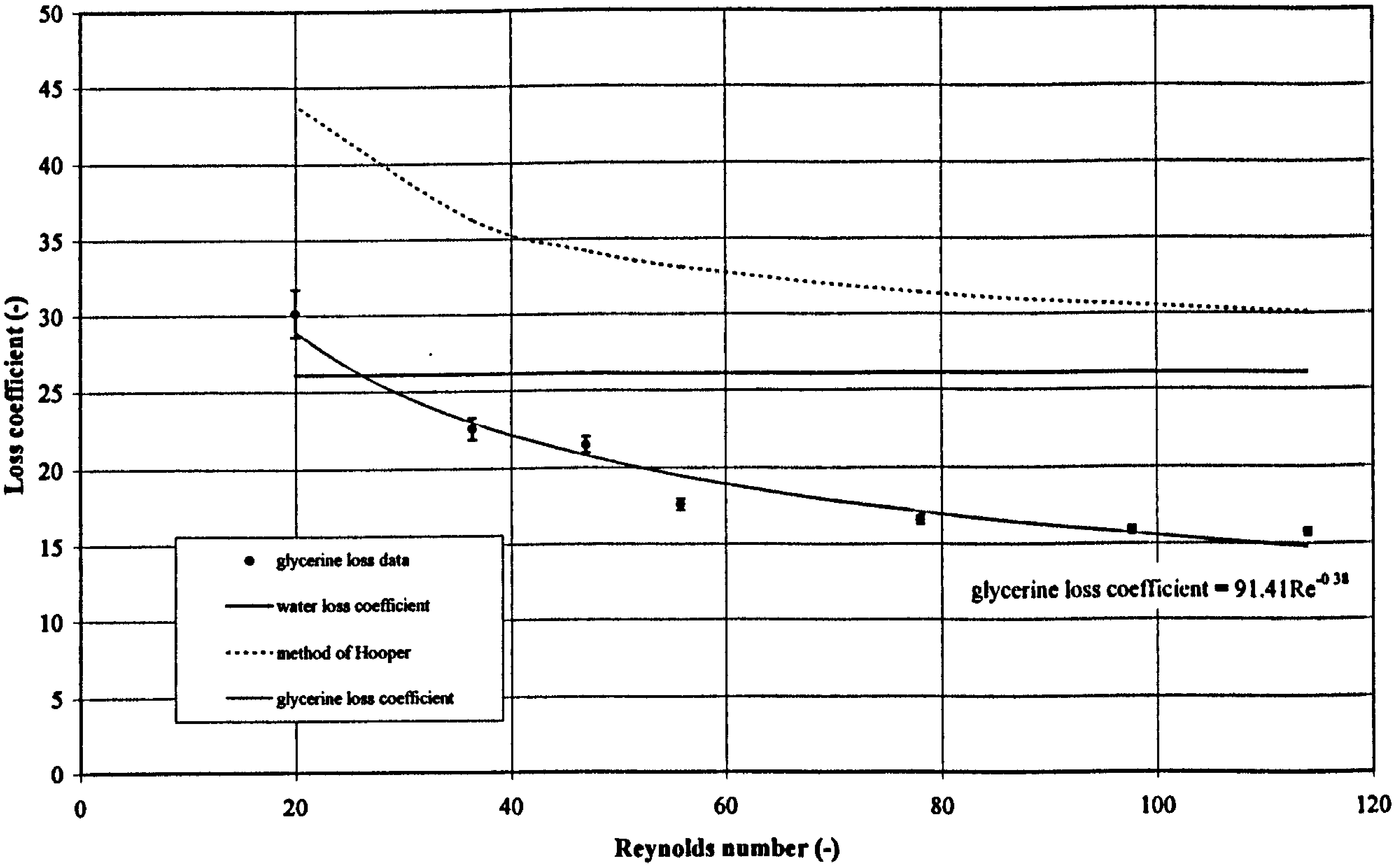

Figure 7.25: In-line Orifice Plate Single-Phase Loss & Pressure Drop Coefficients

19 at loss coefficients of 2.6 and 41.5 for orifice plates with diameter ratios of 0.577 and 0.289 respectively.

The two-phase data of Section 6.3.2 was first compared to the method of ESDU [117]. To determine the two-phase pressure drop across the orifice plate Equation 6.4 was used with the ESDU [117] definition of two-phase multiplier for an orifice plate;

$$\phi_{lo}^2 = \left[1 + x\left\{\left(\frac{v_g}{v_l}\right)^{1/6} - 1\right\}\right]\left[1 + x\left\{\left(\frac{v_g}{v_l}\right)^{5/6} - 1\right\}\right] \tag{7.25}$$

The predictions of the ESDU [117] method are shown in Figure 7.26 along with two sets of air-glycerine data points designated *laminar* and *turbulent*. The laminar air-glycerine data points were obtained as described in Section 6.3.2 using the single phase glycerine loss coefficient given in Figure 7.25. To obtain the turbulent air-glycerine data the single-phase loss pressure loss, Δp_{lo}, was calculated using the single-phase loss coefficient, β, for water also shown in Figure 7.25.

At the lower qualities there is good agreement between the ESDU [117] method and the data for both the air-water and air-glycerine but at the higher qualities the agreement is poor for both the water and the laminar and turbulent glycerine data.

Two-phase multipliers were also calculated based on the assumptions of homogeneous and separated flow. Using the homogeneous specific volume defined as;

$$v_h = x v_g + (1-x)v_l \tag{7.26}$$

the homogeneous two-phase multiplier was calculated from;

$$\phi_{lo}^2 = \frac{v_h}{v_l} \tag{7.27}$$

The two-phase multiplier for separated flow was obtained from;

$$\phi_{lo}^2 = \left(\frac{(1-x)^2 v_l}{(1-\alpha)} + \frac{x^2 v_g}{v_l} \right) \tag{7.28}$$

where the void fraction is given by Equations 2.21 & 2.62.

Figure 7.26 shows the resulting homogeneous and separated flow two-phase multipliers for both air-water and air-glycerine flows. The poorest performer is the homogeneous theory. This is most notable with the air-glycerine data where the predicted two-phase multipliers are much higher than the data and do not follow the experimental trend line. In contrast the separated flow theory gives a close fit for all the turbulent air-glycerine data except at the very highest qualities but is a poor predictor of the air-water data. The laminar air-glycerine data is not predicted by either approach.

The method of McNeil [118] for pipeline components with contraction-expansion type geometry's was applied to the in-line orifice plate. This slip model allowed theoretical contracted and expansion pressure losses to be calculated using a programme written in FORTRAN as described in Appendix A.5. An overall pressure loss was found by adding the contracted and expansion pressure losses.

The single-phase loss coefficient derived from the water data was used for both the air-water and air-glycerine results with Equations 6.3 & 6.4 to obtain the two-phase multipliers shown in Figure 7.27. At low qualities the model compares well for both air-water and turbulent air-glycerine flows. At the high qualities although the agreement is not exact it is an improvement on the methods shown in Figure 7.26. At the higher qualities the experimental data may contain compressibility effects and it is only the method of McNeil [118] that can accommodate them.

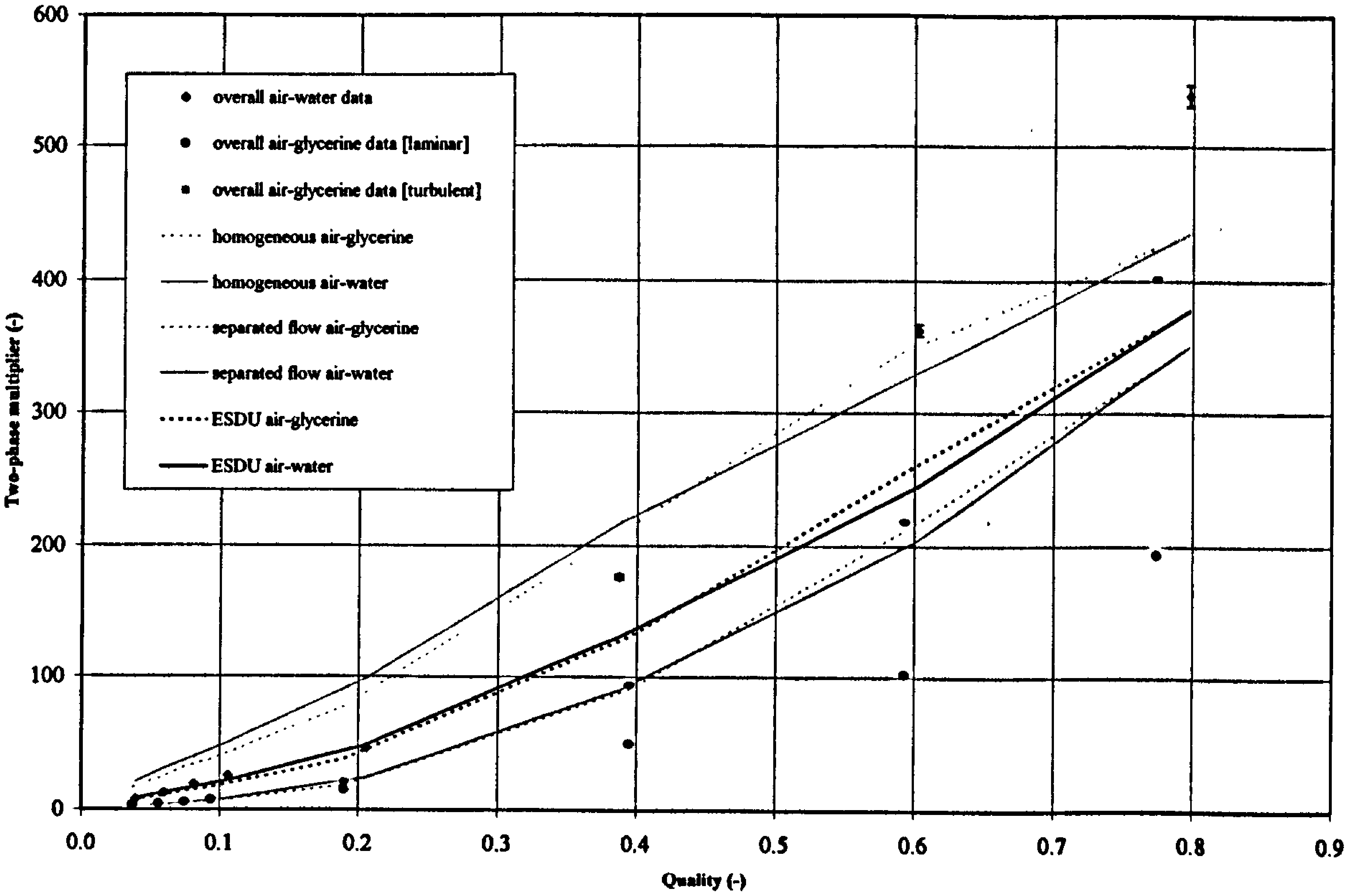

Figure 7.26: Comparison of In-line Orifice Plate Two-phase Correlations.

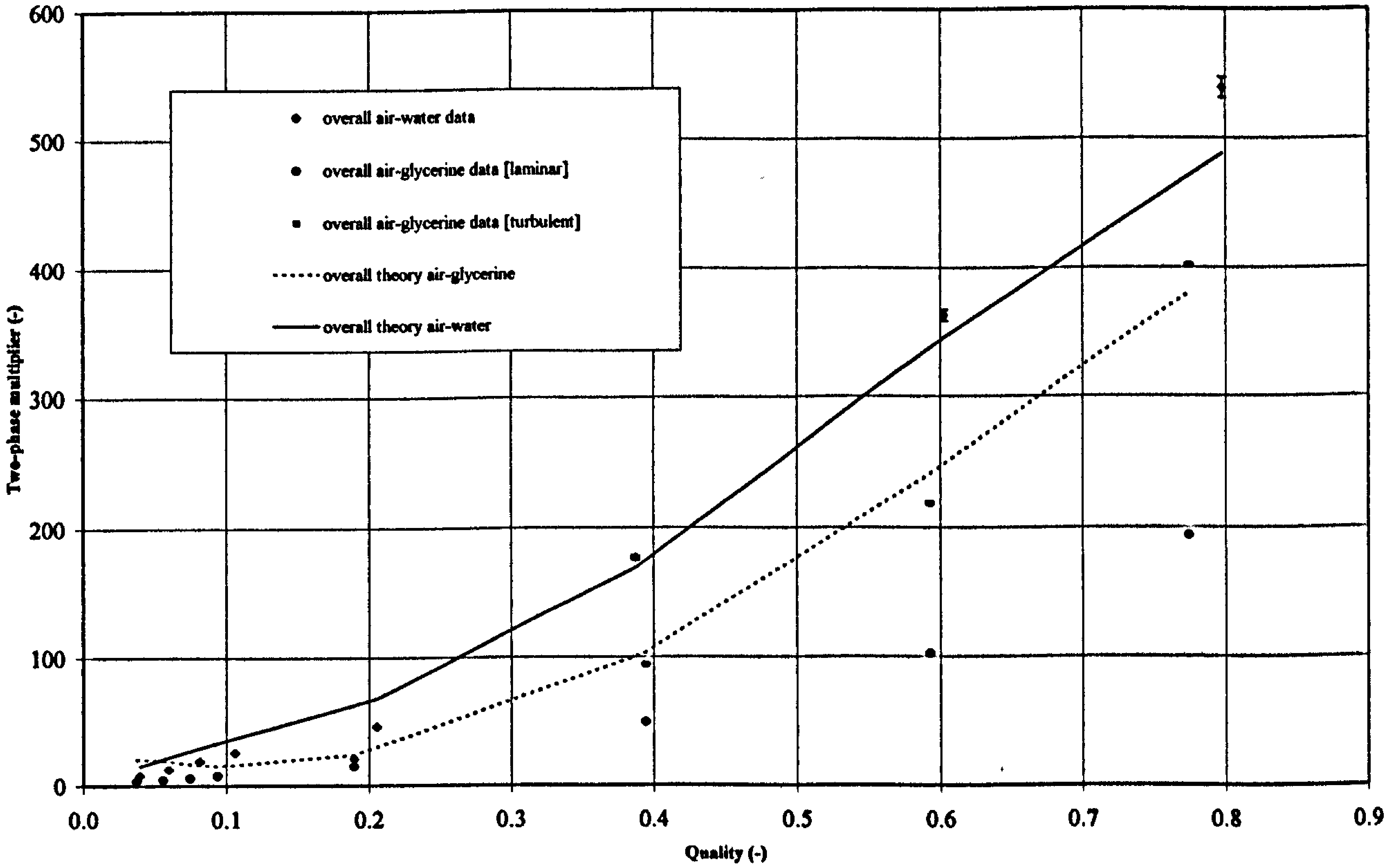

Figure 7.27: In-line Orifice Plate, Method of McNeil [118].

7.4.3 In-line Nozzle

The single-phase discharge and loss coefficients of Section 6.3.3 are plotted against Reynolds number in Figures 7.28 and 7.29 respectively. Figure 7.28 shows the theory of McNeil *et al* [120] (2000) in good agreement with the glycerine data.

In Figure 7.29 an unmodified and modified form of McNeil *et al* [120] is compared to the measured loss coefficients. To obtain the curve that agrees best with the experimental trend the method of McNeil *et al* [120] was modified by incorporating two further losses in addition to those incurred by the conical section of the in-line nozzle. These were the losses due to the abrupt enlargement down stream of the nozzle section, calculated from;

$$\Delta p_{lo} = \left(u_d c_{md} - u_u c_{mu}\right) Q \rho_l \tag{7.30}$$

where u_d and u_u are the velocities up and down stream of the nozzle and c_{md} and c_{mu} are the respective up and down stream momentum correction factors. The losses due to straight length of smaller diameter pipe immediately following the nozzle calculated from;

$$\Delta p_{lo} = \frac{32 f \rho_l L Q^2}{\pi^2 D_d^5} \tag{7.31}$$

where f is the laminar friction factor, Equation 2.3, and D_d and L are the diameter and length of the pipe section immediately down stream of the nozzle. The loss coefficient for both types of losses was calculated from Equation 2.4.

The good agreement obtained using the modified theory demonstrates the strong influence that the higher viscosity has on the wall shear stress at the long throat of the nozzle.

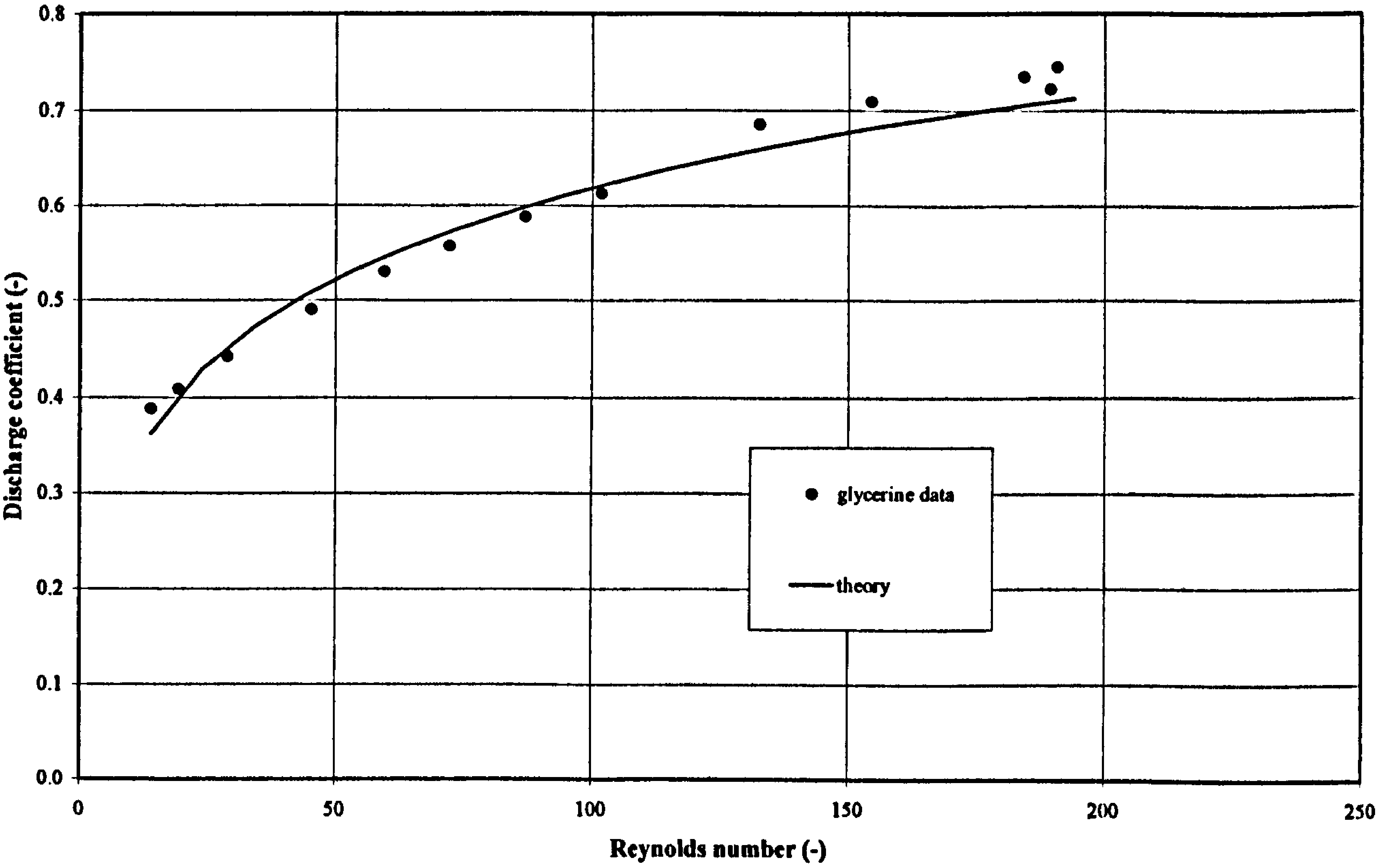

Figure 7.28: In-line Nozzle Single-Phase Discharge Coefficients

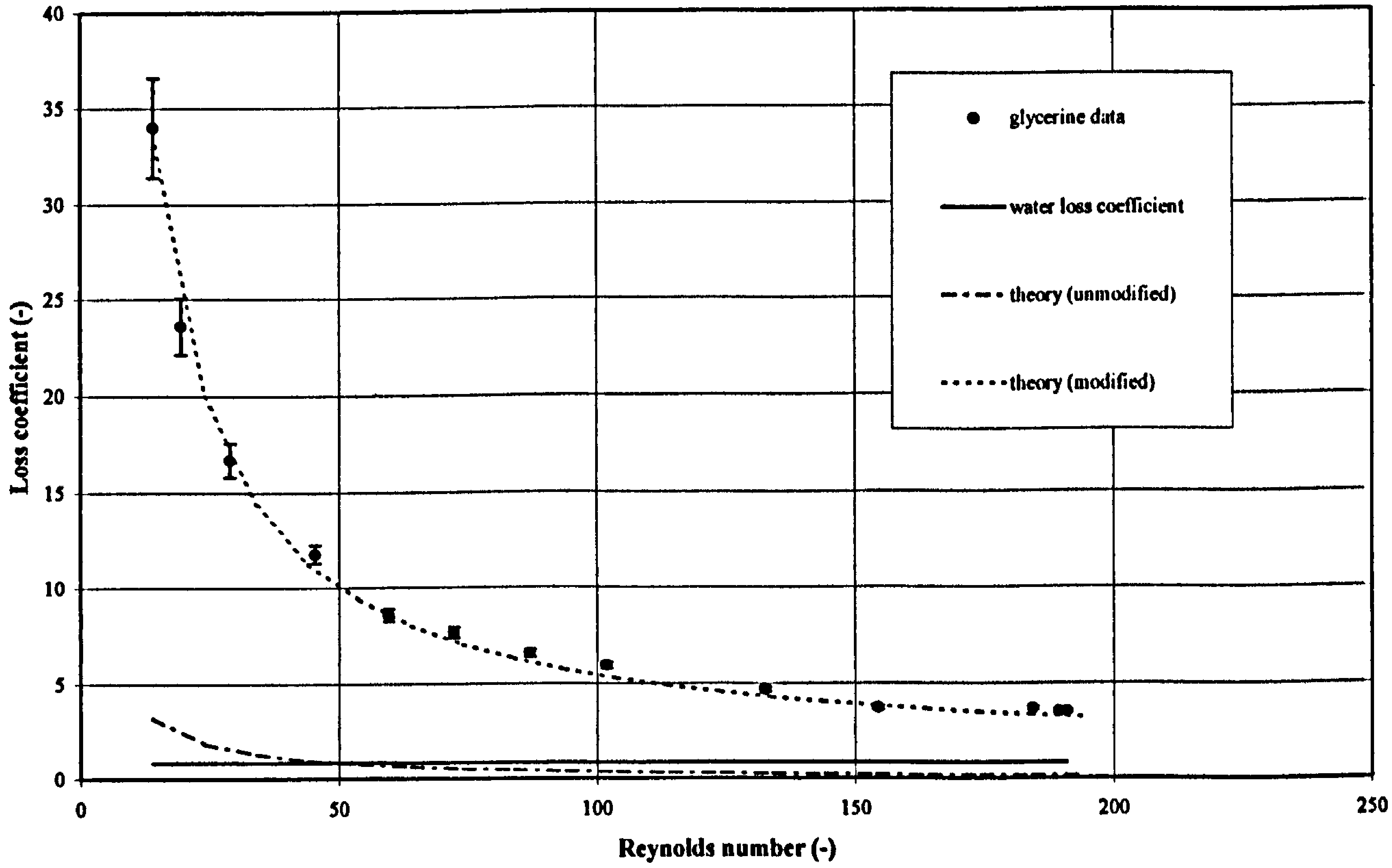

Figure 7.29: In-line Nozzle Loss Coefficient, McNeil *et al* [120]

To model the two-phase data of the in-line nozzle given in Section 6.3.4 two-phase multipliers were calculated based on the assumptions of homogeneous and separated flow using Equations 7.26, 7.27 and 7.28. The resulting two-phase multipliers are shown in Figure 7.30. There is little correlation between these methods and the experimental data.

The slip model of McNeil [118] was applied to the in-line nozzle by calculating the contraction-expansion pressure losses as described in Appendix A.5. Two-phase multipliers were determined using the single-phase water loss coefficient in Equations 6.3 & 6.4. The model and the experimental data are given together in Figure 7.31. The model compares well for the air-water data and greatly improves on the homogeneous and separated flow methods. When the model is compared to the air-glycerine data it significantly under predicts the pressure losses.

In light of the single-phase data results for the in-line nozzle, the two-phase slip model was modified to incorporate the frictional pressure losses due to each geometrically distinct part of the in-line nozzle. Ignoring the gravitational gradient the total pressure loss was found by summing the individual frictional losses calculated for the upstream pipe, the contraction, and the long throat, together with the acceleration pressure loss. A derivation of this model is given in Appendix A.7. This model is shown in Figure 7.31 as the modified air-glycerine theory. It can be seen from Figure 7.31 that this modified approach although over predicting the pressure losses demonstrates the significant effect that frictional pressure losses can have in the high viscosity two-phase flows.

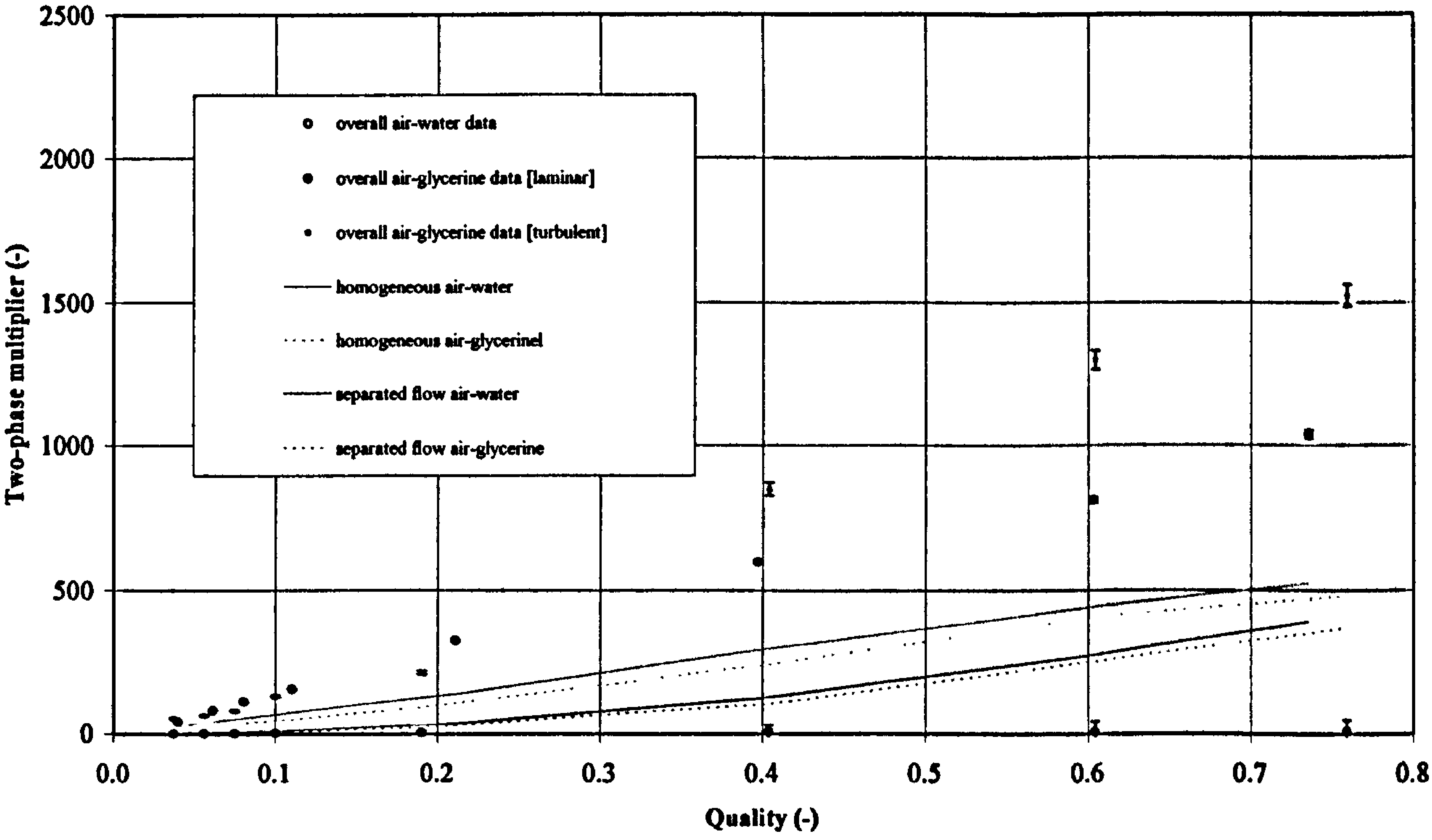

Figure 7.30: Comparison of In-line nozzle Two-phase Correlations

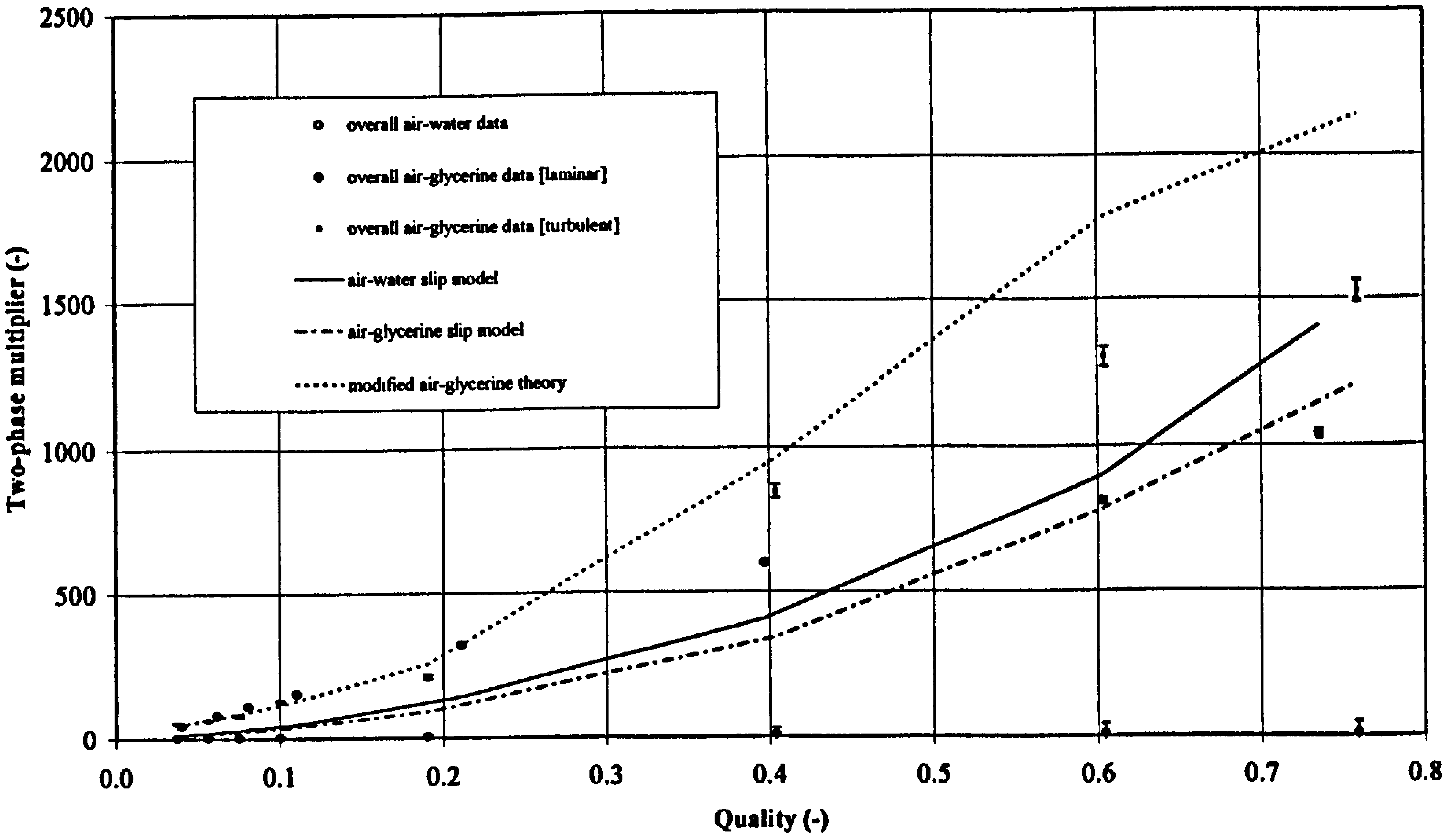

Figure 7.31: In-line Nozzle, Method of McNeil [118]

7.4.4 Globe Valve

The single-phase globe valve data of Section 6.3.5 was compared to the method of Hooper [7] (1981), Equation 2.7. The correlation of Hooper [7] is shown in Figure 7.32 to over predict the loss coefficient with an error that decreases as the Reynolds number increases. The experimental loss coefficient of Figure 7.32 is also not in agreement with the findings of Edwards *et al* [10] for a 1" globe valve. Edwards *et al* [10] reports the loss coefficient as being constant above a Reynolds number of 12 and having a value of 122.

The two-phase data for the globe valve given in Section 6.3.6 is shown in Figure 7.33. There are two sets of air-glycerine data points designated laminar and turbulent. These were obtained as described in Section 6.3.5 using the single-phase loss coefficients given in Figure 7.32 for glycerine and water respectively.

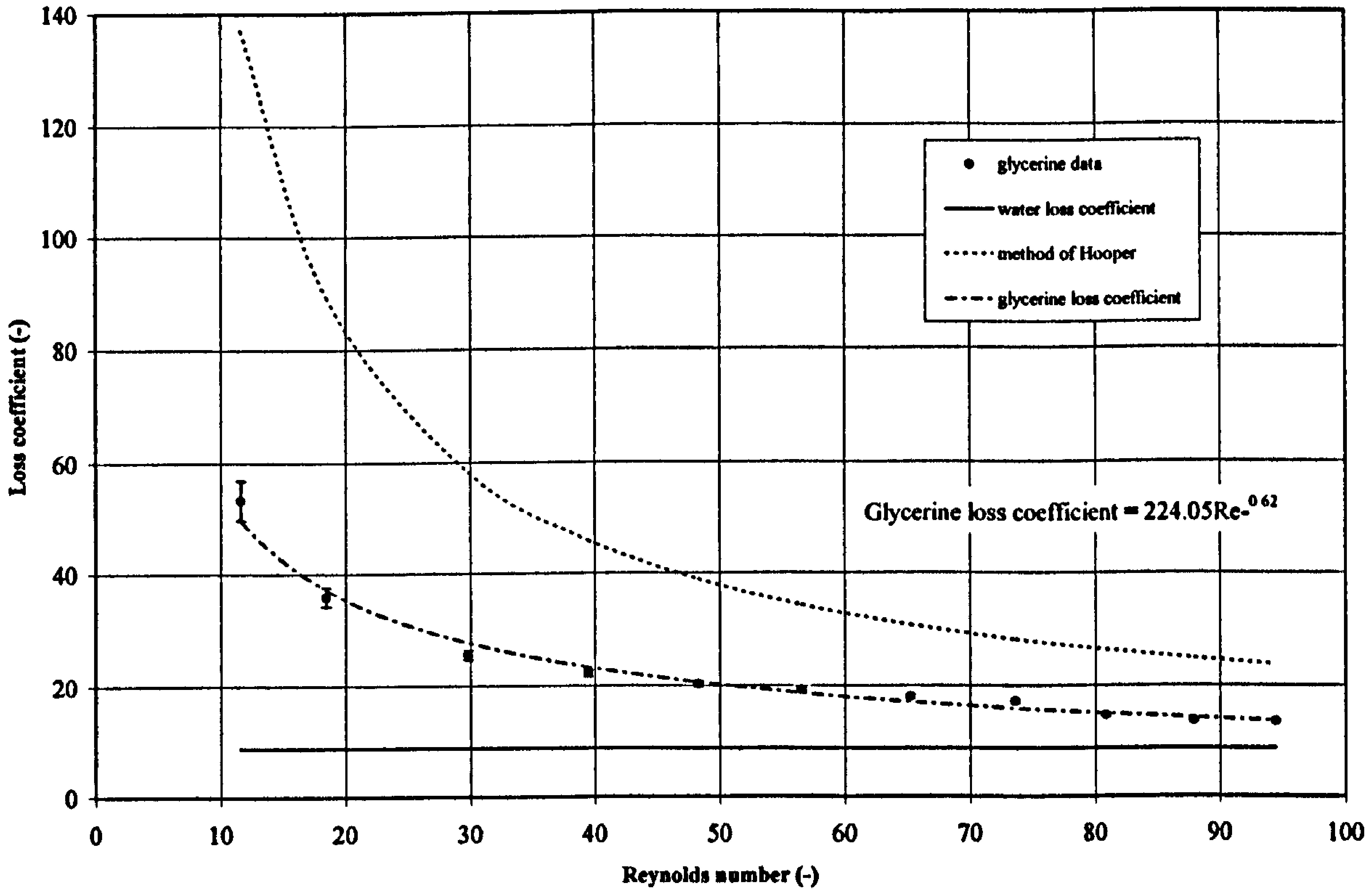

Figure 7.32: In-line Globe Valve Single-Phase Loss Coefficients

To compare the method of ESDU [117] to the data of Figure 7.33 the slip ratio as defined in Equation 2.66, was used along with the two-phase multiplier for a globe valve;

$$\phi_{lo}^{2} = \left\{x v_g / v_l + k(1-x)\right\}\left[x + \frac{(1-x)}{k}\left\{1 + \frac{(k-1)^2}{\left(v_g / v_l\right)^{1/2} - 1}\right\}\right] \qquad (7.32)$$

The method of ESDU [117] is shown in Figure 7.33 with some reasonable agreement being demonstrated for both air-water and air-glycerine results. The air-water trend is largely under predicted at the higher qualities and the laminar air-glycerine are poorly predicted.

As per the in-line orifice plate, two-phase multipliers were calculated based on the assumptions of homogeneous and separated flow for the globe valve using Equations 7.26 through to 7.28. Figure 7.33 shows the resulting homogeneous and separate flow two-phase multipliers for both air-water and air-glycerine flows. At the lower qualities the assumptions of separated flow give a closer fit to the experimental data. The homogeneous theory performs nominally better over the high qualities giving good agreement with the air-glycerine data. Across the range neither method gives particularly reliable predictions nor do they predict the laminar air-glycerine data.

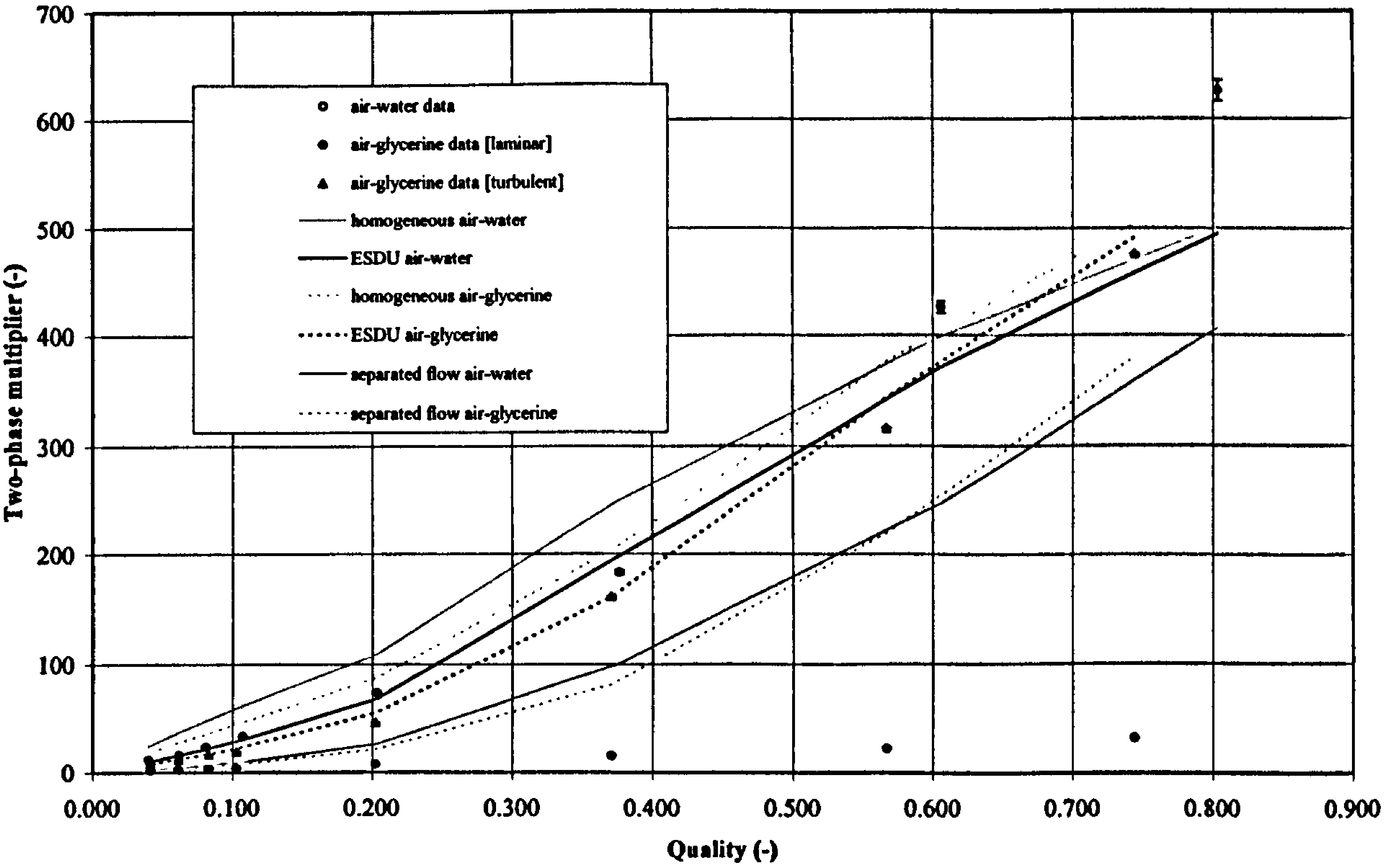

Figure 7.33: Comparison of Globe Valve Two-phase Correlations.

To apply the method of McNeil [118] the globe valve was treated as an equivalent orifice plate where the contraction-expansion pressure losses were calculated as described in Appendix A.5. The resulting two-phase multipliers were determined using Equation 6.4. The model and the experimental data are given together in Figure 7.34. The model compares well for both the air-water and air-glycerine data at low qualities but the air-water predictions become increasingly less accurate beyond a quality of about 0.5. The tendency for all models given in Figures 7.33 & 7.34 to under predict the two-phase multipliers at the high qualities may be an indication of compressible effects. Despite the incorporation of compressibility effects in the method of McNeil [118] in this instance it performs similarly to the homogeneous and ESDU [117] models.

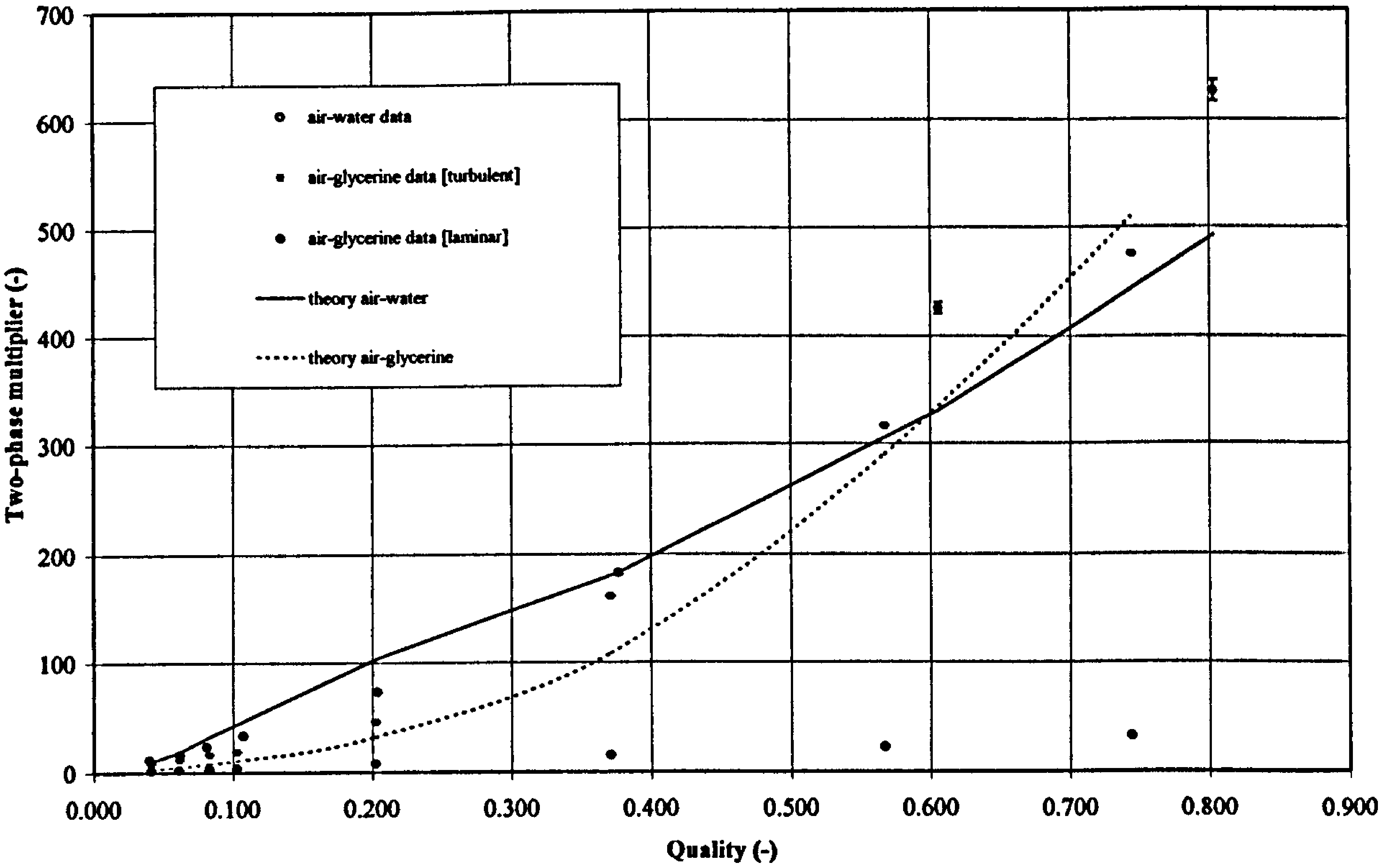

Figure 7.34: Globe Valve, Method of McNeil [118].

7.4.5 Abrupt Enlargement

The single-phase abrupt enlargement data of Section 6.3.7 was compared to the method of Hooper [7] (1981), Equation 2.6. The glycerine loss coefficient predicted by the correlation of Hooper [7], shown in Figure 7.35, is too large. Some of the glycerine data has been omitted as it was considered too erroneous to use, as per the error analysis of Section 7.6.

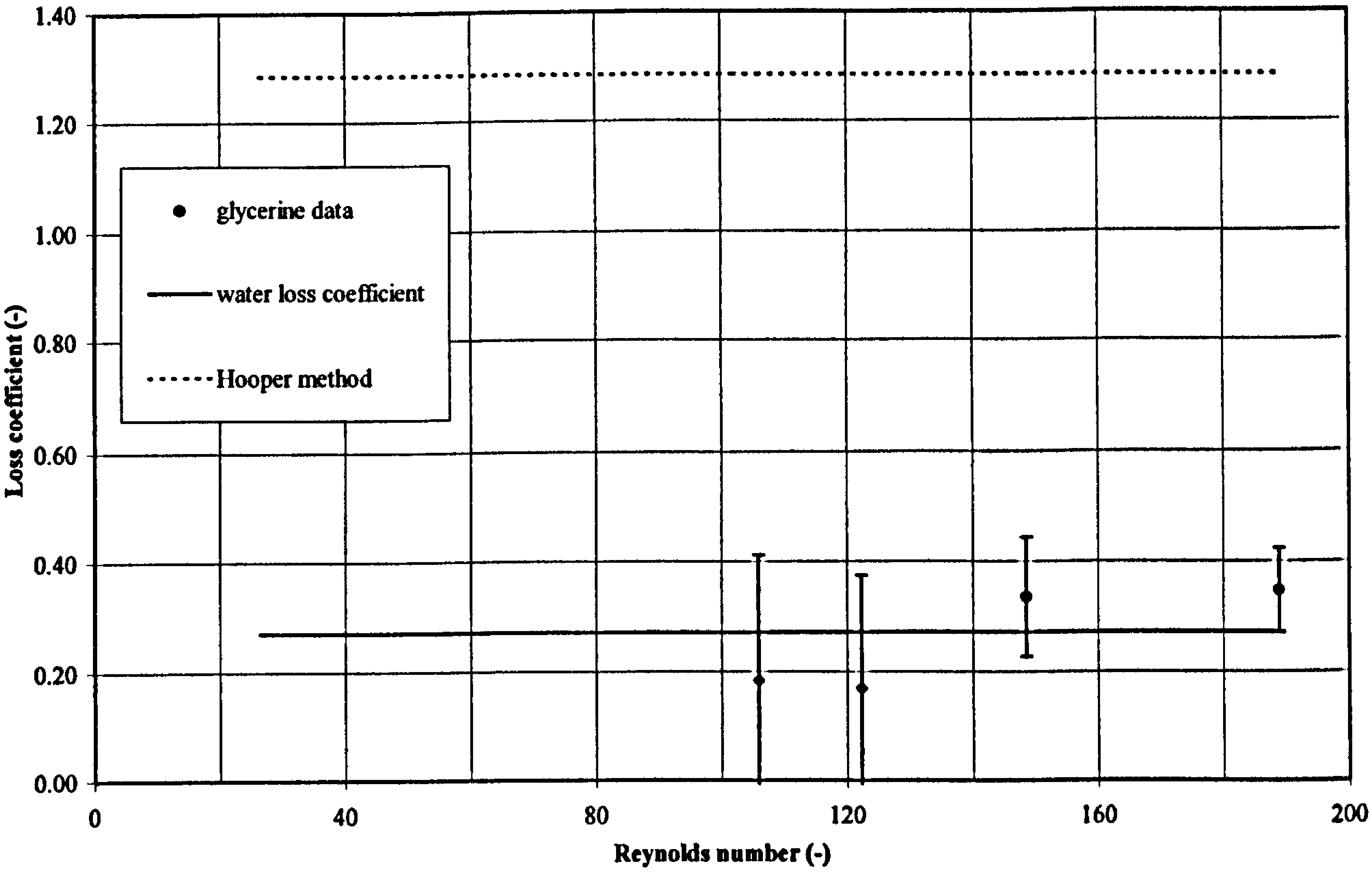

Figure 7.35: Abrupt Enlargement Single-Phase Loss Coefficients

The two-phase data of Section 6.3.8 was first compared to the sudden expansion method of ESDU [117] in Figure 7.36. The ESDU [117] definition for a single-phase all liquid pressure drop across an abrupt enlargement is;

$$\Delta p_{lo} = \frac{G^2 v_l}{2}\left\{\left(\frac{A_1}{A_2}\right)^2 - 1 + \left[1 - \left(\frac{A_1}{A_2}\right)^2\right]\right\} \tag{7.33}$$

Equation 6.4 was used along with Equation 7.33 to obtain the experimental two-phase multiplier. The ESDU [117] method is;

$$\phi_{lo}^2 = \left[1 + x\left\{\left(\frac{v_g}{v_l}\right)^{1/6} - 1\right\}\right]\left[1 + x\left\{\left(\frac{v_g}{v_l}\right)^{5/6} - 1\right\}\right] \tag{7.34}$$

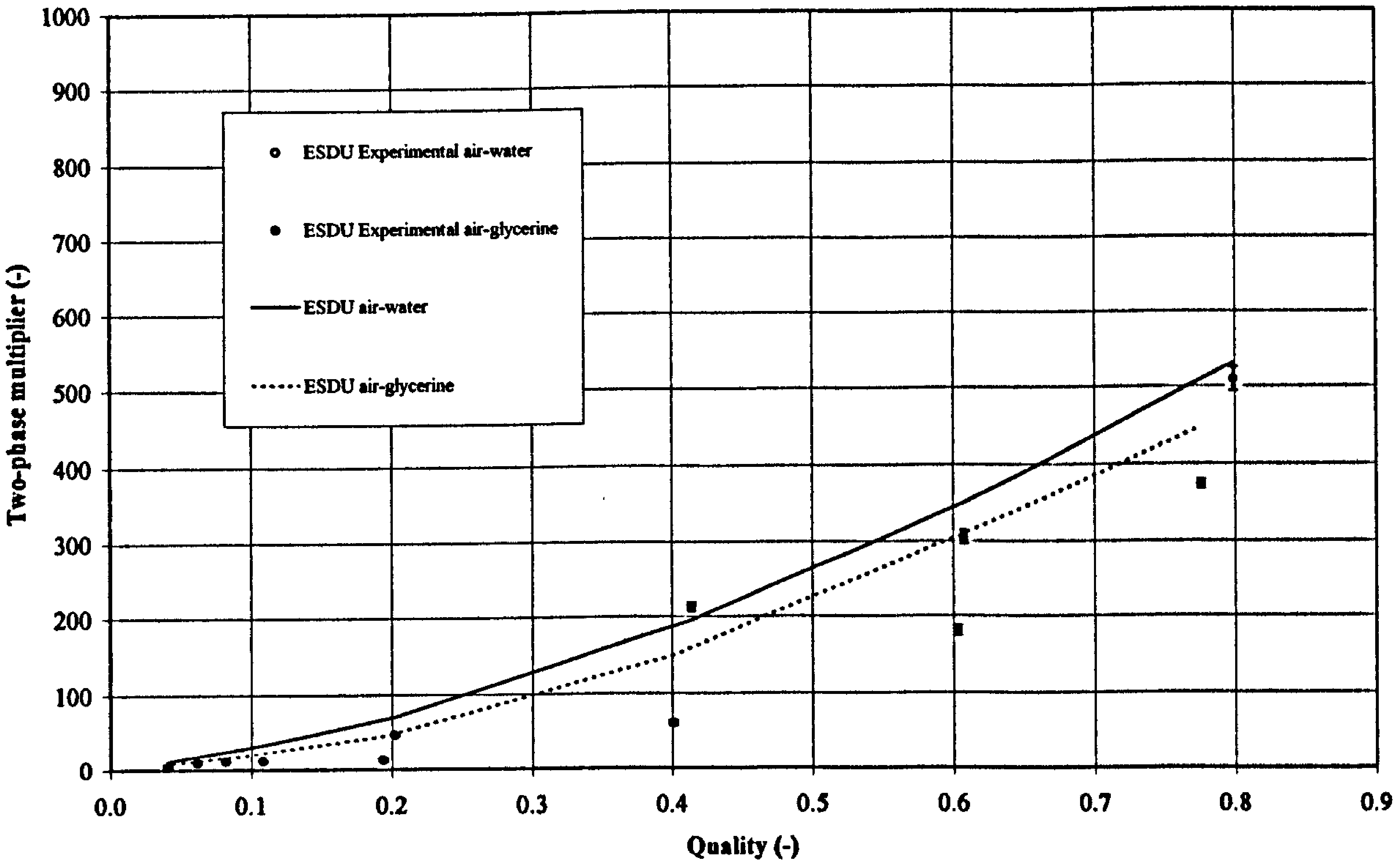

Figure 7.36: Abrupt Enlargement, ESDU [117] Method.

Two-phase multipliers for the homogeneous and separated flow assumptions were calculated for the abrupt enlargement using Equations 7.26, 7.27 and 7.28, and are shown in Figure 7.37.

At the lower qualities both air-water and air-glycerine trends are described well by the ESDU [117] and separated flow methods. At the highest qualities the ESDU [117] method is a good predictor of the air-water data but is very poor when compared to the air-glycerine data. Where as the separated flow assumption is a good predictor of the air-glycerine data but is very poor when compared to the air-water data. The homogeneous assumption is markedly better at predicting the air-water data than the air-glycerine data. None of these methods proved to be wholly accurate.

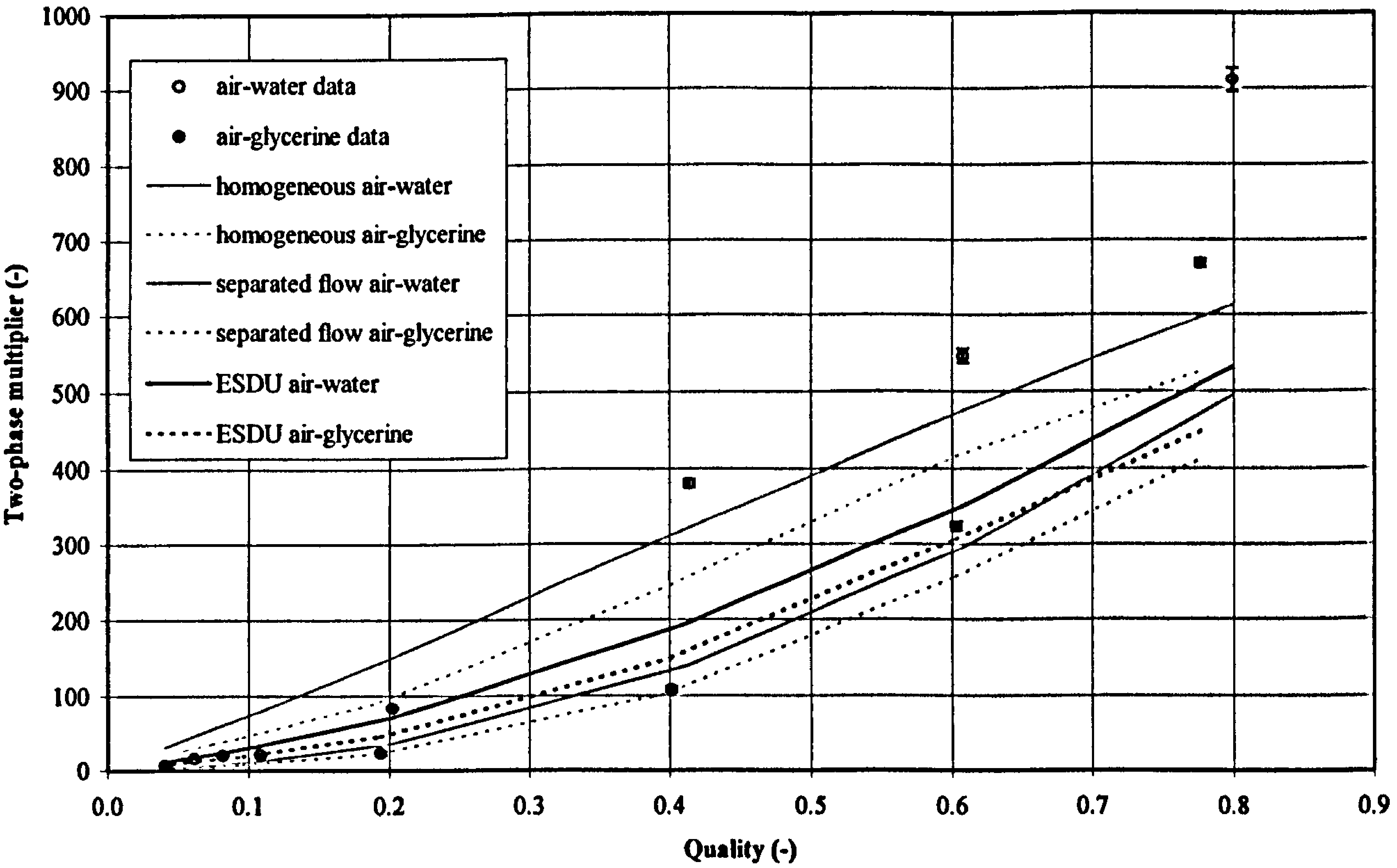

Figure 7.37: Comparison of Abrupt Enlargement Two-phase Correlations.

The method of McNeil [118] was applied to the abrupt enlargement. The single-phase pressure loss, Δp_{lo}, was calculated from Equation 6.3 using the experimental single phase loss coefficient, β, for water of 0.27, determined in Section 6.3.7. Expansion losses were calculated as per Appendix A.5. As can be seen in Figure 7.38 the slip model of McNeil [118] does not accurately predict all the experimental data but in comparison to other models it is the only method to sufficiently distinguish between high and low viscosity flows.

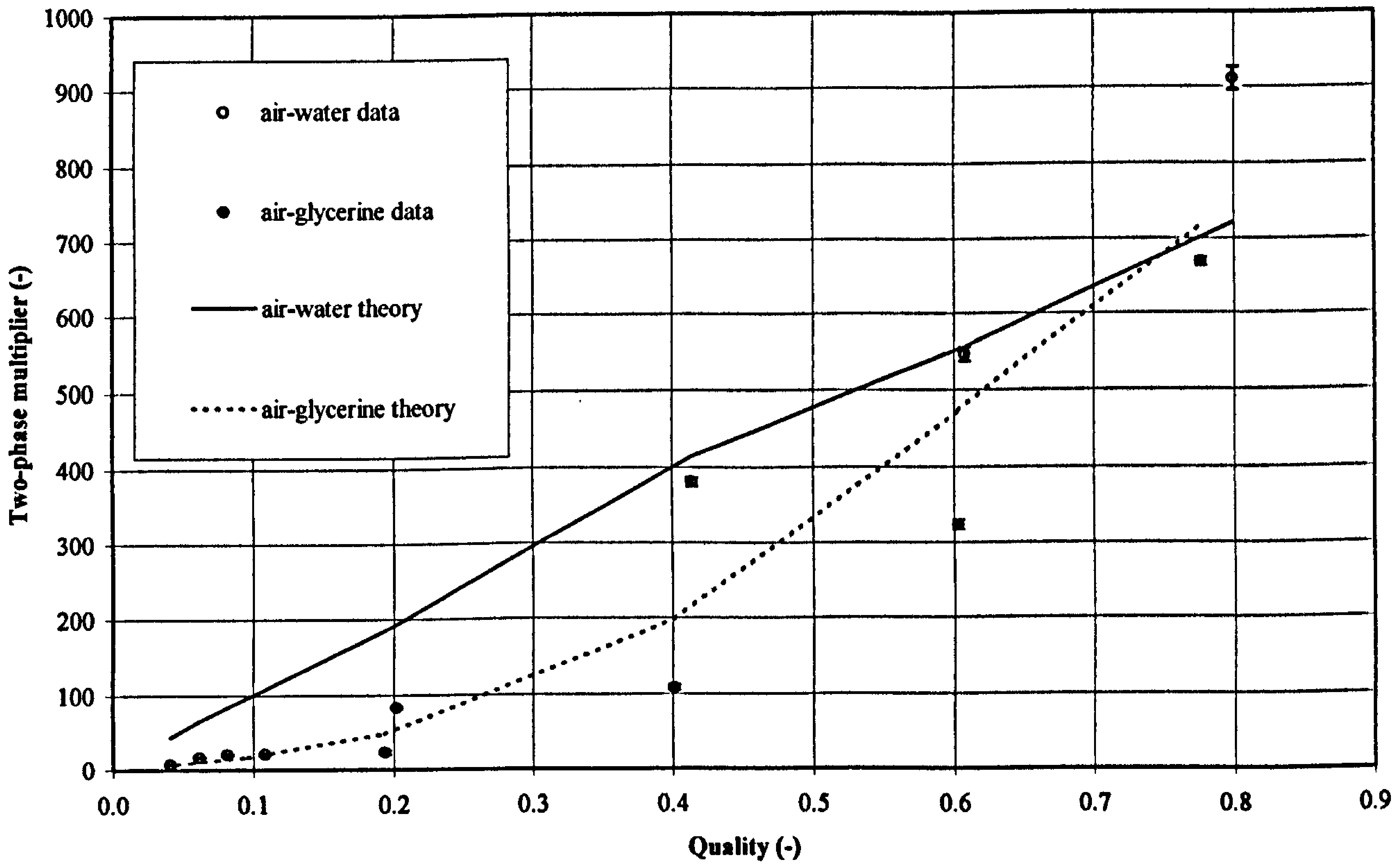

Figure 7.38: Abrupt Enlargement, Method of McNeil [118].

7.4.6 Conclusions

The agreement of measured and predicted void fraction data of Figure7.24 is reasonable. This indicates an acceptable level of reliability exists in applying the film method and extrapolating liquid entrainment values from the pipe length correlations to establish the conditions upstream of the fitting.

A clear pattern emerges from the performance of the two-phase correlations applied across the in-line components. The homogeneous and the separated flow assumptions do not adequately distinguish between low and high viscosity flows. The homogeneous assumption tends to follow the air-water trend whilst the separated flow assumption follows the air-glycerine trend with the ESDU [117] method laying somewhere between the two. The method of ESDU [117] in some instances proved the closest fit to the air-glycerine data i.e., globe valve data, but similarly to the performance of the homogeneous and separated flow models it fails to distinguish sufficiently between low and high viscosity flows.

Although the slip model of McNeil [118] did not provide the best agreement with the data for all in-line fittings it was the most generally applicable method. The model relied upon a greater knowledge of upstream flow conditions and it is evident that this approach was the most successful in accommodating the effects of high viscosity. In this instance the upstream flow conditions were found from the application of the annular flow model which in turn relied on entrainment correlations specific to the flow conditions of this experimental data. At the highest qualities, the model was the best match for the air-water data which may be attributable to the incorporation of compressibility effects present in the highest gas mass fluxes.

Forming the two-phase multiplier from the viscous single-phase data has not provided a satisfactory method of modelling the experimental data of the in-line components. This is demonstrated by the *laminar* experimental two-phase data which is poorly comparable with any of the theoretical two-phase multipliers.

7.5 Pressure Loss Due to Discharge Components

The two pipeline components tested under two-phase discharge conditions were the nozzle and orifice plate. The acquisition of data for the discharge nozzle and orifice plate are described in Sections 6.7 and 6.8 respectively.

7.5.1 Discharge Nozzle

The single-phase data, described in Section 6.4.1 are compared to the contraction theory of McNeil *et al* [120] in Figure 7.39. Over most of the range the agreement is good. A degree of discrepancy is shown over the 40 mPas nominal viscosity data which may be due to an inconsistency in the test liquid viscosity.

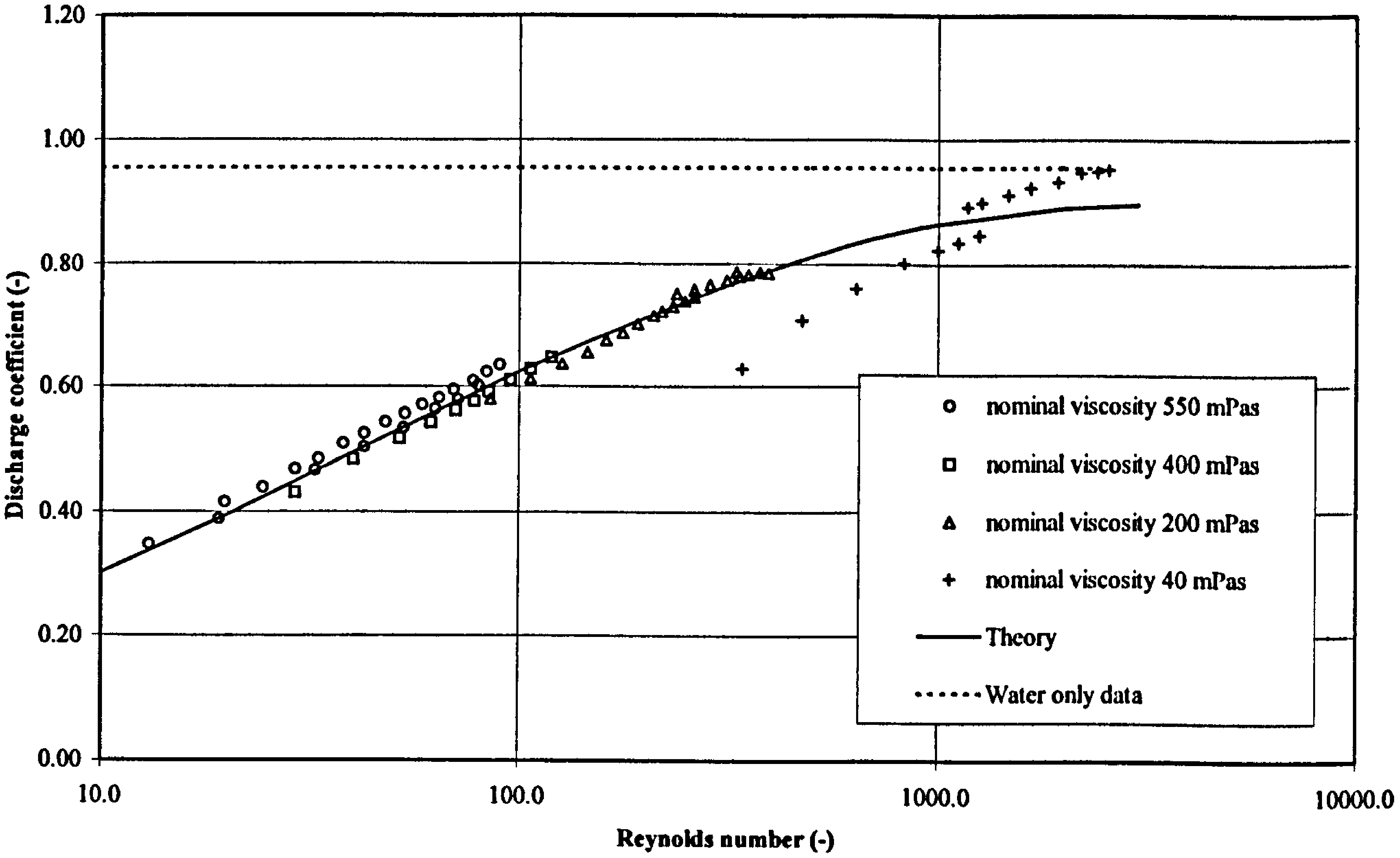

Figure 7.39: Discharge Nozzle Coefficient, method of McNeil *et al* [120]

The method of McNeil [118] for pipeline components with contraction-expansion type geometry was applied to the discharge nozzle. To obtain the upstream flow conditions, i.e., slip and entrainment, the annular flow model described in Section 7.3.1 was applied. This required knowledge of the upstream wall shear stress which, for the in-line components, had been obtained from the experimental pressure gradient. The wall shear stress for the discharge components was calculated using Equation 7.20. The all liquid two-phase multiplier was calculated from Equations 4.49 and 2.50 using Chisholm C parameter values of 21 and 25 for air-water and air-glycerine respectively. In Figure 7.40 the slip model reasonably predicts the air-water pressure drops but consistently under predicts the air-glycerine pressure drops over the entire quality range.

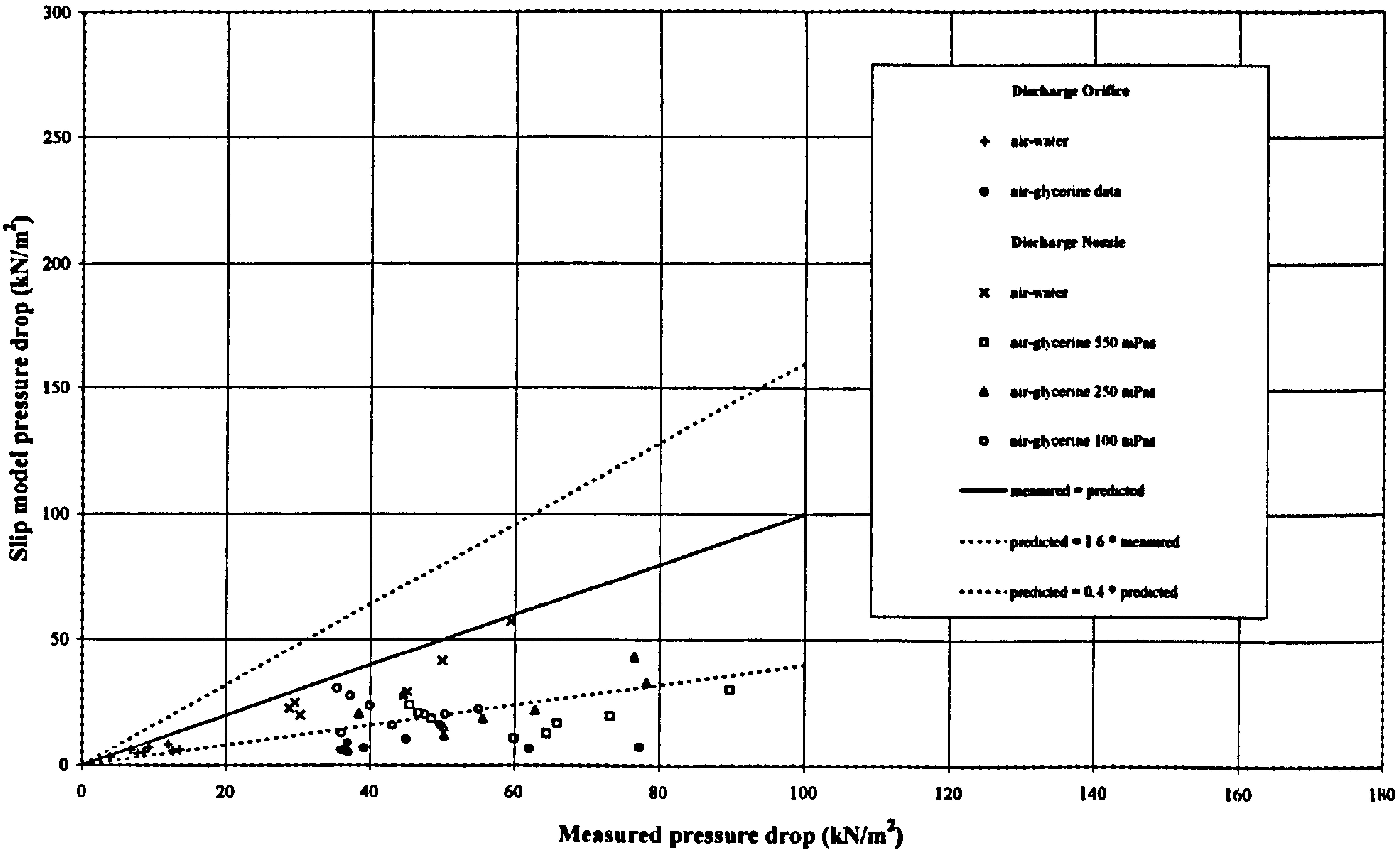

Figure7.40: Discharge Nozzle & Orifice Plate, slip model of McNeil [118]

In Section 7.4.3 the two-phase flow in the in-line nozzle was modelled by calculating separately the frictional losses attributable to each part of the nozzle. This approach, a derivation of which is given in Appendix A.7, was also used for the discharge nozzle. Assuming negligible gravitational loss the total pressure drop was found from the summation of the frictional pressure drop due to the upstream pipe, the contraction, and the short length of pipe down stream at the discharge point. The application of this model is given by McNeil & Stuart [124] (2004) and is described as the annular flow model.

The effect of including the frictional losses on the discharge nozzle theory can be seen in Figure 7.41. Although the modified model gives a greater scatter of prediction it does not exhibit the same systematic error that was evident in the slip model of McNeil [118].

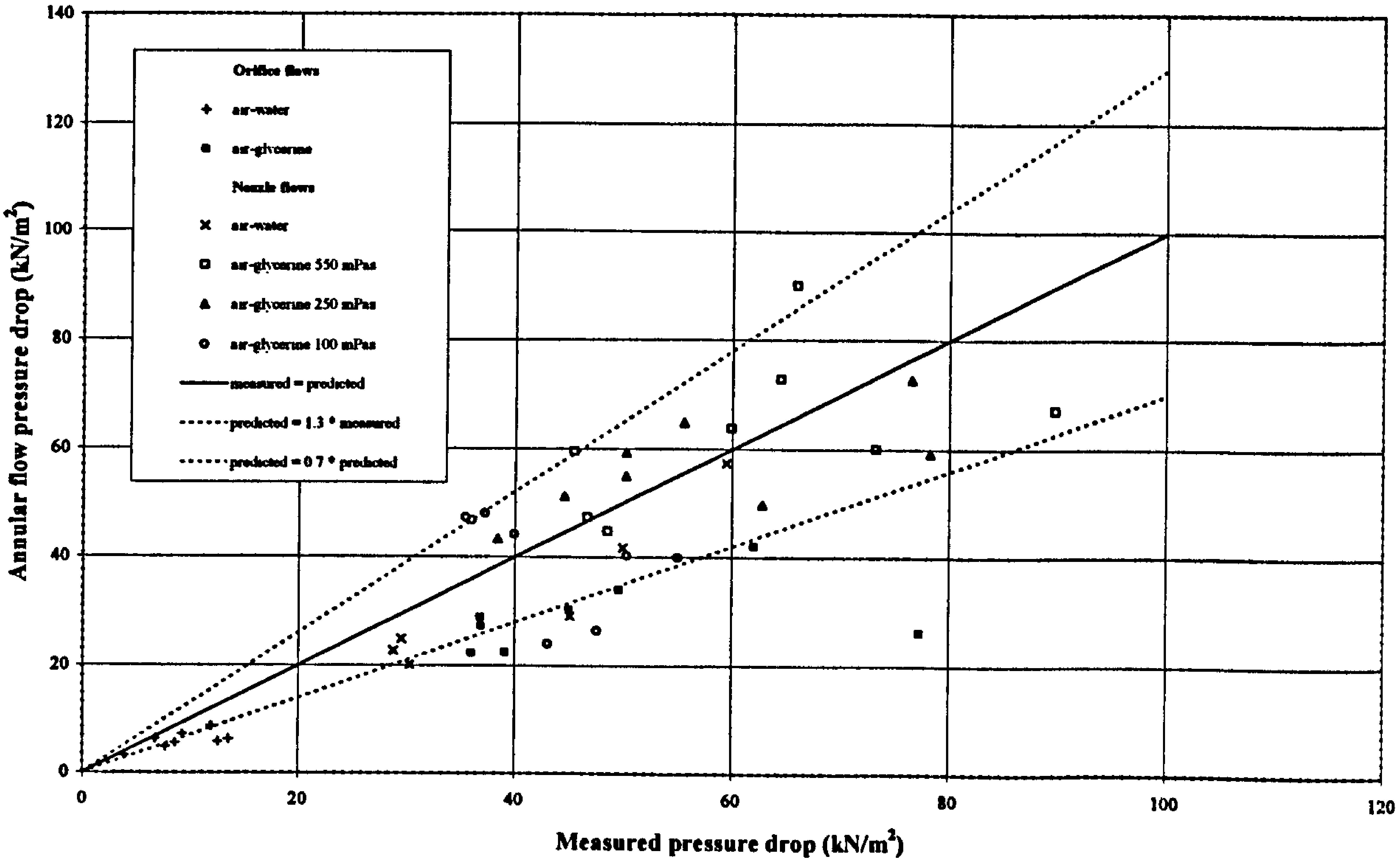

Figure 7.41: Discharge Nozzle, Annular Flow Model, McNeil & Stuart [124]

7.5.2 Discharge Orifice

The single-phase data, described in Section 6.4.3 are compared to the contraction theory of McNeil *et al* [120] in Figure 7.42. It is assumed for this comparison that the flow contracted along a conical path from the pressure tapping to the orifice plate. Below a Reynolds number of around 60 good agreement is observed.

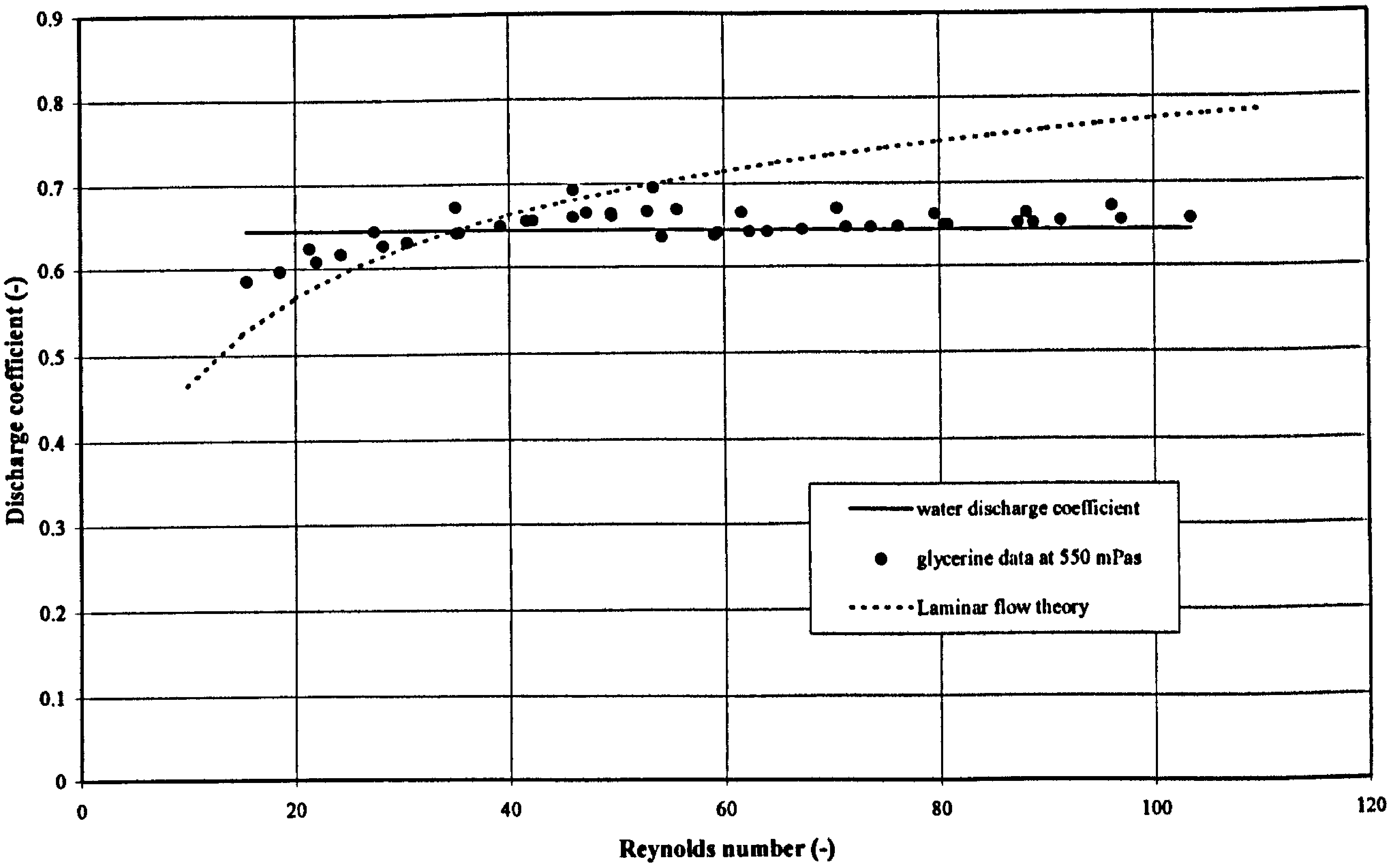

Figure7.42: Discharge Orifice, Method of McNeil *et al* [120]

As per the discharge nozzle, the method of McNeil [118] for pipeline components was applied to the discharge orifice plate. The upstream slip and entrainment were obtained from the annular flow model using the wall shear stress calculated from Equation 7.20. The Chisholm C parameter values were 21 and 25 for air-water and air-glycerine respectively. In Figure 7.40 the slip model under predicts the air-glycerine pressure drops but the air-water pressure drops predictions are reasonable.

It should be noted that the air-water mass fluxes were in the region of 50% less than that of the air-glycerine mass fluxes.

To improve the air-glycerine predictions the annular flow model, McNeil & Stuart [124],which was applied to the in-line nozzle Section 7.4.3 and the discharge nozzle was used. The two-phase flow was treated in the same manor as the single-phase flow by assuming that the flow contracted along a conical path from the pressure tapping to the orifice plate. A comparison is made with the experimental data in Figure 7.41 and is reasonable.

7.5.3 Conclusions

The discharge coefficient of a high viscosity single-phase flow in a discharge nozzle can be reasonably modelled. The modelling of viscous flow in a discharge orifice plate is less satisfactory.

Application of a slip model to predict the pressure drop across the discharge components for a two-phase flow proved unconvincing. Although air-water values were predicted the model substantially under predicted the pressure losses for all other viscosities over the full range of qualities. Including wall friction substantially improved matters suggesting that nozzle flow models must include friction forces if the liquid viscosity is large.

7.6 Error Analysis

The local pressure transducer was accurate to ± 0.2 % of the recorded value and the flow rate measurement was accurate to 1.0% of the recorded value. An error analyses was performed to determine the uncertainty that the instrumentation produced in the measured flow properties such as loss coefficients and two-phase multipliers.

The basis of the analysis is similar to that described as the Monte Carlo Method described by Springer [125] (2003). A random error data set was generated from which measured flow properties could be calculated and compared to the initial flow properties to give an indication of the probable error. The error data set was produced from the experimental data by imposing on each data point a randomly produced fluctuation that lay within the limits of the measurement errors. Flow properties were then determined using the error data set by applying the same analysis that had been used to obtain flow properties from the initial experimental data.

The cycle of generating an error data set and then the calculating the resulting flow properties was repeated until the standard deviation tended towards a constant. It required 640 permutations before the error data could be considered the probable error. The error analysis procedure was applied to the data for all in-line components both single and two-phase and is shown as error bars in Figures 7.25 to 7.39.

Component	Air-water		Air-glycerine	
	Min	Max	Min	Max
In-line Orifice	0.4	1.7	1.1	1.5
In-line Nozzle	1.2	1.4	2.7	3.4
Globe Valve	0.1	1.5	1.5	2.3
Abrupt Enlargement	1.7	4.4	7.9	45.3

Table 7.2: Typical Range of Percentage Error

Chapter 8

DISCUSSION & CONCLUSIONS

Highly viscous two-phase data has been obtained for pipe flow and standard pipeline components for a range of qualities. A less extensive data set was also obtained for which viscosity was varied. Data were analysed by the application of a data reduction method based upon annular flow assumptions. The scrutinisation of the resulting local flow properties allowed the influence of viscosity on two-phase flow to be explored.

The process of collecting two-phase data was difficult and resulted in the routine operation of the test facility being relatively demanding. High viscosity data acquisition consisted of many facets, void fraction, liquid viscosity, purging, momentum forces and temperature regulation. The control and measurement of each element needed to be executed with timing and care to ensure that data was both consistent and reliable. This translated to the adoption of a strict and rigorous methodology which in practice was labour intensive and hugely time consuming. The inclusion of a highly viscous liquid phase in the development of the test facility resulted in several major design difficulties;

- The heating and cooling processes required to maintain the viscosity of the test liquid due to the hygroscopic nature of glycerine.

- A collection system that induced and accelerated the disengagement of entrained air bubbles from the discharging liquid.

- A method of extraction and removal of the discharging mist laden air.

The effect of viscosity on a two-phase flow is significant. This study differentiated between viscosity effects and other flow phenomena by directly comparing viscous flows with air-water flows of equivalent mass fluxes and quality. This approach allowed some of the effects of high viscosity to be easily observed whilst others were identified through a more extensive analysis.

An immediately apparent influence of high viscosity is the significant reduction in disturbances and noise. This was evident from the routine operation of the experimental rig. Much of the vibration and fluctuations present in the air-water flows were noticeably absent from the majority of the air-glycerine tests. Another easily observable viscosity effect is the elevated pressure drop gradients. High viscosity flows have a considerable effect on the pressure drop, demonstrated by simply comparing equivalent air-water and air-glycerine flows shown in Figure 6.1. These elevated pressure gradients are attributed to increased friction forces, evident from the increased wall shear stresses. The air-glycerine wall shear stresses shown in Figures 7.8 - 7.15 are in some cases, a factor of four times as large as the equivalent air-water values.

Void fraction measurements given in Figure 6.2 reveal the effect that increasing liquid viscosity has upon the slip ratio. The void fraction values can be seen to reduce as the liquid viscosity increases. In Figures 7.8 through to 7.15, air-water and air-glycerine flows of the same quality are compared. As expected, the viscous forces retard the movement of the liquid phase resulting in a smaller core and greater liquid film thickness. The degree to which this influences void fraction and hence the slip ratio was only predicted by the annular flow model given in the analysis.

Also attributable to viscosity is a reduction in the entrained liquid fraction. Unlike wall shear stress and the slip ratio, the mechanisms by which viscosity alters the entrainment are more complex and, as a result, the effect of viscosity on entrainment is less clearly defined. A deficiency in the present understanding of entrainment mechanisms led to the assumption of the data reduction method of Chapter 7 that the entrained liquid droplets travel at the gas velocity. The validity of this assumption holds true in this instance but the resulting entrainment relationship is only applicable to annular flows that match these experimental conditions. Several mechanisms of entrainment may exist, varying in the influence with viscosity and flow conditions. McNeil & Stuart [122] concluded that a complete understanding of entrained liquid requires a more detailed study.

The performance of existing methods for the prediction of pressure drop in pipe flows and pipeline components were evaluated in Chapter 7. The experimental pressure drop trends for a vertical pipe flow of Figure 7.1 were only closely predicted by the C parameter method of Chisholm [56]. A C value of 25 best correlated air-water and air-glycerine data. Neither the Friedel [50] nor the B parameter method of Chisholm [121] were found to be applicable for high viscosity flows.

The single-phase data obtained for in-line and discharge components confirms findings of earlier studies i.e., McNeil *et al* [13] that the viscous forces are significant at low Reynolds numbers. This is demonstrated by the behaviour of laminar discharge and loss coefficients which are not constant until a critical value of the Reynolds number is achieved. The method of McNeil *et al* [120] proved successful at low Reynolds numbers because it attempts to model the actual flow path of each geometry and considers viscous and inertia forces.

For highly viscous flows the homogeneous multiplier is a poor predictor for all pipeline components. The separated flow model provides reasonably consistent predictions at qualities less than 0.4. At the higher qualities this is not maintained.

Neither homogeneous nor the separated flow models adequately differentiate between air-water and air-glycerine flows to be generally applicable.

The ESDU [117] recommendations for pipeline components was of limited value as the correlations failed to sufficiently discriminate between air-water and air-glycerine flows. Viscosity effects are only incorporated in the definitions of the two-phase multipliers through changes in the two-phase specific volumes. This may help explain the poor response the correlations had when applied to the high viscosity flows. Despite the mixed performances of the homogeneous, separated flow and ESDU [117] models, common to all three was the poor comparison with the experimental *laminar* two-phase multipliers. It was clear that in all cases the use of viscous single-phase loss coefficients to form the two-phase multiplier is unhelpful.

Another factor in the poor performance of the pipeline component correlations may be the occurrence of compressibility effects. An indication of this is given in Figures 7.26, 7.31 and 7.34 where, over the higher qualities of 0.6, 0.7 and 0.8, the correlations consistently under predict the data trends. It is not clear what size of contribution compressible flow makes to the pipeline pressure drop.

Only the slip model of McNeil [118] incorporated compressible flow effects for modelling in-line component two-phase flows. The model required the properties of upstream liquid entrainment and slip ratio to predict pressure losses across changes in section. The incorporation of the annular flow model of Section 7.3.1 along with the method of McNeil [118] was designed to improve the accuracy with which the pressure losses could be predicted. Although the model does not accurately predict pressure losses in all cases, it is evident that by incorporating entrainment and slip ratio values the model is the most responsive to the effects of compressibility and high viscosity.

What was clear from the modelling of the in-line and discharge nozzle data was the effect viscosity had on the friction pressure loss in single and two-phase flows. Through certain geometries this was comparable in size with the equivalent acceleration component and could only be adequately modelled by determining the specific flow paths dictated by the geometry of each fitting.

This study has evaluated the characteristics of a high viscosity two-phase and related single-phase flow for pipe length and in-line components. The behaviour of Newtonian two-phase mixtures over the quality range of 0.04 to 0.8, travelling under subsonic conditions in the annular flow region has been examined. Through the application and response of various models and correlations the effects of viscosity are considered to be;

- High viscosity causes elevated viscous forces in single-phase flow that dominate the energy losses below a critical Reynolds number. The critical Reynolds number is in the region of 50 but is geometry dependent. Above this critical Reynolds number a transition range exists where viscous and inertia forces must both be considered.

- In a two-phase flow the presence of a highly viscous liquid will result in much greater pressure gradients due to much higher interfacial and wall shear stresses. Although high viscosity has a dampening effect on the flow behaviour, less noise and disturbance is experienced in the instrumentation, the pressure losses experienced are far greater.

- Large viscous forces retard the movement of the liquid film in an annular flow and this in turn results in the slip ratio being much larger than would be encountered in an equivalent air-water flow. The most appropriate method for predicting void fraction is the film method, used in the annular flow model and based on the work of Ambrosini *et al* [98]. Other methods are not applicable.

- The entrained liquid fraction reduces with viscosity. The mechanisms that govern liquid entrainment are not clearly understood.

- The frictional pressure gradient was best predicted using the Chisholm [56] method with a C parameter of 25. Other methods cannot reliably be applied.

- Pipe fitting models based on the single-phase pressure loss and two-phase multiplier approach have limited application. The approach used by the slip model of McNeil [118], a model that incorporates both viscous and compressibility effects, is a more likely candidate, although it was applied with limited success.

Future single-phase work for pipe-line components would gain from a study of the transition from low to high viscosities. Further insight into the behaviour and nature of losses due to pipe line components requires a broader experimental base to draw from. The modelling of viscous flows through components where the internal geometry is more complex will require an empirical approach that will need to include more geometric detail than is required by low viscosity methods.

Future two-phase experimental work would be improved with the addition of instrumentation that could measure the entrained liquid fraction. This will enable the mechanisms by which liquid is drawn from the annular film by the gas stream to be better understood. For in-line components, testing over a range of liquid viscosities would allow the transition of viscosity effects to be observed.

PAGE
NUMBERING
AS ORIGINAL

APPENDIX A

A.1 Derivation Flow Nozzle Discharge Coefficient - Equation for 4.4

Using the energy equation the flow rate through a nozzle with an entrance area, A, a throat area, A_o, and a discharge coefficient of C_D is given as;

$$Q = \frac{A_0 c_D \sqrt{\frac{2\Delta p}{\rho}}}{\left[1 - \left(\frac{A_0}{A}\right)^2\right]^{1/2}} \qquad \text{(A.1)}$$

If all the geometric and fluid properties are gathered in one term, k, then Equation A.1 becomes;

$$Q = c_D k \sqrt{\Delta p} \qquad \text{(A.2)}$$

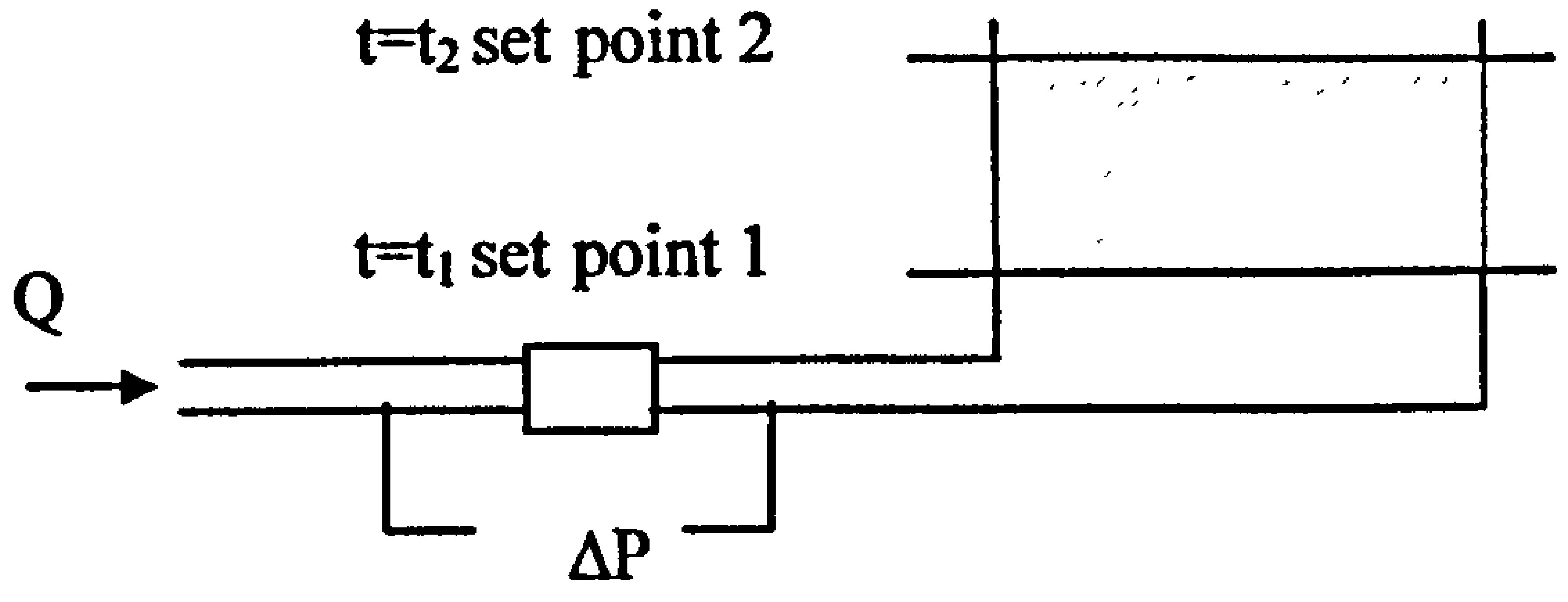

Figure A.1: Calibration Tank

For any given time interval as shown in Figure A.1, the volume as a function of the flow rate will be given by;

$$V_1 = \int_1^2 Q_1 dt = n c_D k \int_1^2 \Delta p^{1/2} dt \qquad V_2 = \int_3^4 Q_2 dt = (1-n) c_D k \int_3^4 \Delta p^{1/2} dt \qquad \text{(A.3)}$$

Over the time period, t_1 to t_2, if the relationship between time and pressure is considered to be linear, the change in pressure can then represented by a straight line of gradient, m, and a constant, c;

$$\Delta p = mt + c \tag{A.4}$$

If Equation A.4 is substituted into Equation A.3 the volume over the first time interval, V_1, and the volume over any other subsequent time intervals, V_2, become;

$$V_1 = nc_D k \int_{t_1}^{t_2} (mt + c)^{1/2} dt \qquad V_2 = (1 - n)c_D k \int_{t_3}^{t_4} (mt + c)^{1/2} dt \tag{A.5}$$

And after integrating volume, V_1, becomes;

$$V_1 = \frac{2n}{3}\frac{c_D k}{m}\left[(mt + c)^{3/2}\right]_{t_1}^{t_2} = \frac{2}{3}\frac{c_D k}{m}\left[(mt_2 + c)^{3/2} - (mt_1 + c)^{3/2}\right] \tag{A.6}$$

Similarly for the proceeding volume, V_2;

$$V_2 = \frac{2(n-1)}{3}\frac{c_D k}{m}\left[(mt_3 + c)^{3/2} - (mt_4 + c)^{3/2}\right] \tag{A.7}$$

By rearranging Equation A.7 in terms of n, and substituting into Equation A.6 the discharge coefficient can be expressed as;

$$C_D = \frac{3m}{2k}\left[\frac{V_2}{\left[(mt_2 + c)^{3/2} - (mt_1 + c)^{3/2}\right]} + \frac{V_1}{\left[(mt_4 + c)^{3/2} - (mt_3 + c)^{3/2}\right]}\right] \tag{A.8}$$

A.2 Derivation of Equation 4.3

For a gamma ray passing through a medium of thickness, t, with a mass attenuation coefficient, σ, and a density, ρ, the attenuated intensity, I, is related to the incident intensity, I_o, by:

$$I = I_0 e^{-\sigma\rho t} \tag{A.9}$$

For the chord of length, m, shown in Figure A.2, the ratio of attenuated to incident radiation intensity, for a liquid of density, ρ_l, mass attenuation coefficient, σ_l, passing through a tube with material properties of, density, ρ_t, and a mass attenuation coefficient of, σ_t, is given by;

$$\frac{I_l}{I_0} = e^{-(2\sigma_t\rho_t t_t + 2\sigma_l\rho_l m)} \tag{A.10}$$

For the flow of a gas of density, ρ_g, and a mass attenuation coefficient, σ_g, passing through the same tube the ratio of attenuated to incident radiation intensity is given by;

$$\frac{I_g}{I_0} = e^{-(2\sigma_t\rho_t t_t + \sigma_g\rho_g m)} \tag{A.11}$$

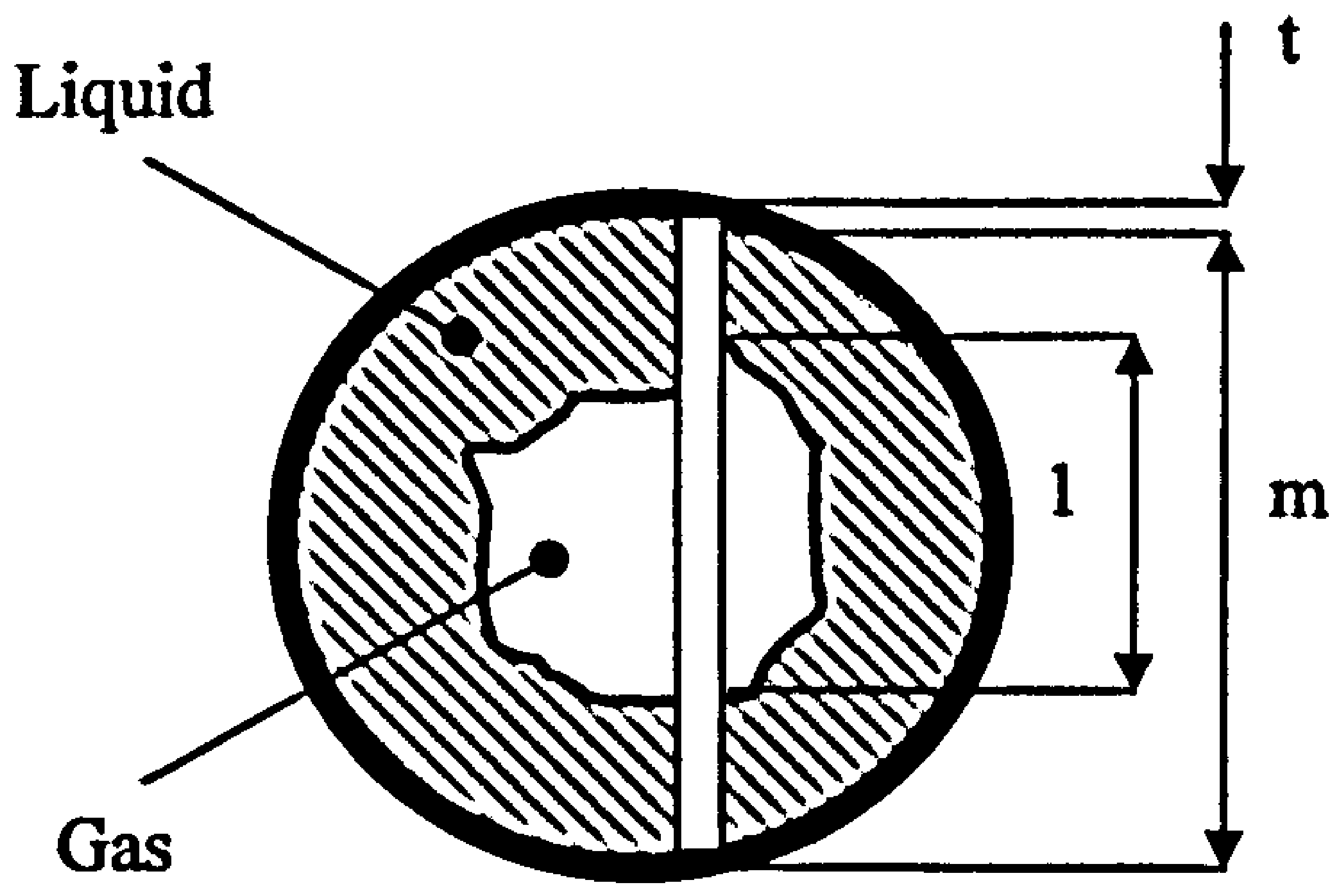

Figure A.2: Tube Cross Section – Annular Flow

If the tube contains a two-phase annular flow the attenuation ratio becomes;

$$\frac{I_{gl}}{I_o} = e^{-\left[2\sigma_t \rho_t t_t + \sigma_g \rho_g l + \sigma_l \rho_l (m-1)\right]} \tag{A.12}$$

The local void fraction is defined by the ratio of the gas and liquid chord lengths;

$$\alpha = \frac{1}{m} \tag{A.13}$$

Resolving Equations A.10, A.12, A.13 & A.14 allows the void fraction to expressed as;

$$\alpha = \frac{\ln\left[\frac{I}{I_l}\right]}{\ln\left[\frac{I_g}{I_l}\right]} \tag{A.14}$$

A.3 Derivation of Momentum Equation 7.9 for Liquid Film Flow

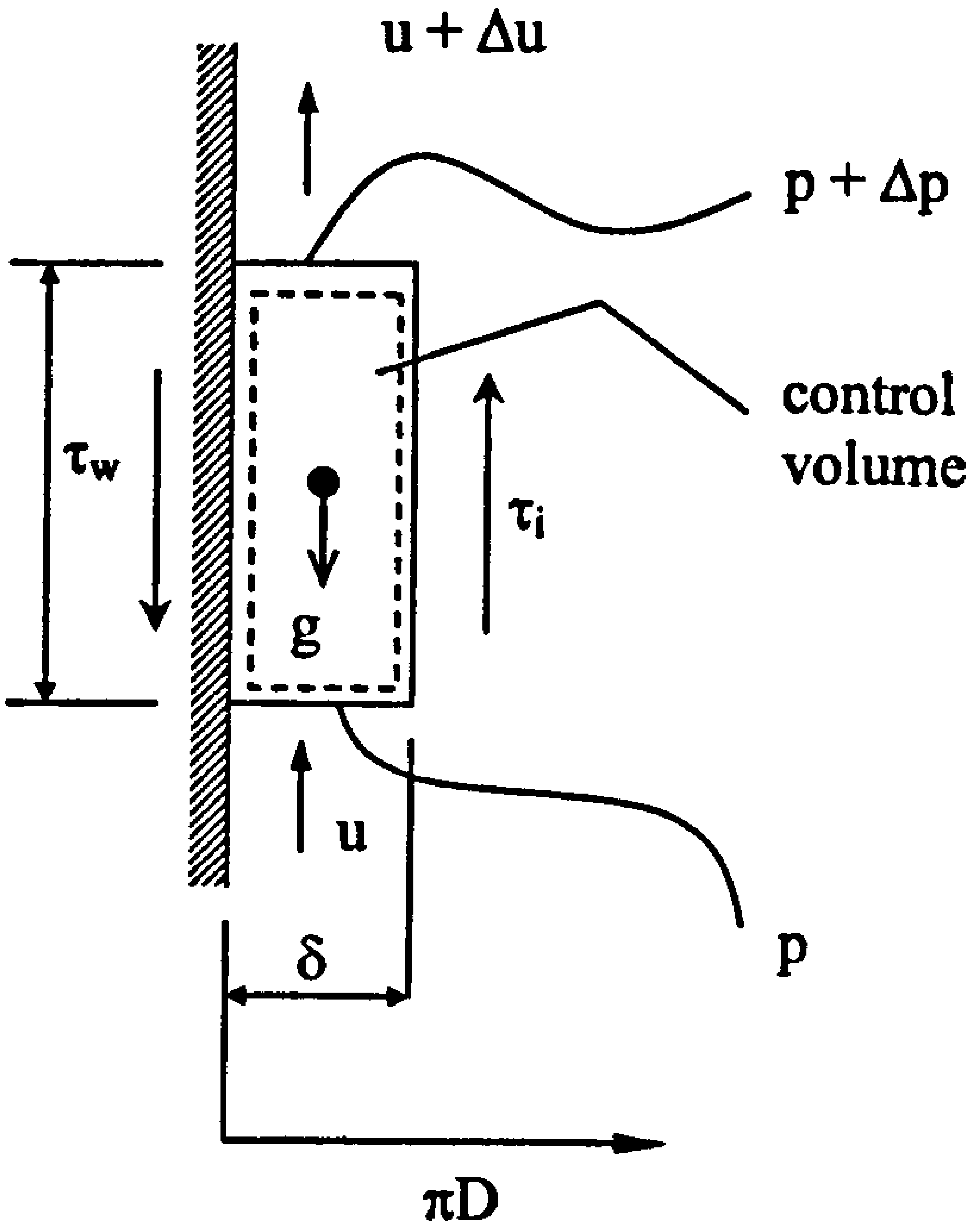

Figure A.3: Control element in liquid film flow

Summing all the forces acting on the control element depicted in Figure A.3 gives;

$$\sum_n Forces = \frac{d}{dt}(momentum)_n \tag{A.15}$$

$$p\pi D\delta - (p+\Delta p)\pi D\delta - \tau_w \Delta z \pi D + \tau_i \Delta z \pi D - g\rho_l \pi D\delta \Delta z = M\frac{du}{dt} \tag{A.16}$$

Simplifying the r.h.s. and differentiating with respect to z gives;

$$-\pi D\delta \frac{dp}{dz} - \tau_w \pi D + \tau_i \pi D - g\rho_l \pi D\delta = M\frac{du}{dz} \tag{A.17}$$

Expanding the l.h.s gives;

$$-\pi D\delta \frac{dp}{dz} - \tau_w \pi D + \tau_i \pi D - g\rho_l \pi D\delta = \rho_l u \pi D\delta \frac{du}{dz} \tag{A.18}$$

Simplifying and ignoring the acceleration effects in the film gives;

$$\frac{dp}{dz} = \frac{(\tau_i - \tau_w)}{\delta} - g\rho_l \tag{A.19}$$

A.4 Derivation of Momentum Equation 7.10 for Core Flow

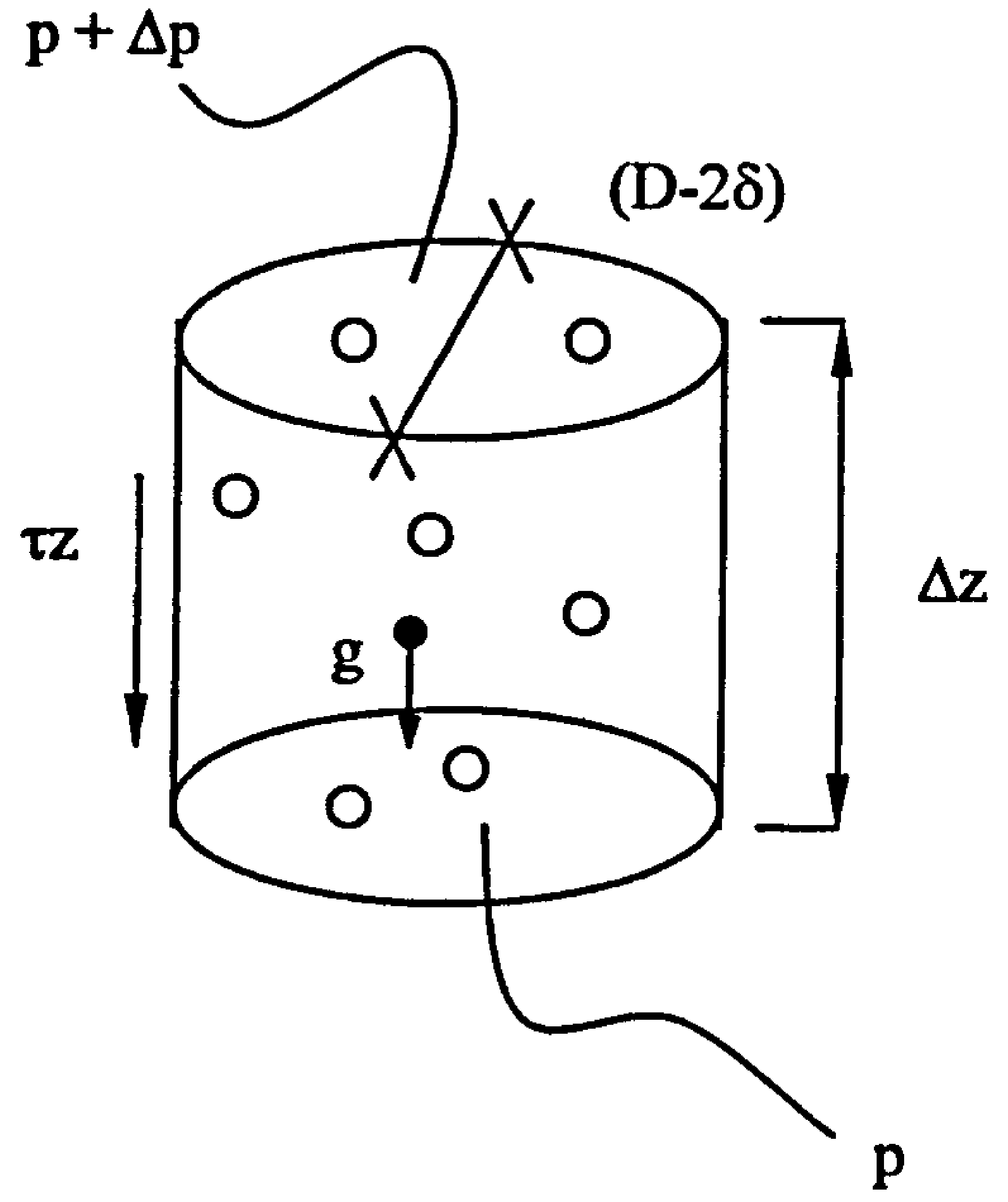

Figure A.4: Element in core flow

Summing all the forces acting on the control element depicted in Figure A.4 gives;

$$\sum_n Forces = \frac{d}{dt}(momentum)_n \tag{A.20}$$

Assuming that the entrained liquid velocity is equal to the gas velocity then;

$$\frac{-\Delta p\pi(D-2\delta)^2}{4} - \frac{g(D-2\delta)^2\pi\Delta z}{4v_c} - \tau_i\pi(D-2\delta)\Delta z = \frac{G_c^2\pi(D-2\delta)^2\Delta v_c}{4} \tag{A.21}$$

Simplifying gives;

$$-\Delta p(D-2\delta) - \frac{g}{4v_c}(D-2\delta)\Delta z - \tau_i\Delta z = \frac{G_c^2(D-2\delta)\Delta v_c}{4} \tag{A.22}$$

Differentiating with respect to z gives;

$$-\frac{dp}{dz}(D-2\delta)\tfrac{1}{4} - \frac{g(D-2\delta)}{4v_c} - \tau_i = \frac{G_c^2(D-2\delta)}{4}\frac{dv_c}{dz} \tag{A.23}$$

$$\frac{dp}{dz} = -\frac{g}{v_c} - \frac{4\tau_i}{(D-2\delta)} - G_c^2\frac{dv_c}{dz} \tag{A.24}$$

A.5 Implementation of the Method of McNeil [118] (2000)

To apply the method of McNeil [118] (2000) a FORTRAN programme was written. The programme contained an iterative procedure that determined stagnation properties, Mach numbers and the contraction area. A flow diagram of the programme is given in Figure A.5. The upstream entrained liquid fraction and slip ratio were determined using the correlations of Govan *et al* [59] (1988) and Premoli *et al* [58] (1970) respectively.

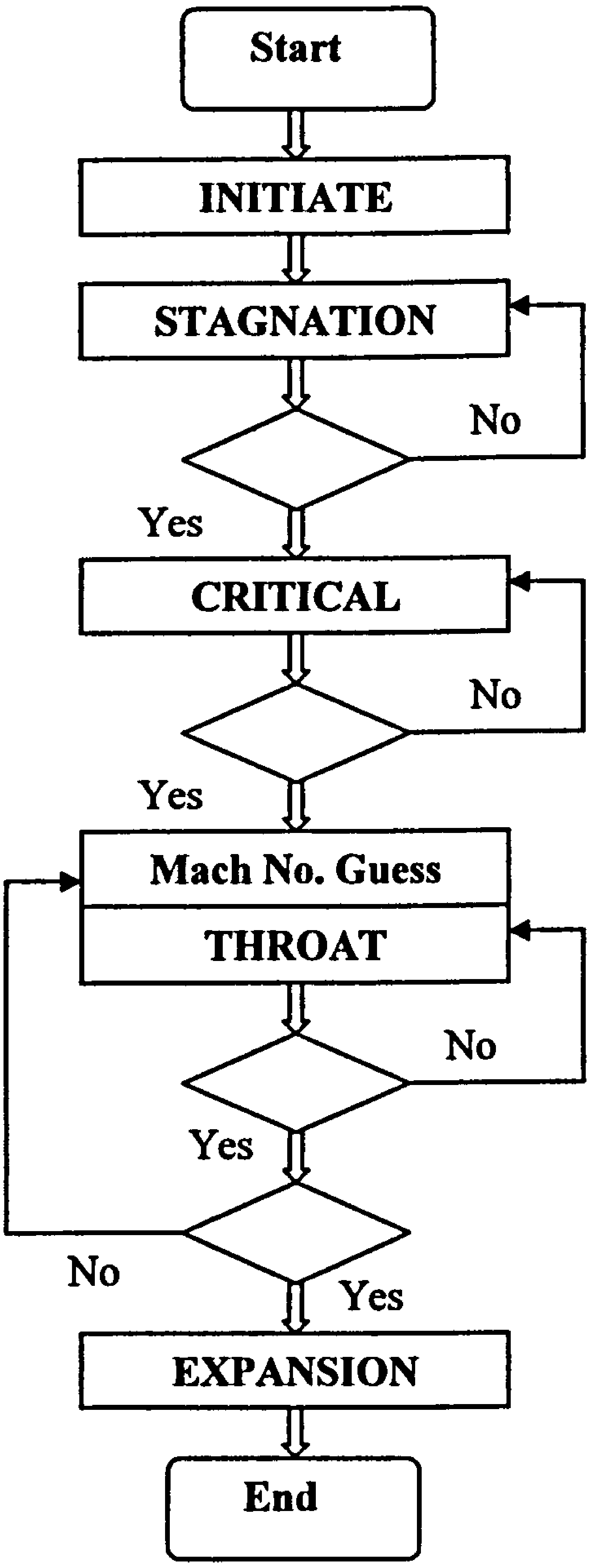

Read upstream values for slip, entrainment, mass flow rate and pressure.

Set convergence criteria and calculate stagnation conditions.

Calculate G and H parameters. Is the stagnation pressure ratio resolved?

Set convergence criteria, let Mach=1, calculate critical conditions.

Calculate G and H parameters. Is the critical pressure ratio resolved?

Set convergence criteria and calculate throat conditions.

Calculate G and H parameters. Is the throat pressure ratio resolved?

Calculate compressible contraction coefficient and throat area. Is the throat area the same as the physical area?

Calculate pressure loss due to expansion.

Figure A.5: Flow Diagram for Orifice_Loss_2000

Theoretical vena-contracta areas were calculated using incompressible and compressible contraction coefficients. The incompressible contraction coefficient, C_{ci}, and the effective diameter ratio, β_{eff}, were obtained from the experimental single-phase loss coefficients and the simultaneous solution of Equations A.25 & A.26;

$$C_{ci} = \frac{1}{1 + 0.639\left(1 - \beta^2\right)} \tag{A.25}$$

$$k = \frac{1}{C_{ci}^2 \beta_{eff}^2} - 1 \qquad (A.26)$$

A force defect coefficient was calculated from the incompressible contraction coefficient allowing the compressible contraction coefficient, C_c, to be found. The effective diameter ratio, contraction, loss and force defect coefficients are given in Table A.1.

Property	Globe Valve	Orifice Plate
Incompressible contraction coefficient, C_{ci}	0.743	0.692
Single-phase loss coefficient, k	8.673	34.83
Effective diameter ratio, β_{eff}	0.678	0.55
Force defect coefficient	0.44	0.401

Table A.1: Incompressible Contraction Coefficients

In addition to the pressure loss induced by the contraction part of the orifice plate it was also necessary to determine the pressure loss due to the expansion directly following the contraction. The measured gas specific volume was to used to re-evaluate the slip ratio, fluid specific volume and momentum correction factor, at the throat and again down stream of the expansion. The pressure loss was then calculated in accordance with McNeil [118] by the application of the momentum equation from the vena-contracta, subscript 1, to the down stream pipe, subscript 2;

$$p_1 - p_2 = G_2\left(c_{m2} G_2 v_2 - c_{m1} G_1 v 1\right) \qquad (A.27)$$

This second pressure loss, due to the expansion, added to that of the contraction gave the total pressure loss for the orifice plate.

A.6 Void Fraction Measurement

Several techniques have been employed to provide accurate measurement of the void fraction. One of the least complex methods is to use a pair of quick closing valves. This approach was used by Andeen & Griffith [55] (1968), Hughmark & Pressburg [80] (1961), Kasturi & Stepanek [101] (1972), Weiss *et al* [103] (1985), Willis [64], and Anderson & Mantzouranis [65]. Two valves, the bores of which are flush with the pipe diameter, are located a known distance apart on a straight length of pipe and operated simultaneously. When a steady fully developed two-phase flow is established in the pipe the two valves are closed and the volume of captured liquid is measured. Although advantageous due to the simplicity of this method, the use of quick closing valves involves interrupting the two-phase flow, and at higher mass fluxes and pressures this may not be practical.

The conductance method employs two probes situated flush with the non-conducting wall containing the annular film of a two-phase flow. By monitoring the conductance between the probes the liquid film thickness can be established. Averaging techniques are applied to the conductance signals generated by the probes as ripples and roll waves on the liquid film surface causes the liquid film thickness to fluctuate. This method has been used by Hewitt *et al* [126] (1964), Bennett & Thornton [127] (1961) and Collier & Hewitt [66].

Another popular method for measuring the void fraction is the use of ionising radiation sources. If a beam of gamma radiation is directed at a medium of uniform thickness, the thickness of the medium can be determined from the resulting attenuation of the gamma ray beam. If the intensity of the initial radiation is I_o, then the attenuated radiation, I, for a medium of thickness, t, with a mass attenuation coefficient, σ, and a density, ρ, is given by;

$$I = I_o e^{-\sigma_m \rho t} \tag{A.28}$$

Petrick & Swanson [128] (1958) used this relationship to derive an expression for the void fraction. By deriving expressions for the two extreme conditions, the pipe full of gas, $\alpha=1$ and the pipe full of liquid, $\alpha=0$, the resulting expression for void fraction can be shown to be;

$$\alpha = \frac{\ln(I/I_l)}{\ln(I_g/I_l)} \tag{A.29}$$

A derivation of Equation A.29 is given in Appendix A.2.

In addition to Petrick & Swanson [128], early investigators, including, Isbin *et al* [129] (1957) and Pike *et al* [130] (1965), improved the practice of using ionising sources through the selection of appropriate ionising sources and shielding. The selection of ionising sources is critical because if the energy of the selected source is too high then the attenuation of the gamma rays passing through the gas-liquid flow would be insignificant in comparison with the initial source intensity. For this reason, monoenergetic sources are favoured since they permit the use of Equation A.29 to describe the relationship of attenuation and intensity. Shielding is also critical in the generation of a narrow collimated or 'pencil' beam of gamma rays. This single beam of monoenergetic gamma photons can be more accurately directed across any tube or channel.

A.7 Derivation of Nozzle Flow Model

First consider single-phase liquid flow in a nozzle;

$$\frac{dp}{dz}=\left(\frac{dp}{dz}\right)_F+\left(\frac{dp}{dz}\right)_A \qquad (A.30)$$

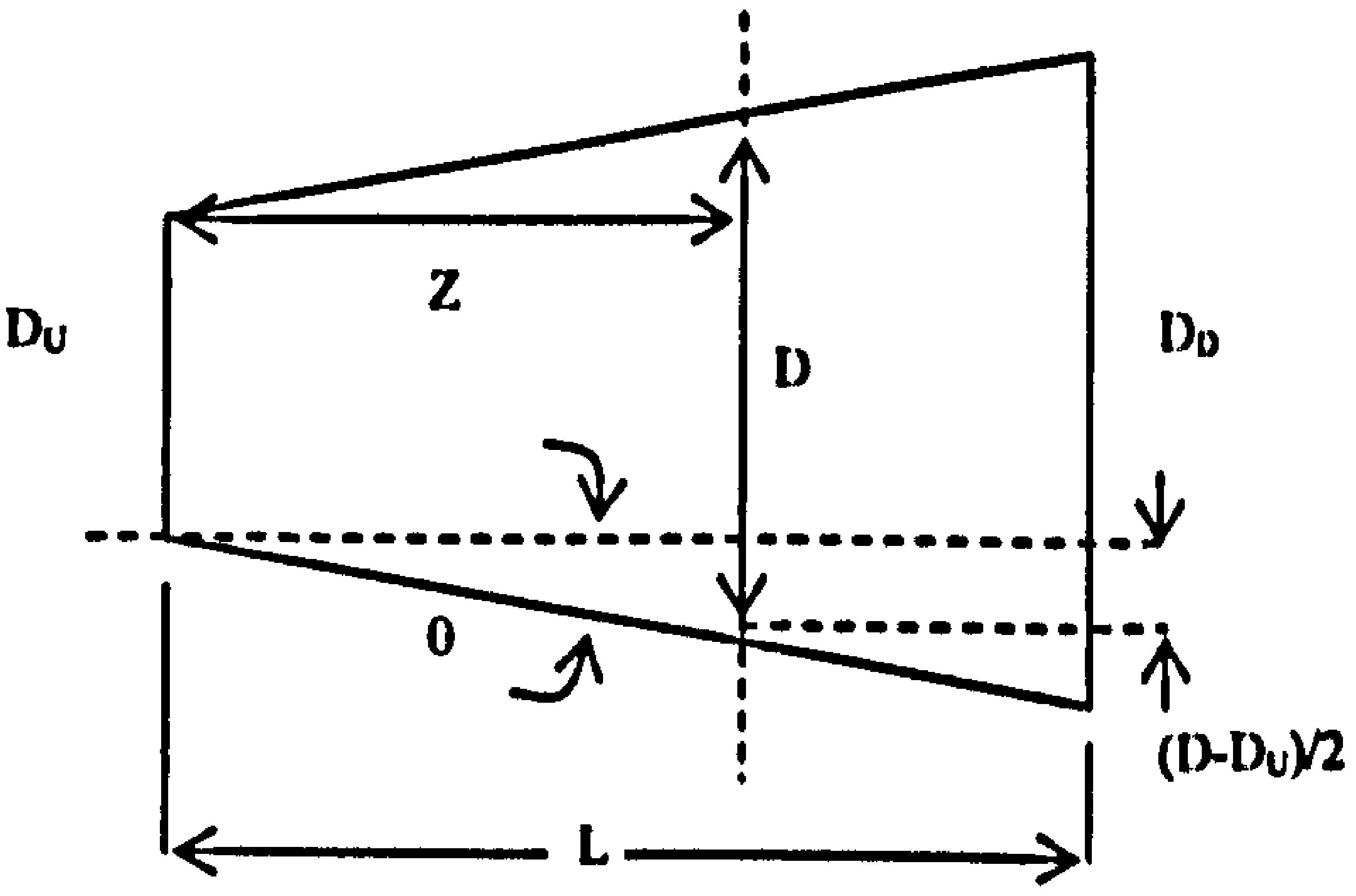

$$\left(\frac{dp}{dz}\right)_F=-\frac{4f}{D}\frac{\rho u^2}{2}=-\frac{2f}{D}\rho u^2 \qquad (A.31)$$

For laminar flow;

$$f=\frac{16}{\mathrm{Re}}=\frac{16\mu^2}{\rho uD} \qquad (A.32)$$

$$\Rightarrow\left(\frac{dp}{dz}\right)_F=-\frac{32\mu u}{D^2} \qquad (A.33)$$

$$\Rightarrow\left(\frac{dp}{dz}\right)_F=-32\mu u_U\frac{D_U^2}{D^4} \qquad (A.34)$$

$$Tan\theta=\frac{(D-D_U)}{2Z}=\frac{(D_D-D_U)}{2L} \qquad \Rightarrow z=L\frac{(D-D_u)}{(D_D-D_u)} \qquad (A.35)$$

$$dp_F=-32\mu u_u\frac{D_u^2}{D^4}dz \qquad \Rightarrow dz=L\frac{dD}{(D_D-D_U)}$$

$$=-32\mu u_U\frac{D_U^2}{D^4}\frac{LdD}{(D_D-D_U)} \qquad (A.36)$$

$$\Rightarrow P_{F_D}-P_{F_U}=-\frac{32\mu u_U D_U^2}{(D_D-D_U)}L\int_{D_U}^{D_D}\frac{dD}{D^4}=\frac{32}{3}\frac{\mu u_U D_U^2}{(D_D-D_U)}L\left[\frac{1}{D_D^3}-\frac{1}{D_U^3}\right] \qquad (A.37)$$

$$\Rightarrow P_{F_U}-P_{F_D}=\Delta P_F=\frac{32}{3}\frac{\mu u_U D_U^2 L}{(D_U-D_D)}\frac{(D_U^3-D_D^3)}{(D_D^3D_U^3)}=\frac{32}{3}\frac{\mu u_U D_U^2}{(D_D^3D_U^3)}\left(D_U^2+D_UD_D+D_D^2\right)$$

$$=\frac{32}{3}\mu\frac{u_U D_U^2 L}{D_D^3D_U^3}\left(D_U^2+D_UD_D+D_D^2\right) \qquad (A.38)$$

$$=\frac{32}{3}\mu\left(\frac{u_U D_U^2}{D_D^2}\right)\frac{L}{D_D D_U}\left(1+\beta+\beta^2\right) \quad \text{where,} \quad \beta=\frac{D_D}{D_U} \tag{A.39}$$

$$\Delta P_F=\frac{32}{3}\mu\frac{u_D L}{D_D D_U}\left(1+\beta+\beta^2\right) \tag{A.40}$$

$$\mathrm{Re}_D=\frac{\rho u_D D_D}{\mu}$$

$$\Delta P_F=\frac{32}{3}\frac{u_D L\rho}{D_U\,\mathrm{Re}_D}\left(1+\beta+\beta^2\right) \quad \text{where,} \quad f_D=\frac{16}{\mathrm{Re}_D} \tag{A.41}$$

$$\Rightarrow \Delta P_F=\frac{2}{3}\frac{f_D L}{D_U}\rho u_D^2\left(1+\beta+\beta^2\right) \tag{A.42}$$

$$\Delta P_F=\frac{4}{3}\frac{f_D L}{D_U}\frac{\rho u_D^2}{2}\left(1+\beta+\beta^2\right) \tag{A.43}$$

$$\left(\frac{dp}{dz}\right)_A=-\rho u\frac{d_U}{d_z} \tag{A.44}$$

$$\Rightarrow dp_A=-\rho u d_U \tag{A.45}$$

$$\Rightarrow p_{A_D}-p_{A_U}=-\frac{\rho}{2}\left(u_D^2-u_U^2\right) \tag{A.47}$$

$$\Rightarrow \Delta p_A=p_{A_U}-p_{A_D}=\frac{\rho}{2}\left(u_D^2-u_U^2\right) \tag{A.48}$$

$$\Delta p_{NOZ}=\Delta p_A+\Delta p_F \tag{A.49}$$

$$\Delta P_{NOZ}=\frac{\rho}{2}\left(u_D^2-u_U^2\right)+\frac{4}{3}\frac{f_D L}{D_{\blacksquare}}\frac{\rho u_D^2}{2}\left(1+\beta+\beta^2\right) \tag{A.50}$$

$$\Delta P_{NOZ}=\frac{v_L}{2}\left(G_D^2-G_U^2\right)+4\frac{f_D L}{D_{\blacksquare}}\frac{G_D^2 v_L}{2}\left(\frac{1+\beta+\beta^2}{3}\right) \tag{A.51}$$

For two-phase flow;

$$\Delta p_{TP}=\Delta p_A+\Delta p_F \tag{A.52}$$

$$\Delta p_A=\phi_{Lo}^2\Delta p_{A_{Lo}} \tag{A.53}$$

$$\Delta p_{A_{Lo}} = \frac{v_L}{2}\left(G_D^2 - G_U^2\right) \tag{A.54}$$

$$\phi_{Lo}^2 = C_m \frac{v}{v_L} \tag{A.55}$$

$$\Delta p_F = \Delta p_L \phi_L^2 \tag{A.56}$$

$$\Delta P_L = \frac{4 f_D L}{D_h}(1-x)^2 \frac{G_D^2 v_L}{2}\left(\frac{1+\beta+\beta^2}{3}\right) \tag{A.57}$$

$$f_D = \frac{16}{\mathrm{Re}_D} \qquad \mathrm{Re}_D = (1-x)\frac{G_D D_D}{\mu_L}$$

APPENDIX B

B.1 Rosemount Pressure Transducer Signal Conversion

Calculation for flow nozzle 1 - 26.02 mm diameter

Current signal range from pressure transducer: 4 – 20 mA

Voltage signal range from pressure transducer: 1 – 5 v

With the upper range value (URV) for flow nozzle 1set to 7475 N/m^2 the pressure plotted against voltage is shown in Figure B.1.

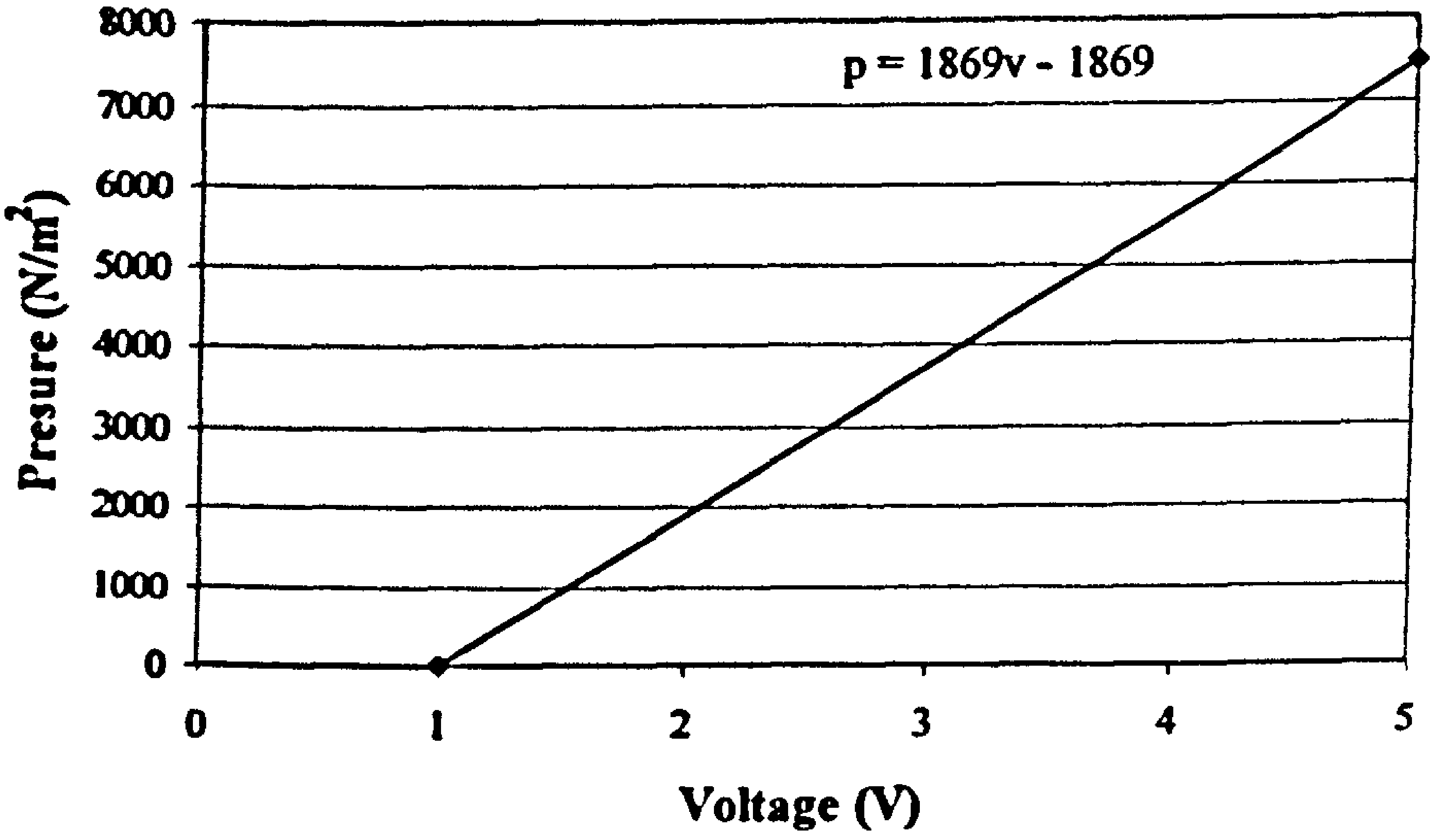

Figure B.1: Pressure versus Voltage

From the graph an equation for a line of gradient, m, and a constant, c;

$$p = mv + c \tag{B.1}$$

When the pressure is, 0, the equation can be written as;

$$0 = 1m + c \tag{B.2}$$

And when the pressure is at maximum the equation becomes;

$$7475 = 5m + c \tag{B.3}$$

By combing Equations B.2 & B.3 the gradient, m, is given as:

$$7475 = 5m - m$$
$$m = \frac{7475}{4}$$
$$\underline{\underline{m = 1869}}$$

The constant, c, is found from;

$$7475 = 5m + c$$
$$c = 7475 - (5x1869)$$
$$\underline{\underline{c = 1869}}$$

The conversion from voltage to pressure is then;

$$p = mv - c$$
$$p = 1869v - 1869$$
$$\underline{\underline{p = 1869(v-1) = \tfrac{1}{4}URV(v-1)}}$$

APPENDIX C

C.1 Single-Phase Glycerine Solution Viscosity & Calibration Tests

C.1.1 Viscosity Curves

Test Date	x^3	x^2	x	con
01-Mar-01	-9.00E-04	9.70E-02	-3.8274	55.483
13-Mar-01	-7.00E-04	8.13E-02	-3.2605	48.098
22-Mar-01	-1.00E-03	9.85E-02	-3.4522	46.032
27-Mar-01	-1.01E-03	9.40E-02	-3.178	40.960
02-Apr-01	-8.37E-04	8.11E-02	-2.849	38.090
06-Apr-01	-1.73E-03	1.42E-01	-4.146	46.310
04-May-01	-6.03E-04	5.93E-02	-2.108	28.620
31-May-01	-6.80E-04	6.63E-02	-2.335	31.25
04-Jun-01	-6.24E-04	6.41E-02	-2.361	32.650
11-Jun-01	-9.38E-04	8.81E-02	-2.974	38.03
25-Jun-01	-7.21E-04	7.17E-02	-2.547	33.980
11-Jul-01	-5.57E-04	6.17E-02	-2.343	31.94
25-Jul-01	-4.63E-04	4.18E-02	-1.366	17.28
13-Aug-01	-3.12E-04	2.94E-02	-0.9992	13.11
18-Aug-01	-5.46E-05	6.46E-03	-0.2753	4.561
30-Aug-01	-1.62E-04	1.80E-02	-0.7133	10.76
22-Oct-01	-5.09E-05	5.04E-03	-1.87E-01	2.875

Table C.1: Viscosity Curves [Units: centi poise & Temperature °C]

C.1.2 Calibration Curves

Test Date	x^2	x	con	Flow Nozzle dia.	Flow Nozzle No.
02-Apr-01	-7.91E-06	2.73E-03	0.455	13.6	2
09-Mar-01	-6.04E-05	9.43E-03	0.2074	6.44	3
16-Feb-01	-3.16E-06	1.53E-03	0.5416	26.02	1
06-Jun-01	-8.86E-06	2.86E-03	0.4722	13.6	2
05-Jun-01	-5.78E-06	1.85E-03	0.5973	26.02	1
15-Jun-01	-8.66E-06	2.26E-03	0.5493	26.02	1
19-Jun-01	-8.48E-06	2.85E-03	0.4368	13.6	2
20-Jun-01	-9.98E-06	2.67E-03	0.52	26.02	1
17-Jul-01	-3.98E-06	1.77E-03	0.5353	26.02	1
18-Jul-01	-7.03E-06	2.95E-03	0.3939	13.6	2
19-Jul-01	-4.02E-06	2.00E-03	0.474	13.6	2
20-Jul-01	-4.01E-06	2.01E-03	0.4869	13.6	2
03-Aug-01	-8.85E-07	7.15E-04	0.6735	26.02	1
25-Jul-01	-1.08E-06	9.57E-04	0.5692	13.6	2
25-Jul-01	-2.99E-06	1.80E-03	0.4115	6.44	3
13-Aug-01	-5.61E-07	5.76E-04	0.6668	26.02	1
21-Aug-01	-1.16E-08	6.91E-05	0.7783	26.02	1
18-Aug-01	-1.26E-08	1.01E-04	0.7051	13.6	2
22-Aug-01	-2.55E-07	7.26E-04	0.2936	6.44	3
13-Aug-01	-9.79E-07	7.26E-04	0.6275	26.02	1
13-Aug-01	-4.23E-08	1.86E-04	0.7049	13.6	2
22-Oct-01	-1.24E-07	3.93E-04	5.43E-01	13.6	2

Table C.2: Flow Nozzle Calibration Curves, *Re* versus c_D

C.1.3 Pipe Flow Viscosity & Calibration Reference

Test Date (dd/mm/yy)	**Data Tag (-)**	**Flow Nozzle (-)**	**Test Description (-)**	**Calibration Date (dd/mm/yy)**	**Viscosity Date (dd/mm/yy)**
14-Feb-01	001	cn26.02	Pipe	16-Feb-01	01-Mar-01
15-Feb-01	001	cn26.02	Pipe	16-Feb-01	01-Mar-01
21-Feb-01	001	cn26.02	Pipe	16-Feb-01	01-Mar-01
21-Feb-01	002	cn26.02	Pipe	16-Feb-01	01-Mar-01
21-Feb-01	003	cn26.02	Pipe	16-Feb-01	01-Mar-01
21-Feb-01	004	cn26.02	Pipe	16-Feb-01	01-Mar-01
21-Feb-01	005	cn26.02	Pipe	16-Feb-01	01-Mar-01
21-Feb-01	006	cn26.02	Pipe	16-Feb-01	01-Mar-01
21-Feb-01	007	cn26.02	Pipe	16-Feb-01	01-Mar-01
21-Feb-01	008	cn26.02	Pipe	16-Feb-01	01-Mar-01
05-Mar-01	001	cn13.6	Pipe	02-Apr-01	01-Mar-01
05-Mar-01	002	cn13.6	Pipe	02-Apr-01	01-Mar-01
05-Mar-01	003	cn13.6	Pipe	02-Apr-01	01-Mar-01
05-Mar-01	004	cn13.6	Pipe	02-Apr-01	01-Mar-01
05-Mar-01	005	cn13.6	Pipe	02-Apr-01	01-Mar-01

Table C.3: Pipe Flow, Viscosity & Calibration Curves

Test Date (dd/mm/yy)	**Data Tag (-)**	**Flow Nozzle (-)**	**Test Description (-)**	**Calibration Date (dd/mm/yy)**	**Viscosity Date (dd/mm/yy)**
12-Aug-01	001	cn26.02	Pipe - Vis2	13-Aug-01	13-Aug-01
12-Aug-01	002	cn26.02	Pipe - Vis2	13-Aug-01	13-Aug-01
12-Aug-01	003	cn26.02	Pipe - Vis2	13-Aug-01	13-Aug-01
12-Aug-01	004	cn26.02	Pipe - Vis2	13-Aug-01	13-Aug-01
12-Aug-01	005	cn26.02	Pipe - Vis2	13-Aug-01	13-Aug-01
12-Aug-01	006	cn26.02	Pipe - Vis2	13-Aug-01	13-Aug-01
12-Aug-01	007	cn26.02	Pipe - Vis2	13-Aug-01	13-Aug-01
12-Aug-01	008	cn26.02	Pipe - Vis2	13-Aug-01	13-Aug-01

Table C.4: Pipe Flow, Nominal Viscosity 200 mPas & Calibration Curves

Test Date (dd/mm/yy)	**Data Tag (-)**	**Flow Nozzle (-)**	**Test Description (-)**	**Calibration Date (dd/mm/yy)**	**Viscosity Date (dd/mm/yy)**
24-Aug-01	001	cn26.02	Pipe - Vis3	21-Aug-01	18-Aug-01
24-Aug-01	002	cn26.02	Pipe - Vis3	21-Aug-01	18-Aug-01
24-Aug-01	003	cn26.02	Pipe - Vis3	21-Aug-01	18-Aug-01
24-Aug-01	004	cn26.02	Pipe - Vis3	21-Aug-01	18-Aug-01
24-Aug-01	005	cn26.02	Pipe - Vis3	21-Aug-01	18-Aug-01
24-Aug-01	006	cn26.02	Pipe - Vis3	21-Aug-01	18-Aug-01
24-Aug-01	007	cn26.02	Pipe - Vis3	21-Aug-01	18-Aug-01
24-Aug-01	009	cn26.02	Pipe - Vis3	21-Aug-01	18-Aug-01
24-Aug-01	010	cn26.02	Pipe - Vis3	21-Aug-01	18-Aug-01

Table C.5: Pipe Flow, Nominal Viscosity 50 mPas & Calibration Curves

Property 100% Glycerine	**Value**	**Units**	**Conditions**
Surface tension	66	Dyn/cm	Fluid bounded by air
Density	1.261	g/cm^3	@ 20°C
Boiling point	290	°C	
Specific heat capacity	2.38	J/g.K	

Table C.6: Properties of Glycerine

C.1.4 Discharge Components Viscosity & Calibration Reference

Test Date (dd/mm/yy)	Data Tag (-)	Flow Nozzle (-)	Test Description (-)	Calibration Date (dd/mm/yy)	Viscosity Date (dd/mm/yy)
09-Apr-01	001	cn13.6	Nozzle Dis.	02-Apr-01	06-Apr-01
09-Apr-01	002	cn13.6	Nozzle Dis.	02-Apr-01	06-Apr-01
09-Apr-01	003	cn13.6	Nozzle Dis.	02-Apr-01	06-Apr-01
09-Apr-01	004	cn13.6	Nozzle Dis.	02-Apr-01	06-Apr-01
09-Apr-01	005	cn13.6	Nozzle Dis.	02-Apr-01	06-Apr-01
09-Apr-01	006	cn13.6	Nozzle Dis.	02-Apr-01	06-Apr-01
09-Apr-01	007	cn13.6	Nozzle Dis.	02-Apr-01	06-Apr-01
04-Jun-01	029	cn13.6	Nozzle Dis.	06-Jun-01	04-Jun-01
04-Jun-01	030	cn13.6	Nozzle Dis.	06-Jun-01	04-Jun-01
04-Jun-01	031	cn13.6	Nozzle Dis.	06-Jun-01	04-Jun-01
04-Jun-01	032	cn13.6	Nozzle Dis.	06-Jun-01	04-Jun-01
04-Jun-01	033	cn13.6	Nozzle Dis.	06-Jun-01	04-Jun-01
04-Jun-01	034	cn13.6	Nozzle Dis.	06-Jun-01	04-Jun-01
04-Jun-01	035	cn13.6	Nozzle Dis.	06-Jun-01	04-Jun-01
04-Jun-01	036	cn13.6	Nozzle Dis.	06-Jun-01	04-Jun-01
04-Jun-01	037	cn13.6	Nozzle Dis.	06-Jun-01	04-Jun-01
04-Jun-01	038	cn13.6	Nozzle Dis.	06-Jun-01	04-Jun-01
04-Jun-01	039	cn13.6	Nozzle Dis.	06-Jun-01	04-Jun-01
04-Jun-01	040	cn13.6	Nozzle Dis.	06-Jun-01	04-Jun-01
04-Jun-01	041	cn13.6	Nozzle Dis.	06-Jun-01	04-Jun-01
04-Jun-01	042	cn13.6	Nozzle Dis.	06-Jun-01	04-Jun-01
04-Jun-01	043	cn13.6	Nozzle Dis.	06-Jun-01	04-Jun-01
23-Jul-01	015	cn13.6	Nozzle Dis.	20-Jul-01	11-Jul-01
23-Jul-01	016	cn13.6	Nozzle Dis.	20-Jul-01	11-Jul-01
23-Jul-01	017	cn13.6	Nozzle Dis.	20-Jul-01	11-Jul-01
23-Jul-01	018	cn13.6	Nozzle Dis.	20-Jul-01	11-Jul-01
23-Jul-01	019	cn13.6	Nozzle Dis.	20-Jul-01	11-Jul-01

Table C.7: Discharge Nozzle, Viscosity & Calibration Curves

Test Date (dd/mm/yy)	Data Tag (-)	Flow Nozzle (-)	Test Description (-)	Calibration Date (dd/mm/yy)	Viscosity Date (dd/mm/yy)
23-Jul-01	020	cn13.6	Nozzle Dis.	20-Jul-01	11-Jul-01
23-Jul-01	021	cn13.6	Nozzle Dis.	20-Jul-01	11-Jul-01
23-Jul-01	022	cn13.6	Nozzle Dis.	20-Jul-01	11-Jul-01
23-Jul-01	023	cn13.6	Nozzle Dis.	20-Jul-01	11-Jul-01
23-Jul-01	024	cn13.6	Nozzle Dis.	20-Jul-01	11-Jul-01

Table C.8: Discharge Nozzle, Viscosity & Calibration Curves

Test		Flow	Test	Calibration	Viscosity
Date	Data Tag	Nozzle	Description	Date	Date
(dd/mm/yy)	(-)	(-)	(-)	(dd/mm/yy)	(dd/mm/yy)
02-Aug-01	009	cn13.6	Nozzle Dis.	25-Jul-01	13-Aug-01
02-Aug-01	010	cn13.6	Nozzle Dis.	25-Jul-01	13-Aug-01
02-Aug-01	011	cn13.6	Nozzle Dis.	25-Jul-01	13-Aug-01
02-Aug-01	012	cn13.6	Nozzle Dis.	25-Jul-01	13-Aug-01
02-Aug-01	013	cn13.6	Nozzle Dis.	25-Jul-01	13-Aug-01
02-Aug-01	014	cn13.6	Nozzle Dis.	25-Jul-01	13-Aug-01
02-Aug-01	015	cn13.6	Nozzle Dis.	25-Jul-01	13-Aug-01
02-Aug-01	016	cn13.6	Nozzle Dis.	25-Jul-01	13-Aug-01
02-Aug-01	017	cn13.6	Nozzle Dis.	25-Jul-01	13-Aug-01
02-Aug-01	018	cn13.6	Nozzle Dis.	25-Jul-01	13-Aug-01
02-Aug-01	019	cn13.6	Nozzle Dis.	25-Jul-01	13-Aug-01
02-Aug-01	020	cn13.6	Nozzle Dis.	25-Jul-01	13-Aug-01
02-Aug-01	021	cn26.02	Nozzle Dis.	13-Aug-01	13-Aug-01
02-Aug-01	022	cn26.02	Nozzle Dis.	13-Aug-01	13-Aug-01
02-Aug-01	023	cn26.02	Nozzle Dis.	13-Aug-01	13-Aug-01
02-Aug-01	024	cn26.02	Nozzle Dis.	13-Aug-01	13-Aug-01
02-Aug-01	025	cn26.02	Nozzle Dis.	13-Aug-01	13-Aug-01
02-Aug-01	026	cn26.02	Nozzle Dis.	13-Aug-01	13-Aug-01
02-Aug-01	027	cn26.02	Nozzle Dis.	13-Aug-01	13-Aug-01
02-Aug-01	028	cn26.02	Nozzle Dis.	13-Aug-01	13-Aug-01
02-Aug-01	029	cn26.02	Nozzle Dis.	13-Aug-01	13-Aug-01

Table C.9: Discharge Nozzle, Nominal Viscosity 200 mPas & Calibration Curves

Test Date (dd/mm/yy)	Data Tag (-)	Flow Nozzle (-)	Test Description (-)	Calibration Date (dd/mm/yy)	Viscosity Date (dd/mm/yy)
30-Aug-01	001	cn13.6	Nozzle Dis.	18-Aug-01	18-Aug-01
30-Aug-01	002	cn13.6	Nozzle Dis.	18-Aug-01	18-Aug-01
30-Aug-01	003	cn13.6	Nozzle Dis.	18-Aug-01	18-Aug-01
30-Aug-01	004	cn13.6	Nozzle Dis.	18-Aug-01	18-Aug-01
30-Aug-01	005	cn13.6	Nozzle Dis.	18-Aug-01	18-Aug-01
30-Aug-01	006	cn13.6	Nozzle Dis.	18-Aug-01	18-Aug-01
30-Aug-01	007	cn13.6	Nozzle Dis.	18-Aug-01	18-Aug-01
30-Aug-01	008	cn26.02	Nozzle Dis.	21-Aug-01	18-Aug-01
30-Aug-01	009	cn26.02	Nozzle Dis.	21-Aug-01	18-Aug-01
30-Aug-01	010	cn26.02	Nozzle Dis.	21-Aug-01	18-Aug-01
30-Aug-01	011	cn26.02	Nozzle Dis.	21-Aug-01	18-Aug-01
30-Aug-01	012	cn26.02	Nozzle Dis.	21-Aug-01	18-Aug-01
30-Aug-01	013	cn26.02	Nozzle Dis.	21-Aug-01	18-Aug-01
30-Aug-01	014	cn26.02	Nozzle Dis.	21-Aug-01	18-Aug-01
30-Aug-01	015	cn26.02	Nozzle Dis.	21-Aug-01	18-Aug-01

Table C.10: Discharge Nozzle, Nominal Viscosity 50 mPas & Calibration Curves

Test Date (dd/mm/yy)	Data Tag (-)	Flow Nozzle (-)	Test Description (-)	Calibration Date (dd/mm/yy)	Viscosity Date (dd/mm/yy)
01-Jun-01	020	cn13.6	Orifice Dis.	06-Jun-01	31-May-01
01-Jun-01	021	cn13.6	Orifice Dis.	06-Jun-01	31-May-01
01-Jun-01	022	cn13.6	Orifice Dis.	06-Jun-01	31-May-01
01-Jun-01	023	cn13.6	Orifice Dis.	06-Jun-01	31-May-01
01-Jun-01	024	cn13.6	Orifice Dis.	06-Jun-01	31-May-01
01-Jun-01	025	cn13.6	Orifice Dis.	06-Jun-01	31-May-01
01-Jun-01	026	cn13.6	Orifice Dis.	06-Jun-01	31-May-01
01-Jun-01	027	cn13.6	Orifice Dis.	06-Jun-01	31-May-01
01-Jun-01	028	cn13.6	Orifice Dis.	06-Jun-01	31-May-01
01-Jun-01	029	cn13.6	Orifice Dis.	06-Jun-01	31-May-01
01-Jun-01	030	cn13.6	Orifice Dis.	06-Jun-01	31-May-01
01-Jun-01	031	cn13.6	Orifice Dis.	06-Jun-01	31-May-01
01-Jun-01	032	cn13.6	Orifice Dis.	06-Jun-01	31-May-01
01-Jun-01	033	cn13.6	Orifice Dis.	06-Jun-01	31-May-01
01-Jun-01	034	cn13.6	Orifice Dis.	06-Jun-01	31-May-01
01-Jun-01	035	cn13.6	Orifice Dis.	06-Jun-01	31-May-01

Table C.11: Discharge Orifice, Viscosity & Calibration Curves

Test Date (dd/mm/yy)	Data Tag (-)	Flow Nozzle (-)	Test Description (-)	Calibration Date (dd/mm/yy)	Viscosity Date (dd/mm/yy)
01-Jun-01	036	cn13.6	Orifice Dis.	06-Jun-01	31-May-01
01-Jun-01	037	cn13.6	Orifice Dis.	06-Jun-01	31-May-01
01-Jun-01	038	cn13.6	Orifice Dis.	06-Jun-01	31-May-01
01-Jun-01	039	cn13.6	Orifice Dis.	06-Jun-01	31-May-01
01-Jun-01	040	cn13.6	Orifice Dis.	06-Jun-01	31-May-01
01-Jun-01	041	cn13.6	Orifice Dis.	06-Jun-01	31-May-01
01-Jun-01	042	cn13.6	Orifice Dis.	06-Jun-01	31-May-01
04-Jun-01	009	cn13.6	Orifice Dis.	06-Jun-01	04-Jun-01
04-Jun-01	010	cn13.6	Orifice Dis.	06-Jun-01	04-Jun-01
04-Jun-01	011	cn13.6	Orifice Dis.	06-Jun-01	04-Jun-01
04-Jun-01	012	cn13.6	Orifice Dis.	06-Jun-01	04-Jun-01
04-Jun-01	013	cn13.6	Orifice Dis.	06-Jun-01	04-Jun-01
04-Jun-01	014	cn13.6	Orifice Dis.	06-Jun-01	04-Jun-01
04-Jun-01	015	cn13.6	Orifice Dis.	06-Jun-01	04-Jun-01
04-Jun-01	016	cn13.6	Orifice Dis.	06-Jun-01	04-Jun-01
04-Jun-01	017	cn13.6	Orifice Dis.	06-Jun-01	04-Jun-01
04-Jun-01	018	cn13.6	Orifice Dis.	06-Jun-01	04-Jun-01
04-Jun-01	019	cn13.6	Orifice Dis.	06-Jun-01	04-Jun-01
04-Jun-01	020	cn13.6	Orifice Dis.	06-Jun-01	04-Jun-01
04-Jun-01	021	cn26.02	Orifice Dis.	17-Jul-01	04-Jun-01
04-Jun-01	022	cn26.02	Orifice Dis.	17-Jul-01	04-Jun-01
04-Jun-01	023	cn26.02	Orifice Dis.	17-Jul-01	04-Jun-01
04-Jun-01	024	cn26.02	Orifice Dis.	17-Jul-01	04-Jun-01
04-Jun-01	025	cn26.02	Orifice Dis.	17-Jul-01	04-Jun-01
04-Jun-01	026	cn26.02	Orifice Dis.	17-Jul-01	04-Jun-01
04-Jun-01	027	cn26.02	Orifice Dis.	17-Jul-01	04-Jun-01
04-Jun-01	028	cn26.02	Orifice Dis.	17-Jul-01	04-Jun-01

Table C.12: Discharge Orifice, Viscosity & Calibration Curves

C.1.5 In-line Components Viscosity & Calibration Reference

Test Date (dd/mm/yy)	Data Tag (-)	Flow Nozzle (-)	Test Description (-)	Calibration Date (dd/mm/yy)	Viscosity Date (dd/mm/yy)
04-May-01	001	cn26.02	Orifice In-line	16-Feb-01	04-May-01
04-May-01	002	cn26.02	Orifice In-line	16-Feb-01	04-May-01
04-May-01	003	cn26.02	Orifice In-line	16-Feb-01	04-May-01
04-May-01	004	cn26.02	Orifice In-line	16-Feb-01	04-May-01
04-May-01	005	cn13.6	Orifice In-line	02-Apr-01	04-May-01
04-May-01	006	cn13.6	Orifice In-line	02-Apr-01	04-May-01
04-May-01	007	cn13.6	Orifice In-line	02-Apr-01	04-May-01

Table C.13: In-line Orifice, Viscosity & Calibration Curves

Test Date (dd/mm/yy)	Data Tag (-)	Flow Nozzle (-)	Test Description (-)	Calibration Date (dd/mm/yy)	Viscosity Date (dd/mm/yy)
14-Jun-01	001	cn13.6	Globe Valve	19-Jun-01	11-Jun-01
14-Jun-01	002	cn13.6	Globe Valve	19-Jun-01	11-Jun-01
14-Jun-01	003	cn13.6	Globe Valve	19-Jun-01	11-Jun-01
14-Jun-01	004	cn13.6	Globe Valve	19-Jun-01	11-Jun-01
14-Jun-01	005	cn13.6	Globe Valve	19-Jun-01	11-Jun-01
14-Jun-01	006	cn13.6	Globe Valve	19-Jun-01	11-Jun-01
14-Jun-01	007	cn13.6	Globe Valve	19-Jun-01	11-Jun-01
14-Jun-01	008	cn13.6	Globe Valve	19-Jun-01	11-Jun-01
14-Jun-01	009	cn26.02	Globe Valve	17-Jul-01	11-Jun-01
14-Jun-01	010	cn26.02	Globe Valve	17-Jul-01	11-Jun-01
14-Jun-01	011	cn26.02	Globe Valve	17-Jul-01	11-Jun-01

Table C.14: Globe Valve, Viscosity & Calibration Curves

Test Date (dd/mm/yy)	Data Tag (-)	Flow Nozzle (-)	Test Description (-)	Calibration Date (dd/mm/yy)	Viscosity Date (dd/mm/yy)
29-Jun-01	001	cn26.02	Nozzle In-line	17-Jul-01	11-Jul-01
29-Jun-01	002	cn26.02	Nozzle In-line	17-Jul-01	11-Jul-01
29-Jun-01	003	cn26.02	Nozzle In-line	17-Jul-01	11-Jul-01
29-Jun-01	004	cn26.02	Nozzle In-line	17-Jul-01	11-Jul-01
29-Jun-01	005	cn26.02	Nozzle In-line	17-Jul-01	11-Jul-01
02-Jul-01	001	cn13.6	Nozzle In-line	19-Jun-01	25-Jun-01
02-Jul-01	002	cn13.6	Nozzle In-line	19-Jun-01	25-Jun-01
02-Jul-01	003	cn13.6	Nozzle In-line	19-Jun-01	25-Jun-01
02-Jul-01	004	cn13.6	Nozzle In-line	19-Jun-01	25-Jun-01
02-Jul-01	005	cn13.6	Nozzle In-line	19-Jun-01	25-Jun-01
02-Jul-01	006	cn13.6	Nozzle In-line	19-Jun-01	25-Jun-01
02-Jul-01	007	cn13.6	Nozzle In-line	19-Jun-01	25-Jun-01
02-Jul-01	008	cn13.6	Nozzle In-line	19-Jun-01	25-Jun-01

Table C.15: In-line Nozzle, Viscosity & Calibration Curves

Test Date (dd/mm/yy)	Data Tag (-)	Flow Nozzle (-)	Test Description (-)	Calibration Date (dd/mm/yy)	Viscosity Date (dd/mm/yy)
11-Jul-01	001	cn13.6	Abrupt Enl.	19-Jun-01	25-Jun-01
11-Jul-01	002	cn13.6	Abrupt Enl.	19-Jun-01	25-Jun-01
11-Jul-01	003	cn13.6	Abrupt Enl.	19-Jun-01	25-Jun-01
11-Jul-01	004	cn13.6	Abrupt Enl.	19-Jun-01	25-Jun-01
11-Jul-01	005	cn13.6	Abrupt Enl.	19-Jun-01	25-Jun-01
11-Jul-01	006	cn13.6	Abrupt Enl.	19-Jun-01	25-Jun-01
13-Jul-01	001	cn26.02	Abrupt Enl.	20-Jun-01	11-Jul-01
13-Jul-01	002	cn26.02	Abrupt Enl.	20-Jun-01	11-Jul-01
13-Jul-01	003	cn26.02	Abrupt Enl.	20-Jun-01	11-Jul-01

Table C.16: Abrupt Enlargement, Viscosity & Calibration Curves

C.2 Two-Phase Glycerine Solution Viscosity & Calibration Tests

C.2.1 Viscosity Curves

Test Date	x^3	x^2	x	con
16-Feb-01	-9.00E-04	9.70E-02	-3.8274	55.483
13-Mar-01	-7.00E-04	8.13E-02	-3.2605	48.098
22-Mar-01	-1.00E-03	9.85E-02	-3.4522	46.032
27-Mar-01	-1.01E-03	9.40E-02	-3.178	40.960
02-Apr-01	-8.37E-04	8.11E-02	-2.849	38.090
06-Apr-01	-1.73E-03	1.42E-01	-4.146	46.310
04-May-01	-6.03E-04	5.93E-02	-2.108	28.620
15-May-01	-6.32E-04	6.08E-02	-2.12	28.280
23-May-01	-7.97E-04	7.46E-02	-2.52	32.400
31-May-01	-6.80E-04	6.63E-02	-2.335	31.125
04-Jun-01	-6.24E-04	6.41E-02	-2.361	32.650
11-Jun-01	-9.38E-04	8.81E-02	-2.974	38.030
25-Jun-01	-7.21E-04	7.17E-02	-2.547	33.980
11-Jul-01	-5.57E-04	6.17E-02	-2.343	31.94
25-Jul-01	-4.63E-04	4.18E-02	-1.366	17.28
03-Aug-01	-2.97E-04	2.91E-02	-1.036	14.34
18-Aug-01	-5.46E-05	6.46E-03	-0.2753	4.561
30-Aug-01	-1.62E-04	1.80E-02	-0.7133	10.76
22-Oct-01	-5.09E-05	5.04E-03	-1.87E-01	2.875

Table C.17: Viscosity Curves [Units: centi poise & Temperature °C]

C.2.2 Calibration Curves

Date	x^2	x	con	Flow Nozzle dia.	Flow Nozzle No.
16-Feb-01	-4.59E-06	1.83E-03	0.5242	26.02	1
05-Mar-01	-1.44E-05	4.22E-03	0.371	13.6	2
09-Mar-01	-6.02E-05	7.77E-03	0.2096	6.44	3
12-Mar-01	-8.27E-06	2.60E-03	0.4228	13.6	2
28-Mar-01	-7.37E-06	2.56E-03	0.4284	13.6	2
02-Apr-01	-7.43E-06	2.54E-03	0.4198	13.6	2
02-Apr-01	-2.04E-05	4.49E-03	0.2712	6.44	3
02-Apr-01	-7.91E-06	2.73E-03	0.455	13.6	2
09-Mar-01	-6.04E-05	9.43E-03	0.2074	6.44	3
16-Feb-01	-3.16E-06	1.53E-03	0.5416	26.02	1
06-Jun-01	-8.86E-06	2.86E-03	0.4722	13.6	2
05-Jun-01	-5.78E-06	1.85E-03	0.5973	26.02	1
21-Jun-01	-5.39E-05	7.70E-03	0.2501	6.44	3
03-Aug-01	-8.85E-07	7.15E-04	0.6735	26.02	1
25-Jul-01	-1.08E-06	9.57E-04	0.5692	13.6	2
25-Jul-01	-3.04E-06	1.82E-03	0.4074	6.44	3
13-Aug-01	-5.45E-07	5.71E-04	0.6735	26.02	1
21-Aug-01	-1.58E-08	6.91E-05	0.7783	26.02	1
18-Aug-01	-1.26E-08	1.01E-04	0.7051	13.6	2
22-Aug-01	-5.46E-07	2.39E-04	0.5638	6.44	3
22-Oct-01	-1.24E-07	3.93E-04	5.43E-01	13.6	2

Table C.18: Flow Nozzle Calibration Curves, *Re* versus c_D

C.2.3 Pipe Flow Viscosity & Calibration Reference

Test Date (dd/mm/yy)	Data Tag (-)	Flow Nozzle (-)	Test Description (-)	Calibration Date (dd/mm/yy)	Viscosity Date -Test (dd/mm/yy)
28-Feb-01	003	cn26.02	Pipe Flow Subsonic	16-Feb-01	16-Feb-01
13-Mar-01	001	cn13.6	Pipe Flow Subsonic	02-Apr-01	13-Mar-01
14-Mar-01	001	cn13.6	Pipe Flow Subsonic	02-Apr-01	13-Mar-01
15-Mar-01	001	cn13.6	Pipe Flow Subsonic	02-Apr-01	13-Mar-01
16-Mar-01	001	cn13.6	Pipe Flow Subsonic	02-Apr-01	13-Mar-01
20-Mar-01	001	cn6.44	Pipe Flow Subsonic	09-Mar-01	13-Mar-01
26-Mar-01	001	cn6.44	Pipe Flow Subsonic	09-Mar-01	22-Mar-01
30-Mar-01	001	cn6.44	Pipe Flow Subsonic	09-Mar-01	22-Mar-01

Table C.19: Pipe Discharge, Viscosity & Calibration Curves

Test Date (dd/mm/yy)	Data Tag (-)	Flow Nozzle (-)	Test Description (-)	Calibration Date (dd/mm/yy)	Viscosity Date -Test (dd/mm/yy)
03-Aug-01	001	cn13.6	Pipe Flow - Viscosity 2	25-Jul-01	03-Aug-01
03-Aug-01	002	cn13.6	Pipe Flow - Viscosity 2	25-Jul-01	03-Aug-01
08-Aug-01	001	Cn13.6	Pipe Flow - Viscosity 2	25-Jul-01	03-Aug-01
08-Aug-01	002	Cn13.6	Pipe Flow - Viscosity 2	25-Jul-01	03-Aug-01
09-Aug-01	001	Cn13.6	Pipe Flow - Viscosity 2	25-Jul-01	03-Aug-01
09-Aug-01	002	Cn6.44	Pipe Flow - Viscosity 2	25-Jul-01	03-Aug-01
10-Aug-01	001	Cn6.44	Pipe Flow - Viscosity 2	25-Jul-01	03-Aug-01
10-Aug-01	002	Cn6.44	Pipe Flow - Viscosity 2	25-Jul-01	03-Aug-01

Table C.20: Pipe Flow, Nominal Viscosity 200 mPas & Calibration Curves

Test Date (dd/mm/yy)	Data Tag (-)	Flow Nozzle (-)	Test Description (-)	Calibration Date (dd/mm/yy)	Viscosity Date –Test (dd/mm/yy)
19-Aug-01	001	cn13.6	Pipe Discharge - Viscosity 3	18-Aug-01	18-Aug-01
21-Aug-01	001	cn13.6	Pipe Discharge - Viscosity 3	18-Aug-01	18-Aug-01
21-Aug-01	002	cn13.6	Pipe Discharge - Viscosity 3	18-Aug-01	18-Aug-01
23-Aug-01	002	cn13.6	Pipe Discharge - Viscosity 3	18-Aug-01	18-Aug-01
23-Aug-01	003	cn6.44	Pipe Discharge - Viscosity 3	22-Aug-01	18-Aug-01
22-Aug-01	001	cn6.44	Pipe Discharge - Viscosity 3	22-Aug-01	18-Aug-01
22-Aug-01	002	cn6.44	Pipe Discharge - Viscosity 3	22-Aug-01	18-Aug-01
23-Aug-01	001	cn6.44	Pipe Discharge - Viscosity 3	22-Aug-01	18-Aug-01

Table C.21: Pipe Flow, Nominal Viscosity 50 mPas & Calibration Curves

C.2.4 Discharge Components Viscosity & Calibration Reference

Test Date (dd/mm/yy)	Data Tag (-)	Flow Nozzle (-)	Test Description (-)	Calibration Date (dd/mm/yy)	Viscosity Date -Test (dd/mm/yy)
21-Mar-01	001	cn13.6	Nozzle Discharge Subsonic	02-Apr-01	22-Mar-01
22-Mar-01	001	cn13.6	Nozzle Discharge Subsonic	02-Apr-01	22-Mar-01
23-Mar-01	001	cn13.6	Nozzle Discharge Subsonic	02-Apr-01	22-Mar-01
23-Mar-01	002	cn13.6	Nozzle Discharge Subsonic	02-Apr-01	22-Mar-01
27-Mar-01	001	cn13.6	Nozzle Discharge Subsonic	02-Apr-01	27-Mar-01
27-Mar-01	002	cn6.44	Nozzle Discharge Subsonic	09-Mar-01	27-Mar-01
27-Mar-01	003	cn6.44	Nozzle Discharge Subsonic	09-Mar-01	27-Mar-01
06-Apr-01	001	cn6.44	Nozzle Discharge Subsonic	09-Mar-01	06-Apr-01

Table C.22: Nozzle Discharge, Viscosity & Calibration Curves

Test Date (dd/mm/yy)	Data Tag (-)	Flow Nozzle (-)	Test Description (-)	Calibration Date (dd/mm/yy)	Viscosity Date –Test (dd/mm/yy)
26-Jul-01	001	cn13.6	Nozzle Dis Subsonic – Vis2	25-Jul-01	25-Jul-01
26-Jul-01	002	cn13.6	Nozzle Dis Subsonic – Vis2	25-Jul-01	25-Jul-01
25-Jul-01	003	cn13.6	Nozzle Dis Subsonic – Vis2	25-Jul-01	25-Jul-01
25-Jul-01	004	cn13.6	Nozzle Dis Subsonic – Vis2	25-Jul-01	25-Jul-01
25-Jul-01	005	cn13.6	Nozzle Dis Subsonic – Vis2	25-Jul-01	25-Jul-01
27-Jul-01	003	cn6.44	Nozzle Dis Subsonic – Vis2	25-Jul-01	25-Jul-01
27-Jul-01	004	cn6.44	Nozzle Dis Subsonic – Vis2	25-Jul-01	25-Jul-01
27-Jul-01	005	cn6.44	Nozzle Dis Subsonic – Vis2	25-Jul-01	25-Jul-01

Table C.23: Discharge Nozzle, Nominal Viscosity 200 mPas & Calibration Curves

Test Date (dd/mm/yy)	Data Tag (-)	Flow Nozzle (-)	Test Description (-)	Calibration Date (dd/mm/yy)	Viscosity Date –Test (dd/mm/yy)
28-Aug-01	006	cn13.6	Nozzle Dis Subsonic - Vis3	18-Aug-01	30-Aug-01
29-Aug-01	001	cn13.6	Nozzle Dis Subsonic - Vis3	18-Aug-01	30-Aug-01
29-Aug-01	002	cn13.6	Nozzle Dis Subsonic - Vis3	18-Aug-01	30-Aug-01
29-Aug-01	003	cn13.6	Nozzle Dis Subsonic - Vis3	18-Aug-01	30-Aug-01
29-Aug-01	004	cn6.44	Nozzle Dis Subsonic - Vis3	22-Aug-01	30-Aug-01
29-Aug-01	005	cn6.44	Nozzle Dis Subsonic - Vis3	22-Aug-01	30-Aug-01
29-Aug-01	006	cn6.44	Nozzle Dis Subsonic - Vis3	22-Aug-01	30-Aug-01
29-Aug-01	007	cn6.44	Nozzle Dis Subsonic - Vis3	22-Aug-01	30-Aug-01

Table C.24: Discharge Nozzle, Nominal Viscosity 40 mPas & Calibration Curves

Test Date (dd/mm/yy)	Data Tag (-)	Flow Nozzle (-)	Test Description (-)	Calibration Date (dd/mm/yy)	Viscosity Date -Test (dd/mm/yy)
24-May-01	001	cn13.6	Orifice Discharge Subsonic	02-Apr-01	23-May-01
24-May-01	002	cn13.6	Orifice Discharge Subsonic	02-Apr-01	23-May-01
24-May-01	003	cn13.6	Orifice Discharge Subsonic	02-Apr-01	23-May-01
24-May-01	004	cn13.6	Orifice Discharge Subsonic	02-Apr-01	23-May-01
25-May-01	001	cn13.6	Orifice Discharge Subsonic	02-Apr-01	23-May-01
25-May-01	002	cn6.44	Orifice Discharge Subsonic	09-Mar-01	23-May-01
25-May-01	003	cn6.44	Orifice Discharge Subsonic	09-Mar-01	23-May-01
31-May-01	003	cn6.44	Orifice Discharge Subsonic	09-Mar-01	31-May-01

Table C.25: Discharge Orifice, Viscosity & Calibration Curves

C.2.5 In-line Components Viscosity & Calibration Reference

Test Date (dd/mm/yy)	Data Tag (-)	Flow Nozzle (-)	Test Description (-)	Calibration Date (dd/mm/yy)	Viscosity Date -Test (dd/mm/yy)
09-May-01	001	cn13.6	Orifice In-line	02-Apr-01	04-May-01
10-May-01	001	cn13.6	Orifice In-line	02-Apr-01	04-May-01
10-May-01	002	cn13.6	Orifice In-line	02-Apr-01	04-May-01
11-May-01	001	cn13.6	Orifice In-line	02-Apr-01	04-May-01
11-May-01	002	cn13.6	Orifice In-line	02-Apr-01	04-May-01
14-May-01	001	cn6.44	Orifice In-line	09-Mar-01	15-May-01
14-May-01	002	cn6.44	Orifice In-line	09-Mar-01	15-May-01
07-Jun-01	001	cn6.44	Orifice In-line	09-Mar-01	31-May-01

Table C.26: In-line Orifice Plate, Viscosity & Calibration Curves

Test Date (dd/mm/yy)	Data Tag (-)	Flow Nozzle (-)	Test Description (-)	Calibration Date (dd/mm/yy)	Viscosity Date -Test (dd/mm/yy)
07-Jun-01	002	cn13.6	Globe Valve	06-Jun-01	04-Jun-01
08-Jun-01	001	cn13.6	Globe Valve	06-Jun-01	04-Jun-01
08-Jun-01	002	cn13.6	Globe Valve	06-Jun-01	04-Jun-01
11-Jun-01	001	cn13.6	Globe Valve	06-Jun-01	11-Jun-01
11-Jun-01	002	cn13.6	Globe Valve	06-Jun-01	11-Jun-01
12-Jun-01	001	cn6.44	Globe Valve	21-Jun-01	11-Jun-01
12-Jun-01	003	cn6.44	Globe Valve	21-Jun-01	11-Jun-01
13-Jun-01	003	cn6.44	Globe Valve	21-Jun-01	11-Jun-01

Table C.27: Globe Valve, Viscosity & Calibration Curves

Test Date (dd/mm/yy)	Data Tag (-)	Flow Nozzle (-)	Test Description (-)	Calibration Date (dd/mm/yy)	Viscosity Date -Test (dd/mm/yy)
25-Jun-01	001	cn13.6	Nozzle In-line	06-Jun-01	25-Jun-01
25-Jun-01	002	cn13.6	Nozzle In-line	06-Jun-01	25-Jun-01
26-Jun-01	001	cn13.6	Nozzle In-line	06-Jun-01	25-Jun-01
26-Jun-01	002	cn13.6	Nozzle In-line	06-Jun-01	25-Jun-01
27-Jun-01	001	cn13.6	Nozzle In-line	06-Jun-01	25-Jun-01
27-Jun-01	002	cn6.44	Nozzle In-line	21-Jun-01	25-Jun-01
28-Jun-01	001	cn6.44	Nozzle In-line	21-Jun-01	25-Jun-01
28-Jun-01	002	cn6.44	Nozzle In-line	21-Jun-01	25-Jun-01

Table C.28: In-line Nozzle, Viscosity & Calibration Curves

Test Date (dd/mm/yy)	Data Tag (-)	Flow Nozzle (-)	Test Description (-)	Calibration Date (dd/mm/yy)	Viscosity Date -Test (dd/mm/yy)
06-Jul-01	001	cn13.6	Abrupt Enlargement	06-Jun-01	25-Jun-01
09-Jul-01	001	cn13.6	Abrupt Enlargement	06-Jun-01	25-Jun-01
09-Jul-01	002	cn13.6	Abrupt Enlargement	06-Jun-01	25-Jun-01
10-Jul-01	001	cn13.6	Abrupt Enlargement	06-Jun-01	25-Jun-01
10-Jul-01	002	cn13.6	Abrupt Enlargement	06-Jun-01	25-Jun-01
12-Jul-01	001	cn6.44	Abrupt Enlargement	21-Jun-01	25-Jun-01
12-Jul-01	002	cn6.44	Abrupt Enlargement	21-Jun-01	25-Jun-01
12-Jul-01	003	cn6.44	Abrupt Enlargement	21-Jun-01	25-Jun-01

Table C.29: Abrupt Enlargement, Viscosity & Calibration Curves

APPENDIX D

D.1 Single-Phase Data

D.1.1 Discharge Component Water Data

Test Date (dd/mm/yy)	Volume flow rate (m^3/s)	Flow Nozzle (-)	Measured Momentum (N)
03-Aug-00	0.00197	CN1	7.6
03-Aug-00	0.00182	CN1	6.9
03-Aug-00	0.00173	CN1	5.8
03-Aug-00	0.00150	CN1	4.2
03-Aug-00	0.00123	CN1	2.7
03-Aug-00	0.00110	CN1	2.0
03-Aug-00	0.00092	CN1	1.2
03-Aug-00	0.00076	CN1	0.7

Table D.1: Pipe discharge

Test Date (dd/mm/yy)	4.00 (N/m^2)	flow rate (m^3/s)	Flow Nozzle (-)	Measured Momentum (N)
12-Oct-01	22594	0.00089	CN2	6.0
12-Oct-01	27586	0.00099	CN2	7.2
12-Oct-01	31624	0.00106	CN2	8.3
12-Oct-01	36322	0.00113	CN2	9.6
12-Oct-01	40306	0.00119	CN2	10.6
12-Oct-01	45622	0.00126	CN2	12.0
12-Oct-01	48385	0.00131	CN2	12.9
12-Oct-01	53350	0.00136	CN2	14.3

Table D.2: Nozzle Discharge

Test Date (dd/mm/yy)	4.10 (N/m^2)	flow rate (m^3/s)	Flow Nozzle (-)	Measured Momentum (N)
12-Oct-01	30286	0.00070	CN2	5.4
12-Oct-01	39841	0.00081	CN2	7.2
12-Oct-01	50236	0.00090	CN2	8.9
12-Oct-01	62499	0.00101	CN2	11.2
12-Oct-01	77778	0.00112	CN2	13.9
12-Oct-01	96086	0.00124	CN2	17.3

Table D.3: Orifice Discharge

D.1.2 Pipe Flow Water Data

Test		Test length local pressure - gauge											Flow
Date	Data Tag	0.00	0.25	0.50	0.75	1.00	1.40	1.90	2.40	2.90	3.40	flow rate	Nozzle
(dd/mm/yy)	(-)	(N/m^2)	(N/m^2)	(N/m^2)	(N/m^2)	(N/m^2)	(N/m^2)	(N/m^2)	(N/m^2)	(N/m^2)	(N/m^2)	(m^3/s)	(-)
5-Oct-01	020	41508	38960	36464	33934	31429	27332	22329	17290	12198	7149	4.085E-04	CN2
5-Oct-01	021	42528	39858	37343	34742	32166	27933	22814	17636	12448	7264	6.038E-04	CN2
5-Oct-01	023	43991	41164	38600	35920	33243	28764	23535	18162	12756	7389	8.218E-04	CN2
5-Oct-01	024	45366	42403	39786	37024	34249	29570	24215	18642	13030	7523	9.956E-04	CN2
5-Oct-01	025	47173	44019	41362	38468	35509	30580	25111	19289	13471	7721	1.191E-03	CN2
5-Oct-01	026	49161	45813	43137	40104	37047	31767	26106	20022	13904	7905	1.363E-03	CN2
5-Oct-01	027	42745	40059	37540	34922	32331	28074	22933	17706	12492	7286	7.224E-04	CN1
5-Oct-01	028	44611	41746	39159	36407	33679	29150	23846	18394	12904	7471	9.393E-04	CN1
5-Oct-01	029	46779	43688	41007	38131	35264	30373	24916	19144	13369	7686	1.162E-03	CN1
5-Oct-01	030	49355	45964	43225	40209	37186	31844	26165	20046	13927	7910	1.385E-03	CN1
5-Oct-01	031	51477	47902	45079	41489	38786	33067	27201	20808	14381	8107	1.539E-03	CN1

Table D.4: Pipe Flow

D.1.3: In-Line Components Water Data

Test		Test length local pressure - gauge											Flow
Date	Data Tag	0.00	0.25	0.50	0.75	1.00	1.40	1.90	2.40	2.90	3.40	flow rate	Nozzle
(dd/mm/yy)	(-)	(N/m^2)	(N/m^2)	(N/m^2)	(N/m^2)	(N/m^2)	(N/m^2)	(N/m^2)	(N/m^2)	(N/m^2)	(N/m^2)	(m^3/s)	(-)
19-Sep-01	001	46619	44092	41618	39060	36581	27752	22714	17555	12414	7291	5.232E-04	CN1
19-Sep-01	002	51781	49069	46566	43953	41393	28492	23357	18014	12672	7423	7.554E-04	CN1
19-Sep-01	003	57362	54461	51986	49211	46418	29099	23839	18319	12778	7397	9.496E-04	CN1
19-Sep-01	004	66406	63269	60577	58019	55253	30082	24796	18989	13204	7594	1.153E-03	CN1
19-Sep-01	005	78435	74944	72354	69679	66745	31563	25980	19757	13614	7693	1.386E-03	CN1
19-Sep-01	006	92221	89112	86370	83133	79951	33187	27394	20719	14212	7957	1.627E-03	CN1
19-Sep-01	007	108607	105102	102324	99012	96077	34963	28983	21830	14838	8193	1.948E-03	CN1

Table D.5: In-line Globe Valve

Test		Test length local pressure - gauge											Flow	Component
Date	Data Tag	0.00	0.25	0.50	0.75	1.00	1.40	1.90	2.40	2.90	3.40	flow rate	Nozzle	P.Drop
(dd/mm/yy)	(-)	(N/m^2)	(N/m^2)	(N/m^2)	(N/m^2)	(N/m^2)	(N/m^2)	(N/m^2)	(N/m^2)	(N/m^2)	(N/m^2)	(m^3/s)	(-)	(N/m^2)
20-Sep-01	009	42396	39789	37288	34699	32171	27631	22591	17500	12369	7273	5.217E-04	CN1	808
20-Sep-01	010	43585	41087	38518	35760	33290	28156	23012	17792	12477	7303	7.352E-04	CN1	1537
20-Sep-01	012	45474	42778	40183	37446	34837	29078	23843	18331	12879	7485	9.440E-04	CN1	2618
20-Sep-01	013	47927	44861	42130	39426	36649	30019	24706	19004	13263	7640	1.132E-03	CN1	3874
20-Sep-01	014	50754	47540	44868	41907	38921	31249	25801	19795	13765	7902	1.349E-03	CN1	5666
20-Sep-01	015	53341	49852	47095	44080	41033	32336	26689	20377	14078	7955	1.548E-03	CN1	7491
20-Sep-01	016	56204	52501	49651	46468	43291	33482	27649	21127	14494	8152	1.804E-03	CN1	9489
20-Sep-01	017	60236	56152	53281	49910	46568	35251	29180	22246	15137	8416	1.950E-03	CN1	12197

Table D.6: In-line Nozzle

Test		Test length local pressure - gauge											Flow	Component
Date	Data Tag	0.00	0.25	0.50	0.75	1.00	1.40	1.90	2.40	2.90	3.40	flow rate	Nozzle	P.Drop
(dd/mm/yy)	(-)	(N/m^2)	(N/m^2)	(N/m^2)	(N/m^2)	(N/m^2)	(N/m^2)	(N/m^2)	(N/m^2)	(N/m^2)	(N/m^2)	(m^3/s)	(-)	(N/m^2)
21-Sep-01	009	52549	49969	47465	45013	42620	27352	22303	17245	12157	6502	5.287E-04	CN1	15679
21-Sep-01	016	54908	52427	49868	47273	44464	27466	22474	17347	12230	6604	6.149E-04	CN1	18466
21-Sep-01	010	65899	63221	60467	58063	55516	28156	23026	17743	12487	6668	7.308E-04	CN1	32918
21-Sep-01	011	84439	81554	78956	76243	73561	29015	23758	18237	12708	6735	9.530E-04	CN1	56415
21-Sep-01	015	96387	93418	90845	88009	85378	31322	26034	20407	14781	8621	1.023E-03	CN1	64053
21-Sep-01	012	106153	103352	100900	97880	95071	29770	24439	18661	12883	6709	1.176E-03	CN1	
21-Sep-01	013	131329	128093	125473	122522	119953	30994	25498	19447	13348	6922	1.368E-03	CN1	
21-Sep-01	014	163741	160352	157468	154263	151311	32139	26510	20113	13648	6947	1.561E-03	CN1	

Table D.7: In-line Orifice Plate

Test		Test length local pressure - gauge											Flow
Date	Data Tag	0.00	0.25	0.50	0.75	1.00	1.40	1.90	2.40	2.90	3.40	flow rate	Nozzle
(dd/mm/yy)	(-)	(N/m^2)	(N/m^2)	(N/m^2)	(N/m^2)	(N/m^2)	(N/m^2)	(N/m^2)	(N/m^2)	(N/m^2)	(N/m^2)	(m^3/s)	(-)
24-Sep-01	001	42415	39705	36983	34082	31571	27614	22568	17470	12345	7256	5.096E-04	CN1
24-Sep-01	002	43823	40925	38004	34737	32231	28286	23133	17876	12594	7375	7.319E-04	CN1
24-Sep-01	003	45119	42078	38957	35330	32826	28935	23690	18270	12827	7465	8.919E-04	CN1
24-Sep-01	004	47065	43791	40377	36188	33718	29888	24526	18870	13203	7641	1.083E-03	CN1
24-Sep-01	005	48966	45220	41784	37013	34566	30850	25370	19486	13583	7800	1.237E-03	CN1
24-Sep-01	006	51651	47510	43789	38146	35841	32279	26603	20392	14095	8021	1.443E-03	CN1
24-Sep-01	007	54919	50182	46078	39290	37321	33859	28022	21376	14662	8222	1.672E-03	CN1
24-Sep-01	008	59425	53974	49330	41026	39443	36283	30160	22927	15586	8615	1.934E-03	CN1

Table D.8: Abrupt Enlargement

D.1.4 Pipe Flow Glycerine Solution Data

Test Date (dd/mm/yy)	Test length local pressure - gauge 0.00 (N/m^2)	0.25 (N/m^2)	0.50 (N/m^2)	0.75 (N/m^2)	1.00 (N/m^2)	1.40 (N/m^2)	1.90 (N/m^2)	2.40 (N/m^2)	2.90 (N/m^2)	3.40 (N/m^2)	Temp. (^{o}C)	Liquid Viscosity (Ns/m^2)	flow rate (m^3/s)	Flow Nozzle (-)
14-Feb-01	198942	186792	175437	163282	151417	131712	107307	83062	58872	34316	27.7	0.5197	6.970E-04	CN1
15-Feb-01	89092	83827	78562	73357	68072	59422	48512	37502	26227	15146	27.9	0.5115	2.072E-04	CN1
21-Feb-01	106922	100482	94202	87802	81267	70767	57722	44622	31547	18181	27.7	0.5197	2.785E-04	CN1
21-Feb-01	184637	173307	161922	150612	139767	121152	98347	75907	53522	31201	25.1	0.6530	5.682E-04	CN1
21-Feb-01	160737	151083	141465	131575	121881	105952	86340	66684	46980	27183	25.1	0.6530	4.792E-04	CN1
21-Feb-01	147645	138895	130077	121095	112233	97784	79628	61600	43648	25219	25	0.6586	4.372E-04	CN1
21-Feb-01	137049	128685	120330	111903	103842	90278	73550	56714	40196	23197	25.2	0.6475	3.815E-04	CN1
21-Feb-01	123390	115992	109317	101727	94326	82049	66848	51674	36563	20908	25.5	0.6313	3.265E-04	CN1
21-Feb-01	115002	108102	101209	94197	87154	75812	61740	47687	33549	19561	25.1	0.6530	2.881E-04	CN1
21-Feb-01	98940	93027	87077	81024	75097	65367	53232	41079	28932	16756	25.1	0.6530	2.209E-04	CN1
5-Mar-01	184372	172892	161637	150207	138907	121602	98922	76137	53347	30641	24.8	0.6700	5.513E-04	CN1
5-Mar-01	161862	152372	142547	132512	122677	106697	86307	66467	46657	26841	24.8	0.6700	4.602E-04	CN2
5-Mar-01	141170	132391	123998	115448	106947	93329	76146	58757	41357	23930	24.8	0.6700	3.824E-04	CN2
5-Mar-01	127419	119645	111882	104037	96222	83470	67948	52359	36669	21073	24.9	0.6643	3.210E-04	CN2
5-Mar-01	107281	100790	94324	87811	81244	70667	57463	44263	31130	18005	24.9	0.6643	2.447E-04	CN2

Table D.9: Pipe Flow Data

D.1.5 Discharge Components Glycerine Solution Data

Test Date (dd/mm/yy)	4.10 (N/m^2)	Temperatur (^{o}C)	Liquid Viscosity (Ns/m^2)	flow rate (m^3/s)	Flow Nozzle (-)
9-Apr-01	45686	21.8	0.547	0.000712	CN2
9-Apr-01	39844	21.7	0.551	0.000641	CN2
9-Apr-01	33170	21.6	0.556	0.00057	CN2
9-Apr-01	26074	21.6	0.556	0.000478	CN2
9-Apr-01	19501	21.5	0.560	0.00039	CN2
9-Apr-01	13250	21.5	0.560	0.000297	CN2
9-Apr-01	6401	21.7	0.551	0.000172	CN2
4-Jun-01	3680	21.2	0.547	0.000117	CN2
4-Jun-01	5904	21.2	0.547	0.000177	CN2
4-Jun-01	8027	21.2	0.547	0.000218	CN2
4-Jun-01	10048	21.2	0.547	0.00026	CN2
4-Jun-01	12148	21.2	0.547	0.000296	CN2
4-Jun-01	14198	21.3	0.543	0.000336	CN2
4-Jun-01	16811	21.3	0.543	0.00038	CN2
4-Jun-01	19510	21.4	0.538	0.00042	CN2
4-Jun-01	22943	21.4	0.538	0.000467	CN2
4-Jun-01	25991	21.5	0.533	0.00051	CN2
4-Jun-01	29123	21.7	0.524	0.00055	CN2
4-Jun-01	32603	21.7	0.524	0.000595	CN2
4-Jun-01	38039	21.8	0.519	0.000658	CN2
4-Jun-01	41211	21.9	0.515	0.0007	CN2
4-Jun-01	45143	22.0	0.510	0.000747	CN2
23-Jul-01	6273	22.9	0.394	0.000191	CN2
23-Jul-01	9476	22.9	0.394	0.000263	CN2
23-Jul-01	13735	22.9	0.394	0.00034	CN2
23-Jul-01	17555	22.9	0.394	0.000403	CN2
23-Jul-01	21071	23.0	0.390	0.000457	CN2
23-Jul-01	24722	23.0	0.390	0.000507	CN2
23-Jul-01	27548	23.0	0.390	0.000549	CN2
23-Jul-01	32153	23.1	0.386	0.000612	CN2
23-Jul-01	37963	23.1	0.386	0.000685	CN2
23-Jul-01	44299	23.2	0.383	0.000761	CN2

Table D.10: Discharge Nozzle

Test Date (dd/mm/yy)	4.10 (N/m^2)	Temperatur (°C)	Liquid Viscosity (Ns/m^2)	flow rate (m^3/s)	Flow Nozzle (-)
2-Aug-01	8738	21.3	0.214	0.000303	CN2
2-Aug-01	12127	21.3	0.214	0.000377	CN2
2-Aug-01	15685	21.4	0.212	0.000446	CN2
2-Aug-01	19660	21.4	0.212	0.000513	CN2
2-Aug-01	22328	21.5	0.210	0.000563	CN2
2-Aug-01	25759	21.5	0.210	0.000617	CN2
2-Aug-01	29243	21.5	0.210	0.00067	CN2
2-Aug-01	32979	21.6	0.209	0.000726	CN2
2-Aug-01	35499	21.6	0.209	0.00076	CN2
2-Aug-01	39071	21.6	0.209	0.000806	CN2
2-Aug-01	42871	21.7	0.207	0.000854	CN2
2-Aug-01	45899	21.8	0.205	0.000892	CN2
2-Aug-01	37483	21.8	0.205	0.000812	CN1
2-Aug-01	43813	21.9	0.204	0.000885	CN1
2-Aug-01	51271	21.9	0.204	0.000967	CN1
2-Aug-01	58441	22.1	0.201	0.001044	CN1
2-Aug-01	65018	22.2	0.199	0.00111	CN1
2-Aug-01	71111	22.2	0.199	0.001166	CN1
2-Aug-01	78287	22.3	0.197	0.00123	CN1
2-Aug-01	84983	22.4	0.196	0.001278	CN1
2-Aug-01	92495	22.5	0.244	0.001336	CN1
30-Aug-01	3616	41	0.037	0.000215	CN2
30-Aug-01	6049	40.1	0.038	0.000314	CN2
30-Aug-01	8861	40.8	0.037	0.000407	CN2
30-Aug-01	12955	41.1	0.036	0.00052	CN2
30-Aug-01	18118	41	0.037	0.00063	CN2
30-Aug-01	22165	40.9	0.037	0.000708	CN2
30-Aug-01	26437	41.1	0.036	0.000784	CN2
30-Aug-01	22117	40.7	0.037	0.000755	CN1
30-Aug-01	26119	40.4	0.038	0.000827	CN1
30-Aug-01	34907	40.2	0.038	0.000971	CN1
30-Aug-01	45841	39.7	0.039	0.001125	CN1
30-Aug-01	56623	40.4	0.038	0.001264	CN1
30-Aug-01	69808	40.5	0.038	0.001425	CN1
30-Aug-01	83202	40.5	0.038	0.001558	CN1
30-Aug-01	96023	40.3	0.038	0.00168	CN1

Table D.11: Discharge Nozzle Continued

Test Date (dd/mm/yy)	4.10 (N/m^2)	Temperatur (°C)	Liquid Viscosity (Ns/m^2)	flow rate (m^3/s)	Flow Nozzle (-)
1-Jun-01	1484	21.4	0.499325	0.000126	CN2
1-Jun-01	2038	21.5	0.495045	0.000150	CN2
1-Jun-01	2689	21.6	0.490809	0.000176	CN2
1-Jun-01	3194	21.6	0.490809	0.000194	CN2
1-Jun-01	4097	21.7	0.486618	0.000223	CN2
1-Jun-01	4977	21.4	0.499325	0.000248	CN2
1-Jun-01	6388	21.4	0.499325	0.000285	CN2
1-Jun-01	7772	21.4	0.499325	0.000319	CN2
1-Jun-01	8829	21.4	0.499325	0.000343	CN2
1-Jun-01	10348	21.4	0.499325	0.000374	CN2
1-Jun-01	11686	21.5	0.495045	0.000400	CN2
1-Jun-01	13244	21.5	0.495045	0.000427	CN2
1-Jun-01	14524	21.5	0.495045	0.000449	CN2
1-Jun-01	17689	21.6	0.490809	0.000475	CN2
1-Jun-01	19429	21.6	0.490809	0.000498	CN2
1-Jun-01	22114	21.7	0.486618	0.000534	CN2
1-Jun-01	24596	21.7	0.486618	0.000565	CN2
1-Jun-01	27469	21.8	0.482471	0.000598	CN2
1-Jun-01	30709	21.8	0.482471	0.000635	CN2
1-Jun-01	34363	22	0.474308	0.000674	CN2
1-Jun-01	37373	22.0	0.474	0.000705	CN2
1-Jun-01	41358	22.1	0.470	0.000743	CN2
1-Jun-01	46066	22.2	0.466	0.000785	CN2
4-Jun-01	3158	20.9	0.562	0.000195	CN2
4-Jun-01	4798	21	0.557	0.000248	CN2
4-Jun-01	7927	21.1	0.552	0.000318	CN2
4-Jun-01	10337	21.2	0.547	0.000371	CN2
4-Jun-01	12898	21.2	0.547	0.000421	CN2
4-Jun-01	14414	21.2	0.547	0.000442	CN2
4-Jun-01	18342	21.3	0.543	0.00048	CN2
4-Jun-01	21609	21.3	0.543	0.000522	CN2
4-Jun-01	24646	21.4	0.538	0.000561	CN2
4-Jun-01	30881	21.6	0.528	0.000633	CN2
4-Jun-01	36574	21.6	0.528	0.000692	CN2
4-Jun-01	43379	21.7	0.524	0.000757	CN2

Table D.12: Discharge Orifice

Test Date (dd/mm/yy)	4.10 (N/m^2)	Temperatur (°C)	Liquid Viscosity (Ns/m^2)	flow rate (m^3/s)	Flow Nozzle (-)
4-Jun-01	7187	21.0	0.557	0.000317	CN1
4-Jun-01	11301	21.2	0.547	0.00041	CN1
4-Jun-01	15179	21.2	0.547	0.000477	CN1
4-Jun-01	21607	21.3	0.543	0.000544	CN1
4-Jun-01	27413	21.4	0.538	0.000618	CN1
4-Jun-01	35015	21.5	0.533	0.000691	CN1
4-Jun-01	41935	21.6	0.528	0.000758	CN1
4-Jun-01	47955	21.7	0.524	0.00082	CN1

Table D.13: Discharge Orifice Continued

D.1.6 In-Line Components Glycerine Solution Data

Test	Test length local pressure - gauge											Liquid		Flow
Date	0.00	0.25	0.50	0.75	1.00	1.40	1.90	2.40	2.90	3.40	Temp.	Viscosity	flow rate	Nozzle
(dd/mm/yy)	(N/m^2)	(N/m^2)	(N/m^2)	(N/m^2)	(N/m^2)	(N/m^2)	(N/m^2)	(N/m^2)	(N/m^2)	(N/m^2)	(°C)	(Ns/m^2)	(m^3/s)	(-)
14-Jun-01	69554	65418	61253	57039	52880	45030	36636	28173	19889	11521	21.8	0.5341	1.010E-04	CN2
14-Jun-01	82728	77786	72939	68001	63059	53112	43180	33307	23418	13560	21.6	0.5436	1.632E-04	CN2
14-Jun-01	105310	99065	92944	86722	80532	66677	54287	41852	29405	16954	21.6	0.5436	2.640E-04	CN2
14-Jun-01	124284	116942	109713	102438	95261	77719	63083	48633	34120	19704	21.6	0.5436	3.493E-04	CN2
14-Jun-01	139997	131846	123861	115779	107726	86808	70540	54272	38078	21891	21.7	0.5388	4.234E-04	CN2
14-Jun-01	154077	145358	136564	127692	118920	94570	76851	59248	41567	23893	21.8	0.5341	4.917E-04	CN2
14-Jun-01	166974	157478	147979	138496	129004	101515	82472	63516	44638	25591	22	0.5248	5.572E-04	CN2
14-Jun-01	179620	169619	159576	149401	139324	108548	88173	67866	47673	27481	22.1	0.5202	6.230E-04	CN2
14-Jun-01	181528	172020	161930	151777	141364	109972	89427	68826	48383	27812	22	0.5248	6.904E-04	CN1
14-Jun-01	188648	178148	167562	156886	146438	113094	91894	70699	49547	28499	22.2	0.5157	7.378E-04	CN1
14-Jun-01	196690	185710	174806	163788	153074	117169	95124	73226	51366	29705	22.3	0.5112	7.857E-04	CN1

Table D.14: In-line Globe Valve Data

Test	Test length local pressure - gauge											Liquid		Flow	Comp.
Date	0.00	0.25	0.50	0.75	1.00	1.40	1.90	2.40	2.90	3.40	Temp.	Viscosity	flow rate	Nozzle	P.Drop
(dd/mm/yy)	(N/m^2)	(N/m^2)	(N/m^2)	(N/m^2)	(N/m^2)	(N/m^2)	(N/m^2)	(N/m^2)	(N/m^2)	(N/m^2)	(°C)	(Ns/m^2)	(m^3/s)	(-)	(N/m^2)
29-Jun-01	250355	235265	220706	205616	191400	154519	126676	97289	68065	39085	22.4	0.4146	0.001278	CN1	12423
29-Jun-01	236874	223358	209849	195753	183069	147525	121188	93064	65015	37085	22.5	0.4104	0.001275	CN1	11607
29-Jun-01	211927	199754	187445	175330	162822	132000	108169	83304	58334	33097	23.2	0.3827	0.001148	CN1	9675
29-Jun-01	183599	172697	161889	151261	140404	115268	94364	72582	50958	29275	23.2	0.3827	0.000962	CN1	7296
29-Jun-01	162710	153783	144447	134697	125140	103028	84203	64824	45486	26278	23.3	0.3789	0.000817	CN1	5636
2-Jul-01	71874	67539	63226	58827	54474	46471	37774	29078	20451	11758	21.3	0.5269	0.00012	CN2	380
2-Jul-01	79817	74997	70203	65331	60513	51452	41816	32154	22512	12921	21.6	0.5128	0.000162	CN2	621
2-Jul-01	94335	88607	83021	77287	71629	60494	49210	37872	26572	15251	21.8	0.5037	0.000237	CN2	1135
2-Jul-01	116745	109710	102792	95742	88749	74282	60353	46442	32522	18619	22.2	0.4861	0.000358	CN2	2114
2-Jul-01	134004	125841	117801	109767	102627	85454	69437	53396	37421	21499	22.3	0.4818	0.000467	CN2	3072
2-Jul-01	147781	138909	130103	121189	112481	93229	75803	58311	40812	23393	22.6	0.4692	0.000552	CN2	3884
2-Jul-01	159365	150027	140605	130983	121649	100440	81764	62856	44100	25307	23	0.4570	0.00065	CN2	4797
2-Jul-01	171125	160927	151401	141099	130957	107748	87772	67408	47148	26975	23	0.4452	0.00074	CN2	5747

Table D.15: In-line Nozzle Data

Test	Test length local pressure - gauge											Liquid		Flow	Comp.
Date	0.00	0.25	0.50	0.75	1.00	1.40	1.90	2.40	2.90	3.40	Temperatur	Viscosity	flow rate	Nozzle	P.Drop
(dd/mm/yy)	(N/m^2)	(N/m^2)	(N/m^2)	(N/m^2)	(N/m^2)	(N/m^2)	(N/m^2)	(N/m^2)	(N/m^2)	(N/m^2)	(°C)	(Ns/m^2)	(m^3/s)	(-)	(N/m^2)
4-May-01	225676	213671	201392	189080	177101	130040	106279	81883	57420	32826	21.3	0.4786	0.00089	CN1	47959
4-May-01	197657	186578	175878	164812	153913	116220	94562	72800	51027	29209	21.3	0.4786	0.00076	CN1	33827
4-May-01	166924	157530	148159	139297	130559	101652	82788	63683	44585	25558	21.2	0.4826	0.00061	CN1	22517
4-May-01	135657	127849	120193	112300	104577	84265	68536	52802	37167	21368	20.9	0.4950	0.00045	CN1	11941
4-May-01	131205	123570	116157	108495	100875	81758	66425	51200	35945	20656	20.7	0.5035	0.00039	CN2	10474
4-May-01	113247	106602	100077	93357	86538	71459	58136	44777	31460	18043	20.6	0.5078	0.0003	CN2	6575
4-May-01	84328	79360	74301	69249	64295	54496	44133	33765	24038	13955	20.3	0.5210	0.00017	CN2	2211

Table D.16: In-line Orifice Data

Test	Test length local pressure - gauge											Liquid		Flow
Date	0.00	0.25	0.50	0.75	1.00	1.40	1.90	2.40	2.90	3.40	Temp.	Viscosity	flow rate	Nozzle
(dd/mm/yy)	(N/m^2)	(N/m^2)	(N/m^2)	(N/m^2)	(N/m^2)	(N/m^2)	(N/m^2)	(N/m^2)	(N/m^2)	(N/m^2)	(°C)	(Ns/m^2)	(m^3/s)	(-)
11-Jul-01	90223	82619	75077	67409	59873	50232	40828	31432	22050	12745	22.6	0.4692	0.000156	CN2
11-Jul-01	111897	101850	91862	81747	71819	59710	48515	37352	26192	15036	22.8	0.4610	0.000241	CN2
11-Jul-01	140169	126724	113377	99997	86956	71881	58392	44912	31484	18021	23.1	0.4491	0.000362	CN2
11-Jul-01	161445	145531	129745	113891	98345	81220	65896	50672	35528	20311	23.4	0.4375	0.000467	CN2
11-Jul-01	179008	160992	143409	125797	108384	89593	72750	56008	39267	22517	23.8	0.4227	0.000564	CN2
11-Jul-01	189134	169974	150981	131686	112905	93245	75797	58214	40712	23191	24.1	0.4120	0.000634	CN2
13-Jul-01	171493	154539	137717	120671	104077	85836	69736	53608	37476	21555	22.1	0.4273	0.000554	CN1
13-Jul-01	207553	186389	165201	143752	122831	101428	82275	63194	44222	25174	22.8	0.3982	0.000745	CN1
13-Jul-01	233445	208883	185327	160441	136478	113147	91897	70564	49232	28196	23.4	0.3751	0.000892	CN1

Table D.17: Abrupt Enlargement Data

Test	Test length local pressure - gauge											Liquid		Flow
Date	0.00	0.25	0.50	0.75	1.00	1.40	1.90	2.40	2.90	3.40	Temp.	Viscosity	flow rate	Nozzle
(dd/mm/yy)	(N/m^2)	(N/m^2)	(N/m^2)	(N/m^2)	(N/m^2)	(N/m^2)	(N/m^2)	(N/m^2)	(N/m^2)	(N/m^2)	(^oC)	(Ns/m^2)	(m^3/s)	(-)
12-Aug-01	80730	75744	70787	65759	60832	52856	42935	33027	23126	13264	22.4	0.1959	4.362E-04	CN1
12-Aug-01	90301	84791	79281	73723	68315	59332	48202	37122	26000	14851	22.4	0.1959	5.727E-04	CN1
12-Aug-01	98297	92995	86927	81223	75307	65510	53288	40972	28654	16391	22.3	0.1974	7.154E-04	CN1
12-Aug-01	109037	102252	95599	88884	82237	71400	57997	44602	31172	17764	22.4	0.1959	8.466E-04	CN1
12-Aug-01	118220	110915	103824	96622	89367	77600	63005	48469	33897	19339	22.4	0.1959	9.820E-04	CN1
12-Aug-01	127926	120150	112800	105255	97407	84440	68651	52796	36872	21076	22.4	0.1959	1.129E-03	CN1
12-Aug-01	139748	131069	122396	113835	105670	92189	75292	57807	40525	23078	22.6	0.1929	1.346E-03	CN1
12-Aug-01	150595	141446	132119	122893	113776	98755	80255	61790	43209	24646	22.7	0.1914	1.499E-03	CN1

Table D.18: Pipe Flow Data 200 mPas Nominal Viscosity

Test	Test length local pressure - gauge											Liquid		Flow
Date	0.00	0.25	0.50	0.75	1.00	1.40	1.90	2.40	2.90	3.40	Temp.	Viscosity	flow rate	Nozzle
(dd/mm/yy)	(N/m^2)	(N/m^2)	(N/m^2)	(N/m^2)	(N/m^2)	(N/m^2)	(N/m^2)	(N/m^2)	(N/m^2)	(N/m^2)	(°C)	(Ns/m^2)	(m^3/s)	(-)
24-Aug-01	53703	50383	47089	43757	40457	35212	27863	21906	15284	8641	40	0.0387	2.829E-04	CN1
24-Aug-01	55866	52436	48964	45636	42006	36709	29620	22471	15928	8993	39.6	0.0395	4.658E-04	CN1
24-Aug-01	57980	54487	51012	47379	43828	38044	30883	23705	16589	9367	39.4	0.0399	6.205E-04	CN1
24-Aug-01	60251	56493	52864	49161	45367	39463	32035	24539	17085	9621	39.3	0.0401	7.806E-04	CN1
24-Aug-01	61931	58104	54312	50439	46704	40570	32923	25254	17555	9886	38.9	0.0410	8.829E-04	CN1
24-Aug-01	64224	60285	56377	52392	48502	42053	34147	26198	18230	10305	38.6	0.0416	1.023E-03	CN1
24-Aug-01	66932	62774	58642	54574	50541	43901	35644	27350	19034	10710	38.4	0.0420	1.188E-03	CN1
24-Aug-01	71184	66909	62680	58182	54055	46667	37799	29012	20123	11416	38.4	0.0420	1.421E-03	CN1
24-Aug-01	78199	73773	69643	64245	59733	52378	42232	32324	22742	12837	38.6	0.0416	1.620E-03	CN1

Table D.19: Pipe Flow Data 50 mPas Nominal Viscosity

D.2 Two-Phase Data

D.2.1 Pipe Flow Air-Water Data

Test	Test length local pressure - gauge										Liquid	Air	Gas	Void_F	Void_F
Date (dd/mm/yy)	0.00 (N/m^2)	0.25 (N/m^2)	0.50 (N/m^2)	0.75 (N/m^2)	1.00 (N/m^2)	1.40 (N/m^2)	1.90 (N/m^2)	2.40 (N/m^2)	2.90 (N/m^2)	3.40 (N/m^2)	Mass flux (kg/m^{2}s)	Mass flux (kg/m^{2}s)	Temp. (°C)	CL (-)	Off Set (-)
26-Sep-01	40822	37674	35482	32735	30014	26707	21645	16166	9363	5483	770.0	33.4	21.4	0.910	0.907
26-Sep-01	29086	27360	25670	23919	22271	18978	15638	11806	8027	4358	501.9	32.8	20.8	0.915	0.907
26-Sep-01	31490	29459	27725	25966	23913	20855	17141	13189	9241	5287	462.7	41.0	20.2	0.918	0.914
26-Sep-01	37712	35439	33315	31099	28709	25238	20810	16307	11495	6759	453.6	53.1	19.8	0.925	0.925
26-Sep-01	40523	37985	35698	33296	30671	26812	22026	17159	12126	7084	290.3	75.0	20.0	0.940	0.942
26-Sep-01	42713	39796	37525	34926	32360	27852	23056	17958	12595	7239	151.4	106.3	19.9	0.944	0.957
26-Sep-01	33815	31302	30012	28302	26294	22146	18676	14494	9795	5372	83.8	131.2	20.3	0.935	0.968
26-Sep-01	45736	42600	40884	38419	35975	30694	25979	20393	14064	7967	30.6	143.8	19.9	0.938	0.966

Table D.20: Pipe Flow Data 1

Test						Test length local pressure - gauge						Liquid	Air	Gas
Date	Data Tag	0.00	0.25	0.50	0.75	1.00	1.40	1.90	2.40	2.90	3.40	Mass flux	Mass flux	Temp.
(dd/mm/yy)	(-)	(N/m^2)	(N/m^2)	(N/m^2)	(N/m^2)	(N/m^2)	(N/m^2)	(N/m^2)	(N/m^2)	(N/m^2)	(N/m^2)	(kg/m^{2}s)	(kg/m^{2}s)	(^{o}C)
04-Apr-02	001	41234	39133	36202	33186	30820	24930	21147	15820	10866	5781	777.6	33.5	19.5
05-Apr-02	001	42182	38456	36843	34089	31208	25784	21200	16673	10809	6071	647.5	43.0	19.3
05-Apr-02	002	42984	40163	37691	34888	32285	27512	22872	17599	11947	6550	563.1	50.0	18.9
04-Apr-02	004	37445	35279	32999	30959	28336	25016	20445	15674	11003	5953	466.6	54.4	19.7
05-Apr-02	003	44510	41687	39194	36537	33661	29273	23938	18501	12950	7259	287.7	75.2	18.7
04-Apr-02	006	36799	34294	32157	29927	27650	23708	19363	14936	10329	5600	153.4	112.6	19.4
04-Apr-02	007	37117	34547	32766	30624	28529	24405	20222	15668	10844	5852	81.3	125.1	19.6
04-Apr-02	008	40817	38029	36378	34196	32021	27115	22779	17655	12041	6431	36.5	150.1	19.7

Table D.21: Pipe Flow Data 2

D.2.2 In-line Components Air-Water Data

Test	Test length local pressure - gauge										Liquid	Air	Gas	Void_F	Void_F
Date	0.00	0.25	0.50	0.75	1.00	1.40	1.90	2.40	2.90	3.40	Mass flux	Mass flux	Temp.	CL	Off Set
(dd/mm/yy)	(N/m2)	(N/m2)	(N/m2)	(N/m2)	(N/m2)	(N/m2)	(N/m2)	(N/m2)	(N/m2)	(N/m2)	(kg/m2s)	(kg/m2s)	(oC)	(-)	(-)
18-Sep-01	52591	50351	48599	46538	45492	22309	16632	11057	7588	4229	604.9	25.1	22.8	0.901	0.880
18-Sep-01	52728	50954	48792	46111	43838	20710	17174	12583	7733	300	478.2	31.5	22.3	0.907	1.053
18-Sep-01	52317	50648	49198	47703	46176	20542	16855	12514	8408	4182	429.0	37.8	21.7	0.933	1.039
18-Sep-01	54613	53172	52066	50469	48574	20879	16988	12962	8793	4952	367.7	44.1	21.6	0.931	0.908
18-Sep-01	64993	63307	61819	60251	58474	24868	19862	15004	10271	5695	246.9	63.1	21.1	0.928	0.920
18-Sep-01	30111	29109	28361	27428	26550	10816	8617	6360	4255	2340	83.5	50.4	21.2	0.931	0.992
19-Sep-01	31133	30270	29583	28769	28133	10580	8589	6492	4462	2604	36.8	56.6	22.8	0.964	0.943
19-Sep-01	37775	36760	36250	35495	34769	9761	8273	6401	4382	2507	18.3	74.7	22.1	0.960	1.087

Table D.22: In-line Globe Valve Data

Test	Test length local pressure - gauge										Liquid	Air	Gas	Void_F	Void_F	Comp.
Date	0.00	0.25	0.50	0.75	1.00	1.40	1.90	2.40	2.90	3.40	Mass flux	Mass flux	Temp.	CL	Off Set	P.Drop
(dd/mm/yy)	(N/m^2)	(N/m^2)	(N/m^2)	(N/m^2)	(N/m^2)	(N/m^2)	(N/m^2)	(N/m^2)	(N/m^2)	(N/m^2)	(kg/m^2s)	(kg/m^2s)	(^oC)	(-)	(-)	(N/m^2)
20-Sep-01	37178	35120	32829	31196	29820	18797	16271	12039	7222	4259	607.8	25.2	22.4	0.901	0.855	4662
20-Sep-01	33674	31961	30463	28817	27696	15339	13736	10754	7388	3174	481.8	31.5	21.8	0.919	0.824	5176
20-Sep-01	35796	33976	32516	30999	29533	16178	14239	11246	7901	4666	432.7	37.8	21.2	0.919	0.847	6274
20-Sep-01	35433	33653	32069	30585	29087	15538	13984	11042	7811	4613	356.7	44.1	21.1	0.930	0.847	6425
20-Sep-01	37531	35679	33937	32186	30545	15191	14019	11175	8008	4742	235.8	63.1	21.0	0.944	0.872	7911
20-Sep-01	18129	17039	16215	15259	14401	8696	7656	6010	4279	2539	76.6	50.4	21.4	0.934	0.923	3482
20-Sep-01	17270	16240	15475	14587	13781	9188	7389	5771	3998	1517	37.4	56.7	21.1	0.928	0.946	3798
20-Sep-01	21154	19875	19132	18125	17057	10309	9159	6790	5001	1357	27.0	74.9	21.1	0.928	0.935	5814

Table D.23: In-line Nozzle Data

Test	Test length local pressure - gauge										Liquid	Air	Gas	Void_F	Void_F	Comp.
Date	0.00	0.25	0.50	0.75	1.00	1.40	1.90	2.40	2.90	3.40	Mass flux	Mass flux	Temp.	CL	Off Set	P.Drop
(dd/mm/yy)	(N/m^2)	(N/m^2)	(N/m^2)	(N/m^2)	(N/m^2)	(N/m^2)	(N/m^2)	(N/m^2)	(N/m^2)	(N/m^2)	(kg/m^{2}s)	(kg/m^{2}s)	(^{o}C)	(-)	(-)	(N/m^2)
21-Sep-01	75095	72680	70518	69373	68679	19887	17352	12679	7716	1189	613.7	25.2	21.3	0.901	0.896	48641
21-Sep-01	75485	73806	71372	70881	68385	18767	16392	11815	7480	4261	495.6	31.5	21.1	0.916	0.906	52205
21-Sep-01	81287	79916	79104	77105	75473	17533	15744	12351	8330	4717	428.0	37.9	20.5	0.920	0.911	59155
21-Sep-01	86157	84542	83082	81347	80185	17915	16376	12533	8748	4993	373.0	44.2	20.4	0.923	0.916	64337
21-Sep-01	84211	82540	80802	79319	77495	16239	13910	9409	4910	513	244.3	63.1	20.4	0.941	0.935	65341
21-Sep-01	53671	52799	52112	51191	50351	9221	8846	6751	4694	2549	79.9	50.5	21.0	0.942	0.938	47960
21-Sep-01	55777	54902	54188	53519	52846	8917	8341	6301	4334	2300	37.5	56.8	20.5	0.945	0.940	53563
21-Sep-01	56273	55339	54866	54371	53299	7859	6910	5269	3578	1583	16.0	63.1	20.4	0.942	0.939	58666

Table D.24: In-line Orifice Plate Data

Test	Test length local pressure - gauge										Mass Flow	Mass Flow	Gas	Void_F	Void_F
Date	0.00	0.25	0.50	0.75	1.00	1.40	1.90	2.40	2.90	3.40	Rate	Rate	Temp.	CL	Off Set
(dd/mm/yy)	(N/m^2)	(N/m^2)	(N/m^2)	(N/m^2)	(N/m^2)	(N/m^2)	(N/m^2)	(N/m^2)	(N/m^2)	(N/m^2)	(kg/s)	(kg/s)	(°C)	(-)	(-)
25-Sep-01	35573	31371	26912	21578	18892	13215	11816	9575	6926	4208	0.319	0.0135	21.8	0.896	0.897
25-Sep-01	34651	30163	25534	20864	17144	12854	11597	9367	6581	3926	0.258	0.0169	22.1	0.919	0.918
25-Sep-01	37086	32018	27374	21888	17460	13055	12038	9905	7004	4103	0.228	0.0203	21.6	0.928	0.930
25-Sep-01	38637	33964	28787	23214	17865	13842	12696	10244	7294	4289	0.195	0.0236	21.2	0.936	0.941
25-Sep-01	38468	33161	27357	21222	15332	12424	12046	9831	7077	4160	0.134	0.0338	20.8	0.956	0.958
25-Sep-01	18453	16197	13786	10983	8621	8061	6745	6198	4927	2158	0.038	0.0270	20.7	0.954	0.954
25-Sep-01	15029	13276	11441	9236	7451	6832	6020	4751	3290	1190	0.020	0.0304	20.4	0.941	0.952
25-Sep-01	20213	18021	15485	12044	9791	9546	8203	6356	4350	1883	0.010	0.0402	20.1	0.941	0.965

Table D.25: Abrupt Enlargement Data

D.2.3 Discharge Components Air-Water Data

Test Date (dd/mm/yy)	2.90 (N/m^2)	3.40 (N/m^2)	4.00 (N/m^2)	Liquid mass flow rate (kg/s)	Gas mass flow rate (kg/s)	Gas Temperatue (°C)
15-Oct-01	17649	12623	8608	0.1539	0.0067	22.2
15-Oct-01	18363	12987	6777	0.1320	0.0084	21.9
15-Oct-01	21140	15323	9257	0.1141	0.0101	22.1
15-Oct-01	23735	18743	11959	0.1039	0.0118	22.1
15-Oct-01	10305	7315	3869	0.0333	0.0102	22.2
15-Oct-01	13357	12080	7735	0.0216	0.0135	22.1
15-Oct-01	19205	17892	13544	0.0119	0.0169	21.9
15-Oct-01	18182	16732	12611	0.0044	0.0169	21.8

Table D.26: Discharge Orifice Data

Test Date (dd/mm/yy)	4.00 (N/m^2)	Exit Pressure (N/m^2)	Liquid mass flow rate (kg/s)	Gas mass flow rate (kg/s)	Inlet Temperatue (°C)	Void_F CL (-)	Void_F OffSet (-)
27-Jan-01	45093		0.3222	0.0135	20.1	0.87308	0.91211
27-Jan-01	49938		0.2600	0.0169	20.1	0.88294	0.92627
27-Jan-01	59456		0.2314	0.0203	20.1	0.87547	0.82515
30-Jan-01	75983		0.1324	0.0339	19.7	0.94104	0.96865
30-Jan-01	30296		0.0303	0.0272	18.1	0.94249	0.99124
30-Jan-01	28808		0.0152	0.0306	16.5	0.89547	1.14554
30-Jan-01	29508		0.0062	0.0342	14.2	0.92005	1.14356

Table D.27: Discharge Nozzle Data

D.2.4 Pipe Flow Air-Glycerine Solution Data

Test Date (dd/mm/yy)	Test length local pressure - gauge										Liquid Mass flux (kg/m^{2}s)	Air Mass flux (kg/m^{2}s)	Gas Temp. (^{o}C)	Liquid Temp. (^{o}C)	Liquid Viscosity (Ns/m^2)	Void_F CL (-)	Void_F Off Set (-)
	0.00 (N/m^2)	0.25 (N/m^2)	0.50 (N/m^2)	0.75 (N/m^2)	1.00 (N/m^2)	1.40 (N/m^2)	1.90 (N/m^2)	2.40 (N/m^2)	2.90 (N/m^2)	3.40 (N/m^2)							
13-Mar-01	275405	262107	248329	232669	214864	188605	157675	125139	91322	54871	883.6	33.9	18.6	24.7	0.662	0.732	0.748
14-Mar-01	225440	213897	203457	192627	180109	159130	132932	106052	77184	46606	610.8	35.9	19.1	25.0	0.646	0.753	0.708
28-Feb-01	209807	199267	188542	177602	166432	147847	124017	98737	72397	43646	471.9	41.1	19.1	25.2	0.623	0.766	0.818
15-Mar-01	247767	236592	223992	211234	198529	176042	148202	118749	87212	53334	508.5	53.5	18.5	24.7	0.662	0.795	0.779
16-Mar-01	243380	231380	219117	206997	194449	172945	143455	115014	84864	52119	314.5	75.2	19.2	23.9	0.706	0.837	0.856
20-Mar-01	257124	244858	232074	219172	207019	185425	157320	127539	95353	59748	162.9	106.9	19.2	24.9	0.651	0.877	0.895
26-Mar-01	229224	218202	207331	196028	184857	167875	142763	116639	87547	55179	81.5	130.1	19.9	23.0	0.657	0.904	0.884
30-Mar-01	186174	177840	168656	159616	153069	142487	122682	100414	75703	47960	38.2	150.4	19.6	21.5	0.740	0.982	0.990

Table D.28: Pipe Flow Nominal Viscosity 550 mPas Data

Test	Test length local pressure - gauge										Liquid	Air	Gas	Liquid	Liquid	Void_F	Void_F
Date (dd/mm/yy)	0.00 (N/m^2)	0.25 (N/m^2)	0.50 (N/m^2)	0.75 (N/m^2)	1.00 (N/m^2)	1.40 (N/m^2)	1.90 (N/m^2)	2.40 (N/m^2)	2.90 (N/m^2)	3.40 (N/m^2)	Mass flux (kg/m^2s)	Mass flux (kg/m^2s)	Temp. (°C)	Temp. (°C)	Viscosity (Ns/m^2)	CL (-)	Off Set (-)
03-Aug-01	150147	141793	133876	125903	117420	103445	86328	68702	66729	30309	787.75	33.3	22.9	21.8	0.249	0.774	0.713
03-Aug-01	122232	115653	108882	101691	92433	84632	70052	54839	38885	22102	552.11	35.2	22.6	23.7	0.215	0.781	0.722
08-Aug-01	127755	121263	114579	107736	100869	89228	74372	58916	42512	25180	458.83	40.8	23.6	21.6	0.253	0.802	0.787
08-Aug-01	135681	126393	119715	112737	105666	94205	78629	62234	44936	27040	454.34	52.9	21.4	23.5	0.219	0.791	0.755
09-Aug-01	211882	202062	192567	182897	172972	156072	134192	111062	86212	59061	296.77	74.8	22.5	22.9	0.229	0.844	0.818
09-Aug-01	169025	160711	150825	139847	130773	115178	96962	78316	57563	36304	155.45	106.7	20.4	21.7	0.251	0.912	0.901
10-Aug-01	151137	144192	136962	129593	122179	109570	92976	75396	56165	35075	82.80	129.7	21.7	21.8	0.249	0.942	0.957
10-Aug-01	140286	133767	127482	120658	113944	102184	87135	70824	52645	32922	33.77	150.0	21.1	21.4	0.257	0.955	0.992

Table D.29: Pipe Flow Nominal Viscosity 200mPas Data

Test	Test length local pressure - gauge										Liquid	Air	Gas	Liquid	Liquid	Void_F	Void_F
Date	0.00	0.25	0.50	0.75	1.00	1.40	1.90	2.40	2.90	3.40	Mass flux	Mass flux	Temp.	Temp.	Viscosity	CL	Off Set
(dd/mm/yy)	(N/m^2)	(N/m^2)	(N/m^2)	(N/m^2)	(N/m^2)	(N/m^2)	(N/m^2)	(N/m^2)	(N/m^2)	(N/m^2)	(kg/m^2s)	(kg/m^2s)	(^oC)	(^oC)	(Ns/m^2)	(-)	(-)
19-Aug-01	68636	64268	60624	56263	51700	44935	38701	29858	21150	10555	738.36	33.2	25.3	36.4	0.046	0.886	0.869
21-Aug-01	55994	52886	48220	46296	43081	37677	31977	24171	15867	5987	484.66	35.2	23.3	34.7	0.050	0.877	0.873
21-Aug-01	55763	51679	47850	44851	41007	38195	31529	24596	18556	7620	419.95	40.9	22.8	37.9	0.043	0.883	0.872
23-Aug-01	62615	57808	54128	50808	48695	43045	35763	28252	19593	11740	426.48	52.8	23.1	38.4	0.042	0.884	0.875
23-Aug-01	68019	63750	59373	55557	49294	44537	35756	26421	16733	6639	382.44	74.6	24.3	37.9	0.043	0.872	0.897
22-Aug-01	102015	95752	90614	85257	79252	70675	59692	47717	34802	21029	257.52	105.8	24.9	34.9	0.050	0.953	0.953
22-Aug-01	114307	108595	102967	97454	89949	81755	69445	56029	41169	25256	149.47	129.2	23.8	33.1	0.054	0.945	0.944
23-Aug-01	119890	113997	108528	102765	94582	86805	73764	59883	44587	27478	73.43	149.3	23.8	33.1	0.054	0.957	1.004

Table D.30: Pipe Flow Nominal Viscosity 50mPas Data

D.2.5 In-line Components Air-Glycerine Solution Data

Test	Test length local pressure - gauge										Liquid	Air	Gas	Liquid	Liquid	Void_F	Void_F
Date	0.00	0.25	0.50	0.75	1.00	1.40	1.90	2.40	2.90	3.40	Mass flux	Mass flux	Temp.	Temp.	Viscosity	CL	Off Set
(dd/mm/yy)	(N/m^2)	(N/m^2)	(N/m^2)	(N/m^2)	(N/m^2)	(N/m^2)	(N/m^2)	(N/m^2)	(N/m^2)	(N/m^2)	(kg/m^{2}s)	(kg/m^{2}s)	(°C)	(°C)	(Ns/m^2)	(-)	(-)
07-Jun-01	192981	183780	174246	165058	155686	127121	105556	83877	60534	36133	587.5	25.2	21.1	20.5	0.582	0.695	1.014
08-Jun-01	176461	168003	160021	151247	142985	115928	96964	76932	55560	33399	484.8	31.6	20.1	21.7	0.524	0.655	0.693
08-Jun-01	184760	176279	167905	158790	149877	121276	101362	80493	58392	35130	420.7	38.0	19.2	21.8	0.519	0.686	0.709
11-Jun-01	189797	181045	172388	163270	154157	124745	104439	82892	60210	36032	384.9	44.0	22.7	22.1	0.520	0.715	0.804
11-Jun-01	187532	179082	170718	162268	153517	121510	101762	81038	59013	35499	248.7	62.9	22.1	22.2	0.516	0.766	0.779
12-Jun-01	117272	111951	106537	100975	95448	74848	62519	49420	35641	21601	85.8	50.5	20.3	21.8	0.534	0.876	0.868
13-Jun-01	73932	70656	67203	63574	60016	45043	37571	29579	21182	12771	38.6	50.6	19.6	20.8	0.584	0.905	0.904
13-Jun-01	67917	65130	62202	59185	56356	38930	32585	25800	18501	10825	21.7	63.2	19.6	20.4	0.605	0.931	0.936

Table D.31: In-line Globe Valve Data

Test	Test length local pressure - gauge										Liquid	Air	Gas	Liquid	Liquid	Void_F	Void_F	Comp.
Date	0.00	0.25	0.50	0.75	1.00	1.40	1.90	2.40	2.90	3.40	Mass flux	Mass flux	Temp.	Temp.	Viscosity	CL	Off Set	P.Drop
(dd/mm/yy)	(N/m^2)	(N/m^2)	(N/m^2)	(N/m^2)	(N/m^2)	(N/m^2)	(N/m^2)	(N/m^2)	(N/m^2)	(N/m^2)	(kg/m^2s)	(kg/m^2s)	(°C)	(°C)	(Ns/m^2)	(-)	(-)	(N/m^2)
25-Jun-01	185446	176689	167163	159024	149027	124247	103470	81819	59061	35035	649.0	25.1	23.2	22.5	0.473	0.702	0.691	5657
25-Jun-01	176675	167749	159159	150374	141173	118123	98781	78040	56615	33800	530.8	31.5	22.0	22.3	0.482	0.719	0.870	5711
26-Jun-01	181001	172127	163286	154263	145121	121600	101913	80824	58795	35628	466.9	37.8	22.0	22.6	0.469	0.803	0.799	5811
26-Jun-01	183942	174477	165050	155241	145401	120019	100098	79124	56704	34867	397.2	44.1	21.6	23.0	0.453	0.824	0.811	6075
27-Jun-01	178600	170261	161841	153043	144296	120006	101395	80909	59212	36308	268.2	63.0	21.8	22.2	0.486	0.877	0.859	6905
27-Jun-01	97302	92466	87664	82729	77834	64317	53666	42426	30499	17926	74.5	50.5	20.7	22.3	0.482	0.913	0.903	4025
28-Jun-01	73209	69641	66082	62361	58609	48095	40069	31554	22709	13365	37.1	56.7	21.7	21.7	0.508	0.933	0.932	4153
28-Jun-01	82763	78870	75001	71109	67086	54624	45770	36354	26325	15649	23.8	74.9	20.6	21.5	0.517	0.957	0.972	6623

Table D.32: In-line Nozzle Data

Test	Test length local pressure - gauge										Liquid	Air	Gas	Liquid	Liquid	Void_F	Void_F	Comp.
Date	0.00	0.25	0.50	0.75	1.00	1.40	1.90	2.40	2.90	3.40	Mass flux	Mass flux	Temp.	Temp.	Viscosity	CL	Off Set	P.Drop
(dd/mm/yy)	(N/m^2)	(N/m^2)	(N/m^2)	(N/m^2)	(N/m^2)	(N/m^2)	(N/m^2)	(N/m^2)	(N/m^2)	(N/m^2)	(kg/m^2s)	(kg/m^2s)	(^oC)	(^oC)	(Ns/m^2)	(-)	(-)	(N/m^2)
09-May-01	200605	191179	181631	172161	161905	126507	106401	84787	62157	37337	656.5	25.2	21.6	21.1	0.487	0.655	0.661	26934
10-May-01	198960	189776	180630	171397	161773	127117	106511	84507	61365	36594	535.9	31.6	19.7	21.3	0.479	0.736	0.713	25773
10-May-01	190097	181602	173130	164734	155844	121402	102059	80988	58784	35193	471.1	37.9	19.9	21.8	0.459	0.766	0.761	25364
11-May-01	210772	202306	194365	185300	175296	137255	115294	91914	67128	40489	427.4	44.1	21.2	20.5	0.512	0.778	0.760	28440
11-May-01	202855	194053	185198	176338	167394	125732	105634	84192	61290	36835	270.1	63.1	20.4	20.6	0.508	0.836	0.804	34032
14-May-01	119510	114162	108976	103783	98426	72445	60539	47937	34582	20389	77.2	50.3	22.6	21.7	0.444	0.876	0.861	22112
14-May-01	97851	94071	90208	86304	82240	54055	45070	35653	25703	15073	39.0	56.7	21.4	21.3	0.459	0.917	0.900	28466
07-Jun-01	107770	104715	101529	97997	94719	49255	41402	33197	23719	14049	21.8	74.7	22.7	22.9	0.427	0.952	0.941	53886

Table D.33: In-line Orifice Plate Data

Test	Test length local pressure - gauge										Mass Flow	Mass Flow	Gas	Liquid	Liquid	Void_F	Void_F
Date	0.00	0.25	0.50	0.75	1.00	1.40	1.90	2.40	2.90	3.40	Rate	Rate	Temp.	Temp.	Viscosity	CL	Off Set
(dd/mm/yy)	(N/m^2)	(N/m^2)	(N/m^2)	(N/m^2)	(N/m^2)	(N/m^2)	(N/m^2)	(N/m^2)	(N/m^2)	(N/m^2)	(kg/s)	(kg/s)	(°C)	(°C)	(Ns/m^2)	(-)	(-)
06-Jul-01	247581	224709	201327	177039	152121	125102	104330	82832	60098	37285	0.350	0.0135	23.5	22.8	0.461	0.635	0.602
09-Jul-01	236151	214515	192633	169227	145215	119576	99920	78908	56942	34207	0.284	0.0168	23.6	22.9	0.457	0.664	0.656
09-Jul-01	234369	212563	190585	167602	143991	118400	98976	78424	56767	34350	0.253	0.0202	22.0	23.5	0.434	0.670	0.662
10-Jul-01	246930	224408	201918	177191	151932	124969	104788	83102	60153	35960	0.222	0.0236	23.3	23.1	0.449	0.821	0.805
10-Jul-01	226702	205567	183919	160958	137490	113516	95478	76103	55507	33553	0.140	0.0337	23.1	23.7	0.426	0.834	0.816
12-Jul-01	135586	122603	109080	94992	80478	66044	55041	43423	31231	18274	0.040	0.0269	24.0	22.7	0.465	0.880	0.867
12-Jul-01	99723	89951	79984	69348	58608	48333	40189	31637	22624	13186	0.020	0.0303	22.9	23.1	0.449	0.909	0.799
12-Jul-01	104514	94282	83861	72718	61218	51674	43064	34152	24613	14540	0.012	0.0400	22.2	23.1	0.449	0.928	0.910

Table D.34: Abrupt Enlargement Data

D.2.6 Discharge Components Air-Glycerine Solution Data

Test Date (dd/mm/yy)	2.90 (N/m^2)	3.40 (N/m^2)	4.00 (N/m^2)	Liquid mass flow rate (kg/s)	Gas mass flow rate (kg/s)	Gas Temp. (°C)	Liquid Temp. (°C)	Liquid Viscosity (Ns/m^2)	Void_F CL (-)	Void_F Off Set (-)	Measured momentum 1 (N)	Measured momentum 2 (N)
24-May-01	94785	71633	36893	0.3210	0.0135	22.8	22.4	0.443	0.662	0.646	None	None
24-May-01	92706	70167	36813	0.2611	0.0168	23.2	22.4	0.443	0.716	0.700	6.4	7.4
24-May-01	101222	79095	44971	0.2285	0.0202	23.4	23.4	0.407	0.698	0.661	9.1	8.2
24-May-01	106580	84058	49591	0.2101	0.0236	22.5	23.3	0.411	0.723	0.684	10.3	9.2
25-May-01	113381	92175	62009	0.1333	0.0337	22.7	22.3	0.447	0.861	0.847	12.3	12.5
25-May-01	67317	55066	35985	0.0394	0.0270	21.4	22.0	0.458	0.904	0.890	7.2	7.4
25-May-01	61068	52555	39127	0.0191	0.0305	20.1	21.4	0.483	0.952	0.956	8.0	7.7
31-May-01	98443	90355	77252	0.0103	0.0402	19.9	21.7	0.474	0.926	0.894	14.7	14.5
28-May-01	215028	179241	124500	0.4725	0.0201	25.1	23	0.423	0.750	0.740	22.8	21.9
29-May-01	143807	113745	70640	0.3663	0.0236	22	21.9	0.465	0.711	0.678	12.1	11.7
30-May-01	116784	91515	54315	0.2692	0.0236	21.5	21.6	0.478	0.807	0.739	9.2	10.7
30-May-01	143879	117007	77098	0.2698	0.0304	20.7	22.3	0.449	0.746	0.671	14.9	14.2
30-May-01	204440	176591	136156	0.1912	0.0502	20.6	22.4	0.445	0.808	0.730	24.2	25.0
31-May-01	179079	158010	126637	0.0724	0.0502	20.9	23.8	0.395	0.880	0.858	23.3	23.2
31-May-01	190976	173350	147621	0.0382	0.0602	20.6	23.5	0.405	0.911	0.881	26.9	27.2
31-May-01	194344	181396	160840	0.0177	0.0670	20.2	22.5	0.442	0.929	0.895	29.9	29.5

Table D.35: Discharge Orifice Plate Data

Test Date (dd/mm/yy)	4.00 (N/m^2)	Exit Pressure (N/m^2)	Liquid mass flow rate (kg/s)	Gas mass flow rate (kg/s)	Gas Temp. (^{o}C)	Liquid Temp. (^{o}C)	Liquid Viscosity (Ns/m^2)	Void_F CL (-)	Void_F Off Set (-)	Measured momentum 1 (N)	Measured momentum 2 (N)
21-Mar-01	59912		0.3435	0.0136	19.2	24.0	0.609	0.646	0.541	9.4	6.5
22-Mar-01	64442		0.2831	0.0169	19.6	23.7	0.623	0.737	0.686	7.7	9.3
23-Mar-01	65905		0.2481	0.0203	19.6	24.7	0.579	0.722	0.688	8.7	9.9
23-Mar-01	73198		0.2210	0.0237	19.6	24.7	0.579	0.744	0.735	10.4	9.0
27-Mar-01	89721		0.1508	0.0339	18.8	23.4	0.520	0.871	0.717	12.2	13.3
27-Mar-01	48516		0.0387	0.0271	18.9	23.2	0.528	0.915	0.785	7.5	7.7
27-Mar-01	46660		0.0198	0.0305	19.1	22.8	0.546	0.942	0.848	7.4	8.2
6-Apr-01	45427		0.0104	0.0339	18.9	18.9	0.698	0.917	0.917	7.5	9.5
28-Mar-01	112961	35850	0.4734	0.0203	19.6	22.3	0.694	0.629	0.451	17.0	14.3
2-May-01	109335	30100	0.4138	0.0237	20.7	22.7	0.426	0.713	0.689	14.5	15.6
3-Apr-01	88999	22033	0.2917	0.0236	22.6	21.6	0.597	0.759	0.710	14.0	12.8
4-Apr-01	114271	31522	0.2890	0.0305	19.9	21.8	0.587	0.762	0.735	16.2	17.7
4-Apr-01	164785	55339	0.2083	0.0503	19.7	22.7	0.544	0.823	0.789	21.8	23.3
1-May-01	141256	42970	0.0695	0.0502	21	20.1	0.530	0.858	0.836	21.8	21.6
5-Apr-01	160006	52308	0.0411	0.0603	20.1	21.7	0.592	0.908	0.899	######	26.7
6-Apr-01	161087	51608	0.0165	0.0671	19	19	0.692	0.925	0.928	######	28.5

Table D.36: Discharge Nozzle Nominal Viscosity 500mpAs Data

Test Date (dd/mm/yy)	2.90 (N/m^2)	3.40 (N/m^2)	4.00 (N/m^2)	Exit Pressure (N/m^2)	Liquid mass flow rate (kg/s)	Gas mass flow rate (kg/s)	Gas Temp. (°C)	Liquid Temp. (°C)	Liquid Viscosity (Ns/m^2)	Void_F CL (-)	Void_F Off Set (-)	Measured momentum (N)	Measured lmomentum 2 (N)
26-Jul-01	82958	67543	50215		0.327278	0.0135	23.6	22.0	0.253	0.765	0.711	9.5	4.6
26-Jul-01	82223	67888	50221		0.25498	0.0168	23.3	22.0	0.253	0.764	0.852	8.2	5.8
25-Jul-01	87515	73030	55525		0.223526	0.0202	24.1	22.0	0.253	0.712	0.639	10.2	7.3
25-Jul-01	94604	80119	62794		0.203565	0.0235	24.6	22.1	0.251	0.775	0.707	11.7	8.3
25-Jul-01	109433	95402	78213		0.131102	0.0335	25.8	22.2	0.249	0.827	0.761	14.3	11.2
27-Jul-01	55432	47689	38401		0.039385	0.0269	23.2	23.2	0.231	0.870	0.862	8.2	5.6
27-Jul-01	60586	53735	44527		0.022278	0.0337	22.7	22.7	0.240	0.897	0.891	10.1	7.4
27-Jul-01	94097	87094	76501		0.016406	0.0466	23.2	23.2	0.231	0.913	0.907	16.8	13.5
27-Jul-01	140718	121771	98273	27754	0.478924	0.0202	23.5	23.5	0.226	0.688	0.676	17.8	14.1
30-Jul-01	134828	117083	95543	28325	0.37018	0.0235	25.2	25.2	0.200	0.746	0.706	15.8	13.4
30-Jul-01	109216	93956	75357	19825	0.263986	0.0236	21.8	21.8	0.257	0.764	0.750	13.5	9.9
31-Jul-01	130984	114619	94971	27761	0.244491	0.0303	22.8	22.8	0.238	0.796	0.783	16.4	13.6
31-Jul-01	187661	170629	149408	53693	0.192775	0.0500	22.2	22.2	0.249	0.843	0.837	26.0	21.8
31-Jul-01	-67425	142306	126540	39528	0.073955	0.0500	22.4	22.4	0.246	0.876	0.864	23.0	19.8
31-Jul-01	162302	151396	136365	41858	0.035673	0.0601	22.2	22.2	0.249	0.910	0.900	25.7	22.2
31-Jul-01	166517	158176	146995	43409	0.019482	0.0667	22.1	22.1	0.251	0.948	0.952	29.7	25.5

Table D.37: Discharge Nozzle Nominal Viscosity 200mPas Data

Test Date (dd/mm/yy)	2.90 (N/m^2)	3.40 (N/m^2)	4.00 (N/m^2)	Exit Pressure (N/m^2)	Liquid mass flow rate (kg/s)	Gas mass flow rate (kg/s)	Gas Temp. (°C)	Liquid Temp. (°C)	Liquid Viscosity (Ns/m^2)	Void_F CL (-)	Void_F OffSet (-)	Measured momentum 1 (N)	Measured momentum 2 (N)
27-Aug-01	87683	77317	75478	18620	0.4356	0.0201	25.4	36.3	0.085	0.847	0.836	18.3	12.5
27-Aug-01	75332	65473	60313	15740	0.3192	0.0235	23.9	38.4	0.076	0.844	0.826	13.4	11.6
27-Aug-01	113158	103501	94281	29881	0.3174	0.0303	23.9	35.6	0.089	0.820	0.803	19.1	17.9
28-Aug-01	104409	94933	86965	26330	0.2429	0.0303	23.1	36.4	0.085	0.884	0.881	20.0	17.1
28-Aug-01	195103	187687	176205	67660	0.1767	0.0501	21.9	37.3	0.081	0.900	0.910	33.0	31.4
28-Aug-01	175519	168257	155833	57080	0.1140	0.0501	21.7	33.0	0.102	0.906	0.908	28.7	26.9
28-Aug-01	187479	180396	169909	59432	0.0665	0.0600	22.4	34.4	0.094	0.944	0.949	31.0	29.2
28-Aug-01	188065	179579	168868	54263	0.0321	0.0667	22.5	31.1	0.113	0.954	0.951	31.0	29.2
28-Aug-01	47984	41703	35979		0.2930	0.0135	23.1	40.1	0.068	0.854	0.866	10.0	9.6
29-Aug-01	55721	48637	43040		0.2428	0.0169	22.4	36.3	0.085	0.878	0.852	11.0	9.2
29-Aug-01	65327	55206	47572		0.2243	0.0202	22.3	39.4	0.071	0.850	0.859	11.4	11.0
29-Aug-01	73377	67291	54985		0.1756	0.0236	22.9	37.9	0.078	0.820	0.826	12.1	11.0
29-Aug-01	69512	58889	50307		0.1412	0.0236	22.7	39.2	0.072	0.822	0.829	11.6	10.2
29-Aug-01	58667	52234	39892		0.0678	0.0270	22.4	36.2	0.086	0.863	0.871	9.8	8.6
29-Aug-01	53784	49042	37202		0.0391	0.0303	22.7	34.6	0.093	0.874	0.885	9.4	8.1
29-Aug-01	52427	47226	35406		0.0174	0.0337	22.4	30.4	0.117	0.893	0.900	9.7	8.1

Table D.38: Discharge Nozzle Nominal Viscosity 50mPas Data

APPENDIX E

E.1 Quadratic Constants for Test Length Pressure Gradient

E.1.1 Air-water Two-phase Tests

Nominal Quality	a2	a1	a0
0.04	349.31	-11714	41416
0.06	214.13	-11359	42155
0.08	1.3885	-10559	42525
0.1	-127.98	-9082.2	38460
0.2	-79.121	-10658	44467
0.4	0.6147	-9332.2	37613
0.6	-249.7	-8723.8	38902
0.8	-381.9	-8586.8	39684

Table E.1: Quadratic constants.

E.1.2 Air-glycerine Two-phase Tests

Nominal Quality	a2	a1	a0
0.04	-1724.4	-59222	276691
0.06	-2807.5	-43078	225521
0.08	-2393.3	-40515	209516
0.1	-3122.2	-46528	247989
0.2	-2785.8	-46767	243426
0.4	-3551	-45445	256239
0.6	-3639.1	-38084	227859
0.8	-4432	-24491	183676

Table E.2: Quadratic constants for 550 mPas.

Nominal Quality	a2	a1	a0
0.04	-689.59	-30719	149295
0.06	-1018.7	-25681	121758
0.08	-1370.6	-25439	127674
0.1	-1290.3	-27042	134216
0.2	-2671	-35544	211297
0.4	-459.93	-37265	169110
0.6	-2294.9	-26094	150774
0.8	-2330.6	-23398	139844

Table E.3: Quadratic constants for 200 mPas.

Nominal Quality	a2	a1	a0
0.04	-463.84	-15085	68081
0.06	-1077.5	-10567	55112
0.08	-675.58	-10976	54321
0.1	-597.8	-12570	61454
0.2	-516.56	-16088	67650
0.4	-888.28	-20418	101233
0.6	-1500	-20771	113787
0.8	-1713.5	-20965	119312

Table E.4: Quadratic constants for 50 mPas.